

**“Simulation study of energy transfer chain  
of DEMONstration Balance of Plant  
on behalf of operation stability”**

Zur Erlangung des akademischen Grades einer

DOKTORIN DER INGENIEURWISSENSCHAFTEN (Dr.-Ing.)

von der KIT-Fakultät für Chemieingenieurwesen und Verfahrenstechnik des

Karlsruher Instituts für Technologie (KIT)

genehmigte

DISSERTATION

von

Maria-Victoria Bologna

aus Stutensee

Tag der mündlichen Prüfung: 12.07.2024

Erstgutachter: Prof. Dr.-Ing. Thomas Wetzel

Zweitgutachter: Prof. Dr.-Ing. Marc Kamlah



This document is licensed under a Creative Commons Attribution-NonCommercial-ShareAlike 4.0 International License (CC BY-NC-SA 4.0):  
<https://creativecommons.org/licenses/by-nc-sa/4.0/deed.en>

**Life is like riding a bicycle.**

**To keep your balance you must keep moving.**

*Albert Einstein*



## Acknowledgements

My special thanks go to Prof. Dr.-Ing. Thomas Wetzels and Prof. Dr.-Ing. Marc Kamlah for being the referents of my doctoral thesis.

I would like to thank Prof. Dr.-Ing. Robert Stieglitz<sup>†</sup> for the methodical support during my doctorate period at the Institute for Neutron Physics and Reactor Technology (INR), Karlsruhe Institute of Technology (KIT).

I thank Dr. Wolfgang Hering for goal-oriented dialogues with insightful comments and suggestions, which have helped to develop my professional skills.

I also thank Prof. Dr. Veit Hagenmeyer for fruitful cooperation in framework of joint initiative “Energy Systems 2050”. I am grateful for the constructive and pleasant collaboration with the Institute for Automation and Applied Computer Science, KIT.

Many thanks go to the members of the department Facility Design, System Dynamics and Safety at INR for valuable recommendations during my Ph.D. study. My special thanks go to very competent IT administration for their support with the required simulation tools.

Many thanks go to Oliveira, Césaire Pasquet and Haseeb Nawaz for providing valuable insights during their work at INR, what also contributed to success of the research study. I am thankful for constructive sharing of experience with Ph.D. fellows and colleagues during national and international workshops. Many interesting talks encouraged me to move on with my work.

I want to express special thanks from the bottom of my heart to my parents and my brother, who always accompanied me with patience, motivation and love. With their strong support, I could believe in my strengths and successfully finalize my doctoral thesis, which is dedicated to my family. Finally, I want to thank my grandfather and my aunt from far away for their strong moral support on my way towards the finish of my doctoral thesis.

Karlsruhe, July 2024

Maria-Victoria Bologna



## Danksagung

Mein besonderer Dank geht für das entgegengebrachte Vertrauen an Herrn Prof. Dr.-Ing. Thomas Wetzel und Prof. Dr.-Ing. Marc Kamlah als Gutachter meiner Doktorarbeit.

Ich bedanke mich bei Herrn Prof. Dr.-Ing. Robert Stieglitz<sup>†</sup> für die methodische Unterstützung während meiner Promotionszeit am Institut für Neutronenphysik und Reaktortechnik, KIT.

Ein großer Dank geht an Dr. Wolfgang Hering für seine professionellen Ratschläge sowie zielgerichteten Empfehlungen. Dadurch konnte ich meinen Wissenshorizont namentlich erweitern.

Ich danke ebenfalls Herrn Prof. Dr. Veit Hagenmeyer für die angenehme, produktive Zusammenarbeit im Rahmen des HGF-Projektes „Energiesysteme 2050“. Außerdem bin ich dankbar für die Unterstützung der Kollegen aus dem Institut für Automatisierung und Angewandte Informatik, KIT.

Ich möchte mich zudem bei allen Mitarbeitern vom INR bedanken, die mich moralisch unterstützt haben. Mein besonderer Dank geht an die kompetente IT-Administration bezüglich der großen Unterstützung zur Bereitstellung aller erforderlichen Simulationsprogrammen. Darüber hinaus möchte ich Joel Oliveira, Césaire Pasquet und Haseeb Nawaz für die wertvollen Erkenntnisse aus ihrer Arbeit danken, die auch zum Erfolg des Forschungsprojektes beigetragen haben. Ich bin dankbar für den konstruktiven Erfahrungsaustausch mit vielen Doktoranden und Kollegen während der nationalen und internationalen Workshops. Außerdem haben viele interessante Gespräche mich motiviert, meine Doktorarbeit mit Kreativität und guter Laune bis zum Schluss zu führen.

Nichts ist zufällig, denn ohne die liebevolle Unterstützung meiner Familie sei meine Doktorarbeit niemals zu Ende gebracht worden. Daher ist diese Doktorarbeit meiner geliebten Familie gewidmet. Mein unermesslich großer Dank geht an meinen Eltern und meinem Bruder, die mich immer mit Liebe begleitet und für eine große Stärkung in meinem Leben gesorgt haben. Mit ihrem Glauben an meinen Stärken konnte ich meine Dissertation erfolgreich verwirklichen. Auf meinen Weg zur erfolgreichen Absolvierung der Doktorarbeit bin ich ebenfalls meinem Großvater und meiner Tante, aus weiter Entfernung, für ihre moralische Unterstützung dankbar.





## Abstract

In the thesis, the study is carried out, focusing on the objectives related to design of DEMONstration Balance of Plant (DEMO BoP), as well as on plant performance and operation challenges. The scope of the work is the study of transient behaviour of DEMO BoP energy transfer chain through the simulations using MATLAB<sup>®</sup>/Simulink. For this purpose, a vast analysis of design and operational parameters of DEMO BoP is carried out, including Primary Heat Transfer System (PHTS), Intermediate Heat Transfer and Storage System (IHTS) and Power Conversion System (PCS), which are used as input simulation data. In DEMO IHTS system, HITEC molten salt (MS) is applied as both heat transfer fluid and sensible thermal energy storage medium. In the thesis, an extended literature survey of HITEC properties is performed. A set of functional relations, which describe temperature dependence of HITEC thermo-physical parameters, is defined for novel customized MATLAB<sup>®</sup> module. A model, which describes mass and heat transfer phenomena in thermal storage tank, is reviewed. The results are applied for development of novel customized MATLAB<sup>®</sup> module for simulation of heat losses to environment from thermal storage tanks. The results of simulations of temporal evolution of MS temperature inside thermal storage tanks, as well as heat losses to environment, are evaluated through comparison with numerical data, known from literature survey. The simulation models for DEMO PHTS-IHTS and DEMO PCS systems are developed. For these models, MATLAB<sup>®</sup> Library standard, as well as customized modules are applied. The modules' governing equations and corresponding assumptions are discussed. The results of simulations are used for optimization of design of thermal storage tanks, as well as for study of interplay between storage tank geometrical parameters and MS properties. The simulations of temporal evolution of mass and heat flows in DEMO PHTS-IHTS and DEMO PCS systems during fusion reactor cycling operation are carried out. The study is extended with simulation of temporal evolution of mechanical power output downstream DEMO PCS steam turbines. The results of simulations using MATLAB<sup>®</sup>/Simulink are evaluated and verified through the comparison with the data from quasi-stationary simulations. The verification shows good correlation between simulated parameters' values. Finally, MATLAB<sup>®</sup>/Simulink simulation model for DEMO BoP energy transfer chain is developed. The novelty consists in coupling of DEMO PHTS-IHTS and DEMO PCS models through thermal ports. The obtained results of numerical simulations confirm the ability of the developed MATLAB<sup>®</sup>/Simulink model to be applied for the study of transient behaviour of DEMO BoP energy transfer chain on behalf of operation stability.



## Kurzfassung

In der Doktorarbeit liegen die Schwerpunkte auf dem Design, sowie auf der Anlagenleistung und den betrieblichen Herausforderungen von DEMONstration Balance of Plant (DEMO BoP) für die Fusionstechnologie. Das Ziel der Arbeit ist die Untersuchung des transienten Verhaltens der Energieübertragungskette von DEMO BoP mittels MATLAB®/Simulink. Für das Simulationsmodell des Primärwärmeübertragungssystems (PHTS), des Zwischenwärmeübertragungs- und Speichersystems (IHTS), sowie des Energieumwandlungssystems (PCS), wurde eine umfassende Studie der Design- und Betriebsparameter, die als Simulationsdateninput gelten, durchgeführt. HITEC-Salzschnmelze wurde als Wärmeübertragungsflüssigkeit sowie als ein sensibles Wärmeenergiespeichermedium für DEMO IHTS ausgewählt. Dafür wurde eine erweiterte Literaturrecherche zu den Eigenschaften der Salzschnmelze erbracht. Eine Reihe von analytischen Gleichungen, die die Temperaturabhängigkeit von thermophysikalischen Parametern des HITEC beschreiben, wurde definiert und in einem neuen angepassten MATLAB®-Modul eingeführt. Ein geeignetes Modell wurde entwickelt, welches die Massen- und Wärmeübertragungsphänomene im thermischen Energiespeicherbehälter beschreibt. Ein neuartiger MATLAB®-Modul wurde zur Simulation von Wärmeverlusten aus dem Speicherbehälter an die Umgebung entwickelt. Die Simulationsergebnisse zur Wärmeübertragung aus dem Speicherbehälter an die Umgebung wurden mit bekannten Literaturdaten verglichen und evaluiert. Die Simulationsmodelle von DEMO PHTS-IHTS- und DEMO PCS-Systemen wurden mit MATLAB®/Simulink entwickelt. Zur Modellentwicklung wurden sowohl Standardmodule der MATLAB®-Bibliothek, als auch die selbst neuangepassten MATLAB®-Module eingesetzt. Dabei liegt der Schwerpunkt auf der Beschreibung der entsprechenden Randbedingungen für die physikalischen Modelle, sowie der maßgeblichen Gleichungen. Die Simulationen wurden zur Optimierung des Designs der thermischen Energiespeicherbehälter verwendet. Der Zusammenhang zwischen geometrischen Parametern der Speicherbehälter und den Eigenschaften der Salzschnmelze wurde untersucht. In DEMO PHTS-IHTS und DEMO PCS-Systemen wurden Simulationen zur zeitlichen Entwicklung von Massen- und Wärmeströmen während des zyklischen Fusionsreaktorbetriebes durchgeführt. Die Ergebnisse wurden zur Berechnung der mechanischen Leistung hinter den DEMO PCS-Dampfturbinen herangezogen. Die Daten aus MATLAB®/Simulink-Modellen wurden mit Daten aus quasi-stationärem Simulationsmodell verglichen. Die Verifizierung der jeweiligen Simulationsdaten zeigt eine Übereinstimmung zwischen den Ergebnissen von dynamischer und quasi-stationärer Modellierung. Abschließend wurde das

MATLAB<sup>®</sup>/Simulink-Modell zur Untersuchung des transienten Verhaltens der Energieübertragungskette von DEMO BoP entwickelt. Die Neuartigkeit des Modells entsteht in der Modellenkopplung der DEMO PHTS-IHTS mit DEMO PCS mittels thermischer Anschlüsse der entsprechenden Module. Im Hinblick auf die Betriebsstabilität, bestätigen die Ergebnisse der numerischen Simulationen die Eignung des entwickelten MATLAB<sup>®</sup>/Simulink-Modells für die Untersuchung des transienten Verhaltens der Energieübertragungskette von DEMO BoP.

# Nomenclature

## Abbreviations

AUXB	Auxiliary Boiler
BB	Breeding Blanket
CFD	Computational Fluid Dynamics
CSP	Concentrated Solar Power Plant
DCD	Direct Coupling Design
DEMO	DEMONstration Power Plant
DEMO BoP	DEMONstration Balance of Plant
DEMO FPP	DEMONstration Fusion Power Plant
DIV-Cas	Divertor Cassettes
DIV-PFU	Divertor Plasma Facing Units
EBSILON®	Simulation Code
ENTSO-E	European Network of Transmission System Operators
ESI	Energy System Integration
ESS	Energy Storage System
EU	European Union
FW	Feedwater
HCPB	Helium Cooled Pebble Bed
HITEC / HITEC <sup>XL</sup>	Salt Mixture
HP	High Pressure
HTF	Heat Transfer Fluid
HX	Heat Exchanger
IB	Inner Blanket
ICD	Indirect Coupling Design
IHTS	Intermediate Heat Transfer and Storage System
INR	Institute for Neutron Physics and Reactor Technology
ITER	International Thermonuclear Experimental Reactor
KIT	Karlsruhe Institute of Technology
LP	Low Pressure
MATLAB®	Programming Tool
Simulink	Data Flow Graphical Programming Language Tool
MS	Molten Salt

OB	Outer Blanket
PCS	Power Conversion System
PH	Pre-heater
PHTS	Primary Heat Transfer System
PI	Proportional Integral
SDHT	Specific Dissipation Heat Transfer
SG	Steam Generator
SH	Super-heater
SR	Steam Re-heater
TES	Thermal Energy Storage
TL	Thermal Liquid
TOKAMAK	Fusion Reactor
VV	Vacuum Vessel
VVPSS	Vacuum Vessel Pressure Suppression System

## Roman Symbols

Symbol	Definition	Unit
A	Area	m <sup>2</sup>
A, B, V, L, T, H, C, R	Port, block	-
a, b c, k	Constant, coefficient	-
a, b	Radius	m
B	Thickness	m
°C	Grad Celsius	-
c <sub>p</sub>	Specific heat capacity	J/(kg·K)
D	Diameter, “Displacement” parameter	m, -
d	Distance	m
E	Energy	J
$\dot{E}$	Energy flow rate	W
F	Shape factor, water flow rate	-, kg/s
f	Function, Darcy friction factor	-, -
g	Acceleration due to gravity	m/s <sup>2</sup>
Gr	Grashof number	-
GW, GW <sub>th</sub>	Gigawatt, Gigawatt-thermal	-
H	Height	m
h	Hour	-
h	Heat transfer coefficient, enthalpy	W/(m <sup>2</sup> K), J
k	Thermal conductivity	W/(m·K)
K	Kelvin	-
kg	Kilogram	-
L, l	Length, filling level, characteristic length	m
ln	Natural logarithm	-
M, m	Mass	kg
$\dot{m}$	Mass flow rate	kg/s
MW, MWe	Megawatt, Megawatt-electric	-
MPa	Mega-Pascal	-
Nu	Nusselt number	-
Pr	Prandtl number	-
Re	Reynolds number	-

P, p	Pressure, power	Pa (bar), W
S	Area	m <sup>2</sup>
s, sec	Second	-
W	Watt	-
Wh <sub>th</sub>	Watt-hour-thermal	-
Q	Thermal energy, heat	J
$\dot{Q}$	Thermal energy flow	W
q	Specific heat loss per area, condenser heat duty	W/m <sup>2</sup> , kW
t	Time	sec, hour, day
s	Auxiliary transition function	-
SD	Specific dissipation	-
T	Temperature	°C, K
u	Specific internal energy	J/kg
U	Internal energy	J
v	Velocity	m/s
V	Volume	l, m <sup>3</sup>
$\dot{V}$	Volumetric flow rate	m <sup>3</sup> /s
W	Work, width	J, m
$\dot{W}$	Work flow, mechanical power	J/s, W
z	Level of height	m
€	Euro	-
\$	Dollar	-



## Greek Symbols

<b>Symbol</b>	<b>Definition</b>	<b>Unit</b>
$\alpha$	Thermal diffusivity	$\text{m}^2/\text{s}$ , Pa
$\beta$	Volumetric heat capacity	$\text{J}/(\text{m}^3\cdot\text{K})$
$\lambda$	Laminar friction constant	-
$\gamma$	Surface tension	N/m
$\varepsilon$	Bed void fraction, surface emissivity, surface roughness	-
$\eta$	Efficiency	-
$\mu$	Dynamic viscosity	Pa·s, $\text{kg}/(\text{m}\cdot\text{s})$
$\nu$	Kinematic viscosity	$\text{m}^2/\text{s}$
$\pi$	Mathematical constant	-
$\rho$	Density	$\text{kg}/\text{m}^3$
$\sigma$	Stefan-Boltzmann constant	$\text{W}/(\text{m}^2\cdot\text{K}^4)$
$\tau$	Characteristic time for equilibrium of a phase-change event	s
$\omega$	Angular velocity	$\text{s}^{-1}$
$\Delta$	Difference	-

## Subscripts / Superscripts

<b>Script</b>	<b>Definition</b>
A, B	Ports
air	Air
amb	Ambiant
Avr	Average
bottom	Bottom
ch	Characteristic linear dimension
chain	Chain
cr	Critical
cold	Cold
cond	Conductive
conv	Convective
cor	Corrected
dyn	Dynamic
dry	Dry
forced	Forced
fluid	Fluid
HITEC	HITEC molten salt
hot	Hot
i	Number
ideal	Ideal
in / out	Inner / Outer (Inlet / Outlet)
ins	Insulation
loss	Heat loss to environment
mech	Mechanical
min / max	Minimum / Maximum
m	Melting point
natural	Natural
net	Net
Nom	Nominal
nw	Non-wetted

op	Operating
part	Part
pipe	Pipe
rad	Radiative
rel	Relative
roof	Roof
sim	Simulation
sky	Sky
surface	Surface
T	Temperature
tank	Tank
therm, th	Thermal
total	Total
tube	Tube
vap	Vapour
wall	Wall
wet	Wet
$\infty$	Bulk



# Table of Contents

<b>Acknowledgements</b> .....	<b>I</b>
<b>Danksagung</b> .....	<b>III</b>
<b>Abstract</b> .....	<b>V</b>
<b>Kurzfassung</b> .....	<b>VII</b>
<b>Nomenclature</b> .....	<b>IX</b>
<b>1 Introduction</b> .....	<b>1</b>
1.1 Road map for Fusion Power Plant.....	1
1.2 DEMONstration Balance of Plant.....	3
1.3 DEMONstration Intermediate Heat Transfer and Storage System design concept .....	6
1.3.1 Storage of thermal energy .....	7
1.3.2 DEMO IHTS two tank design concept.....	8
1.4 Scope and tasks of the thesis .....	9
<b>2 Simulation of HITEC molten salt properties</b> .....	<b>13</b>
2.1 Properties of heat transfer fluids.....	13
2.2 Properties of HITEC molten salt.....	17
2.3 Stability and compatibility of HITEC molten salt .....	19
2.3.1 Thermal and chemical stability of HITEC molten salt.....	19
2.3.2 Compatibility of HITEC molten salt with constructive materials.....	20
2.4 Simulation of thermo-physical properties of HITEC molten salt .....	21
2.5 Sensitivity of simulated parameters on HITEC molten salt temperature.....	26
2.6 Conclusions .....	29
<b>3 Simulation model of DEMO IHTS thermal storage tank</b> .....	<b>31</b>
3.1 Heat transfer model of thermal storage tank .....	31
3.2 MATLAB®/Simulink model of DEMO IHTS thermal storage tank .....	35
3.3 Conclusions .....	40
<b>4 Temporal evolution of DEMO IHTS thermal storage tank parameters</b> ..	<b>41</b>
4.1 Design parameters for simulation model of DEMO IHTS thermal storage tanks .....	41
4.2 Interplay between molten salt filling level and thermal storage tank geometry .....	42
4.3 Heat losses to environment from thermal storage tanks .....	48
4.4 Evaluation and validation of simulation model for heat losses to environment .....	52
4.5 Conclusions .....	56

<b>5 Simulation model of DEMO PHTS-IHTS and DEMO PCS systems.....</b>	<b>57</b>
5.1 Development of DEMO PHTS-IHTS simulation model .....	57
5.2 Modules of DEMO PHTS-IHTS simulation model.....	59
5.2.1 Thermal liquid pipeline module .....	59
5.2.2 Fixed-displacement pump module .....	62
5.2.3 PHTS Inner Blanket/Outer Blanket Loops module.....	64
5.2.4 PCS steam generator module.....	69
5.3 Development of DEMO PCS simulation model .....	70
5.4 Modules of DEMO PCS simulation model.....	71
5.4.1 Steam generator module .....	71
5.4.2 Pre-heater and super-heater modules.....	74
5.4.3 High-pressure and low-pressure steam turbines with re-heater modules.....	78
5.4.4 Steam condenser module .....	80
5.4.5 Feedwater pump module .....	81
5.5 Conclusions .....	83
<b>6 Simulation of temporal evolution of mass and heat flows in DEMO PHTS-IHTS and DEMO PCS systems .....</b>	<b>85</b>
6.1 Simulation of temporal evolution of molten salt filling level in DEMO IHTS thermal storage tanks.....	85
6.2 Simulation of temporal evolution of mass flow in DEMO PHTS-IHTS system.....	89
6.3 Simulation of temporal evolution of heat flow in DEMO PHTS-IHTS system .....	90
6.4 Simulation of temporal evolution of liquid volume fraction in DEMO PCS steam generator.....	92
6.5 Simulation of temporal evolution of mass flow in DEMO PCS modules .....	94
6.6 Simulation of temporal evolution of heat flow in DEMO PH-SG-SH modules.....	95
6.7 Simulation of temporal evolution of DEMO PCS mechanical power .....	98
6.8 Evaluation of the results of numerical simulations .....	99
6.8.1 Verification of simulation data for DEMO PHTS-IHTS model .....	99
6.8.2 Verification of simulation data for DEMO PCS model .....	103
6.9 Conclusions .....	106
<b>7 Simulation model of DEMO BoP energy transfer chain.....</b>	<b>107</b>
7.1 Development of simulation model for DEMO BoP energy transfer chain .....	107
7.2 Coupling of DEMOnstration Fusion Power Plant to external electrical grid .....	112

7.3 Conclusions .....	114
<b>8 Summary and outlook.....</b>	<b>115</b>
8.1 Summary .....	115
8.2 Outlook.....	118
<b>References .....</b>	<b>119</b>
<b>Publications, conferences, seminars and supervision contribution.....</b>	<b>143</b>
<b>A Appendix .....</b>	<b>145</b>
A.1 DEMONstration Balance of Plant coupling design concepts .....	145
A.2 DEMO BoP quasi-stationary simulation model.....	150
A.3 TES single tank design concept.....	153
A.4 TES operational parameters for DEMO BoP and CSP plants.....	155
A.5 DEMONstration Balance of Plant parameters .....	156
A.6 DEMONstration Balance of Plant systems' design and operational parameters .....	158
A.7 MATLAB®/Simulink Custom Library: Rankine Cycle model .....	176
<b>List of Figures .....</b>	<b>179</b>
<b>List of Tables.....</b>	<b>183</b>





# 1 Introduction

From 1970 onwards, energy demand in the world has rapidly grown, being satisfied mainly by fossil fuels [1-4]. Nowadays, world's actions are crucial to create a sustainable energy system, in which renewable energy sources, that proved long-term security of supply, have to replace fossil fuels [5-9]. In Germany, the strategic transformation of energy system is focused on the development of decarbonized multi-modal energy system with variable renewable energy sources and system integration. This development demands comprehensive multiple view over the infrastructure and components, stability and controllability, reliability, safety, economic viability, environmental compatibility, legislation, as well as social and ethical aspects [10-17].

Being a part of strategic development, the Energy System Integration 2050 (ESI 2050), a joint initiative of research field energy of Helmholtz Association in Germany, is aimed on the improvement of understanding of energy systems and development of technological solutions for use by politics and industry [8]. The initiative focuses on the integration of relevant technology elements into energy system and addresses those aspects of energy system that make all individual components to form a whole [18-27].

To provide zero-carbon emissions, large-scale expansion of renewable technologies has to be realized [4, 28]. In this way, wind and solar energy underbid fossil-fuel power plants [18, 28, 29]. Nuclear energy remains a low-carbon option for generating electricity with significant gains [2].

Fusion energy opens possibilities to provide a cost-efficient and sustainable solution to European and global energy needs [30]. Fusion, as a based-load energy generation option, is expected to contribute to decarbonization and climate change mitigation measure from its market penetration after 2050 [3, 5, 31-35].

## 1.1 Road map for Fusion Power Plant

The European Commission proposal for EURATOM programme in Horizon 2020 states an ambitious roadmap to fusion electricity (see Fig. 1.1). The International Thermonuclear Experimental Reactor (ITER) and DEMONstration Fusion Power Plant (DEMO FPP) are some of its key facilities [36]. The scope of ITER, which is one of the most ambitious energy projects, is to build world's largest TOKAMAK reactor to prove the feasibility of fusion as a large-scale energy source [37].

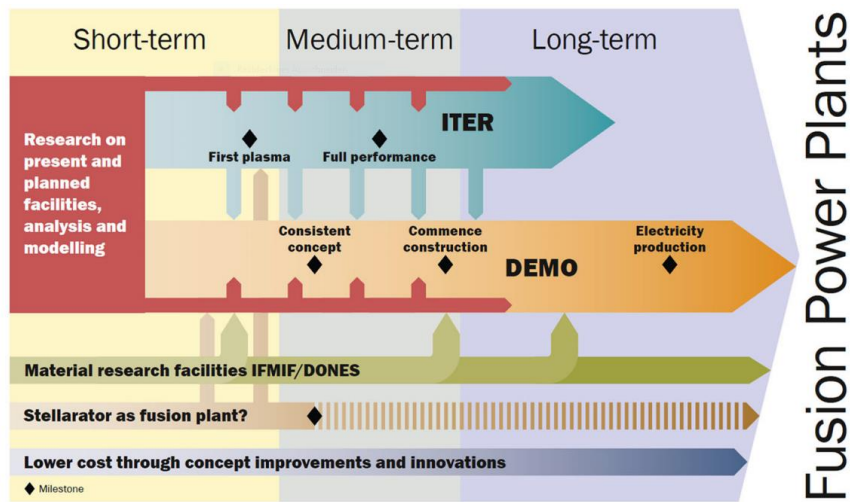


Fig. 1.1: The European Fusion Roadmap [36].

ITER is the first fusion device designed to produce net fusion power of 500 MW over a significant long pulse with only about 50 MW input heating power, injected to heat the plasma. It is expected that most of important milestones, which should be achieved by putting ITER into operation, should provide ground for many systems, materials and technologies, needed for development of commercial scale fusion reactors [32, 38-40].

Aside to ITER, the research work is underway on the conception of next-stage machine - DEMONstration Fusion Power Plant, which has to upgrade all technologies to the level of performance, reliability and efficiency required for production of electricity [37]. DEMO FPP is considered as a decisive step between ITER and commercial Fusion Power Plant [41, 42]. DEMO FPP has to demonstrate all technologies for construction of a commercial Fusion Power Plant, including an adequate level of availability. DEMO FPP requires innovations in material technologies, integration design of largest components with lowest cost, simple manufacturing as well as standardization of parts, high level of component reliability, maintainability and inspectability [26, 29]. The safety credit needs to be given to the systems, structures and components [43-45]. Integrated analysis is necessary for comprehensive identification of hazards and safety functions [46, 47].

The conceptual DEMO projects, such as Korean-DEMO and EU-DEMO, are under consideration [41, 42]. Korean-DEMO construction is expected to be completed by 2037 and to be used as a component test facility during its 1<sup>st</sup> operation phase, which is projected up to 2050. During the 2<sup>nd</sup> phase, most in-vessel components have to be replaced for full steady-state operation and electricity generation. A central requirement to EU-DEMO is to produce net electricity to external grid predictably in the range of 300-500 MW.

## 1.2 DEMOnstration Balance of Plant

The DEMOnstration Balance of Plant (DEMO BoP) is an engineering term, comprising all supporting and auxiliary systems, which are needed for energy conversion and delivering [40, 48]. The objectives of DEMO BoP development are to design an environmentally sound, viable, flexible and stable energy system by integrating individual technologies [33, 45, 47-54].

The schematic view of the interface of DEMOnstration Balance of Plant systems is presented in Fig. 1.2. The large number of system interdependencies give rise to a high degree of DEMO BoP complexity, what strongly influences on plant design, safety and maintainability, and demands large-scale investigations of DEMO BoP during pre-conceptual design [38, 55]. Here, any effort to reduce the complexity of DEMO BoP has a beneficial return on system design, operation safety, plant availability, power grid stability and costs [46, 56-60].

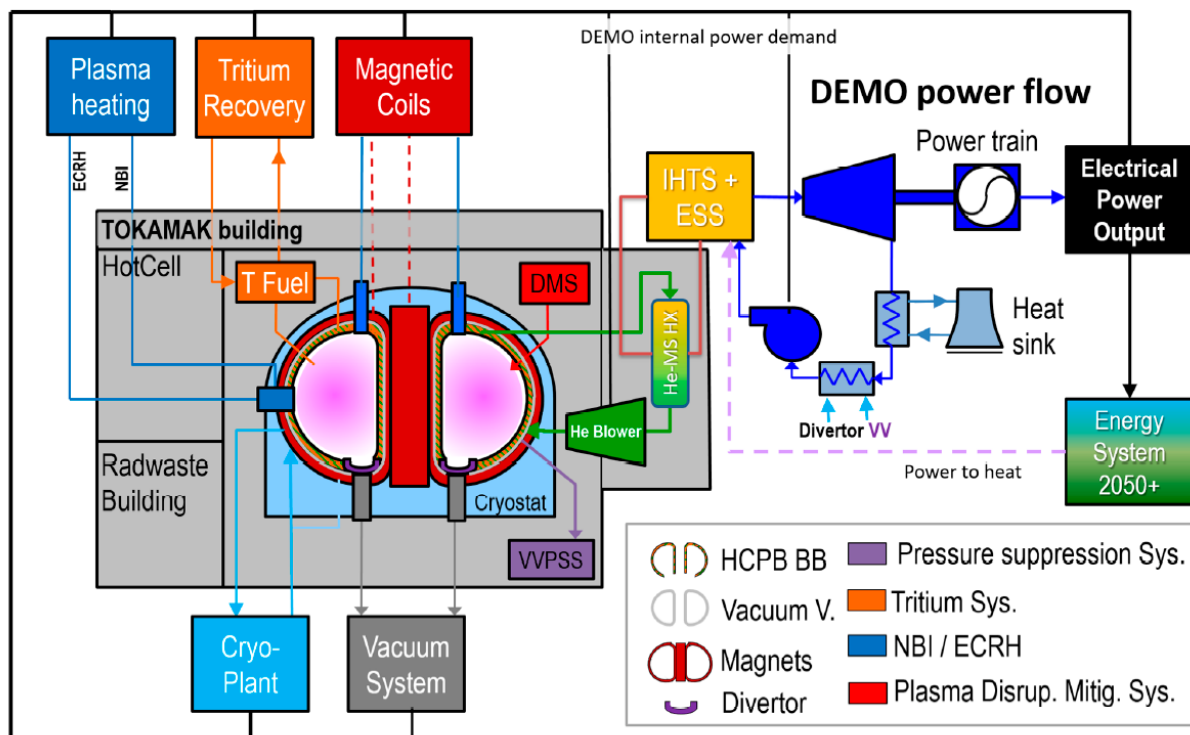


Fig. 1.2: Interface of the systems of DEMOnstration Balance of Plant with Helium Cooled Pebble Bed Indirect Coupling Design (ICD) concept: BB - Breeding Blanket, ESS - Energy Storage System, VV - Vacuum Vessel, VVPSS - Vacuum Vessel Pressure Suppression System [51, 55].

The schematic view of DEMO BoP electrical system is presented in Fig. 1.3. Major consumers are the cooling and cryogenic systems for helium breeding blanket model, requiring ~80% of total power demand between 120-250 MW. The Pulsed-Power Electrical Network, which is identified with the Coil Power Supply and Heating Power Supply systems, supplies pulsed loads that requires time-changing power during plasma operation. Turbine Generator Electrical Network provides large pulsed power, which is needed to supply the superconducting coils, and connects DEMO power train to external grid.

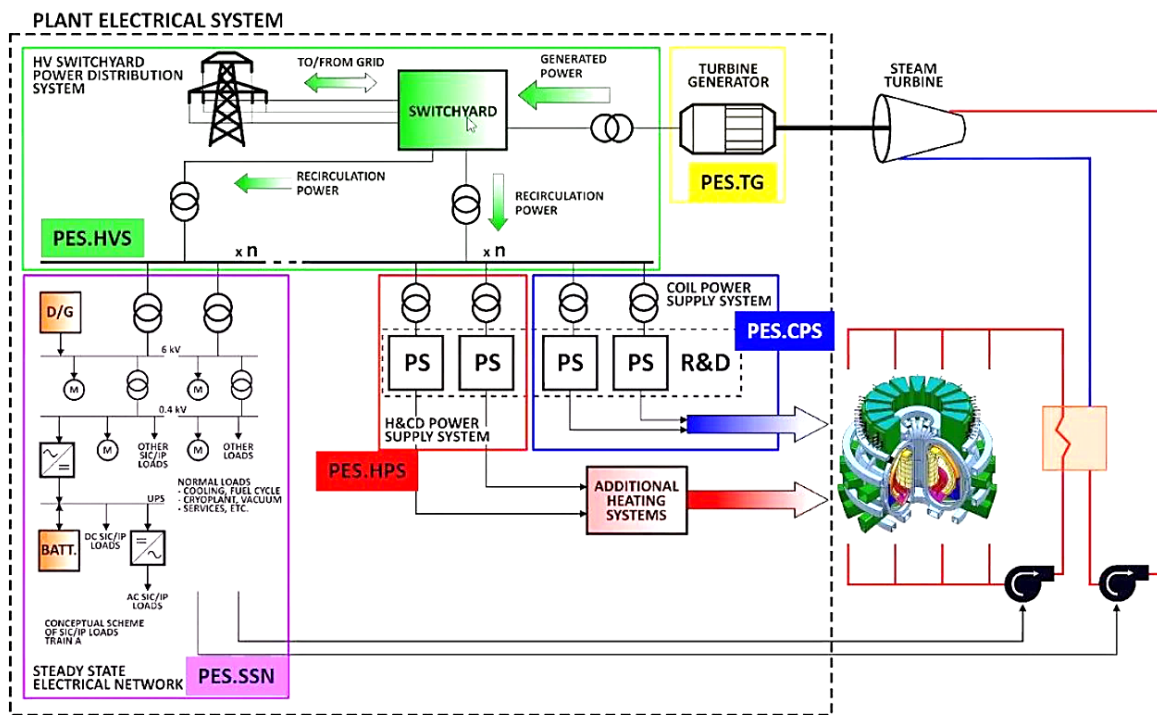


Fig. 1.3: DEMO BoP electrical distribution system [56].

The schematic view to DEMO BoP ICD concept is presented in Fig. 1.4. The concept includes fusion reactor TOKAMAK as a heat source, Primary Heat Transfer System (PHTS), Intermediate Heat Transfer and Storage System (IHST), Power Conversion System (PCS) and plenty of auxiliary equipment [51-56]. The transitions between plasma operation states, hence pulse-to-dwell and dwell-to-pulse, are the most challenging issues for coupling between DEMO Primary Heat Transfer System and Power Conversion System [5]. Previously for DEMO BoP, Direct Coupling Design (DCD) and Indirect Coupling Design (ICD) concepts are proposed (see Appendix A.1) to identify the main requirements and feasible architectures [38, 51, 55]. DCD and ICD concepts are studied, based on feasibility, applicability, integrity, performance and safety consequences, as well as the costs, which are taken into account.

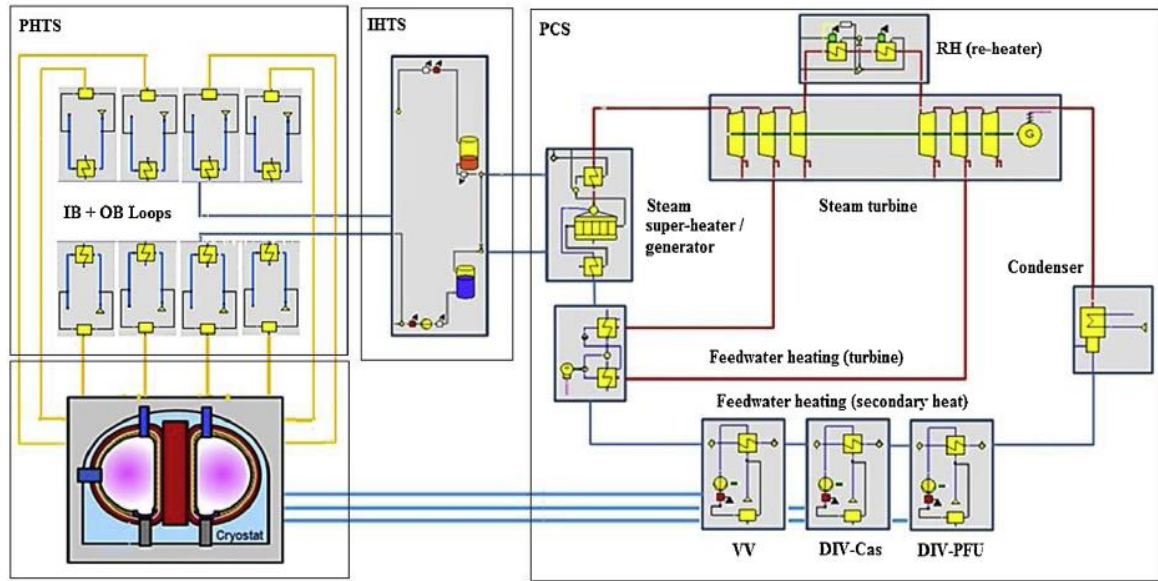


Fig. 1.4: Scheme of DEMO BoP design concept [33].

The main requirements are considered here, namely to avoid disconnection from the grid for pulse-dwell transitions and to reduce the impact of frequent temperature transients to structures. The study shows that ICD concept provides the accumulation of thermal power during plasma pulses that is released further to DEMO PCS during dwell operation [55]. DEMO IHTS is used to smooth the generated pulsed plasma power, ensuring continuous conversion process with stable production of electricity and long plant lifetime. The use of DEMO IHTS allows the electrical generators to operate in steady state without any interruptions and fluctuations during plasma phase [40, 41, 47].

In DEMO BoP (see Fig. 1.4), the fusion reactor operates in a cycle mode. A single operation cycle includes pulse (7200 sec) and dwell (600 sec) time intervals. Dwell time is needed for removal of ash and dust from fusion reactor chamber, as well as for loading of central solenoids [52]. Breeding Blanket (BB) system surrounds the plasma and is responsible for heat extraction due to cooling mechanism, to absorb the energy from neutrons produced within plasma by nuclear fusion reaction. The blanket system removes heat at an adequate thermodynamic efficiency that requires the coolants to be used at high temperature and pressure [26]. The cooling of blanket with helium is the preferable solution, which relies on chemical and radiological gas inertness at high temperature [61-63].

Helium Cooled Pebble Bed (HCPB) consists of lithiated ceramics as solid breeder, beryllium pebbles as neutron multiplier, and EUROFER as structural material, which consists of reduced-activation ferritic-martensitic steel. HCPB uses as a coolant high-pressure helium at 8 MPa. The coolant removes heat from plasma and deposit volumetrically in the surrounding in-vessel structures, what covers ~80% of total fusion power. The rest of fusion power with additional, auxiliary heating power of ~100 MW is deposited as surface heat by plasma-facing components [51-54, 56, 61, 64].

Breeding Blanket system is segmented into eight loops, each providing heat transfer into two sectors through top/upper ports, what offers benefits, referred to safety, maintenance and component size [26, 55]. Each loop incorporates two helium blowers. Helium flows through heat exchangers (HXs), ensuring heat transfer from fusion reactor blanket walls to Thermal Energy Storage (TES) system [61-63, 65-69].

DEMO IHTS stores thermal energy from BB PHTS during pulse time, manages inlet temperature to BB PHTS through the HX secondary-side inlet temperature, and transfers thermal energy to pre-heater/steam generator/super-heater, as requested by DEMO PCS. During dwell operation, the mass flow rate of heat transfer fluid (HTF) is adjusted to the need of BB decay heat removal using a dedicated small pump [47, 55].

Power Conversion System follows DEMO IHTS and is coupled through the generator to electrical grid. In DEMO PCS, heat is transferred to steam generator [70]. Secondary heat sources, such as Vacuum Vessel (VV), Divertor Cassettes (DIV-Cas) and Divertor Plasma Facing Units (DIV-PFU) are used for heating feedwater on return line to steam generator (Fig. 1.4). To increase the power output, two fluid re-heaters are installed between steam turbines. Subsequently, steam is returned back into the circuit through condenser.

Quasi-stationary simulations of DEMO BoP are previously carried out using EBSILON<sup>®</sup> code, which is a simulation tool for thermodynamic cycle processes [84, 97-101]. The code system library contains the components for power plant processes, as well as material data library, including the parameters of heat transfer fluids [102]. DEMO BoP main operational parameters, calculated through EBSILON<sup>®</sup>, are joined in Appendix A.2, Table A2.1. The schemes of quasi-stationary simulation model of DEMO BoP, that is substantial for fusion reactor pulse and dwell operation, are presented in Appendix A.2, Fig. A2.1 and Fig. A2.2.

## 1.3 DEMONstration Intermediate Heat Transfer and Storage System design concept

### 1.3.1 Storage of thermal energy

In order to store an excess amount of hot heat transfer fluid, the Thermal Energy Storage system is applied. The operation of TES system depends on heat transfer fluid (HTF) properties, on design of storage system and its integration. TES technologies can exploit the storage of thermal energy in form of thermochemical, latent or sensible heat storage. Thermochemical heat storage is based on heat capacity and its change as a function of temperature, being accompanied by chemical reaction [71]. To store thermochemical energy, elevated HTF temperature is used to promote a reversible, endothermic reaction. The absorbed thermal energy is stored as chemical bonds within reaction products. The reverse exothermic process can be induced through catalysis, when energy needs to be recovered [72]. For latent heat storage, heat from HTF induces a phase change in the material to store energy isothermally at transition temperature, undergoing a solid-liquid transition. For sensible heat storage, it is characteristic that thermal energy in HTF is used to heat a single-phase material to a defined temperature or thermal energy is retained within an excess volume of HTF [73]. As sensible heat storage materials remain in a single phase during operating temperature range, the charging and discharging processes are completely reversible for unlimited cycles. Sensible heat storage is the simplest method to store thermal energy, especially for medium-size systems [73-79]. For DEMO IHTS operating temperatures, see Fig. 1.5, the gravimetric storage density for sensible heat storage is expected to be lower than for thermochemical heat storage and higher than for latent heat storage [71].

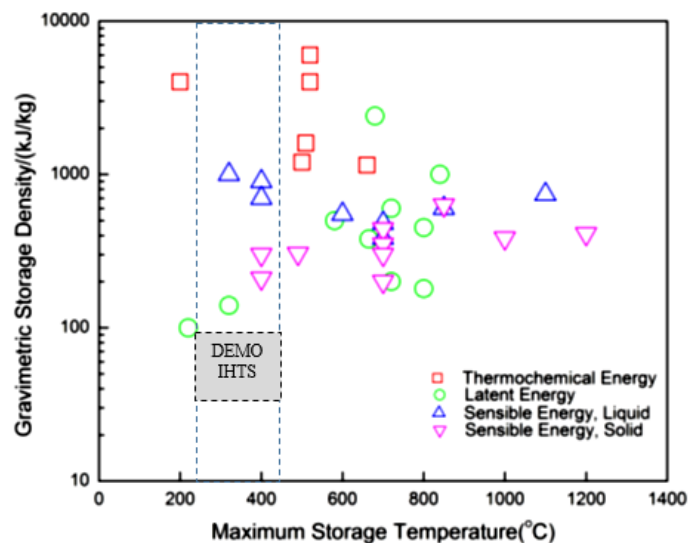


Fig. 1.5: Gravimetric storage density as function of maximum storage temperature [71].

### **1.3.2 DEMO IHTS two tank design concept**

In the current work, the focus of the study relies on DEMO BoP ICD concept with IHTS, which includes two thermal storage tanks. In the applied approach, the heat transfer fluid for DEMO PHTS differs from HTF for DEMO IHTS and the heat transfer fluids are not in direct contact [73, 80, 81]. The applied approach supposes heat transfer to the second HTF for thermal storage in a separate loop, involving corresponding heat exchangers.

A two tank storage concept involves the use of a hot and a cold tank with HTF inside at its highest and lowest temperatures [74, 75, 77-80, 82-85]. TES system comprises heat exchangers, pipelines as well as pumps, which ensure the flow of heat transfer fluid between thermal storage tanks through heat exchangers [78, 79, 86-94]. In comparison with thermocline single tank TES design (see Appendix A.3), two tank TES concept, being commercially proved, ensures higher thermal energy conversion efficiency and promises more effective performance.

The two tank TES design concept [95, 96] is known to be tested at Demonstration Solar Tower Plant Project „Solar Two” (see Appendix A.4). The two tank TES design concept has been also applied at Solar Energy Generating Systems (see Appendix A.4), which is an ultimate parabolic trough power plant, that comprises parabolic trough collectors with the tracking system, receiver, heat transfer medium with thermal storage, steam turbine and electric generator [92]. The Solar Energy Generating System applies mineral oil as heat transfer fluid [92]. The steam generator converts thermal energy into pressure energy of a gaseous medium, steam turbine converts pressure energy into rotational kinetic energy, and electrical generator converts rotational energy into electrical energy [95]. The use of two tank oil thermal storage system allows power plant to shift electric power generation from periods, when solar energy is available, to periods, when the utility’s peak electric demand occurs.

The ICD two tank TES system is applied for DEMO IHTS (see Fig. 1.4), whose concept enables both long-term storage of HTF in hot thermal storage tank and usage of hot HTF loop circulation for steam generation. In DEMO PHTS, thermal energy is transferred in heat exchangers from the first HTF (helium) to the second HTF (molten salt), which circulates in DEMO IHTS. DEMO IHTS includes cold and hot thermal storage tanks filled with the heat transfer fluid, which is also used as sensible heat storage medium, as well as corresponding pipelines and pumps. During dwell operation of fusion reactor, hot HTF is pumped from DEMO IHTS hot thermal storage tank through DEMO PCS SG stage heat exchangers into cold thermal storage tank, hence high temperature steam is produced, ensuring continuous turbine operation [47, 70].



## 1.4 Scope and tasks of the thesis

The scope of the thesis is to study the transient behaviour of DEMONstraton Balance of Plant energy transfer chain through the simulation using MATLAB®/Simulink.

Two main objectives are in focus. The first one is the operation stability of DEMO BoP. Here, the application of ICD concept, which includes two tank IHTS system, is a decisive condition. The second object is the simulation of transient behaviour of DEMONstration Balance of Plant energy transfer chain. In the study, the simulation model of DEMO BoP energy transfer chain begins with PHTS heat exchangers and ends at outlet of PCS steam turbines. Electrical generators are outside the frame of simulation tasks.

For the study, MATLAB®/Simulink code is applied for simulation of temporal evolution of mass and heat flows. The advantage of MATLAB® tool is the usage of tool-boxes for modelling of technical systems. Simulink, which is a data flow graphical programming language tool, contains a vast nomenclature of modules, which enables to model the devices and units of real dynamic systems. For models' development, proper modules are connected into diagrams according to their functions. After numerical simulations, the results get transferred into MATLAB® workspace for post-processing and visualization. It is necessary to underline, that MATLAB®/Simulink has not been known to be used previously for dynamic simulation of mass and heat transfer in DEMONstration Balance of Plant.

In the current work, for DEMO IHTS system HITEC molten salt is selected as both heat transfer fluid and sensible heat storage medium. The MATLAB®/Simulink Library has no kind of module, which simulates HITEC thermo-physical properties. Therefore, an extended analysis of HITEC properties and their temperature dependence is a prerequisite for selection of functional relations, which should be introduced in a novel customised MATLAB®/Simulink module.

Regarding the simulation of DEMO BoP energy transfer chain, the DEMO PHTS-IHTS and DEMO PCS models using MATLAB®/Simulink should be developed and correspondingly coupled. Referring to MATLAB®/Simulink Library, there is no module, in which heat transfer among three phases, specifically between HITEC, water and vapor, is modelled. Hence, for DEMO PHTS-IHTS model output, where heat transfer takes place in DEMO IHTS-PCS heat exchangers, the HXs are modelled by usage of Specific Dissipation Heat Transfer (SDHT) modules. For DEMO PCS model input, where heat transfer takes place in a pre-heater (PH),

steam generator (SG) and super-heater (SH), the steam generator is modelled as a two-phase fluid constant volume chamber, and pre-heater and super-heater are modelled as a two-phase fluid pipes. The connection between the output of DEMO PHTS-IHTS model and the input of the DEMO PCS model is realized through the thermal ports of corresponding modules.

To reach the scope, the following tasks of the thesis have been formulated:

1. To analyze HTFs properties with focus on HITEC molten salt and to define functional relations for simulation of temperature dependence of HITEC thermo-physical parameters using novel customized MATLAB® module.
2. To develop a model and to simulate heat losses to environment for DEMO IHTS thermal storage tanks and pipelines.
3. To define DEMO BoP design and operational parameters used as input data for numerical simulation through MATLAB®/Simulink.
4. To develop the simulation models and to study the temporal evolution of mass and heat flows in the DEMO PHTS-IHTS and DEMO PCS systems.
5. To develop the MATLAB®/Simulink model for DEMO BoP energy transfer chain, focusing on temporal evolution of mass and heat flows during pulse and dwell operation of fusion reactor.

Chapter 2 includes the results of literature survey of the properties of various heat transfer fluids. HITEC molten salt (MS), which is in the focus of study, is used for DEMO IHTS system as both heat transfer fluid and sensible thermal energy storage medium. The chapter includes an extended analysis of HITEC thermo-physical properties, as well as MS thermal and chemical stability and compatibility with constructive materials. The chapter maintains the results of analysis of functional relations, which describe thermal evolution of HITEC thermo-physical parameters. A set of analytical correlations is selected for novel customized MATLAB® module. The sensibility of simulated HITEC thermo-physical parameters in dependence of MS temperature is discussed.

Chapter 3 overviews the heat transfer model for a thermal storage tank, including governing equations. The chapter includes the description of MATLAB®/Simulink simulation model of DEMO IHTS thermal storage tank, as well as overview of a novel customized MATLAB® module for simulation of heat losses to the environment.

Chapter 4 defines the design and operational parameters of DEMO IHTS thermal storage tanks, which are applied for numerical simulations. The chapter presents the results of study of the

interplay between molten salt properties and storage tank geometry. The influence of tank height and thermal insulation material thickness on heat losses to environment is studied, using simulations with novel customized MATLAB<sup>®</sup> module. The results of simulations are evaluated through comparison with the data, known from literature survey.

Chapter 5 involves a vast analysis of design and operational parameters of DEMO PHTS-IHTS and PCS systems, which are introduced as input data in MATLAB<sup>®</sup>/Simulink simulation models. The chapter contains the description of developed DEMO PHTS-IHTS and DEMO PCS models. The simulation model of DEMO PHTS-IHTS system includes DEMO PHTS HXs, cold and hot thermal storage tanks, pipelines, corresponding modules for control of heat losses to environment, two fixed-displacement pumps and DEMO PCS SG stage, which includes PCS PH-SG-SH heat exchange modules. Regarding DEMO PCS system, the Rankine Cycle model from MATLAB<sup>®</sup> Library is selected. The newly proposed simulation model differs from the Library model by modelling of DEMO PCS steam generator as a two-phase fluid constant volume chamber. The DEMO PCS pre-heater and super-heater are modelled as two-phase fluid pipes.

Chapter 6 refers to simulation study of temporal evolution of mass and heat flows in DEMO PHTS-IHTS and DEMO PCS systems. The simulation of temporal evolution of HITEC filling level in thermal storage tanks is carried out for fusion reactor single cycle and multi-cycle operation. The study is continued with simulations for DEMO PCS system, focusing on temporal evolution of liquid volume fraction in steam generator, as well as on temporal evolution of mass and heat flows during pulse and dwell operation of fusion reactor. The study includes the data of simulation of temporal evolution of mechanical power output downstream DEMO PCS steam turbines. The results of simulations are evaluated and verified through comparison with numerical data from quasi-stationary simulations using EBSILON<sup>®</sup>.

The chapter 7 is directed to simulation of DEMO BoP energy transfer chain, those model is realized through the coupling of DEMO PHTS-IHTS and DEMO PCS models using corresponding modules thermal ports. The chapter includes the scheme and the description of developed model, as well as the results of simulation of temporal evolution of mechanical power output. The chapter's last paragraph is devoted to coupling of DEMO FPP to external electrical grid.

Chapter 8 summarizes main conclusions of the thesis and gives an outlook towards prospective simulation studies.



## 2 Simulation of HITEC molten salt properties

### 2.1 Properties of heat transfer fluids

Regarding DEMO IHTS system, an extended literature survey of properties of various heat transfer fluids is carried out [86, 103- 132]. The review, those results are presented in Table 2.1 and Table 2.2, shows water to be the lowest priced heat transfer fluid. However, water is not suitable to be used as HTF in the DEMO PHTS-IHTS system.

Thermal oils are more suitable for long-term operation at high temperatures. For example, thermal oil Therminol<sup>®</sup> VP-1, an eutectic mixture of 73.5% diphenyl oxide ( $C_{12}H_{10}O$ ) and 26.5% diphenyl ( $C_{12}H_{10}$ ), can be heated up to 663 K and used in both liquid and vapor phase [107]. However, complex handling, special requirements of components and safety concerns due to flammability limit oil application. Low boiling temperatures, as well as chemical instability at elevated temperatures, have a negative impact and reduce the favorability of thermal oils [115].

Liquid metals can be effectively used for heat transfer [115-132]. Alkali metals are characterized by low density, low melting point, low viscosity and high thermal conductivity. The use of sodium can reduce static load of TES system and energy consumption for heating up thermal storage tanks. Nevertheless, the contact of sodium with oxygen results in a violent, exothermic reaction [133]. If water or humid air is added, then NaOH and  $H_2$  are formed, thus in reaction with oxygen can cause explosions. At  $T < 388$  K sodium reacts with oxygen, forming an oxide layer without further consecutive reactions [134].  $Na_2O$  is formed at  $388 < T < 573$  K, as well as  $Na_2O_2$  is formed at higher temperatures. The choice of structural materials is limited by their compatibility with liquid sodium and operation temperatures [106, 135-139].

Molten salts are preferable HTF candidates for various TES systems [107]. Due to usage of molten salts, thermal energy can be stored as sensible, latent, or even a combination of both heats [140]. Molten salts, which technically are a class of ionic liquids, exhibit properties that are important for operation safety and engineering. Ability for effective heat transfer and low costs make molten salts attractive for large-scale applications. Molten salts are solid-state at standard temperature and pressure, entering liquid phase at elevated temperatures. They have low viscosity and vapor pressure, high density and thermal conductivity, as well as large specific heat capacity, see Table 2.2 [74, 108, 109, 134, 140-155].

HTF	Advantages		Disadvantages	
Water	Low cost: $10^{-4}$ \$/kg High specific heat capacity		Needs high pressure tank High pressure steam Risk of corrosion	
Oils	Low calorific capacity Few hours need to load storage tank Low cost: 0.3 \$/kg Attractive storage price: 4.2 \$/kWh <sub>th</sub>		Low range of temperatures Low thermal conductivity Thermal decomposition Development of mixtures	At high temperatures: - high vapour pressure - expensive pressure-holding storage tank Flammable product
Fluid metals (Na, Pb, Sn)	High charge cycle resistance Small load cycles time Large usable temperature range High chemical stability High boiling point High thermal storage density	<u>Sodium:</u> Low porosity filler material Best calorific capacity High discharge efficiency Requires lower pumping power	High melting points Require heating system	<u>Sodium:</u> Risk of reactions with air/water Required safety concept High price per kWh: 21 €/kWh
Molten salts	Larger usable temperature range High calorific capacity High thermal storage density Accessible price: 0.5-2.6 €/kg	High heat conductivity Low melting point High boiling point Compatibility to alloys	High melting point Limited material compatibility Moderate thermal stability Dissociation reaction Require safety measures	Need heating to reach melting point Solidification problems Require more pump power as Na Lower discharge efficiency as Na Less thermal efficiency as Na

Table 2.1: Characteristics of heat transfer fluids [106-119].

<b>HTF</b>	<b>T<sub>min,op</sub> (T<sub>m</sub>), °C</b>	<b>T<sub>max,op</sub> (T<sub>vap</sub>), °C</b>	<b>ρ, kg/m<sup>3</sup></b>	<b>k, W/(m·K)</b>	<b>c<sub>p</sub>, J/(kg·K)</b>	<b>c<sub>p</sub>·ρ, kWh/(m<sup>3</sup>·K)</b>
Water	50 (0)	140 (100)	1000	0.67	4180	1.161
Mineral oil	200	300	770	0.12	2600	0.556
Synthetic oil	250	350	900	0.11	2300	0.575
Silicone oil	300	400	900	0.10	2100	0.525
Sodium	(97.8)	883	968	141	1230	0.307
Nitrite salts	250	450	1825	0.57	1500	0.760
Nitrate salts	265	565	1870	0.52	1600	0.831
Potassium nitrate	(334)	(750)	2110	0.50	1560	0.914
Sodium nitrate	(306)	(380)	2260	0.50	1365	0.857
Sodium carbonate	(851)	(1600)	2530	5.0	276	0.194
Carbonate salts	450	850	2100	2.0	1800	1.050
Na <sub>2</sub> CO <sub>3</sub> –K <sub>2</sub> CO <sub>3</sub> –Li <sub>2</sub> CO <sub>3</sub>	398	1027	1848	0.47	1612	0.827

Table 2.2: Thermo-physical parameters of heat transfer fluids [80, 106-119].

Low viscosity affects positively the velocity distribution in pipes, though reducing pump power consumption [156-159]. Large specific heat capacity allows reduction of MS mass that is important for cost-effective design solutions [141, 160]. In comparison to thermal oils, MSs are denser, can be directly stored and are accessed at near-ambient pressure. MSs can retain more energy per volume than oil-based HTFs. Molten salts are cheaper than thermal oils.

The biggest challenge of molten salts is their high melting temperature, what leads to complications related to freeze protection of TES equipment. High melting temperatures require an enhanced heat insulation of equipment to avoid damages due to salt solidification [142]. To maintain MS temperature above its melting point, a heating system is usually applied using a fossil fuel burner or electrical heat tracing [143].

An important factor is the compatibility of molten salts with constructive materials [86, 87, 118-121, 146, 149, 150, 161-164]. The material type, processing, surface finishing and chemical composition, molten salt chemical stability, impurities and operating temperature have an impact on the corrosion. The intrinsic corrosion is driven by a difference in free energy of formation among molten salt constituents and the most susceptible transition metal corrosion products. The corrosion through oxidizing contaminants takes place due to residuals, water, oxides and dissolved oxidizing metal salts. Differential solubility and deposition occur due to thermal gradients in MS, forming a metal ion concentration cell. Galvanic corrosion takes place, when materials with different electrochemical potentials are in electrical contact with molten salt, driving the oxidation of anode material. The dissolved contaminants increase both oxidation potential probability and corrosion rate [119]. The soluble oxide ions aggravate corrosion process at high temperatures [122, 123].

The thermal stress is of major importance in terms of stress corrosion cracking of steels in contact with molten nitrate melts. Leaks could occur due to corrosion of highly stressed, hairpin-shaped steam tubes, manufactured from mild steel [125]. Incoloy800 can form a multi-layer, highly protective oxide structure. Salt contaminants can oxidize the constituents of structural alloys [119, 139]. The insoluble products tend to plug valves, pipes and heat transfer surface, consequently. The trace moisture in the melt enhances the corrosion [124].

Chrome steel and nickel-chrome alloys can form complex corrosion products, which are more corrosion resistant than simple iron oxides [126, 127]. The problems can appear, if molten alkali nitrate salts constitute a corrosion system in combination with metal parts [111].



## 2.2 Properties of HITEC molten salt

In the study, HITEC molten salt is applied in DEMO IHTS system. HITEC is an eutectic ternary mixture of sodium nitrate, potassium nitrate and sodium nitrite in wt.% proportion of 7%  $\text{NaNO}_3$  - 40%  $\text{NaNO}_2$  - 53%  $\text{KNO}_3$  [142, 146, 149, 157, 162, 165-168]. Since 1937, HITEC is used as a reactant in various technological processes, such as preheating, high temperature distillation, rubber curing, rotational molding and so forth [161, 168]. It is commercially available and sold under the trade name by Coastal Chemical Company [157]. MS has a crystal structure, and it is produced in either powder or granular form [157, 169, 170]. HITEC is available in almond shaped briquettes, containing no anti-caking agents. HITEC has a solidified structure, is non-fouling, nonexplosive and nonflammable. It is hygroscopic. To prevent caking, HITEC needs to be stored in a dry place. HITEC is characterized by low maintenance and operation costs. The price of  $\sim 0.93$   $\$/\text{kg}$  for HITEC molten salt is lower than of sodium with  $\sim 2$   $\$/\text{kg}$  [80, 157]. Regarding storage costs, in comparison with sodium ( $\sim 21$   $\$/\text{kWh}_{\text{th}}$ ), HITEC can be get at rather reduced price of  $\sim 10.7$   $\$/\text{kWh}_{\text{th}}$  [159].

Literature survey of HITEC thermo-physical properties is carried out, with focus on MS melting point, maximum operating temperature, heat capacity, density, dynamic viscosity and thermal conductivity (see Table 2.3). The review shows that HITEC melting point of  $T_m = 415$  K is  $\sim 11\%$  higher than sodium melting point of  $T_m = 371$  K [157, 167]. HITEC density of  $\rho = 1935$   $\text{kg}/\text{m}^3$  is practically double as high as density of liquid sodium of  $\rho = 968$   $\text{kg}/\text{m}^3$  (see Table 2.2 and Table 2.3). For HITEC, the storage capacity of  $0.756$   $\text{kWh}/(\text{m}^3 \cdot \text{K})$  is over 2 times higher than for liquid sodium with value of  $0.307$   $\text{kWh}/(\text{m}^3 \cdot \text{K})$ . For equivalent operating temperatures, to store same energy amount, HITEC requires a lower thermal storage volume than liquid sodium [108, 119, 140, 142, 144, 146, 149, 171, 172]. In comparison to liquid sodium, HITEC has lower discharge and thermal efficiency. Similar to liquid sodium, HITEC evolves no toxic vapors at  $T < 823$  K [147, 149, 157, 175, 176]. HITEC molten salt is characterized by low vapor pressure [158, 177]. MS dynamic viscosity decreases with growing temperature [87, 162, 165, 175, 178-182]. In ref. [119, 131, 158, 181, 183, 184], HITEC specific heat capacity of  $c_p = 1560$   $\text{J}/(\text{kg} \cdot \text{K})$  is given, what is  $\sim 21\%$  higher than for sodium value of  $c_p = 1230$   $\text{J}/(\text{kg} \cdot \text{K})$ . In ref. [185] is shown, that MS specific heat capacity varies between  $1.37$ - $1.48$   $\text{kJ}/(\text{kg} \cdot \text{K})$ , with a standard error of  $0.01$ - $0.95$   $\text{kJ}/(\text{kg} \cdot \text{K})$ , for the augment in temperature from  $473$  K up to  $543$  K. For the range of  $560 < T < 670$  K, the temperature dependence of HITEC surface tension ( $[\text{N}/\text{m}]$ ) can be described as  $\gamma = 0.14928 - 0.556 \cdot 10^{-4} \cdot T$ , with an uncertainty in value of  $\pm 10\%$  [119, 186, 187].

Reference	Melting point, °C	Max. operating temperature, °C	Melting enthalpy, J/g	Heat capacity, kJ/(kg·K)	Density, kg/m <sup>3</sup>	Dynamic viscosity, mPa·s	Thermal conductivity, W/(m·K)
166	142	450		1.560	1890 (260°C) 1680 (540°C)	4.3 (400°C) 1.2 (540°C)	0.61
191	142	530-590		1.549	1695 (538°C)	1.24 (538°C)	0.57
126	142	625 (degradation)	58.52	1.56 (400°C)	1790 (400°C)	1.3-1.6 (400°C)	0.51-0.61 (400°C)
170	142	454		1.30 1.50	1980 1682 (538°C)	1.24 (538°C)	0.48-0.50 0.571
119	142	535		1.56 (300°C)	1640 (300°C)	3.16(300°C)	
152	142	450-540	60	1.54 (400°C)	1790 (400°C)		
135			81	1.34			0.44
192							0.52 (150-250°C)
118							0.5-0.6 (150°C)
129	149	538					0.60 (242-365°C)
193	142			1.56			0.48
194	142	550		1.40 (solid) 1.56 (liquid)			0.7
146	149	450-500		1.5617			
177	142	450-600		1.50-1.56			
130	142	535		1.57 (300°C)			
195	140	450-500		1.56			
163	142		56.8				
126	139	<550	59.1				
132	142	538					
121	142	535					
176	142	454-538					
186	142	520					

Table 2.3: HITEC molten salt thermo-physical parameters.

HITEC electrical resistivity is  $\sim 1.7 \text{ } \Omega \cdot \text{m}$ . Its coefficient of linear thermal expansion in the solid-state is equal to  $5.13 \cdot 10^{-5} \text{ } ^\circ\text{C}^{-1}$ . For HITEC volumetric thermal expansion coefficient, the value is given by  $3.629 \cdot 10^{-4} \text{ } ^\circ\text{C}^{-1}$ . MS isothermal bulk modulus is 1.72 GPa [143, 157, 175, 182, 188]. At high temperatures, electrical properties of HITEC molten salt can prohibit the usage of hot-wire method for measurement of thermal conductivity [109, 189]. For HITEC thermal conductivity coefficient, the value of  $k = 0.44 \text{ W}/(\text{m} \cdot \text{K})$  is measured in ref. [190], when MS temperature approaches solidification point. In ref. [86], for temperature range of  $423 < T < 523 \text{ K}$ , the thermal conductivity coefficient is calculated as  $k = 0.52 \text{ W}/(\text{m} \cdot \text{K})$ . In ref. [144], this parameter tends to increase with rising temperature from 423 K to 873 K. In ref. [180], thermal conductivity is indicated as an average value of  $k = 0.48 \text{ W}/(\text{m} \cdot \text{K})$ , with a standard deviation of  $0.046 \text{ W}/(\text{m} \cdot \text{K})$ .

## **2.3 Stability and compatibility of HITEC molten salt**

### **2.3.1 Thermal and chemical stability of HITEC molten salt**

The stability of HITEC molten salt depends on oxide ion concentration, furthermore on operating and decomposition temperature, partial pressure, cover gas composition and water vapor concentration [111, 122, 125, 126, 131, 157, 164, 165, 178, 179, 196, 197]. HITEC is chemically and thermally unstable at  $T > 873 \text{ K}$  [447]. In ref. [171], a rapid decomposition of salt mixture at 883 K is reported. With growing temperature above the decomposition level, MS average mass loss rate increases [144, 191, 198-202]. The decomposition of nitrites causes formation of oxides in the salt melt. In ref. [111] is shown that the 1<sup>st</sup> decomposition reaction with nitrite formation is quicker compared to the 2<sup>nd</sup> decomposition reaction with nitrogen or nitrogen oxide release. At high temperatures, HITEC can change the composition from 53%  $\text{KNO}_3$  - 40%  $\text{NaNO}_2$  - 7%  $\text{NaNO}_3$  to 52%  $\text{KNO}_3$  - 28%  $\text{NaNO}_2$  - 18%  $\text{NaNO}_3$  - 2%  $\text{Na}_2\text{O}$ . In this case, MS melting point rises from 415 K to 438 K [119]. The mass losses of alkali metal nitrate salts upon heating may occur due to nitrite and alkali metal oxide formation in the melt. Additionally, oxygen, nitrogen or nitrogen oxides release can result in MS mass losses due to vaporization of nitrates. Ref. [194] shows that in steam generator loop, running at temperature of 811 K, decomposes  $\sim 0.5\%$  of  $\text{NaNO}_2$  per day, according to reaction of  $5 \text{ NaNO}_2 \rightarrow 3 \text{ NaNO}_3 + \text{Na}_2\text{O} + \text{N}_2$ . Thermal decomposition of alkali metal nitrates results in formation of nitrite ions and gaseous products such as  $\text{NO}$ ,  $\text{NO}_2$ ,  $\text{N}_2\text{O}_2$ ,  $\text{N}_2\text{O}_3$ ,  $\text{N}_2\text{O}_4$ ,  $\text{N}_2\text{O}_5$ . The results of long-term tests at  $T = 823 - 873 \text{ K}$  prove the gain of weight up to 5% wt. due to

oxidation reactions [82, 111, 173]. At 923 K, the weight loss is indicated with ~60%. In ref. [142], the weight loss is measured of ~1.48% at 773 K and ~19.12% at 823 K, accordingly. After long-term test at 773 K, nitrite concentration decreases by 7%. After long-term tests at 823 K, nitrite concentration declines by 10%. At  $T > 1073$  K, the reactions can be so quick, that MS appears to boil, because of evolution of nitrogen and  $\text{NO}_x$ . If HITEC gets in contact with air at  $T > 623$  K, nitrite can slowly oxidize by atmospheric oxygen [123]. HITEC can chemically react with organic materials and metals [163]. Organic liquids and vapors, being introduced into molten salt, do not react with MS, but can burn at its surface in air, when they gain access to oxygen [111]. The absorption of  $\text{CO}_2$  and water vapor, that forms alkali metal hydroxides, can alter and decompose the salt mixture [126, 173, 203]. The reactions with  $\text{CO}_2$  and  $\text{H}_2\text{O}$ , as well as the change of molten salt composition, increase MS melting temperature, though changing corrosion potential and characteristics of HITEC molten salt.

### **2.3.2 Compatibility of HITEC molten salt with constructive materials**

At operating temperatures below 723 K, the equipment is usually manufactured from mild carbon steel, due to economic aspects. The corrosion rates are tolerated, as equipment can be depreciated over short time periods [161]. Carbon steel does not possess the requisite strength, what is required for long operation at elevated temperatures [119, 161]. In case of HITEC, the use of cast iron equipment is not recommended due to embrittlement processes of metal and fissure formation. Plain carbon steel can be used to handle with HITEC, though the corrosion rate rises appreciably [86, 157, 198]. At high temperatures, Incoloy 800, SS 347 or similar steels have to be selected as constructive materials [76, 157, 163, 175]. The exposure of Incoloy 800, stainless steel SS 304, SS 304L and SS 316 to thermal convection of draw salt at 648 - 873 K, under argon atmosphere, can result in thin oxide films on alloys and some dissolution of chrome [119, 204]. Impurities degrade the adhesion of oxide scale to metal surface and cause spalling of oxide layer, making possible corrosion attack of the base material [119, 124, 170, 176-178]. Corrosion is not a concern, when Hastelloy 6 and C 276 are used, being in contact with molten salt [125]. Carbon and Cr-Mo steels can be used at  $T < 723$  K [203, 204]. To ensure long-term operation at high temperatures, nickel or austenitic stainless steels need to be applied [127, 203, 205]. The alloys form protective Cr-oxide and Ni-oxide films in addition to Fe-oxide. HITEC is well compatible with low-alloyed carbon steel, Cr-Mo steel (Cr content up to 9 wt.%), stainless Cr-Ni steel (with and without Mo, Nb, Ti), as well as Ni-alloys (Alloy 800) [110, 119, 176, 178, 193, 195].

## 2.4 Simulation of thermo-physical properties of HITEC molten salt

In MATLAB<sup>®</sup> Libraries, no kind of module is available for numerical simulation of thermo-physical properties of HITEC molten salt [102, 206, 207]. Hence, the analysis of temperature dependent functional relations is a prerequisite for selection of correlations, which have to be introduced into a novel customized MATLAB<sup>®</sup> module for simulation of HITEC thermo-physical parameters.

An extended literature survey is carried out for functional relations, which describe the temperature dependence of HITEC density [kg/m<sup>3</sup>], see Table 2.4. The results of simulations (see Fig. 2.1) show that the data for functional relations (2.2)-(2.6) coincide with each other, predicting a linear decrease in MS density by rising operating temperature. The eq. (2.1) underestimates MS density. The eq. (2.3) is similar to eq. (2.2) and shows the function  $\rho(T)$ , in which the temperature is given in degree Celsius.

Temperature	Functional relation	Equation	Reference
T, K	$\rho = 1938 - 0.732 \cdot (T - 200)$	(2.1)	82 83, 208-210
T, K	$\rho = 2080 - 0.733 \cdot (T - 273.15)$	(2.2)	144, 211
T, °C	$\rho = 2084 - 0.732 \cdot T$	(2.3)	212
$470 \leq T \leq 870$ , K	$\rho = 2293.6 - 0.7497 \cdot T$	(2.4)	119
T, K	$\rho = 2279.799 - 0.7324 \cdot T$	(2.5)	180
$420 \leq T \leq 800$ , K	$\rho = 2280 - 0.732 \cdot T$	(2.6)	181, 183

Table 2.4: Functional relations for temperature dependence of HITEC density.

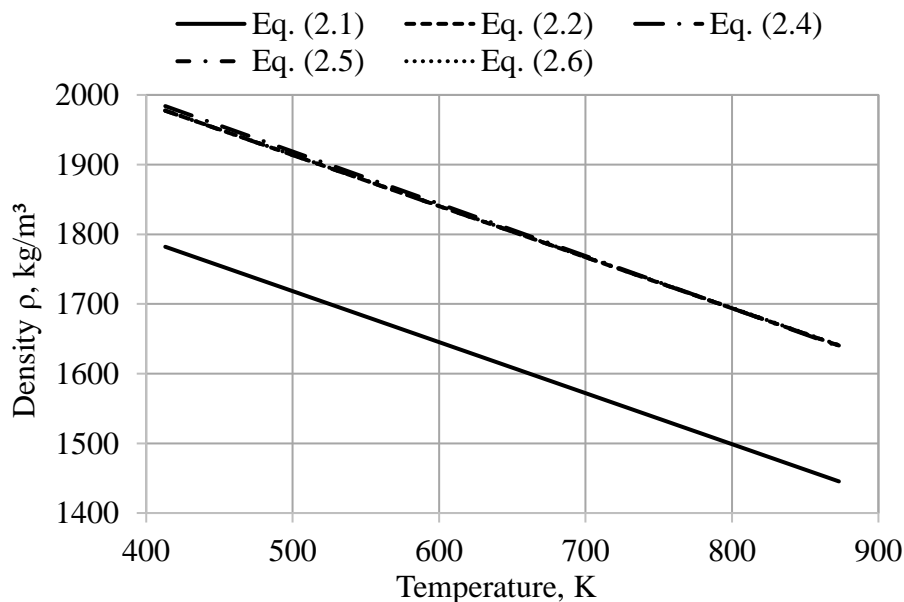


Fig. 2.1: Calculated temperature dependence of HITEC density.

To select the analytical correlation for customized MATLAB<sup>®</sup> module, functional relations are compared to each other. Molten salt densities  $\rho_2$  and  $\rho_4$ - $\rho_6$ , which correspond to eqs. (2.2) and (2.4)-(2.6), are calculated for identical MS temperatures, where the correlation (2.5) is taken as reference one. To compare with, the non-dimensional parameter  $\Delta\rho = \frac{\rho_i - \rho_5}{\rho_5}$  is calculated, where  $i = 2, 4, 6$  correspond to MS density, being calculated with eqs. (2.2), (2.4) and (2.6), see Fig. 2.2. Finally, the correlation (2.5) is selected for novel customized MATLAB<sup>®</sup> module.

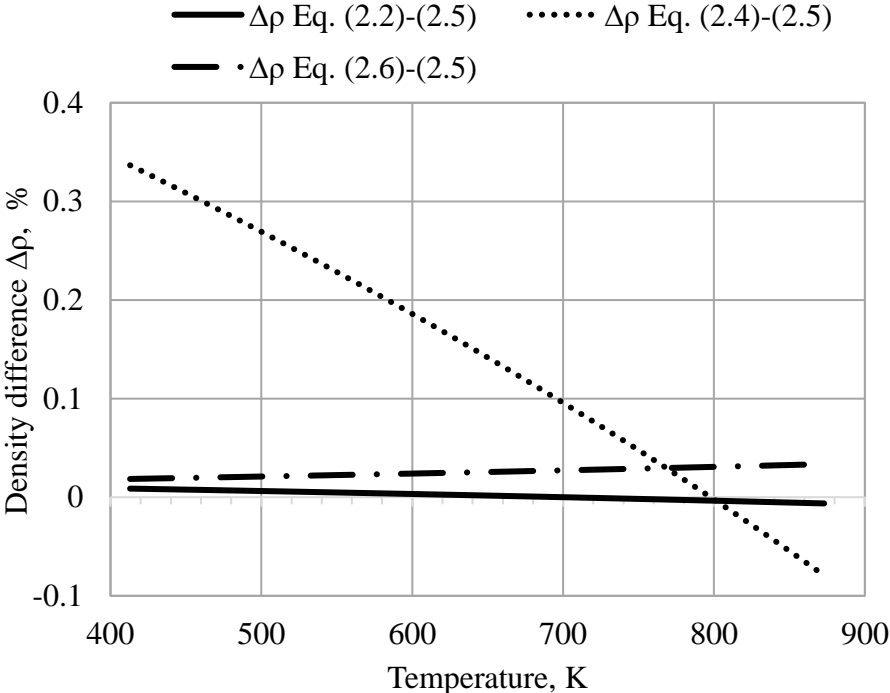


Fig. 2.2: Comparative diagrams for density difference according to eqs. (2.2) and (2.4)-(2.6).

The results of simulations for HITEC density are validated through comparison (see Fig. 2.3) with experimental data from literature survey (see Table 2.3). The calculated values (dashed line) fit close and even match exactly to most of experimental values (black dots). The temperature dependence of molten salt density, see Fig. 2.3, tends to be a declining function with increasing MS temperature.

Exponential as well as 2<sup>nd</sup> and 3<sup>rd</sup> order polynomial correlations are used to describe temperature dependence of HITEC dynamic viscosity, see Table 2.5. For  $T < 600$  K, eqs. (2.13) and (2.14) show lower values than eqs. (2.7), (2.8) and (2.10)-(2.12). For  $T > 600$  K, except of eq. (2.14), the results of simulations practically coincide with each other. Equations (2.8) and (2.9) differ only by temperature unit  $T$ , being introduced either in  $^{\circ}\text{C}$  or  $\text{K}$ .

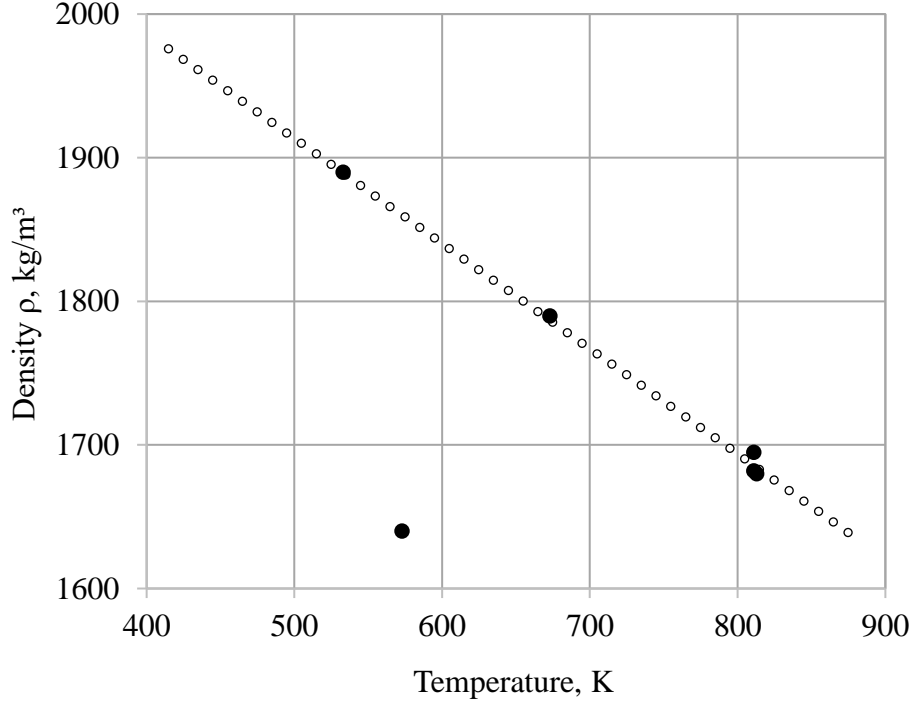


Fig. 2.3: Comparison between simulated and experimental data for HITEC density, dashed line – calculated values according to eq. (2.5), black dots – experimental data from Table 2.3.

Temperature	Functional relation	Equation	Reference
T, K	$\mu = \frac{e^b + e^{-b}}{e^b - e^{-b}} - 0.999, \quad b = 5.9 \cdot \frac{T - 9.638}{990.362}$	(2.7)	144, 211
T=247-500°C	$\mu = e^{[-4.343 - 2.0143 \cdot (\ln T - 5.011)]}$	(2.8)	82, 83, 149, 150, 102, 208, 209, 213
T, K	$\mu = e^{[-4.343 - 2.0143 \cdot (\ln(T - 273) - 5.011)]}$	(2.9)	180, 210
T=150-500°C	$\mu = T^{-2.104} \cdot 10^{5.7374}$	(2.10)	149, 150
T=147-422°C	$\mu = 1.149 \cdot e^{\left[-\frac{810.896}{T+273} + \frac{7.806 \cdot 10^5}{(T+273)^2}\right]}$	(2.11)	149, 150
T=182-507°C	$\mu = 67.57 \cdot 10^{-3} \cdot e^{\frac{2247.11}{T+273}}$	(2.12)	149, 150
T=184-482°C	$\mu = 0.5631 \cdot e^{\left[-\frac{146.9794}{T+273} + \frac{57.4265 \cdot 10^4}{(T+273)^2}\right]}$	(2.13)	149, 150
T=250-450°C	$\mu = 0.75484 \cdot e^{\frac{6418}{R \cdot (T+273)}}$	(2.14)	146, 149, 150

Remark: In eqs. (2.13) and (2.14), the dynamic viscosity is in mPa·s, in other equations the dynamic viscosity is in Pa·s.

Table 2.5: Functional relations for temperature dependence of HITEC dynamic viscosity.

According to ref. [180], equation (2.9) is the most representative correlation, which is used for numerical simulation of HITEC dynamic viscosity, in temperature range of  $525 < T < 773$  K with 3.65% deviation from the mean value. Consequently, eq. (2.9) is selected for MATLAB<sup>®</sup> customized module. The temperature dependent function  $\mu = f(T)$  is shown in Fig. 2.4.

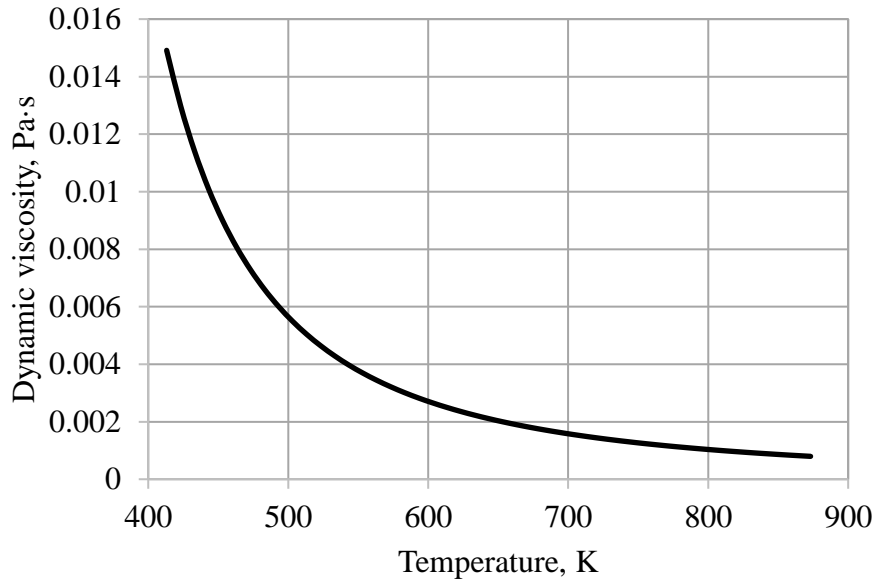


Fig. 2.4: HITEC dynamic viscosity as function of MS temperature.

Referring to HITEC kinematic viscosity  $\nu = \frac{\mu}{\rho}$  [m<sup>2</sup>/s], its temperature dependence can be defined using corresponding data for HITEC density and dynamic viscosity, being calculated by the quotient between eq. (2.9) and eq. (2.5) for selected operating temperatures.

The temperature dependence of HITEC specific heat capacity  $c_p$  [kJ/(kg·K)] is described by eqs. (2.15)-(2.17), see Table 2.6. A linear increase in specific heat capacity with rising temperature is described by eq. (2.15). However, this correlation is related to the temperature range below HITEC molten salt melting point. The numerical data, calculated using eq. (2.17), lie well above the experimental data, known from Table 2.3. Hence, for the simulations using the customized MATLAB<sup>®</sup> module, the eq. (2.16) is selected. It is a linear decreasing functional relation. The diagram for temperature dependence of MS specific heat capacity  $c_p = f(T)$ , calculated according to eq. (2.16), is presented in Fig. 2.5.

For the temperature range of  $410 < T < 820$  K, the temperature dependence of HITEC volumetric heat capacity, which is a product given as  $\beta = \rho \cdot c_p$ , can be calculated using molten salt numerically simulated values for  $\rho$  and  $c_p$ , see eq. (2.5) and eq. (2.16), respectively.



Temperature	Functional relation	Equation	Reference
$T < 140^\circ\text{C}$	$c_p = 1.0184 + 2.6618 \cdot 10^{-3} \cdot T$	(2.15)	133, 214
$413 < T < 903, \text{K}$	$c_p = 1.560 - (T - 273.15) \cdot 10^{-3}$	(2.16)	211
$426 < T < 776, \text{K}$	$c_p = 5.806 - 10.833 \cdot 10^{-3} T + 7.2413 \cdot 10^{-6} \cdot T^2$	(2.17)	119

Table 2.6: Functional relations for temperature dependence of HITEC specific heat capacity.

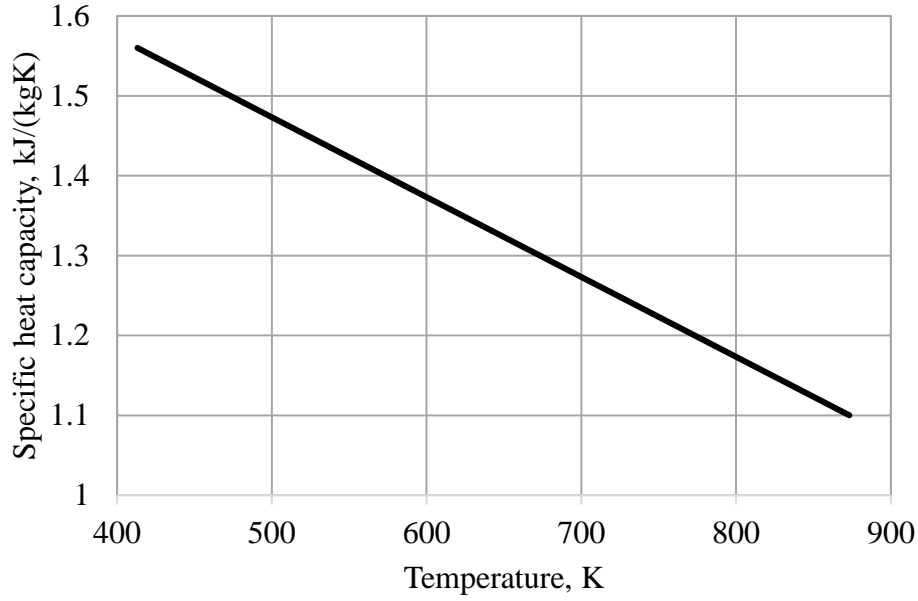


Fig. 2.5: HITEC specific heat capacity as function of MS temperature.

Temperature	Functional relation	Equation	Reference
$T > 260^\circ\text{C}$	$k = 0.421 - 6.53 \cdot 10^{-4} \cdot (T - 260)$	(2.18)	82, 83, 157, 210, 212
$100 < T < 500^\circ\text{C}$	$k = a + b \cdot T + c \cdot T^2$ $a=0.78, b=-1.25 \cdot 10^{-3}, c=1.6 \cdot 10^{-6}$	(2.19)	109
$140 < T < 630^\circ\text{C}$	$k = 0.78 - 1.25 \cdot 10^{-3} \cdot T + 1.6 \cdot 10^{-6} \cdot T^2$	(2.20)	144
$170 < T < 510^\circ\text{C}$	$k = 0.78 - 1.25 \cdot 10^{-3} \cdot (T + 273) + 1.6$ $\cdot 10^{-6} \cdot (T + 273)^2$	(2.21)	194, 211
$147 \leq T < 263^\circ\text{C}$	$k = 2.2627 - 0.01176 \cdot T + 2.551 \cdot 10^{-5}$ $\cdot T^2 - 1.863 \cdot 10^{-8} \cdot T^3$	(2.22)	181, 183
$263 \leq T < 527^\circ\text{C}$	$k = 0.7663 - 6.47 \cdot 10^{-4} \cdot T$	(2.23)	181

Table 2.7: Functional relations for temperature dependence of HITEC thermal conductivity.

The analytical correlations for HITEC thermal conductivity are presented in Table 2.7. The calculations according to eq. (2.18) show a linear decrease in  $k$  for  $T > 260$  °C. The data for eq. (2.18) and eq. (2.22) coincide well for  $T > 263$  °C. The eqs. (2.19)-(2.21) show the tendency of growing thermal conductivity with increasing temperature. The eqs. (2.22) and (2.23) can be used for simulation of the temperature evolution of HITEC thermal conductivity. The eq. (2.22) is useful for temperatures  $T=200-270$  °C, what corresponds to temperature interval between MS critical temperature of  $T_{cr}=200$  °C and MS operating temperature in the cold tank  $T_{cold\ tank}=270$  °C. The eq. (2.23) well describes the function  $k = f(T)$  in the interval of operating temperatures  $T_{cold\ tank} \leq T \leq T_{hot\ tank}$ , where  $T_{hot\ tank}=465$  °C. The temperature evolution of the function  $k = f(T)$  calculated according to eqs. (2.22) and (2.23) is shown in Fig. 2.6.

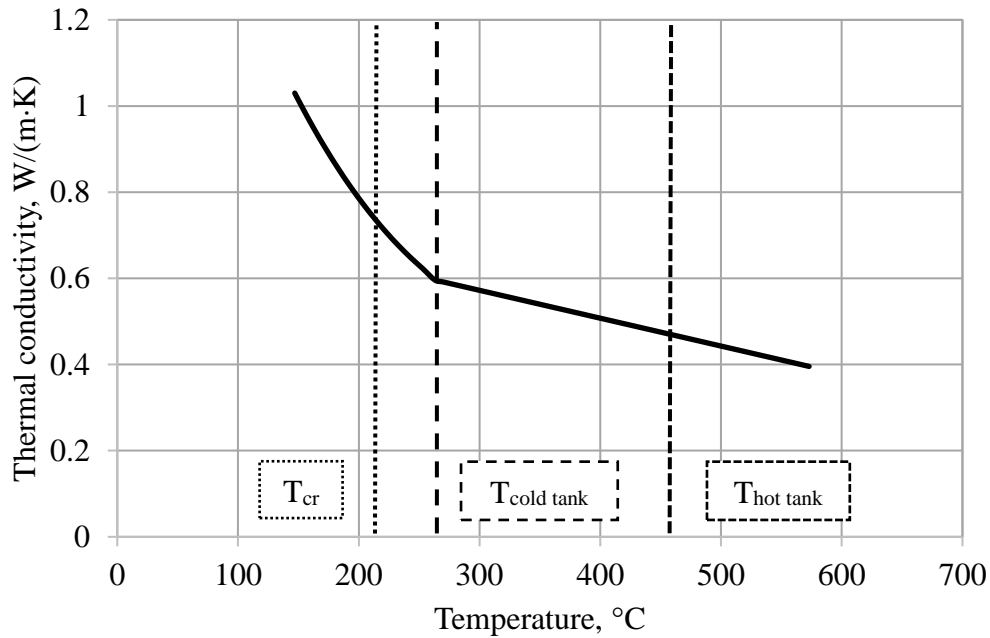


Fig. 2.6: HITEC thermal conductivity as function of MS temperature.

## 2.5 Sensitivity of simulated parameters on HITEC molten salt temperature

The selected equations for HITEC thermo-physical parameters are introduced into novel customized MATLAB<sup>®</sup>/Simulink module, which specifies thermal liquid settings for simulation of temperature dependent HITEC thermo-physical properties.

The analysis of simulated HITEC thermo-physical properties, in dependence on MS operating temperature, shows that with increasing molten salt temperature, the absolute values of defined HITEC thermo-physical parameters decrease (see Table 2.8). Further, HITEC dynamic viscosity is most sensitive to the change in MS operating temperature.

HITEC molten salt	Density	Dynamic viscosity	Specific heat capacity	Thermal conductivity
Increase in MS temperature from $T_1 = 543$ K up to $T_2 = 738$ K	<b>Parameter absolute value</b>			
	Decreases	Decreases	Decreases	Decreases
	<b>Percent of change</b>			
	~7.6%	~66%	~15.1%	~21.9%

Table 2.8: Sensitivity of HITEC molten salt parameters with the change of MS temperature.

Having constant MS mass, with growing HITEC temperature, the volume of molten salt in storage tank increases. By increase in MS operating temperature from  $T_1 = 543$  K up to  $T_2 = 738$  K, the relative value of MS density, given as  $\rho_{rel} = \frac{\rho_{T_2}}{\rho_{T_1}}$ , linearly decreases, and the relative value of molten salt volume, given as  $V_{rel} = \frac{V_{T_2}}{V_{T_1}}$ , linearly increases (see Fig. 2.7). For defined temperature interval, the relative increase in HITEC volume in hot thermal storage tank is ~8.2% (see Table 2.9). As conclusion, thermal expansion of HITEC has to be considered for the design and safe operation of thermal storage tanks. The overview of percentage of the change in relative values of mass and heat transfer parameters for MS temperature growing from  $T_1 = 543$  K up to  $T_2 = 738$  K is summarized in Table 2.9.

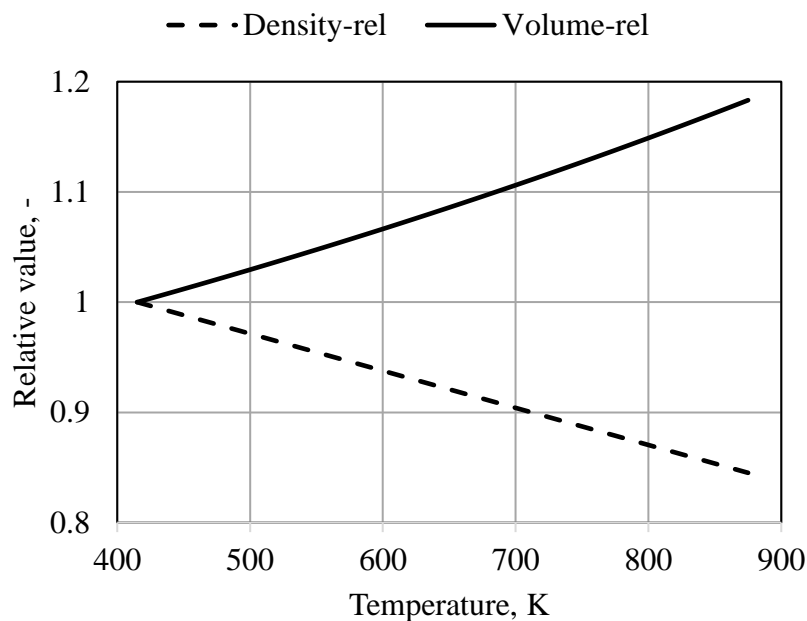


Fig. 2.7: Dependence of HITEC relative density and volume with increasing MS temperature.

Parameter	Equation	Increase in MS temperature from $T_1=543$ K up to $T_2=738$ K
<b>Parameter absolute value</b>		
Molten salt volume	$V_T = \frac{m}{\rho_T}$	Increases
Molten salt velocity in a pipeline	$v_T = \frac{\dot{m}}{\rho_T \cdot S}$	Increases
Stored energy	$E = m \cdot c_p \cdot \Delta T;$ $\Delta T = T_2 - T_1$	Decreases
Reynolds number	$Re = \frac{4 \cdot \dot{m}}{\pi \cdot \mu_T \cdot D_{pipe}}$	Increases
Prandtl number	$Pr = \frac{c_{pT} \cdot \mu_T}{k_T}$	Decreases
<b>Percentage of change for relative value</b>		
Molten salt relative volume	$V_{rel} = \frac{V_{T_2}}{V_{T_1}} = \frac{\rho_{T_1}}{\rho_{T_2}}$	Increase with ~8.2%
Molten salt relative velocity in a pipeline	$v_{rel} = \frac{v_{T_2}}{v_{T_1}} = \frac{\rho_{T_1}}{\rho_{T_2}}$	Increase with ~8.2%
Stored energy relative value	$E_{rel} = \frac{E_{T_2}}{E_{T_1}} = \frac{c_{pT_2}}{c_{pT_1}}$	Decrease with ~15.1%
Relative value of Reynolds number	$Re_{rel} = \frac{Re_{T_2}}{Re_{T_1}} = \frac{\mu_{T_1}}{\mu_{T_2}}$	Increase with ~199%
Relative Prandtl number	$Pr_{rel} = \frac{Pr_{T_2}}{Pr_{T_1}}$	Decrease with ~78%
Remark: $l_{ch}$ - characteristic linear dimension with respect to the object, $D_{pipe}$ – circular pipe diameter		

Table 2.9: Sensitivity of mass and heat transfer parameters with the change of MS temperature.

With increase/decrease in MS operating temperature, the value of stored energy correspondingly vice versa decreases/increases, what has to be taken into consideration for design of DEMO PHTS-IHTS and DEMO IHTS-PCS heat exchangers. For defined temperature interval between  $T_1 = 543$  K and  $T_2 = 738$  K, with increase in MS temperature, the percent of relative value change for stored energy  $E_{rel}$  is ~15.1% (see Table 2.9). HITEC molten salt flow rate through the pipeline is calculated as  $\dot{m} = \rho_T \cdot v_T \cdot S$ , where S is given by cross section of a circular pipe. It is stated that with increase in MS temperature, the velocity  $v_T$  of molten salt increases too.

For defined temperature interval between  $T_1 = 543$  K and  $T_2 = 738$  K, the percentage of change of MS relative velocity is ~8.2% (see Table 2.9). The Reynolds number increases and the Prandtl number decreases with increase in MS operating temperature. Consequently, from the point of view of DEMO IHTS pumps' operation stability, the effect of increasing/decreasing MS velocity in pipelines during increase/decrease in HITEC operating temperature needs to be considered.

## 2.6 Conclusions

The literature survey shows that thermal oils, liquid metals and molten salts can be used as heat transfer fluids in various TES systems.

The ability to ensure effective heat transfer makes molten salts attractive for application as thermal energy storage medium at high operating temperatures.

For DEMO IHTS system, HITEC molten salt is selected as both heat transfer and sensible thermal energy storage medium. HITEC molten salt is nontoxic, non-fouling, nonexplosive and nonflammable, what ensures DEMO IHTS operation safety.

The analysis of functional relations, which describe thermal evolution of HITEC thermo-physical parameters, is carried out.

A defined set of correlations is selected for novel customized MATLAB<sup>®</sup> module, which is developed for simulation of temperature dependent thermo-physical parameters of HITEC molten salt.

Using experimental data from literature survey, as well as the results of numerical simulations through MATLAB<sup>®</sup>/Simulink, following assumptions are formulated for development of simulation model of DEMO IHTS thermal storage tanks:

- Maximum operating temperature of HITEC molten salt has to be below the temperature, when MS thermal degradation begins.
- To avoid molten salt crystallization, MS minimum operating temperature has to be higher than HITEC melting point.
- HITEC molten salt is free of impurities.
- HITEC molten salt is chemically stable in the range of operating temperatures.
- An inert gas has to be used as cover gas in DEMO IHTS thermal storage tanks.
- There has to be no leakage in thermal storage tanks.
- There has to be no direct contact of MS with ambient environment.
- There has to be no contact of molten salt with other heat transfer fluids.
- Constructive material for DEMO IHTS thermal storage tanks and periphery equipment has to be compatible with HITEC molten salt.



### 3 Simulation model of DEMO IHTS thermal storage tank

#### 3.1 Heat transfer model of thermal storage tank

A model of heat transfer is discussed in ref. [190], being focused on a CSP thermal storage tank. Here, the mass and energy balance for control volume in terms of net mass flow, net enthalpy, net heat flow  $\dot{Q}_{net}$  and net work flow  $\dot{W}_{net}$  is given in following

$$\dot{m} = \dot{m}_{in} - \dot{m}_{out}, \quad (3.1)$$

$$U = m \cdot u, \quad (3.2)$$

$$\frac{dU}{dt} = \dot{m}_{in} \cdot h_{in} - \dot{m}_{out} \cdot h_{out} + \dot{Q}_{net} + \dot{W}_{net}, \quad (3.3)$$

where  $m$  indicates control volume mass,  $\dot{m}_{in}$  and  $\dot{m}_{out}$  are entering and leaving mass flows,  $h_{in}$  is specific enthalpy entering the control volume,  $h_{out}$  is specific enthalpy leaving the control volume,  $U$  is total internal energy, and  $u$  is specific internal energy of control volume. The eqs. (3.1)-(3.3) are worthy too for modeling of gas in thermal storage tank above MS level.

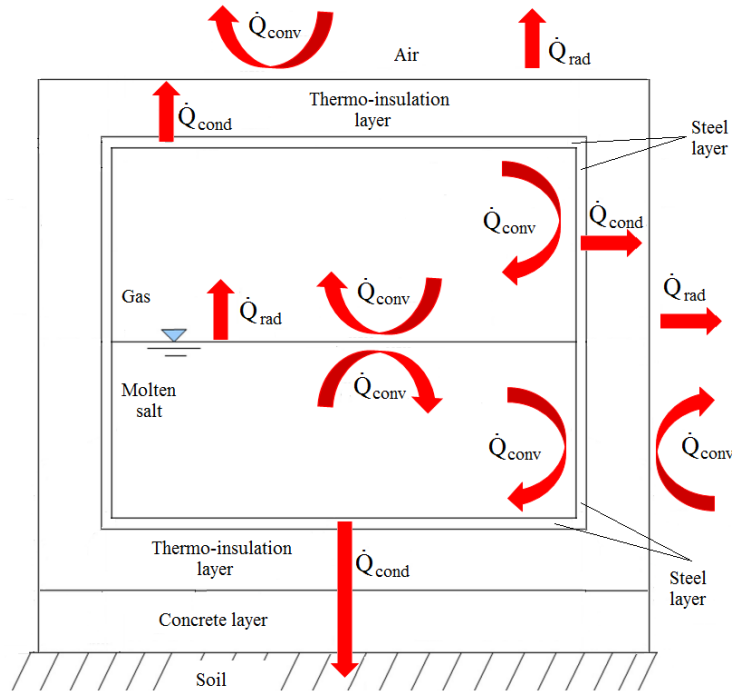


Fig. 3.1: Model scheme of thermal storage tank with molten salt and cover gas.

The model, which is applied in the current study, is shown in Fig. 3.1. It corresponds in main positions to the model, described in ref. [190]. It is assumed that solar irradiation thermal inertia and its contribution to thermal resistance are negligible. Hence, in the model the influence of solar irradiation on heat transfer in thermal storage tank is not taken into consideration [190].

Also it is assumed, that no natural convective air-cooling system is used to cool the concrete footprint. Neither conductive heat losses from concrete footprint into the soil, no natural convective heat losses from concrete footprint to ambient air are assumed. Explicit modelling of heat transfer from concrete to the ground and ambient air is left aside.

For simulation of storage tank roof and bottom, the planar conduction model is applied, which consists of a single element in direction normal to heat conduction. In the model, heat transfer is characteristic for two lateral wall parts, i.e. one for wetted wall and one for non-wetted wall. Heat conduction in vertical direction is not considered, since only one-dimensional heat conduction equations are applied [190]. The convection and radiation models form the interface between MS control volume, tank gas control volume, tank thermal insulation and the environment.

The convective heat transfer between MS inventory and tank's inner steel surfaces is described by natural convection correlations, using Nusselt number Nu, given as

$$\text{Nu} = f(\text{Pr}, \text{Gr}), \quad (3.4)$$

$$\text{Pr} = \frac{\mu \cdot c_p}{k} \quad \text{and} \quad \text{Gr} = \frac{g \cdot \beta \cdot (T_{\text{surface}} - T_{\infty}) \cdot L^3}{\nu^2}, \quad (3.5)$$

where Pr and Gr are Prandtl and Grashof numbers,  $\mu$  is dynamic viscosity,  $c_p$  is specific heat capacity at constant pressure,  $k$  is thermal conductivity,  $g$  is acceleration due to gravity,  $\beta$  is volumetric thermal expansion coefficient,  $T_{\text{surface}}$  is surface temperature,  $T_{\infty}$  is bulk temperature,  $L$  is characteristic length and  $\nu$  is kinematic viscosity [190].

Taking equations for a vertical plate, the average natural convective heat transfer coefficient between molten salt and tank's vertical inner steel wall gas can be calculated as

$$\text{Nu} = \frac{h \cdot L}{k} = 0.68 \cdot \text{Pr}^{1/2} \cdot \frac{\text{Gr}^{1/4}}{(0.952 + \text{Pr})^{1/4}} \quad \text{for } 10 < \text{Gr} < 10^8, \quad (3.6)$$

$$\text{Nu} = \frac{h \cdot L}{k} = 0.13 \cdot (\text{Gr} \cdot \text{Pr})^{1/3}, \quad \text{for } \text{Gr} > 10^9, \quad (3.7)$$

where  $h$  is heat transfer coefficient [190]. Equation (3.7) is used for turbulent flow region. To get a continuous transition between the correlations in transition region, the transformation

$$h = s \cdot h_{\text{laminar}} + (1 - s) \cdot h_{\text{turbulent}}, \quad (3.8)$$

is used, where  $s = f(\text{Gr})$  is an auxiliary transition function, which returns the value 1 and 0 for either laminar or turbulent regions for Grashof numbers [190]. Using the correlation for



horizontal and relatively cool plates facing upwards [190], the average natural convective heat transfer coefficient between MS and tank's steel bottom has to be calculated as

$$\text{Nu} = \frac{h \cdot L}{k} = 0.27 \cdot (\text{Gr} \cdot \text{Pr})^{1/4}, \text{ for } 10^5 < \text{Gr} < 10^{10}. \quad (3.9)$$

Assuming a very thin plate with negligible mass and inconsiderable thermal resistance between MS and cover gas, the control volumes are linked with the natural convection heat transfer correlation for a relatively cool surface, facing downwards for MS control volume, and another correlation for a relatively hot surface, facing upwards for gas control volume [190]. The correlations for the Nusselt number are given as

$$\text{Nu} = \frac{h \cdot L}{k} = 0.54 \cdot (\text{Gr} \cdot \text{Pr})^{1/4}, \text{ for } 10^5 < \text{Gr} < 10^7, \quad (3.10)$$

$$\text{Nu} = \frac{h \cdot L}{k} = 0.15 \cdot (\text{Gr} \cdot \text{Pr})^{1/3}, \text{ for } 10^7 < \text{Gr} < 10^{10}. \quad (3.11)$$

The temperature of an imaginary thin plate represents MS surface temperature. The equations can be applied to interfaces at tank's inner roof surface, as a relatively cool plate facing downwards, and a non-wetted part of tank's inner wall as a relatively cool vertical plate [190].

According to ref. [190], for heat exchange through the radiation between MS surface and non-wetted parts of tank's inner steel jacket it is assumed, that gas above MS level neither emits nor absorbs radiation in specified operating temperature range. Heat transfer by radiation includes its heat transfer between MS surface and tank's inner roof surface of circular planar shapes, as well as heat transfer between MS surface and tank's non-wetted inner wall surface of cylindrical shape. The tank's inner steel surface is treated as gray one. Likewise in ref. [190], the total emissivity of stainless steel surface is set to value of 0.3. As molten salt appears nearly transparent to infrared radiation, MS surface is treated as a quasi-black body with emissivity close to 1.0 and almost all incoming radiation is absorbed by liquid, either at surface or in deeper fluid zones [190]. The MS surface emissivity is set to value of 0.95. The shape-factor between MS surface and tank's inner roof surface is defined by the correlation for two parallel disks having unequal radii and distance  $d$  apart with centers on the same normal to their planes [190]:

$$F_{1-2} = \frac{1}{2 \cdot a^2} \cdot \left( d^2 + a^2 + b^2 - \sqrt{(d^2 + a^2 + b^2)^2 - 4 \cdot a^2 \cdot b^2} \right), \quad (3.12)$$

where  $a$  and  $b$  are radii of a smaller and a larger disk, respectively. In the model, the disks are defined of equal radii, i.e. equal to tank's inner radius [190].

In ref. [190], the coupling to environment is stated by convective and radiative heat exchange between tank's outer surface and environment, which depends on wind speed, as well as ambient air temperature  $T_{\text{air}}$ . The convective part is divided further into heat transfer through natural and forced convection. Average convective heat transfer coefficient between tank's outer surface and ambient air is obtained as

$$h = s \cdot h_{\text{natural}} + (1 - s) \cdot h_{\text{forced}}, \quad (3.13)$$

where  $s = f\left(\frac{Gr}{Re^2}\right)$  is transition function, which is specifically defined as

$$s = 0 \text{ for } \frac{Gr}{Re^2} < 0.7, \text{ and } s = f\left(\frac{Gr}{Re^2}\right) \text{ for } 0.7 \leq \frac{Gr}{Re^2} \leq 10, \text{ and } s = 1 \text{ for } \frac{Gr}{Re^2} > 10. \quad (3.14)$$

For a vertical flat plate, which is exposed to natural convection as well as to forced parallel horizontal flow, forced convection dominates for values  $Gr/Re^2 < 0.7$ , whereas natural convection dominates for value  $Gr/Re^2 > 10$ . Between the values of 0.7 and 10, heat transfer occurs through mixed convection, where heat transfer coefficient is obtained through superposition correlations that even consider flow directions of natural convective, as well as forced convective fluid streams. In the model, the modelling of mixed convection region is left aside [190]. At vertical outer surface, natural convective heat transfer coefficient  $h_{\text{natural}}$  is defined by eq. (3.8) for a vertical wall. Average forced convective heat transfer coefficient  $h_{\text{forced}}$  at vertical outer surface is determined, taking the Nusselt number correlation for cross flow over a cylinder, which is valid for the product of  $Re \cdot Pr > 0.2$  [190], resulting in

$$Nu = \frac{h \cdot L}{k} = 0.3 + \frac{0.62 \cdot Re^{\frac{1}{2}} \cdot Pr^{\frac{1}{3}}}{\left(1 + (0.4/Pr)^{\frac{2}{3}}\right)^{\frac{1}{4}}} \cdot \left(1 + (Re/282000)^{\frac{5}{8}}\right)^{\frac{4}{5}}, \quad Re = \frac{w \cdot D}{\nu}. \quad (3.15)$$

At roof's outer surface, average natural convective heat transfer coefficient  $h_{\text{natural}}$  is obtained by applying the Nusselt number correlation for relatively hot surfaces, facing upwards [190]. Average forced convective heat transfer coefficient  $h_{\text{forced}}$  at roof's outer surface is calculated, giving the correlations for a horizontal plate, which is exposed to forced parallel fluid flow, as

$$Nu = \frac{h \cdot L}{k} = 0.664 \cdot Re^{1/2} \cdot Pr^{1/3}, \text{ for } Re < 5 \cdot 10^5, \quad (3.16)$$

$$Nu = \frac{h \cdot L}{k} = 0.15 \cdot 0.664 \cdot Re^{0.8} \cdot Pr^{\frac{1}{3}}, \text{ for } 0.6 \leq Pr \leq 60 \text{ and } 5 \cdot 10^5 \leq Re \leq 10^7. \quad (3.17)$$

For radiative heat transfer, at tank's outer surface the long wave radiation heat exchange with environment is considered [190]. In the model, for outer roof surface black, the body

temperature is set to sky temperature  $T_{sky}$ . At vertical outer wall surface, the black body boundary temperature is set to ambient air temperature  $T_{amb}$ . In current model, the following equivalence  $T_{sky} = T_{amb}$  is assumed. Hence, the following equations are made up

$$\dot{Q}_{radiation,roof} = A_{roof} \cdot \sigma \cdot \epsilon_{surface} \cdot (T_{surface}^4 - T_{sky}^4), \quad (3.18)$$

$$\dot{Q}_{radiation,wall} = A_{wall} \cdot \sigma \cdot \epsilon_{surface} \cdot (T_{surface}^4 - T_{amb}^4), \quad (3.19)$$

where  $A_{roof}$  and  $A_{wall}$  describe top surface area and circumferential area of the cylinder, respectively,  $\sigma$  is given as Stefan-Boltzmann constant ( $W/m^2 \cdot K^4$ ),  $T_{surface}$  is set as surface temperature,  $T_{sky}$  is indicated as sky temperature and  $T_{amb}$  as ambient air temperature.

### 3.2 MATLAB®/Simulink model of DEMO IHTS thermal storage tank

The simulation model of DEMO IHTS thermal storage tank, which is developed using MATLAB®/Simulink [33], is schematically presented in Fig. 3.2. The module “Thermal Liquid (TL)” is applied for simulation of thermal storage tank, described as a thermal liquid container with variable fluid volume. The thermal storage tank possesses inlet and outlet ports A and B. Ports V, L, T and H are integrated for regulation of liquid volume, as well as for the level, temperature and heat losses to environment. Through port T, tank internal temperature is evolved over time. The pressure at tank inlet is the sum of constant tank pressurization, being specified in the module dialog box, and hydrostatic pressure due to inlet height. The governing correlations for mass, momentum and energy conservation laws, which are presented in Table 3.1, correlate with the equations (3.1) - (3.3).

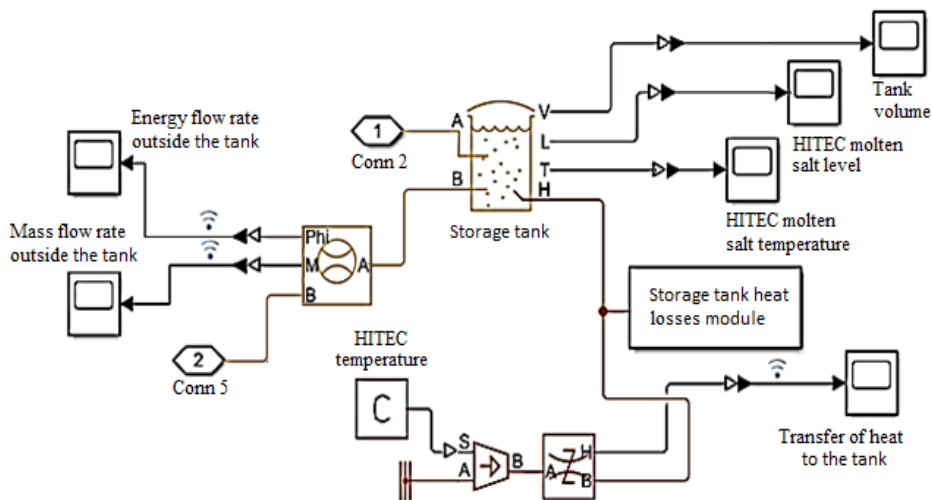


Fig. 3.2: Scheme of simulation model of DEMO IHTS thermal storage tank [33].

Title	Governing equation	Equation number	Remark
Tank fluid volume	$V = \frac{m}{\rho}$	(3.20)	Tank fluid volume is calculated, coming from total fluid mass at each time step.
Mass conservation	$\dot{m} = \dot{m}_A$	(3.21)	
Momentum conservation	$p_A + p_{\text{dyn}} = p_{\text{Ref}} + \rho \cdot g \cdot (z - z_A)$	(3.22)	If $\dot{m}_A \geq 0$ , $p_{\text{dyn}}=0$ If $\dot{m}_A \leq 0$ , $p_{\text{dyn}} = \frac{\dot{m}_A^2}{2 \cdot \rho_A \cdot S_A^2}$
Energy conservation	$\dot{m} \cdot (c_p - h \cdot \alpha) \cdot \Delta T = \dot{E}_A - \dot{m}_A \cdot h + \dot{Q}$	(3.23)	
Abbreviations	<p><math>\rho</math> - fluid density</p> <p><math>m</math> - fluid mass</p> <p><math>\dot{m}</math> - net mass flow rate into tank</p> <p><math>\dot{m}_A</math> - mass flow rate into tank through inlet A</p> <p><math>p_A</math> - fluid pressure at inlet A</p> <p><math>p_{\text{Ref}}</math> - constant tank pressurization</p> <p><math>p_{\text{dyn}}</math> - dynamic pressure</p> <p><math>z</math> - tank level or height relative to tank bottom</p> <p><math>z_A</math> - tank inlet elevation relative to tank bottom</p>	<p><math>\rho_A</math> - liquid density at inlet A</p> <p><math>S_A</math> - tank inlet area</p> <p><math>g</math> - gravitational constant</p> <p><math>c_p</math> - fluid thermal capacity</p> <p><math>\alpha</math> - fluid isobaric bulk modulus</p> <p><math>T</math> - fluid temperature</p> <p><math>\dot{E}_A</math> - energy flow rate into tank through port A</p> <p><math>h</math> - fluid enthalpy</p> <p><math>\dot{Q}</math> - thermal energy flow rate into tank through port H</p>	
Assumptions:			
<ul style="list-style-type: none"> <li>• Absolute pressure of tank fluid volume is assumed as constant, being equal to the value, which is specified in module dialog box.</li> <li>• Tank elevation head affects only inlet pressure calculations.</li> <li>• Fluid momentum is lost at tank inlet due to sudden expansion into tank volume.</li> <li>• Once molten salt with a certain kinetic energy enters in tank, the fluid expands and loses almost all its dynamic energy.</li> </ul>			

Table 3.1: Governing equations for model of thermal storage tank, simulated as a thermal liquid container with variable fluid volume [215].

The “Mass & Energy Flow Rate Sensor” module represents an ideal sensor that measures mass and energy flow rates through thermal liquid node. The orientation of ports A and B establishes the measurement sign, which is positive for the flow from port A to B. Ports M and Phi are physical signal ports, which output the measurement data for mass and energy flow rates, respectively [215]. Across the sensor, no change in pressure or temperature is perceived.

The novel customized MATLAB<sup>®</sup> module for numerical simulation of HITEC thermo-physical properties (see chapter 2, §.2.4) is integrated into simulation model, shown in Fig. 3.2.

To simulate the heat losses from DEMO IHTS thermal storage tanks to environment, a novel customized MATLAB<sup>®</sup> module is developed, see Fig. 3.3. The constellation of customized module corresponds to the model, presented in Fig. 3.1. The model includes the modules [182, 215], which are categorized by conductive, convective and radiative heat transfer.

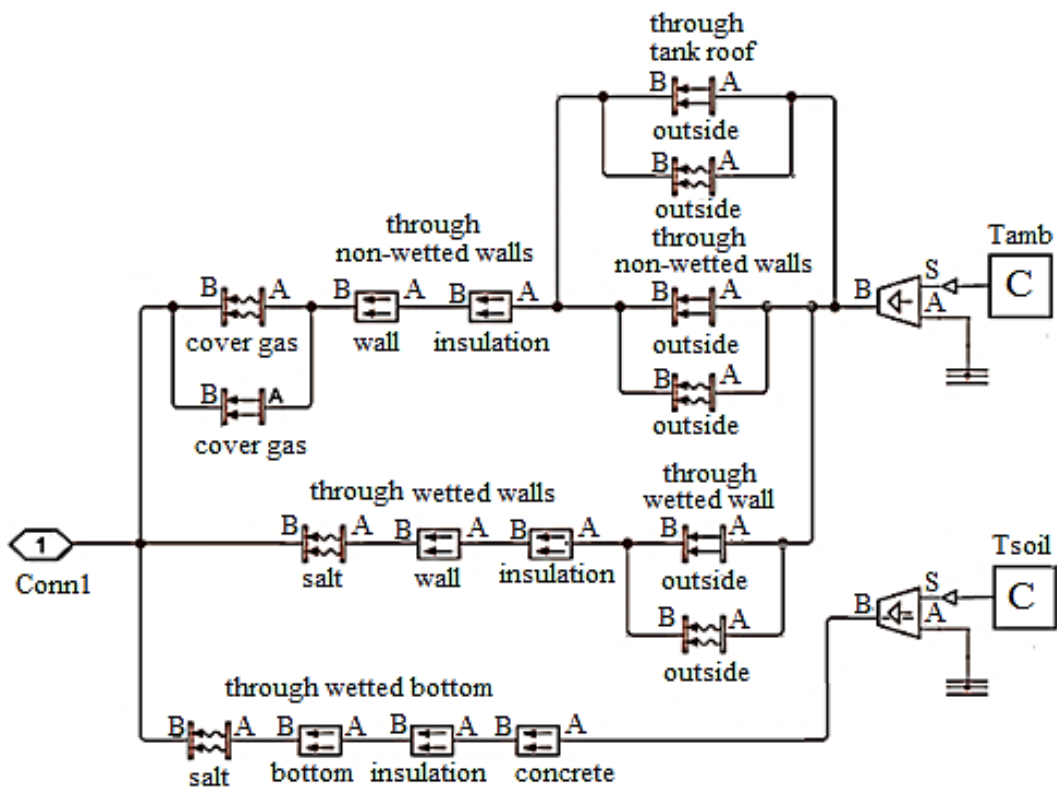
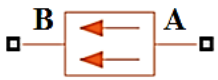
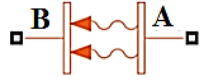
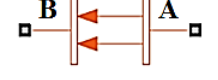


Fig. 3.3: Customized module for heat losses to environment from a thermal storage tank.

For simulations, the already existing MATLAB<sup>®</sup>/Simulink Library modules are applied, reducing the programming effort of modelling [215]. In the modules, terminals A and B are thermal conserving ports, which are associated with material layers. The equations, which govern the operation of the modules, are presented in Table 3.2.

Module	Schematic view	Governing equation	Equation number	Description
Conductive heat transfer		$\dot{Q}_{\text{cond}} = k \cdot \frac{A}{B} \cdot (T_A - T_B)$	(3.24)	Module represents heat transfer by conduction between two layers of the same material. Governing equation: Fourier's law.
Convective heat transfer		$\dot{Q}_{\text{conv}} = h \cdot S \cdot (T_{\text{SA}} - T_{\text{SB}})$	(3.25)	Module describes heat transfer by convection between two bodies by means of fluid motion. Governing equation: Newton law of cooling.
Radiative heat transfer		$\dot{Q}_{\text{rad}} = \sigma \cdot A_S \cdot T_S^4$ $\dot{Q}_{\text{rad}} = \sigma \cdot \varepsilon \cdot A_S \cdot (T_{\text{S1}}^4 - T_{\text{S2}}^4)$	(3.26) (3.27)	Module describes heat transfer by radiation between two bodies. Governing equation: Stefan-Boltzmann law.
Abbreviations	$\dot{Q}$ - heat flow k - thermal conductivity A - area normal to heat flow direction B - layer thickness $T_A$ and $T_B$ – layers' temperatures h - convective heat transfer coefficient			S - surface area in contact with fluid $T_{\text{SA}}$ and $T_{\text{SB}}$ - temperatures on and far from the surface $T_S$ - surface temperature $\sigma$ - Stefan-Boltzmann radiation constant $A_S$ - emitting body surface area $\varepsilon$ - surface emissivity

**Remark:**

For two surfaces with  $\sigma$ ,  $\varepsilon$  and  $A_S$ , if the 1<sup>st</sup> surface is characterized by  $T_{\text{S1}}$  and the 2<sup>nd</sup> one by  $T_{\text{S2}}$ , further condition is given by  $T_{\text{S2}} > T_{\text{S1}}$  and air is enclosed between the surfaces. Radiation heat flow is calculated with eq. (3.26).

Table 3.2: Simulation modules for conductive, convective and radiative heat transfer [215].

For the running of simulations, the MATLAB<sup>®</sup>/Simulink variable-step solver is applied, which includes a minimum and maximum step size for the model by implementing trapezoidal rule using free interpolant. The implicit solver is better fitted for continuous models, as it varies the step size during the simulation process by reducing its value, in order to increase the accuracy, when the states of dynamic model change rapidly during zero-crossing events. The solver default error is at 0.001 and the computed state is accurate to within 0.1%.

### 3.3 Conclusions

The heat transfer model for thermal energy storage tank is reviewed, taking into consideration the results of prior study, discussed in ref. [190].

The governing equations, which describe the heat transfer inside thermal storage tank and heat losses to environment, are analyzed, being in the focus of study.

MATLAB<sup>®</sup>/Simulink simulation model of DEMO IHTS thermal storage tank is developed. Thermal storage tank is modelled as a thermal liquid cylindrical container with variable fluid volume.

A novel customized MATLAB<sup>®</sup> module for numerical simulation of HITEC thermo-physical properties is integrated into DEMO IHTS thermal storage tank simulation model.

For simulation of heat losses to environment from DEMO IHTS thermal storage tank, a novel customized MATLAB<sup>®</sup> module is developed. The modules involve the governing equations, related to convective, conductive and radiative heat transfer.



## 4 Temporal evolution of DEMO IHTS thermal storage tank parameters

### 4.1 Design parameters for simulation model of DEMO IHTS thermal storage tanks

In the simulation model for DEMO IHTS, the cold thermal storage tank, as well as the hot one, is specified as a thermal-insulated flat dome cylinder-shape container with diameter  $D$  and height  $H$  [84, 99, 100, 190]. The main parameters of DEMO IHTS thermal storage tanks are joined in Table 4.1 and in Appendix A.5, Table A5.3.

Parameter	Hot tank	Cold tank
Tank total wall thickness, m		0.045
Tank thermal storage capacity, $MW_{th}$		426
Tank inlet and outlet diameter, m		1.4
Steel SS 1.4301 thermal conductivity, $W/(m \cdot K)$		22
Concrete thermal conductivity, $W/(m \cdot K)$		1.7
HITEC mass, kg		$5.04 \cdot 10^6$
HITEC average mass flow rate, kg/s		7330
HITEC temperature at surface, K	733	538
HITEC temperature at bulk, K	738	543
Argon thermal conductivity, $W/(m \cdot K)$	0.0354	0.0296
Average wind velocity, m/s		5
Air temperature at tank wall surface, K		338
Ambient temperature outside the tank, K		298
Ambient pressure outside the tank, Pa		101325
Insulation layer material	ProRox <sup>®</sup> WM950	KlimaRock <sup>®</sup>
Insulation thermal conductivity, $W/(m \cdot K)$	0.146	0.114

Table 4.1: Technical parameters of DEMO IHTS thermal storage tanks [33, 84, 99, 182].

The tank bottom construction consists of a single-layer steel and another insulation layer. The concrete footprint is 0.5 m thick with an area of  $\sim 2550$  m<sup>2</sup>. Thermal storage tank is manufactured from stainless steel SS 1.4301 [77, 88, 216, 217]. For tank steel floor, roof and lateral wall, the corrosion allowance of 0.02 m is considered [33, 84, 212]. The total thickness of steel layer is 0.045 m. The density of steel amounts to 7900 kg/m<sup>3</sup> at 293 K. Steel thermal conductivity of 22  $W/(m \cdot K)$  is taken at 773 K. Cold storage tank is thermal insulated with

KlimaRock<sup>®</sup> and hot storage tank with ProRox<sup>®</sup> WM950, respectively [212]. The thickness of insulation material is 0.3 m and its density is 60 kg/m<sup>3</sup>. The thermal conductivity for ProRox<sup>®</sup> WM950 at 773 K is given by 0.146 W/(m·K) and for KlimaRock<sup>®</sup> by 0.114 W/(m·K). The simulated critical MS temperature of  $T_{cr} = 473$  K is taken, that is higher than HITEC melting temperature of  $T_m = 415$  K. Molten salt maximum operating temperature lies at  $T_{max} = 738$  K. The modelling of electrical heat tracing of thermal storage tanks is excluded. HITEC is incompressible and only temperature dependence of MS thermo-physical parameters is considered. In thermal storage tank, HITEC bulk temperature lies 5 K higher than MS surface temperature. Molten salt is not contaminated. There appear no chemical reactions between MS and environment. Inside thermal storage tank, homogeneous molten salt temperature is considered, what assumes that even in offline mode of storage system, heat losses to environment offer enough driving force to establish a characteristic natural convection flow profile within the storage tank [190].

In simulations, MS filling level in storage tank varies between 5-95%, depending on pulse or dwell operation period. The height of MS pump inlet varies between 0.1-0.7 m, what defines the MS mass, which can't be pumped out of storage tank [190, 218]. The storage tank is divided in two sections, which correspond to HTF and gas control volumes. Argon is used as a cover gas in the tank dome. Inside storage tank, cover gas is over-pressurized. The thermal conductivity of argon is  $k = 0.0354$  W/(m·K) at 773 K. It is assumed that heat loss induced velocity profile inside the tank provides a good mixing of gas, ensuring a homogeneous temperature distribution. Ambient temperature of 298 K is taken. Average wind speed is 5 m/s. For insulation layer, the maximum temperature of 313 K outside the tank's walls is chosen.

## 4.2 Interplay between molten salt filling level and thermal storage tank geometry

For DEMO IHTS thermal storage tank, which is a thermal-insulated cylindrical container with a flat dome, the specific area and tank height can be calculated as

$$S_H = \frac{\pi \cdot D_{roof}^2}{4} + \frac{\pi \cdot D_{bottom}^2}{4} + \pi \cdot D_{ins} \cdot H = \frac{\pi \cdot D_{roof}^2}{2} \cdot \left( 1 + \frac{2 \cdot H \cdot (D_{roof} + 2 \cdot \Delta D_{ins})}{D_{roof}^2} \right), \quad (4.1)$$

$$H = H_{wet} + H_{nw} \text{ and } D_{roof} = D_{bottom} \quad (4.2)$$

where  $D_{\text{roof}}$ ,  $D_{\text{bottom}}$  and  $D_{\text{ins}}$  describe diameters of roof, bottom and thermal insulation,  $\Delta D_{\text{ins}}$  is thickness of thermal insulation material,  $H$  is height of tank, and  $H_{\text{wet}}$  and  $H_{\text{nw}}$  are heights of wet and non-wetted tank lateral wall, respectively.

Assuming that heat losses through the tank bottom are considerably lower than through the roof [219, 220], given as  $Q_{\text{loss,bot}} \ll Q_{\text{loss roof}}$  and  $\Delta D_{\text{isol}} \ll D_{\text{roof}}$ , the specific surface area is calculated as

$$S_H \approx \frac{\pi \cdot D_{\text{roof}}^2}{4} + \pi \cdot D_{\text{ins}} \cdot H \approx \frac{\pi \cdot D_{\text{roof}}^2}{4} \cdot \left(1 + \frac{4 \cdot H}{D_{\text{roof}}}\right), \quad (4.3)$$

$$S_H = S_{H,\text{wet}} + S_{H,\text{nw}} \approx \frac{\pi \cdot D_{\text{roof}}^2}{4} \cdot \left(1 + \frac{4 \cdot H_{\text{wet}}}{D_{\text{roof}}} + \frac{4 \cdot H_{\text{nw}}}{D_{\text{roof}}}\right), \quad (4.4)$$

$$S_{H,\text{wet}} \approx \pi \cdot D_{\text{roof}} \cdot H_{\text{wet}} \quad \text{and} \quad S_{H,\text{nw}} \approx \frac{\pi \cdot D_{\text{roof}}^2}{4} \cdot \left(1 + \frac{4 \cdot H_{\text{nw}}}{D_{\text{roof}}}\right). \quad (4.5)$$

Regarding only tank lateral wall, the equations for  $S_{H,\text{wet}}$  and  $S_{H,\text{nw}}$  can be written as

$$S_{H,\text{wet}} \approx \pi \cdot D_{\text{roof}} \cdot H_{\text{wet}} \quad \text{and} \quad S_{H,\text{nw}} \approx \pi \cdot D_{\text{roof}} \cdot H_{\text{nw}}. \quad (4.6)$$

The quotient between specific surface area of non-wetted and wetted lateral walls of thermal storage tank can be defined as

$$\frac{S_{H,\text{nw}}}{S_{H,\text{wet}}} = \frac{H - H_{\text{wet}}}{H_{\text{wet}}} = \frac{H}{H_{\text{wet}}} - 1. \quad (4.7)$$

Focusing on stability and safety of operation, the height  $H_{\text{wet}}$  of wetted lateral wall of DEMO IHTS thermal storage tank has to be smaller than total tank height  $H$  tank, independently of TES operation conditions. The value of  $S_{H,\text{nw}}/S_{H,\text{wet}}$  should be  $0.11 \leq S_{H,\text{nw}}/S_{H,\text{wet}} \leq 0.33$  assuming the filling level of thermal storage tank between 75% and 90%. Here the thermal expansion of the molten salt with increase in operating temperature has to be taken into consideration. There should be also enough space above the level of molten salt inside the storage tank to ensure the maintenance of necessary measurement equipment inside the tank space. The last but not least, the geometry of the thermal storage tanks is a decisive factor, which defines the mechanical stability and maintenance costs of the corresponding construction, as well as heat losses to the environment.

The analysis of design parameters shows that thermal storage tanks with various diameters  $D$  and heights  $H$  possess same inner volume, see Fig. 4.1. For instance, thermal storage tanks with  $D_1 = 21$  m and  $H_1 = 10$  m, or  $D_2 = 25$  m and  $H_2 = 7.1$  m, or  $D_3 = 28$  m and  $H_3 = 5.6$  m have similar volume of  $V = 3460 \pm 20$  m<sup>3</sup>. Previously modelled tank with  $D = 23.8$  m and  $H = 7.8$  m

has a volume of  $V = 3468 \text{ m}^3$  [84, 99, 100]. The storage tanks with same volume possess different area of lateral wall, floor and roof. For example, a tank with  $D_1 = 21 \text{ m}$  and  $H_1 = 10 \text{ m}$  has floor and roof area of  $\sim 346 \text{ m}^2$  and lateral wall area of  $\sim 659 \text{ m}^2$ . Thermal storage tank with  $D_3 = 28 \text{ m}$  and  $H_3 = 5.6 \text{ m}$  has floor and roof area of  $\sim 615 \text{ m}^2$  and lateral wall area of  $\sim 492 \text{ m}^2$ .

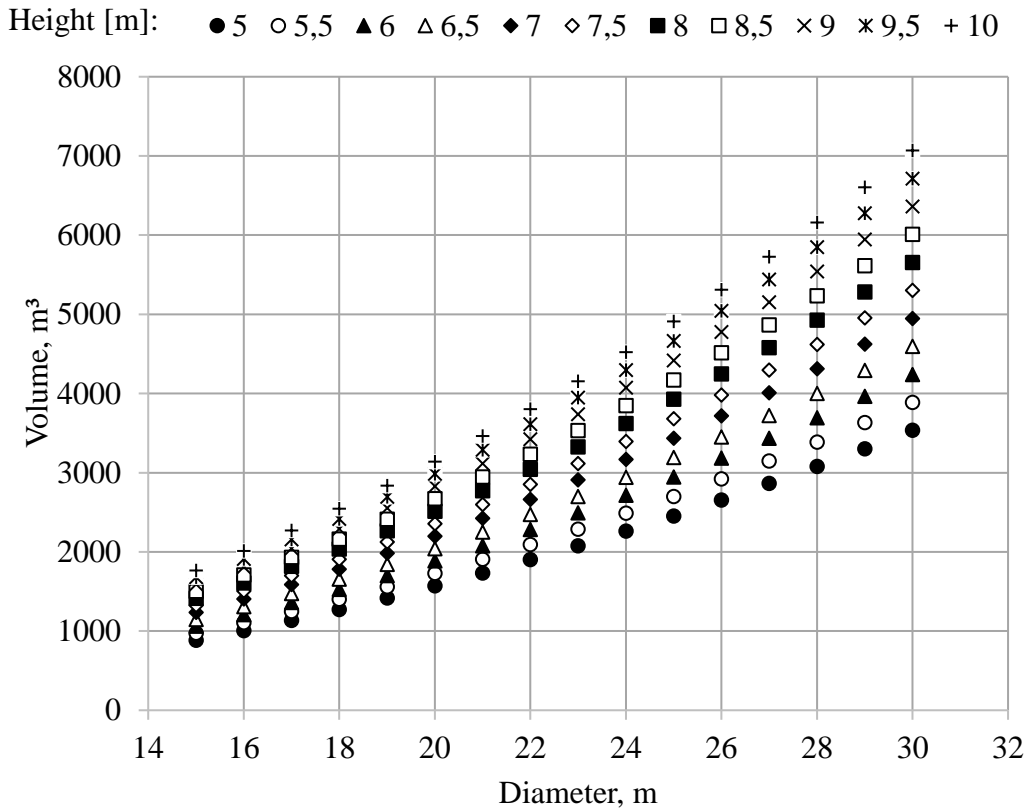


Fig. 4.1: Storage tank volume for variable diameter and height.

For constant diameter with growing tank height, the area of tank lateral wall linearly increases, see Fig. 4.2. For constant height, the increase in tank diameter has a more pronounced impact on tank total area than the increase in height at constant diameter, see Fig. 4.3. For simulations, the cold and hot storage tanks with  $D = 24 \text{ m}$  and  $H = 7.5 \text{ m}$  are selected. These tanks have floor and roof area of  $\sim 452 \text{ m}^2$ . Their lateral wall area of  $\sim 565 \text{ m}^2$  is with  $\sim 3.1\%$  smaller than the lateral wall area of  $\sim 583 \text{ m}^2$  for a storage tank with  $D = 23.8 \text{ m}$  and  $H = 7.8 \text{ m}$ , which has been previously modelled [84, 99, 100].

The influence of HITEC temperature on storage tank parameters is studied for molten salt mass of  $5 \cdot 10^6 \text{ kg}$  and  $6 \cdot 10^6 \text{ kg}$ , respectively. The results of calculations are presented in Table 4.2. For MS mass of  $5 \cdot 10^6 \text{ kg}$  and operating temperature of  $543 \text{ K}$ , HITEC volume in cold storage tank amounts to  $2657 \text{ m}^3$ . Due to thermal expansion, assuming the operating temperature of  $738 \text{ K}$ , molten salt volume in hot storage tank reaches the value of  $2875 \text{ m}^3$ .

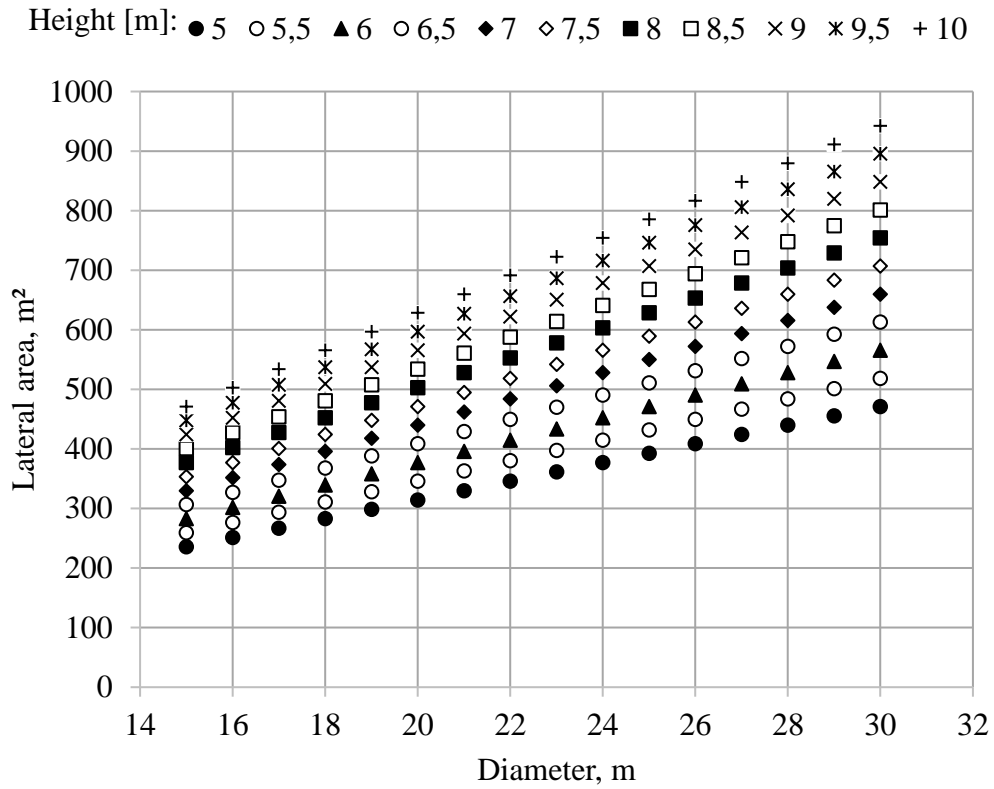


Fig. 4.2: Storage tank lateral wall area for variable diameter and height.

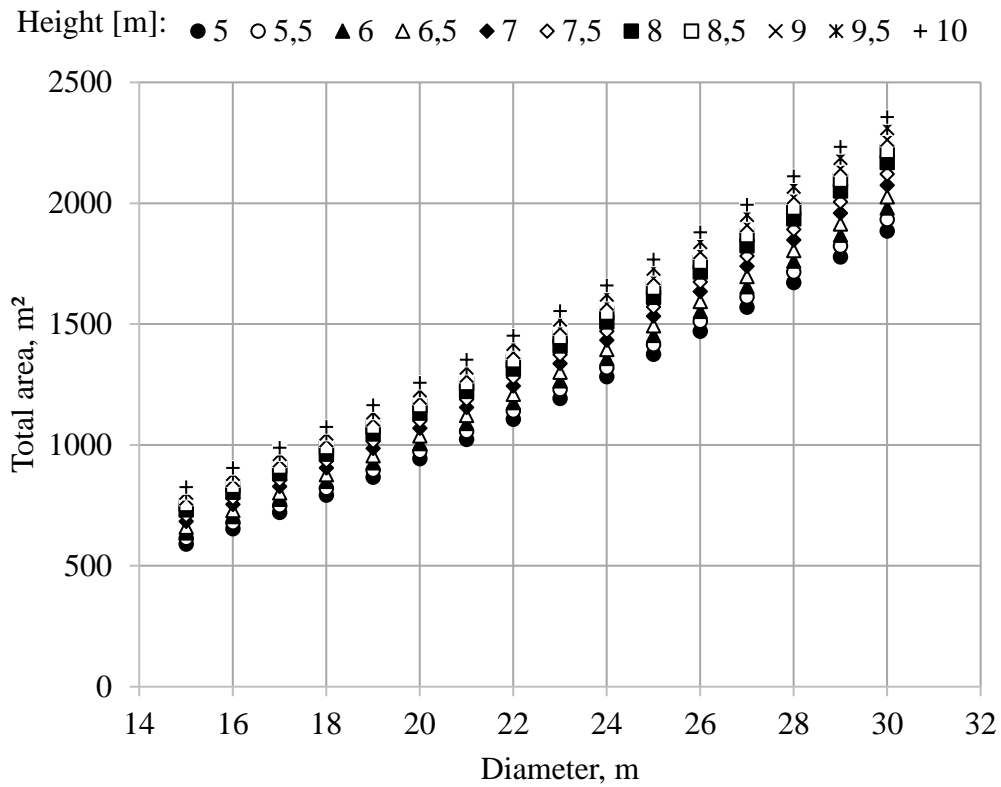


Fig. 4.3 Storage tank total area for variable diameter and height.

Parameter	Temperature, K					
	415	473	543	573	738	763
HITEC density, kg/m <sup>3</sup>	1975	1933	1882	1860	1739	1721
<b>Molten salt mass of 5·10<sup>6</sup> kg</b>						
HITEC volume, m <sup>3</sup>	2531	2586	2657	2688	2875	2906
Increase in MS volume*, m <sup>3</sup>	0	55	126	157	34	375
Increase in MS volume*, %	0	2.17	4.98	6.20	13.6	14.8
*In comparison to V=2531 m <sup>3</sup>						
<b>Molten salt mass of 6·10<sup>6</sup> kg</b>						
HITEC volume, m <sup>3</sup>	3037	3104	3188	3226	3450	3486
Increase in MS volume**, m <sup>3</sup>	0	67	151	189	413	449
Increase in MS volume**, %	0	2.2	4.97	6.22	13.6	14.8
**In comparison to V=3037 m <sup>3</sup>						
<b>Difference in MS volume for molten salt mass of 5·10<sup>6</sup> kg and 6·10<sup>6</sup> kg</b>						
Increase in MS volume***, m <sup>3</sup>	506	573	657	695	919	955
Increase in MS volume***, %	20	22.64	25.6	27.5	36.3	37.7
***In comparison to V=2531 m <sup>3</sup>						

Table 4.2: Volume of HITEC molten salt for variable operating temperature.

Taking into account the tank filling level of 75%, the volume of cold and hot tank each should be ~3543 m<sup>3</sup> and ~3833 m<sup>3</sup>, respectively. For filling level of 90%, the volume of cold and hot storage tank decreases to ~2952 m<sup>3</sup> and ~3194 m<sup>3</sup>, correspondingly. For given HITEC mass of 5·10<sup>6</sup> kg, the increase in temperature from 415 K up to 763 K results in growing MS volume with ~14.8% due to thermal expansion from 2531 m<sup>3</sup> up to 2906 m<sup>3</sup>. For given MS mass of 6·10<sup>6</sup> kg, MS volume rises from 3037 m<sup>3</sup> up to 3486 m<sup>3</sup>. The comparison between MS volume of molten salt mass  $m = 5 \cdot 10^6$  kg at 415 K and  $m = 6 \cdot 10^6$  kg at 763 K ( $V_{5000} = 2531$  m<sup>3</sup> versus  $V_{6000} = 3486$  m<sup>3</sup>) shows an increase in MS volume of 37.7%. Subsequently, the consecutive change of molten salt volume with increase in MS temperature is a critical factor for design and operation safety of DEMO IHTS thermal storage tanks.

Regarding Table 4.3, the simulations are carried out for various MS operating temperature and tank height. At this sight, the cases 1c and 2c are for cold storage tank and the cases 1h and 2h are for hot storage tank. In case 1c, tank height is 7.5 m and for case 2c it is 8.4 m, obtaining a height growth of 12%. Coming to case 1h, the height of storage tank is 7.5 m and for case 2h it is 10 m, receiving a height growth of 25%. Referring to case 1c, MS temperatures of 573 K and 543 K are applied. For case 1h, the simulations are carried out for MS temperatures of 763 K and 738 K, respectively.

Parameter	Cold storage tank			Hot storage tank		
	Case 1c	Case 2c		Case 1h	Case 2h	
HITEC temperature, K	573	543	543	763	738	738
Tank height, m	7.5	7.5	8.4	7.5	7.5	10
<b>HITEC molten salt mass of <math>5 \cdot 10^6</math> kg</b>						
HITEC volume, m <sup>3</sup>	2688	2657	2657	2906	2875	2875
Tank volume, m <sup>3</sup>	3393	3393	3800	3393	3393	4523
HITEC/tank volume, %	79.5	78.3	69.9	85.6	84.7	63.6
<b>HITEC molten salt mass of <math>6 \cdot 10^6</math> kg</b>						
HITEC volume, m <sup>3</sup>	3226	3188	3188	3487	3450	3450
Tank volume, m <sup>3</sup>	3393	3393	3800	3393	3393	4523
HITEC/tank volume, %	95.1	94	83.9	102.8	101.7	76.3

Table 4.3: Ratio between the volume of HITEC molten salt and storage tank volume.

Parameter	Cold tank		Hot tank	
	Case 1c	Case 2c	Case 1h	Case 2h
Inner diameter, m	24		24	
Height, m	7.5	8.4	7.5	10
Lateral wall area, m <sup>2</sup>	565.5	633.3	565.5	754
Tank volume, m <sup>3</sup>	3393	3800	3393	4523
Tank wall thickness, m	0.045		0.045	
Mass of tank bottom, kg	160824		160824	
Mass of tank roof, kg	160824		160824	
Mass of lateral wall, kg	100609	112683	100609	134146
Total mass of tank, kg	422257	434331	422257	455794
Volume of roof insulation, m <sup>3</sup>	136		136	
Volume of lateral wall insulation, m <sup>3</sup>	85.5	95.8	85.5	114
Total volume of insulation*, m <sup>3</sup>	221.5	231.8	221.5	250
Total mass of insulation*, kg	13290	13860	13290	15000
Remark: * Volume of thermal-insulation material both for tank lateral wall and roof				

Table 4.4: Comparative data for DEMO IHTS thermal storage tanks.

In cold tank, for HITEC mass of  $5 \cdot 10^6$  kg and tank height of 7.5 m, the decrease in MS temperature from 573 K to 543 K corresponds to a decline of 1.2% in MS volume and the ratio of HITEC volume to tank volume reduces from 79.5% to 78.3%. Assuming cold tank height of 7.5 m and  $T_{MS} = 573$  K, by increase in MS mass up to  $6 \cdot 10^6$  kg, molten salt volume of 3226 m<sup>3</sup> increases nearly up to tank upper level.

In hot storage tank with  $H = 7.5$  m and  $T_{MS} = 763$  K, by increase in MS mass up to  $6 \cdot 10^6$  kg, HITEC volume rises over tank upper limit volume with ratio of 102.8%. With decrease in molten salt temperature from 763 K to 738 K, the ratio of MS volume to hot tank volume again is over 100%, presenting the value of 101.7%. The results of calculations indicate that a rise in thermal storage tank height from 7.5 m up to 8.4 m increases the tank mass by 2.86% as well as the mass of insulation material by 4.2%, see Table 4.4. With increase in height of tank up to 10 m, the mass of tank and thermal insulation increases with 7.94% and 12.9%, respectively. Consequently, to enable safe operation of DEMO IHTS, it is preferable to select a taller storage tank, including buffer space, to prevent any kind of tank damage or bursting due to thermal expansion of HITEC molten salt.

### 4.3 Heat losses to environment from thermal storage tanks

The simulations of temporal evolution of HITEC molten salt temperature drop in cold and hot storage tanks with  $D = 24$  m and  $H = 7.5$  m are carried out for variable tank height and thermal insulation thickness. HITEC mass of  $5.04 \cdot 10^6$  kg as initial condition is taken. In cold storage tank, the initial HITEC operating temperature is 573 K and in hot storage tank it is 763 K. Ambient conditions remain constant. For the thermal storage tanks, no external electrical heat tracing is applied.

The simulations are evolved for variable thickness of tank thermal insulation between 0.2-0.5 m. In cold storage tank with an insulation thickness of 0.2 m, see Fig. 4.4, MS critical temperature of 473 K is reached after 19 days. The increase in insulation thickness up to 0.5 m results in rising time up to 45 days. For cold storage tank with selected insulation thickness of 0.3 m, the curve for MS temperature drop from 573 K to 473 K can be described, using Microsoft Excel linear approximation equation

$$T_{\text{cold}} = -3.4218 \cdot t + 567.71, \quad (4.8)$$

with residual value of  $R^2 = 0.9937$ .



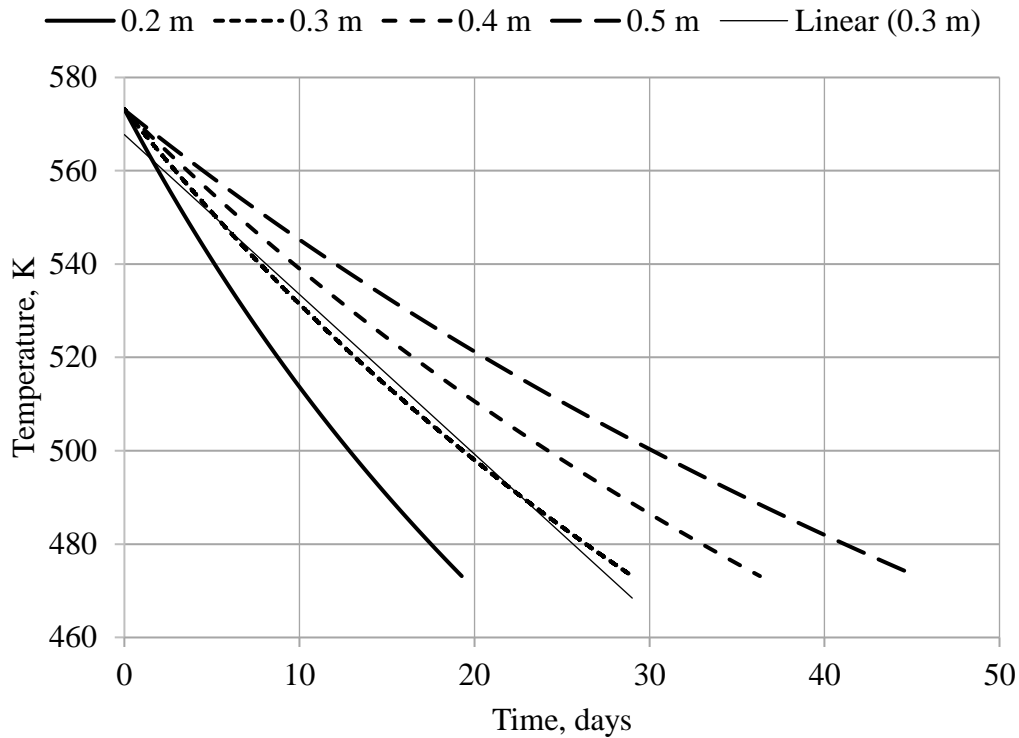


Fig. 4.4: Temperature drop inside cold storage tank for various thermal insulation thickness.

In hot storage tank with an insulation thickness of 0.2 m, HITEC needs 29 days to reach its critical temperature and 80 days are required, if insulation material thickness is 0.5 m (Fig. 4.5). For hot storage tank with selected insulation thickness of 0.3 m, the curve can be approximated through simulation using Microsoft Excel by the following function

$$T_{\text{hot}} = 0.1059 \cdot t^2 - 10.934 \cdot t + 753.08, \quad (4.9)$$

with the residual value of  $R^2 = 0.9984$ .

The results of simulation of temperature drop in dependence of tank height are presented in Fig. 4.6 and Fig. 4.7. For cold tank, the curves 1 and 2 correspond to case 1c (see Table 4.3). The calculated dependences can be approximated using 2<sup>nd</sup> grade polynomic curves through simulation using MS Excel. For example, for cold tank the approximation correlation for curve 2 (Fig. 4.6) is as following

$$T = 0.0715 \cdot t^2 - 5.7574 \cdot t + 542.82, \quad (4.10)$$

with the residual value of  $R^2 = 1$ .

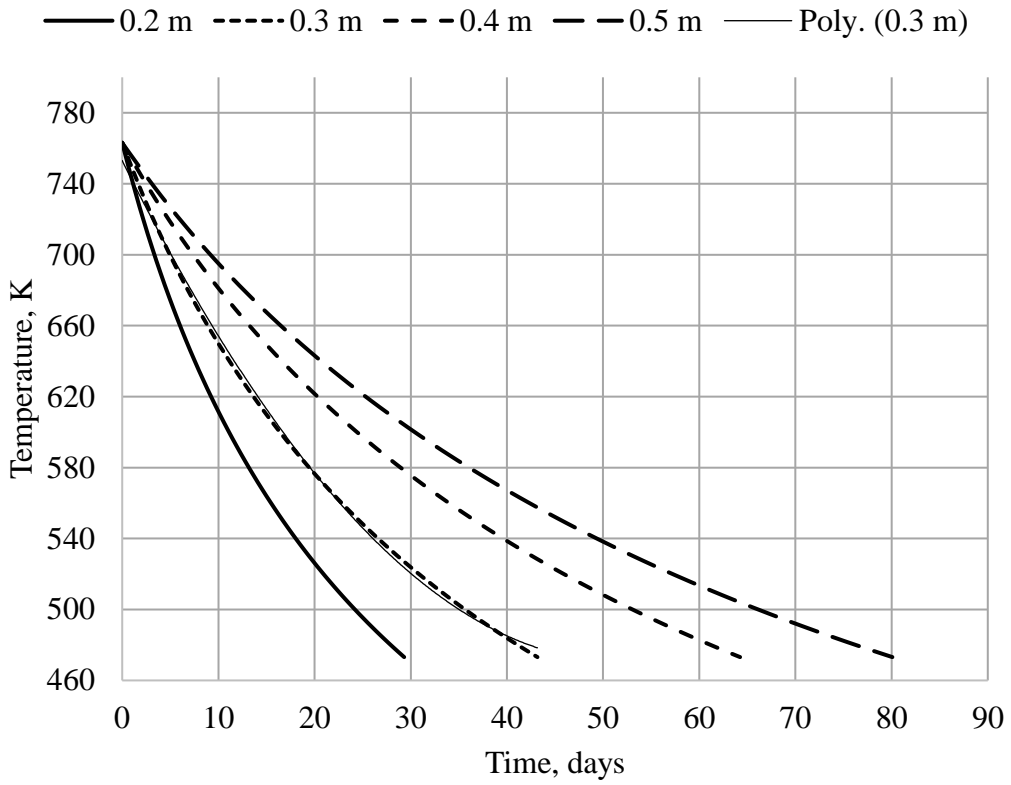


Fig. 4.5: Temperature drop inside hot storage tank for various thermal insulation thickness.

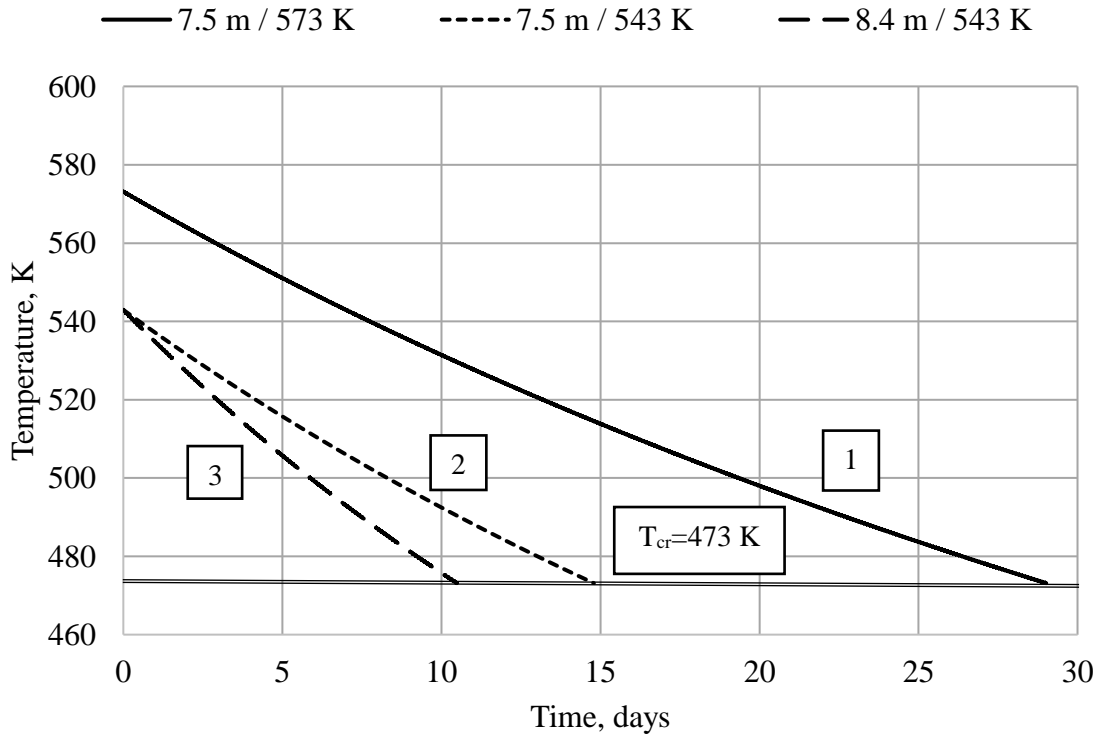


Fig. 4.6: Temperature drop inside cold storage tank with various tank height.

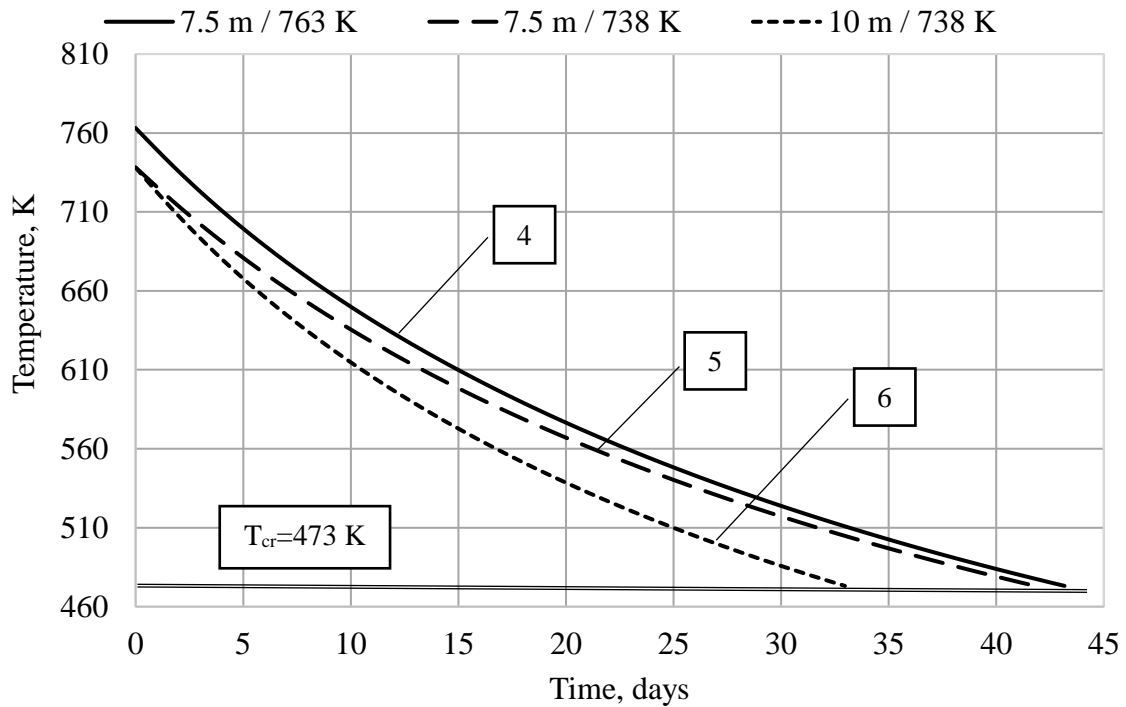


Fig. 4.7: Temperature drop inside hot storage tank with various tank height.

At MS operating temperature of 543 K, the increase in height of cold storage tank from 7.5 m up to 8.4 m results in decrease in cooling time of storage tank from ~14.5 days to ~10.5 days, before HITEC reaches its critical temperature  $T_{cr} = 473\text{ K}$  (see Fig. 4.6). Same tendency is observed for hot storage tank, whereas the curves 4 and 5 correspond to case 1h, see Fig. 4.7 and Table 4.3. The decrease in MS temperature from 763 K to 738 K results in reduction in time of MS cooling from 44 days to 42 days, before HITEC molten salt reaches its critical temperature. For simulation at initial temperature of 738 K, the increase in tank height from 7.5 m to 10 m leads to reduction of MS cooling time from 42 to 33 days, correspondingly.

The simulations using MATLAB<sup>®</sup>/Simulink show that the increase in thickness of thermal insulation decreases the temperature drop per day, what results in reducing specific heat losses per area. The increase in height of thermal storage tank enhances molten salt cooling. Thermal storage tank filling level and heat losses through wet and non-wet tank lateral walls play here a major role. In simulations using MATLAB<sup>®</sup>/Simulink, unchangeable ambient conditions are used. Nevertheless, the fluctuations of ambient temperature, wind velocity, solar irradiation, etc., are important factors, those influence on specific heat losses per area from thermal storage tanks has to be taken into consideration for prospective research studies.

## 4.4 Evaluation and validation of simulation model for heat losses to environment

The results of simulation using developed MATLAB<sup>®</sup>/Simulink model for heat losses to environment (see chapter 3) are compared with the simulation data for the model, which is discussed in ref. [190]. The ref. [190] includes the comparison of numerical results and experimental data for inventory temperature drop in the CSP thermal storage tanks, measured at a commercial parabolic trough collector plant. In the ref. [190], the performed comparison is not seen as the validation of simulation model, because neither the environmental boundary conditions, nor real storage tank construction details are known.

Similar to ref. [190], in the current study, the validation of developed MATLAB<sup>®</sup>/Simulink simulation model for heat losses to environment from thermal storage tanks is not suitable too due to lack of data concerning experimental studies with DEMO IHTS storage tanks. For verification of the developed MATLAB<sup>®</sup>/Simulink simulation model, in the current study, similar to ref. [190], the simulations are carried out for 6-day temperature drop in thermal storage tanks for defined temperature conditions. For MATLAB<sup>®</sup>/Simulink simulations, see Fig. 4.4 and Fig 4.5, storage tanks' diameter of 24 m and tanks' height of 7.5 m are taken. Thermal insulation thickness is 0.3 m. The data for thermal insulation materials are joined in Table 4.1. HITEC molten salt mass is  $5.04 \cdot 10^6$  kg. The specific area of storage tank roof and bottom is  $\sim 452$  m<sup>2</sup> and the area of tank lateral wall is  $\sim 565$  m<sup>2</sup>. The initial HITEC temperature in cold storage tank is 573 K, and in hot storage tank it is 763 K. The simulations for storage tanks are carried out for tanks' upper filling level with molten salt, e.g. over 80% in cold tank and over 86% for hot tank, respectively (see Table 4.3).

The results of simulations using MATLAB<sup>®</sup>/Simulink are compared qualitatively with the numerical data, presented in the ref. [190], taking into consideration the temporal evolution of molten salt temperature in thermal storage tanks. The change of MS temperature due to cooling phenomena in DEMO IHTS thermal storage tanks is visualized in Fig. 4.8. The equations (4.8) and (4.9) are used to describe the temperature drop of HITEC molten salt in cold and hot storage tanks, correspondingly. For DEMO IHTS, the temperature drop rate for cold tank, which is full with molten salt, is  $\Delta T/\Delta t \approx 3.4$  K/day and for full hot tank it is  $\Delta T/\Delta t \approx 10.3$  K/day, respectively (see Fig. 4.9). As for data from ref. [190], for defined tanks geometry and operation conditions the MS temperature drop rate of  $\Delta T/\Delta t \approx 1.1$  K/day for full hot tank and  $\Delta T/\Delta t \approx 5.4$  K/day for the empty cold tank is obtained. Both data from ref. [190] and current simulation results show practically a linear decrease in MS temperature for the first 6 days of simulations.

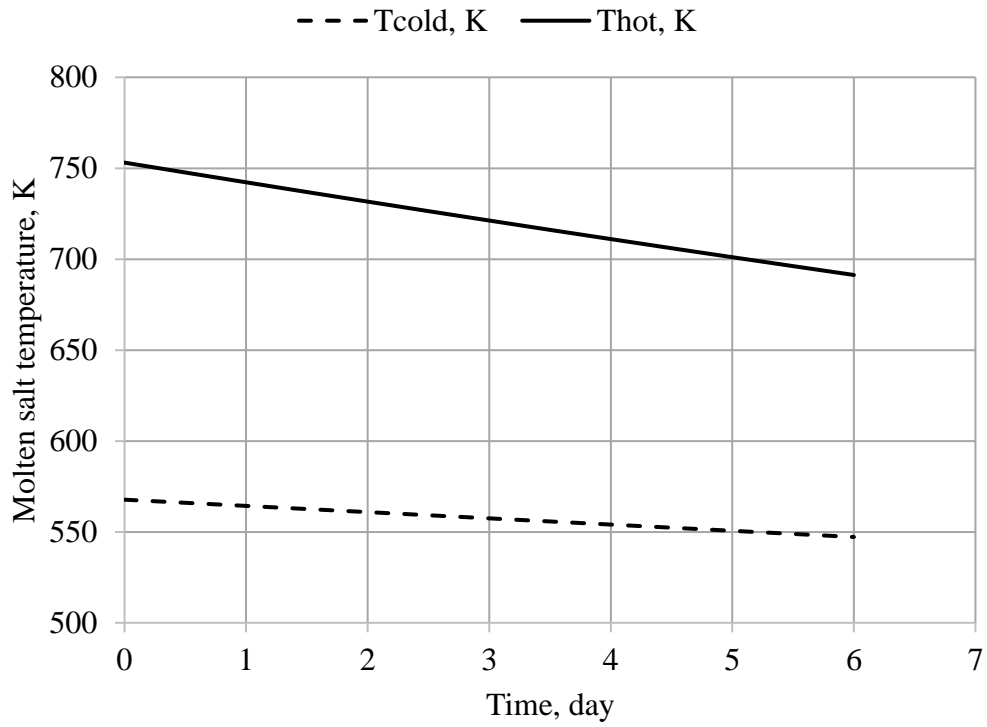


Fig. 4.8: Change of molten salt temperature in storage tanks due to cooling phenomena.

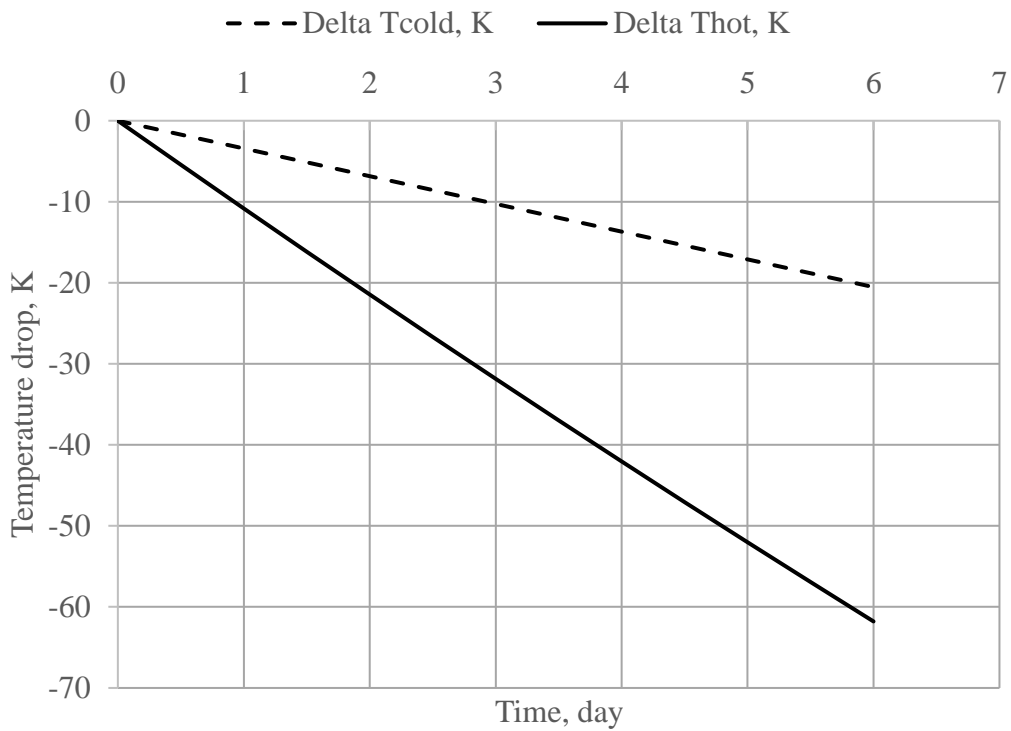


Fig. 4.9: Temperature drop of molten salt in dependence of simulated time interval.

The mean heat losses flow from thermal storage tank are calculated as

$$\dot{Q}_{\text{loss}} = \frac{m \cdot c_p \cdot \Delta T}{\Delta t}, \quad (4.11)$$

where  $m$  describes mass of molten salt in thermal storage tank,  $c_p$  is temperature dependent specific heat capacity of HITEC and  $\Delta T$  is temperature drop for a time interval  $\Delta t$ .

In current study, HITEC specific heat capacity is calculated using novel customized MATLAB® module, see chapter 2, Table 2.6. For cold storage tank the temperature drop rate of  $\Delta T/\Delta t \approx 3.4$  K/day is taken. Considering these conditions, according to eq. (2.16), MS specific heat capacity changes from 1260 J/(kg·K) to 1286 J/(kg·K). Respectively, for calculation with eq. (4.11), for cold storage tank, HITEC mean value of  $c_p = 1273$  J/(kg·K) is taken. For hot storage tank the temperature drop rate is  $\Delta T/\Delta t \approx 10.3$  K/day. According to eq. (2.16), for these conditions the MS specific heat capacity changes from 1080 J/(kg·K) to 1142 J/(kg·K). Hence, for hot storage tank, for calculation with eq. (4.11), the MS mean value of  $c_p = 1111$  J/(kg·K) is chosen.

The simulation data of mean heat losses per day for cold and hot storage tanks are presented in Fig. 4.10. The values of specific heat losses per area are presented in Fig. 4.11, whereas in calculations the area is taken as the sum of the area of tank roof and lateral wall.

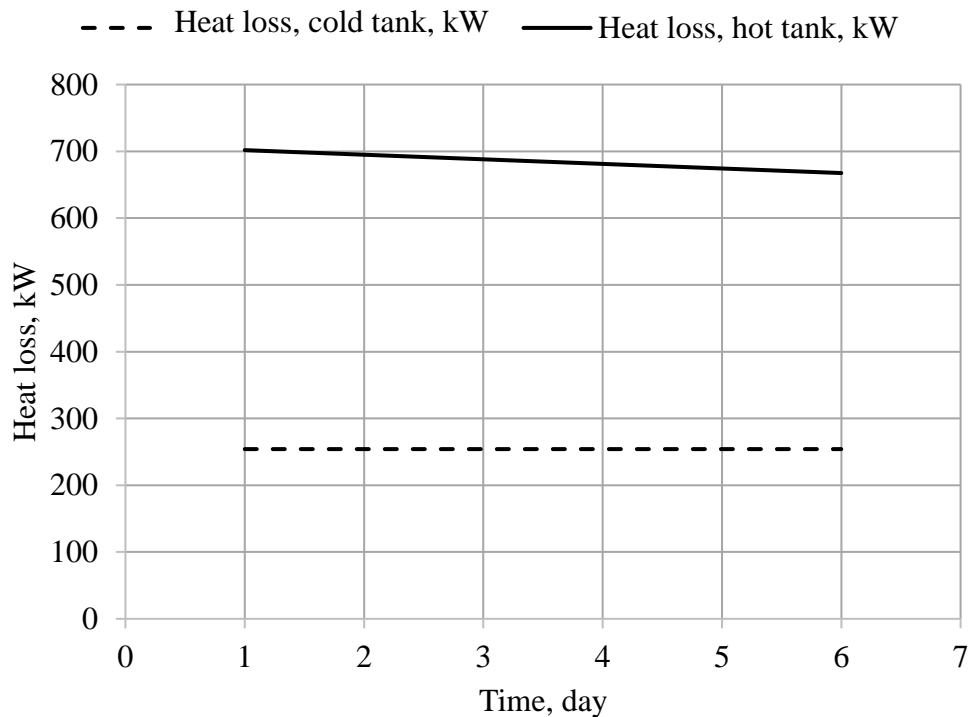


Fig. 4.10: Simulated transient heat loss per day for cold and hot storage tanks.

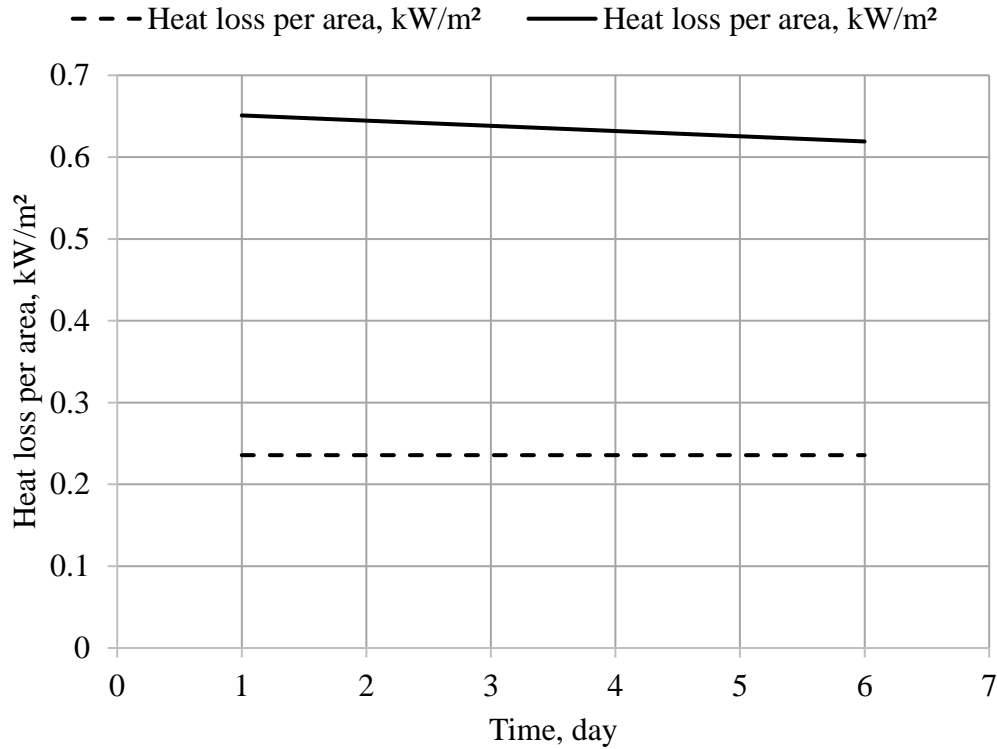


Fig. 4.11: Simulated transient heat loss per area from cold and hot storage tanks per day.

In DEMO IHTS full hot tank, the decrease in heat losses is more pronounced ( $\sim 702$  kW after the 1<sup>st</sup> day and  $\sim 667$  kW after 6<sup>th</sup> day), than in the full cold tank, which remains practically constant at  $\sim 254$  kW for each day. The decrease in heat losses from the hot tank can be explained through the decrease in volume of molten salt in the tank due to MS cooling and growing value of  $S_{H,nw}/S_{H,wet}$ , see eq. (4.7).

As for simulation data from ref. [190], the heat losses from the loaded system for full hot tank ( $T = 659$  K) decrease from  $\sim 275$  kW on the 1<sup>st</sup> day to  $\sim 265$  kW for the 6<sup>th</sup> day. For empty cold tank ( $T = 565$  K), these simulated values are  $\sim 190$  kW after the 1<sup>st</sup> day and  $\sim 165$  kW after the 6<sup>th</sup> day. The main conclusion of the comparative study is that both simulation models similar describe qualitatively the temporal evolution of molten salt temperature in thermal storage tanks and the temporal evolution of heat losses to the environment. The difference in absolute values between MATLAB<sup>®</sup>/Simulink data and the simulation results from ref. [190] can be explained due to difference in initial data, which are introduced into the models, such as geometrical parameters of thermal storage tanks, molten salt thermo-physical properties, as well as environmental conditions.

## 4.5 Conclusions

The design and operational parameters of DEMO IHTS thermal storage tanks are defined, including tank's geometry, properties of constructive and thermal insulation materials, as well as environmental conditions.

For cold storage tank, HITEC molten salt minimum temperature  $T_{\min} = 543$  K is taken, being higher than MS melting point. For hot storage tank, MS maximum temperature of  $T_{\max} = 738$  K is selected, which is lower than temperature of MS thermal degradation.

The interplay between storage tank parameters and MS filling level is studied using MATLAB<sup>®</sup>/Simulink simulations. The results are used to specify the storage tank geometry and operational parameters, which have to be applied for modelling of DEMO PHTS-IHTS system.

Simulations are carried out to study the influence of tank height and thermal insulation material thickness on heat losses to environment from DEMO IHTS thermal storage tanks.

The results of numerical simulations using MATLAB<sup>®</sup>/Simulink are evaluated through comparison with the data, known from literature survey (see ref. [190]). A good, qualitative correlation between the results of simulations is observed.



## 5 Simulation model of DEMO PHTS-IHTS and DEMO PCS systems

The development of simulation models demands the knowledge of DEMO BoP technical data. With this purpose, a vast study of design and operational parameters of DEMO BoP systems, shown in Fig. 5.1, is carried out. The operational and design parameters are presented in Appendices A.5 and A.6. DEMO PHTS main parameters, as well as the data for corresponding heat exchangers, are presented in Appendix A.5, Table A5.1 and Table A5.2. The main parameters for DEMO IHTS and DEMO PCS are highlighted in Appendix A.5, Table A5.3 and Table A5.4, correspondingly. The technical data for DEMO Primary Heat Transfer System and DEMO Intermediate Heat Transfer and Storage System are presented in Appendix A.6, Table A6.1 and Table A6.2, correspondingly. The Table A6.3 and Table A6.4 include the design and operational parameters of DEMO Power Conversion System.

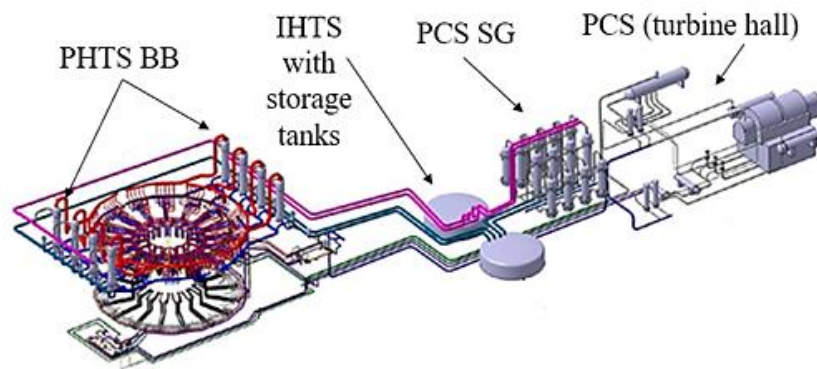


Fig. 5.1: Schematic view of DEMO BoP energy transfer chain [55].

The forthcoming paragraphs are focused on development of DEMO PHTS-IHTS and DEMO PCS simulation models, involving the description of applied modules and governing equations.

### 5.1 Development of DEMO PHTS-IHTS simulation model

The scheme of DEMO PHTS-IHTS simulation model, presented in Fig. 5.2, includes two thermal storage tanks and six pipelines with modules for simulation of heat losses to environment, two fixed-displacement pumps, eight heat exchangers (HXs) of DEMO PHTS system and single PCS steam generator (SG) stage. For the model, following assumptions are formulated: i) HITEC properties are simulated by novel customized MATLAB<sup>®</sup> module; ii) storage tanks, pipelines and pumps are heated up to their operating temperature; iii) pipelines are filled continuously with HITEC molten salt [84, 182]; iv) at the beginning of simulation, the filling level of molten salt in cold storage tank is at maximum.

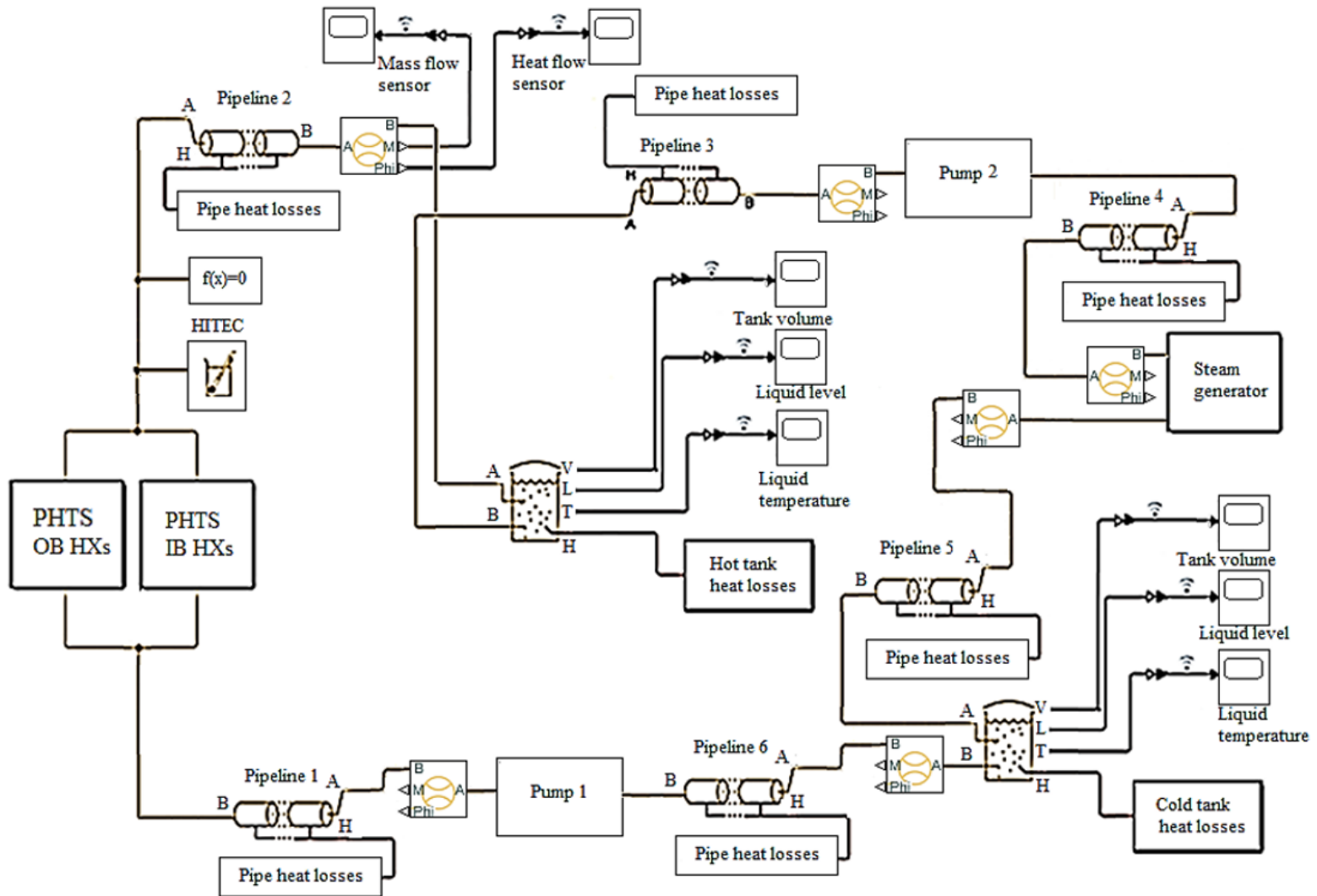


Fig. 5.2: Simulation model of DEMO PHTS-IHTS system [33, 221].

In DEMO IHTS, molten salt is pumped via pump 1 from cold storage tank through PHTS OB/IB HXs into hot storage tank. HITEC gets heated, ensuring thermal energy transport into hot storage tank [33, 221]. Molten salt is pumped with pump 2 from hot storage tank through PCS SG HXs into cold storage tank. Pipeline 1 connects pump 1 with DEMO PHTS HXs. Pipeline 2 connects DEMO PHTS HXs with hot storage tank. Pipeline 3 is used for connection of hot storage tank with pump 2, as well as pipeline 4 connects pump 2 with PCS SG stage. Pipelines 5 and 6 are installed between PCS SG and cold storage tank, as well as between cold storage tank and pump 1, respectively.

Throughout pulse operation, molten salt mass flow through pump 1 is higher than through pump 2. For cold storage tank, molten salt outlet flow is higher than its inlet flow. Hence, during pulse operation, MS filling level in cold storage tank continuously decreases. In hot storage tank, HITEC mass flow is divided into two parts. The first part ( $\dot{m}_{\text{part 1}}$ ) remains in hot storage tank, what results in growing MS filling level. The second part ( $\dot{m}_{\text{part 2}}$ ) gets pumped via pump 2 through the PCS SG HXs, thus returning to cold storage tank.

During dwell operation, HITEC molten salt, which is stored in hot storage tank during pulse operation, is pumped with pump 2 at high flow rate. HITEC flows through PCS SG stage, where heat transfer between MS and water takes place. Thus, HITEC molten salt, whose temperature is reduced, flows to cold storage tank. During dwell operation, MS filling level in hot storage tank decreases, yet in cold storage tank it increases.

## 5.2 Modules of DEMO PHTS-IHTS simulation model

### 5.2.1 Thermal liquid pipeline module

The governing equations for pipeline module are presented in Table 5.1. This module, presented in Fig. 5.3, possesses ports A and B, through which HITEC flow enters and exits the pipeline. An intermediate node I is used for segmented pipeline [215]. Being segmented, the pipeline contains more than one fluid volume and is treated as an assembly of smaller pipelines, whereas each pipeline is associated with a separate instance of module. Through port H, the module controls the temperature across the pipeline. By discretization, mass and energy flows, as well as momentum balance equations, are calculated for each segment. The total mass, momentum and energy accumulation are determined as sums over their volumes. During flow of molten salt through the pipelines, friction losses occur along the pipeline walls, which are defined as pressure loss, being described by eqs. (5.8) and (5.9) for turbulent flow, see Table 5.1 [215].

Title	Governing equation	Equation	Remark
Mass balance	$\dot{m}_A + \dot{m}_B = 0$	(5.1)	
Momentum balance	$p_A - p_B = \Delta p_f + \rho_I \cdot g \cdot \Delta z$	(5.2)	It is expressed by pressure differential over the pipe, which occurs due to pressure at pipe ports, friction at pipe wall and hydrostatic changes due to any change in elevation.
	$p_f = \Delta p_{fA} + \Delta p_{fB}$	(5.3)	
	$\Delta z = z_A - z_B$	(5.4)	
	$p_I = \frac{1}{2} \cdot (p_A + p_B)$	(5.5)	
	$p_A - p_I = \Delta p_{fA} + \rho_I \cdot g \cdot \frac{\Delta z}{2}$ and $p_B - p_I = \Delta p_{fB} - \rho_I \cdot g \cdot \frac{\Delta z}{2}$	(5.6)	
Pressure drop due to friction losses	$\Delta p_{fA} = \frac{v \cdot \lambda}{2 \cdot D^2 \cdot S} \cdot \frac{L}{2} \cdot \dot{m}_A$ and $\Delta p_{fB} = \frac{v \cdot \lambda}{2 \cdot D^2 \cdot S} \cdot \frac{L}{2} \cdot \dot{m}_B$ ,	(5.7)	For laminar flow, where $\lambda = 64$ .
	$\Delta p_{fA} = \frac{1}{2 \cdot \rho_I \cdot S^2} \cdot \left( \frac{f \cdot L}{D} + C_{loss, total} \right) \cdot \dot{m}_A \cdot  \dot{m}_A $	(5.8)	For turbulent flow.
	$\Delta p_{fB} = \frac{1}{2 \cdot \rho_I \cdot S^2} \cdot \left( \frac{f \cdot L}{D} + C_{loss, total} \right) \cdot \dot{m}_B \cdot  \dot{m}_B $	(5.9)	
Energy balance	$\dot{E}_I = \dot{E}_A + \dot{E}_B + \dot{E}_H - \dot{m}_I \cdot g \cdot \Delta z$	(5.10)	
Mass and energy flow in internal node I	$\dot{m}_I = \frac{\dot{m}_A + \dot{m}_B}{2}$ and $E_I = \rho_I \cdot u_I \cdot V$	(5.11)	Calculated in potential energy term.
Abbreviations	$\dot{m}_A$ - mass flow rate at port A $\dot{m}_B$ - mass flow rate at port B $p_A$ - pressure at port A $p_B$ - pressure at port B $p_I$ - pressure at internal node I $\Delta p_f$ - pressure differential due to viscous frictions $\rho_I$ - HITEC density $g$ - gravitational acceleration $\Delta z$ - elevation differential between ports A and B $\dot{E}$ - energy accumulation rate	$\dot{E}_A, \dot{E}_B$ and $\dot{E}_H$ - energy flow rates through ports A, B and H $u_I$ - specific internal energy of fluid at node I $V$ - internal volume of pipe $C_{loss, total}$ - loss coefficient $v$ - HTF kinematic viscosity $\lambda$ - laminar friction constant $D$ - pipe hydraulic diameter $f$ - Darcy friction factor $L$ - effective length of pipe	

Assumptions and simplifications:

- HITEC molten salt is treated as an incompressible HTF, hence its mass within the pipeline does not change with pressure, and for HTF the inertia is ignored.
- Wall of conduit is rigid.

Table 5.1: Governing equations for thermal liquid pipeline module [215].

Title	Governing equation	Equation	Remark
Heat losses via conduction and convection	$E_H = Q_{\text{cond}} + Q_{\text{conv}}$	(5.12)	Heat transfer between pipelines and environment.
	$Q_{\text{cond}} = \frac{k_I \cdot S_H}{D} \cdot (T_H - T_I)$	(5.13)	
	$Q_{\text{conv}} = c_{p,\text{Avr}} \cdot  \dot{m}_{\text{Avr}}  \cdot (T_H - T_A) \cdot \left[ 1 - \exp\left(\frac{h \cdot S_H}{c_{p,\text{Avr}} \cdot  \dot{m}_{\text{Avr}} }\right) \right]$	(5.14)	
	$h = \frac{\text{Nu}_{\text{Avr}} \cdot k_{\text{Avr}}}{D}$	(5.15)	
Nusselt number for turbulent flow	$\text{Nu}_{\text{Avr}} = \frac{f/8 \cdot (\text{Re} - 1000) \cdot \text{Pr}}{1 + 12.7 \cdot (f/8)^{1/2} \cdot (\text{Pr}^{2/3} - 1)}$	(5.16)	Parametrization is provided for heat transfer between MS and pipeline wall. For turbulent flow, average Nusselt number is calculated using Gnielinski correlation.
	$f = \left[ -1.8 \cdot \log_{10} \left( \frac{6.9}{\text{Re}} + \left( \frac{\epsilon_R}{3.7 \cdot D} \right)^{1.11} \right) \right]^{-2}$	(5.17)	
Heat transfer coefficient for turbulent flow	$h = h_N \cdot \frac{D_N^{1.8}}{D^{1.8}} \cdot \frac{\dot{m}_{\text{Avr}}^{0.8}}{\dot{m}_N^{0.8}}$	(5.18)	Nominal surface area of pipe wall: $S_{\text{HN}} = \sqrt{\frac{4 \cdot S}{D}} \cdot L$ . For rigid wall: $h = h_N \cdot \frac{\dot{m}_{\text{Avr}}^{0.8}}{\dot{m}_N^{0.8}}$ .
	$\dot{m}_{\text{Avr}} = \frac{\dot{m}_A + \dot{m}_B}{2}$	(5.19)	
	$h_N = \frac{\dot{m}_N \cdot c_{pN}}{S_{\text{HN}}} \cdot \ln\left(\frac{T_{\text{HN}} - T_{\text{InN}}}{T_{\text{HN}} - T_{\text{OutN}}}\right)$	(5.20)	
Abbreviations	$k_I$ - HITEC thermal conductivity in node I $S_H$ - surface area of pipe wall $D$ - pipe diameter $T_H$ - pipe wall temperature $T_I$ - HTF temperature in pipe internal node I $c_{p,\text{Avr}}$ - HITEC specific heat capacity $T_A$ - HTF inlet port temperature $h$ - heat transfer coefficient of pipe	$\dot{m}_{\text{Avr}}$ and $\dot{m}_N$ - average and nominal mass flow rates through pipe $\text{Nu}_{\text{Avr}}$ - average Nusselt number in pipe $k_{\text{Avr}}$ - average thermal conductivity of HTF of entire pipe $\text{Re}$ and $\text{Pr}$ - Reynolds and Prandtl numbers $f$ - average Darcy friction factor $\epsilon_R$ - absolute roughness of pipe internal surface $T_{\text{HN}}$ , $T_{\text{InN}}$ and $T_{\text{OutN}}$ - nominal wall, inflow and outflow temperatures $S_{\text{HN}}$ - nominal wall surface area	
Assumption: For rigid pipeline, nominal diameter is equal to pipe diameter.			

Table 5.2: Governing equations of pipeline module for heat losses to environment [215].

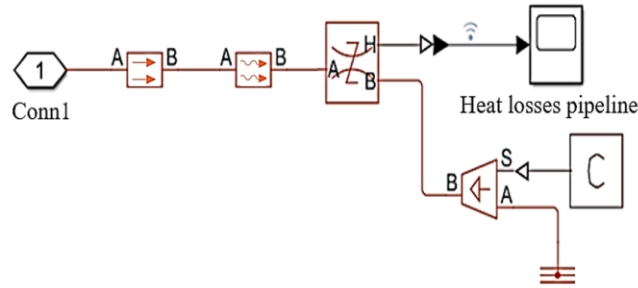


Fig. 5.3: Pipeline module for heat losses to environment.

For every pipeline, a novel module for heat losses to environment is applied, see Fig. 5.3 and Table 5.2, where heat transfer takes place through convection between HITEC molten salt and pipeline walls and through conduction from pipeline walls and thermal insulation to environment [220].

### 5.2.2 Fixed-displacement pump module

The fixed-displacement pump module (see Fig. 5.4) models a pump with a constant volumetric displacement, which extracts power from mechanical rotational network and delivers it to hydraulic, isothermal liquid network. The governing equations for fixed-displacement pump module are joined in Table 5.3 [215, 222]. The design and operational parameters of pumps 1 and 2, see Fig 5.2, are joined in Appendix A.6.

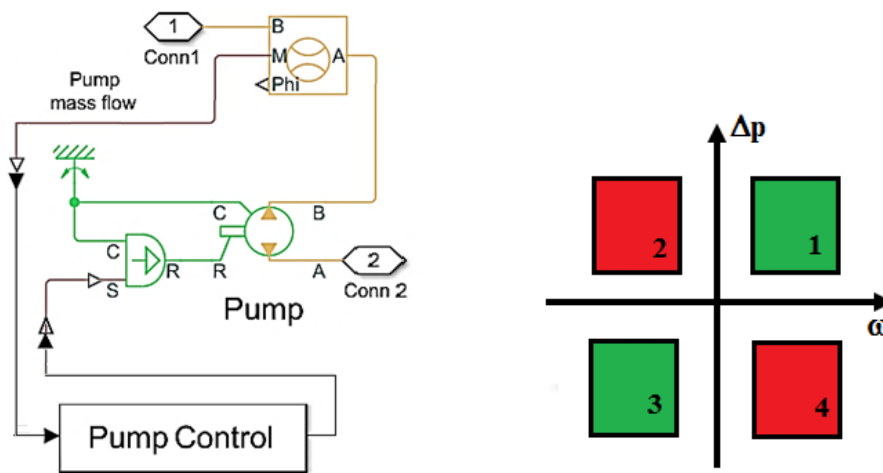


Fig. 5.4: Fixed-displacement pump module with working mode diagram.

The terminals A and B describe pump inlet and outlet. Signal ports M and Phi report mass and energy flow rates. Mechanical, rotational conserving ports R and C are associated with the shaft and casing of the pump.

Title	Governing equation	Equation	Remark
Energy balance	$\dot{E}_A + \dot{E}_B + P_{\text{hydro}} = 0$	(5.21)	Module associates mechanical work done by the pump with an energy exchange.
Pump hydraulic power	$P_{\text{hydro}} = \Delta p \cdot \frac{\dot{m}}{\rho}$	(5.22)	A function of pressure difference between pump ports.
Mechanical power due to torque	$P_{\text{mech}} = \tau \cdot \omega$	(5.23)	
Mass flow rate	$\dot{m} = \dot{m}_{\text{Ideal}} - \dot{m}_{\text{Leak}}$	(5.24)	
	$\dot{m}_{\text{Ideal}} = \rho \cdot D \cdot \omega$	(5.25)	
Driving torque	$\tau = \tau_{\text{Ideal}} + \tau_{\text{Friction}}$	(5.26)	
	$\tau_{\text{Ideal}} = D \cdot \Delta p$	(5.27)	
Analytical parametrization: leakage flow	$\dot{m}_{\text{Leak}} = \frac{K_{\text{HP}} \cdot \rho_{\text{Avg}} \cdot \Delta p}{\mu_{\text{Avg}}}$	(5.28)	Hagen-Poiseuille coefficient $K_{\text{HP}} = \frac{D \cdot \omega_{\text{Nom}} \cdot \mu_{\text{Nom}} \cdot (1 - \eta_{v,\text{Nom}})}{\Delta p_{\text{Nom}}}$
Analytical parametrization: friction torque	$\tau_{\text{Friction}} = \tau_0 + K_{\text{TP}} \cdot  \Delta p  \cdot \tanh \frac{4\omega}{(5e - 5) \cdot \omega_{\text{Nom}}}$	(5.29)	
Abbreviations	$\dot{E}_A$ and $\dot{E}_B$ - energy flow rates at port A and port B $P_{\text{hydro}}$ - pump hydraulic power $\omega$ - shaft angular velocity $\dot{m}$ - actual mass flow rate $\dot{m}_{\text{Ideal}}$ and $\dot{m}_{\text{Leak}}$ - ideal and internal leakage mass flow rates $\dot{m}_{\text{Leak}}$ - internal leakage mass flow rate $\tau$ - actual driving torque $\tau_{\text{Ideal}}$ and $\tau_{\text{Friction}}$ - ideal driving torque and friction torque $\rho$ - HTF average density at thermal liquid ports A and B D - displacement parameter		$\Delta p$ - pressure gain from inlet to outlet, where $K_{\text{HP}}$ is Hagen-Poiseuille coefficient for laminar pipe flows $\mu_{\text{Avg}}$ - HTF average dynamic viscosity $K_{\text{TP}}$ - specified value of friction torque $\tau_0$ - specified no-load torque $\omega_{\text{Nom}}$ - specified nominal shaft angular velocity $\mu_{\text{Nom}}$ - specified nominal dynamic viscosity $\eta_{v,\text{Nom}}$ - specified value of volumetric efficiency $\Delta p_{\text{Nom}}$ - specified value of nominal pressure drop corresponding to specified nominal conditions
Assumptions and simplifications:			
<ul style="list-style-type: none"> <li>Module treats the pump as a quasi-steady component and pump wall is rigid.</li> <li>Effects of fluid inertia, elevation and external leakage are ignored.</li> </ul>			

Table 5.3: Governing equations for fix-displacement pump module [215].

Pressure gain from port A to port B is positive, if the angular velocity at port R is positive relative to port C. Through port A, the pump is connected with the sensor, which measures mass and energy flow rates in HTF network. Pump is coupled with port R to ideal angular velocity source block. Through port S, the control signal is applied, which drives the source [215]. There is no change in pressure or temperature perceived across the sensor.

According to “pump control” module, the controller working mode depends on pressure gain  $\Delta p = p_B - p_A$  from port A to port B and angular velocity  $\omega = \omega_R - \omega_C$ , where  $\omega_R$  and  $\omega_C$  are absolute angular velocities at ports R and C [215]. There are four modes of operation (see Fig. 5.4). Quadrant 1 represents the forward pump mode for specified case of DEMO IHTS pumps 1 and 2, in which positive shaft angular velocity causes a pressure increase from port A to port B. Quadrant 2 represents the reverse motor mode, in which the flow from port B to port A causes a pressure decrease and a negative shaft angular velocity. Quadrant 3 represents the reverse pump mode, in which negative shaft angular velocity causes the pressure increase from port B to port A. Quadrant 4 represents the forward motor mode, in which flow from port A to port B causes the pressure decrease and a positive shaft angular velocity.

The pump model accounts power losses due to leakage and friction. Leakage is internal and occurs only between pump inlet and outlet. The module computes the leakage flow rate and friction torque, using “analytical parameterization data” case, displayed in Table 5.3. The input efficiencies are provided by mechanical and volumetric efficiencies directly by physical signal input ports. The input losses are given by mechanical and volumetric losses directly through physical signal input ports. Mechanical loss is defined as internal friction torque and volumetric loss is described as internal leakage flow rate.

### **5.2.3 PHTS Inner Blanket/Outer Blanket Loops module**

The PHTS Outer Blanket/Inner Blanket (OB/IB) Loops module with heat exchanger modules is shown in Fig. 5.5. DEMO PHTS design and operational parameters are summarized in Appendix A.6.

DEMO PHTS OB and IB Loops are modelled with a set of parallel installed heat exchangers, which have similar design configuration. The heat exchanger module models the heating of fluid through heat conduction over a wall. Helium is used for heat transfer to molten salt in DEMO PHTS-IHTS heat exchangers [84]. For simulations, constant heat capacity of helium is considered. Gas mass flow is divided uniformly between heat exchangers.



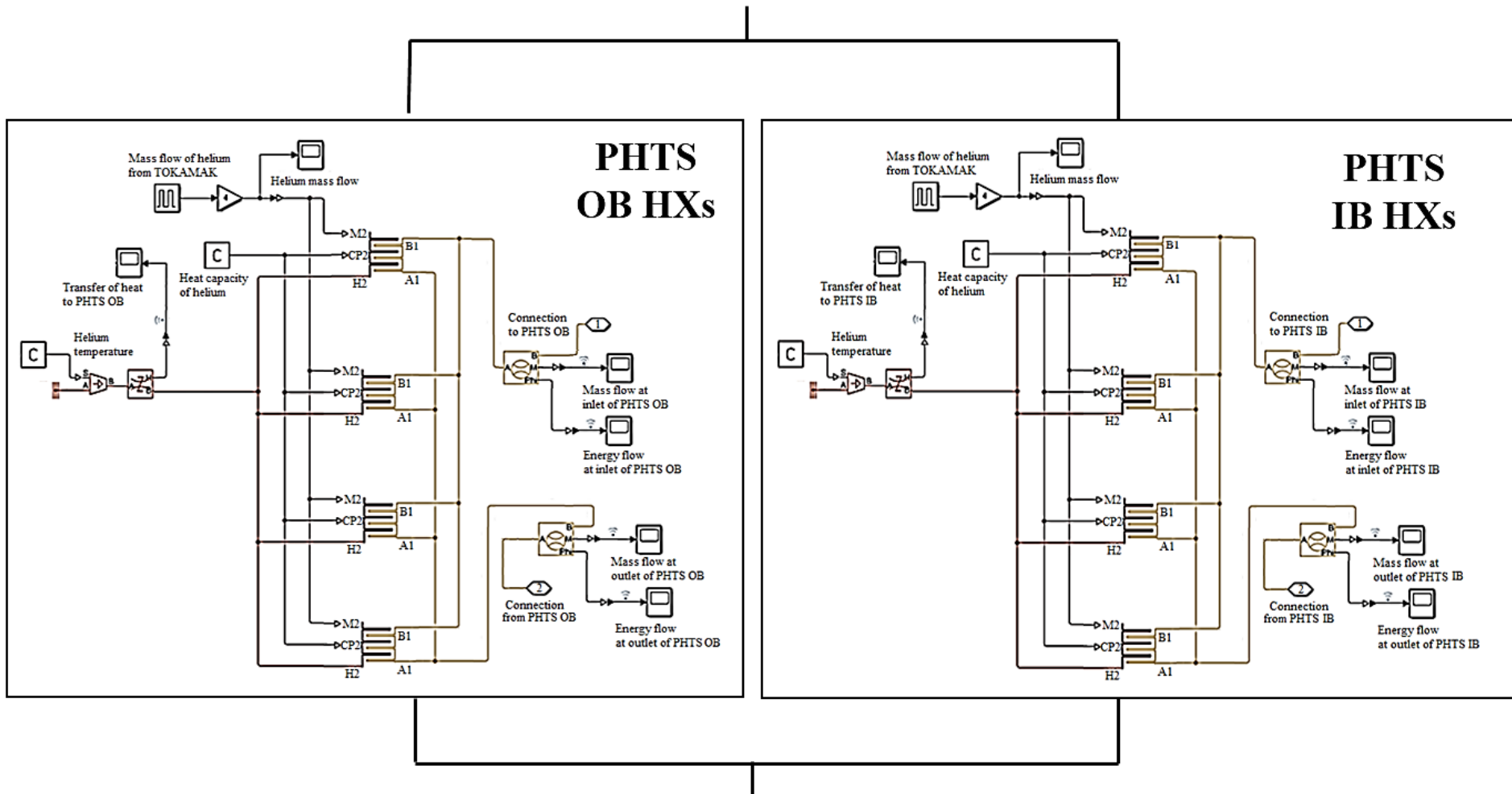


Fig. 5.5: Scheme of PHTS Outer Blanket/Inner Blanket Loops module with heat exchangers.

Gas input temperature lies at 793 K, whereas gas leaves DEMO PHTS HXs at 573 K. HITEC molten salt and helium do not mix with each other. The module, presented in Fig. 5.6, which controls the heat transfer between thermal liquid networks for helium and HITEC, includes Simple Heat Exchange Interface (TL) and Specific Dissipation Heat Transfer (SDHT) modules, whose governing equations are joined in Table 5.4 and Table 5.5 [215]. Ports A1 and B1 are conserving ports, which are associated with HX inlet and outlet. Port CP2 is for isobaric specific heat of helium. Port M2 is for entrance mass flow rate of helium. Port H2 is for inlet temperature of helium. The data regarding pressure losses, thermal effects and initial conditions are integrated in HXs modules. The rate of heat transfer is positive, when the temperature for the first fluid is higher than for the second one.

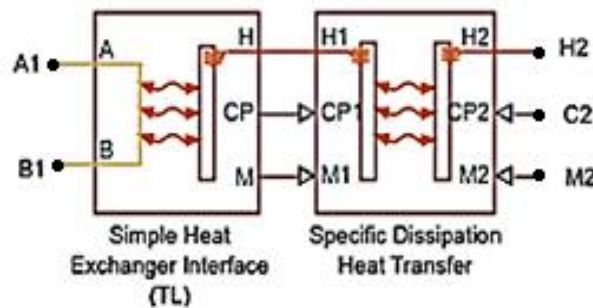


Fig. 5.6: Module for control of heat transfer between different thermal liquid networks [215].

Controlled Temperature Source module represents an ideal energy source in a thermal network. It maintains the controlled temperature difference, regardless of heat flow rate of helium. The temperature difference is set by signal port S. A positive temperature difference gives that the temperature at port B has to be greater than at port A. Pulse Generator module generates square wave pulses. Output signal is generated in a specified time-based mode and is based on simulation running time for cycling operation of fusion reactor. Pulse type for HXs is time-based with respective demand to simulation time, which takes place over a specific time span of 7200 sec for pulse and 600 sec for dwell operation.

The sensors in the simulation model, see Fig. 5.2, 5.4 and 5.5, are used to control mass and heat flows. Heat flow rate sensor represents an ideal heat flow meter, converting heat flow passing through the meter into a control signal, which is proportional to the flow. Regarding process control measurement, sensors' signal ports M and Phi report mass and energy flow rate. Ports A and B are thermal conserving ports in positive flow direction from port A to port B. Port H is a physical signal port that outputs heat flow value. There is no change in pressure or temperature across the sensors.

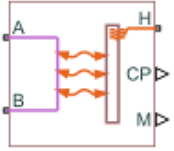
Titel	Governing equation	Equation	Remark
Heat exchange module			Module models pressure drop and temperature change in a gas, as it traverses the length of a thermal interface such as that provided by a heat exchanger.
Mass balance	$\dot{m}_A + \dot{m}_B = \frac{\partial M}{\partial p} \cdot \frac{dp}{dt} + \frac{\partial M}{\partial T} \cdot \frac{dT}{dt}$	(5.30)	Compressibility of gas is considered, what means that mass inside the interface can change with pressure and temperature.
Energy balance	$\dot{E}_A + \dot{E}_B + Q_H = \frac{\partial M}{\partial p} \cdot \frac{dp}{dt} + \frac{\partial M}{\partial T} \cdot \frac{dT}{dt}$	(5.31)	Rate of energy accumulation in internal fluid volume of interface is equal the sum of energy flow rates through all the ports.
Momentum balance	$p_A - p_B = \Delta p_A - \Delta p_B$	(5.32)	Overall pressure drop from one gas port to other is calculated from individual pressure drops from each gas port to internal fluid volume.
	$\Delta p_A = p_A - p \text{ and } \Delta p_B = p_B - p$	(5.33)	
Abbreviations	M - mass of fluid volume of thermal interface p - internal fluid pressure T - internal fluid temperature $\dot{m}_A$ - mass flow rate through gas port A $\dot{m}_B$ - mass flow rate through gas port B	E - total energy in internal fluid volume of thermal interface $\dot{E}_A$ and $\dot{E}_B$ - energy flow rates through gas ports A and B $\dot{Q}_H$ - heat flow rate through thermal port H $p_A$ and $p_B$ - fluid pressures at gas ports A and B $\Delta p_A$ and $\Delta p_B$ - pressure drops from gas ports A and B to internal fluid volume	
Assumptions and simplifications:			
<ul style="list-style-type: none"> <li>• Heat transfer across thermal interface is ignored.</li> <li>• Pressure drop is calculated as a function of mass flow rate from tabulated data, which are specified at reference pressure and temperature.</li> <li>• No work is done on or by fluid inside the interface.</li> <li>• Effects of pressure drop are ignored.</li> </ul>			

Table 5.4: Governing equations for Simple Heat Exchanger Interface module [215].

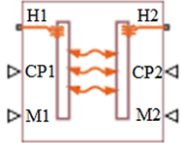
Titel	Governing equation	Equation	Remark
Heat transfer module			Module models heat transfer between two fluids, which are controlled by the signals, with these providing each the entrance mass flow rate and isobaric specific heat.
Heat transfer rate	$\dot{Q} = SD \cdot (T_{1,in} - T_{2,in})$	(5.34)	Heat flows from warmer fluid to cooler fluid. Heat flow rate is positive if fluid 1 enters at a higher temperature than fluid 2.
Specific dissipation	$SD = SD(\dot{m}_1, \dot{m}_2)$	(5.35)	Obtained from specified tabulated data at given mass flow rates.
Maximum heat transfer rate	$SD_{max} = \min(C_1, C_2)$ $C_* = \dot{m}_* \cdot c_{p,*}$	(5.36) (5.37)	Whenever heat flow rate exceeds the maximum value, a warning is issued.
Constraint on maximum heat transfer rate	$\dot{Q} = SD_{max} \cdot (T_{1,in} - T_{2,in})$ for $SD > SD_{max}$ $\dot{Q} = SD \cdot (T_{1,in} - T_{2,in})$ otherwise	(5.38)	It is implemented in form of a piecewise function.
Abbreviations	$T_{in}$ - fluid entrance temperature $\dot{m}$ - entrance mass flow rate	$C_*$ - thermal capacity rates of controlled fluid $c_{p,*}$ - isobaric specific heat of fluid	
Assumptions and simplifications:			
<ul style="list-style-type: none"> <li>• Rate of heat transfer is calculated from specific dissipation, a parameter specified in tabulated form as a function of entrance mass flow rates.</li> <li>• When entrance temperatures differ by one degree, the specific dissipation quantifies the amount of heat exchanged between fluids per unit of time.</li> <li>• Pressure loss and other aspects of flow mechanics are ignored.</li> </ul>			

Table 5.5: Governing equations for Specific Dissipation Heat Transfer module [215].

### 5.2.4 PCS steam generator module

According to DEMO IHTS model, as shown in ref. [100], PCS SG has been previously split in two levels, by connection in series. Subsequently, PCS SG model has been modified, where the steam generator concept has been reduced to a single SG2 level [84]. The large differences of vapor mass flow inside SG components, considering usual initial design with huge difference span between mass flows of 223-842 kg/s, are reduced to an average value of 719 kg/s in a single SG2 stage.

The scheme of the developed PCS SG module is presented in Fig. 5.7. For heat transfer from hot molten salt to water, single steam generator SG2 stage design concept is applied. The stage is modelled with a set of HXs modules, represented by pre-heater (PH), steam generator (SG) and super-heater (SH) [182]. Those design and operational parameters are listed in Appendix A.6. In the model, the heat is not taken into consideration, which comes from the phase change inside steam generator on water/steam side. Inside heat generator module, an entire temperature difference  $\Delta T$  is estimated between steam inlet and HITEC outlet temperature.

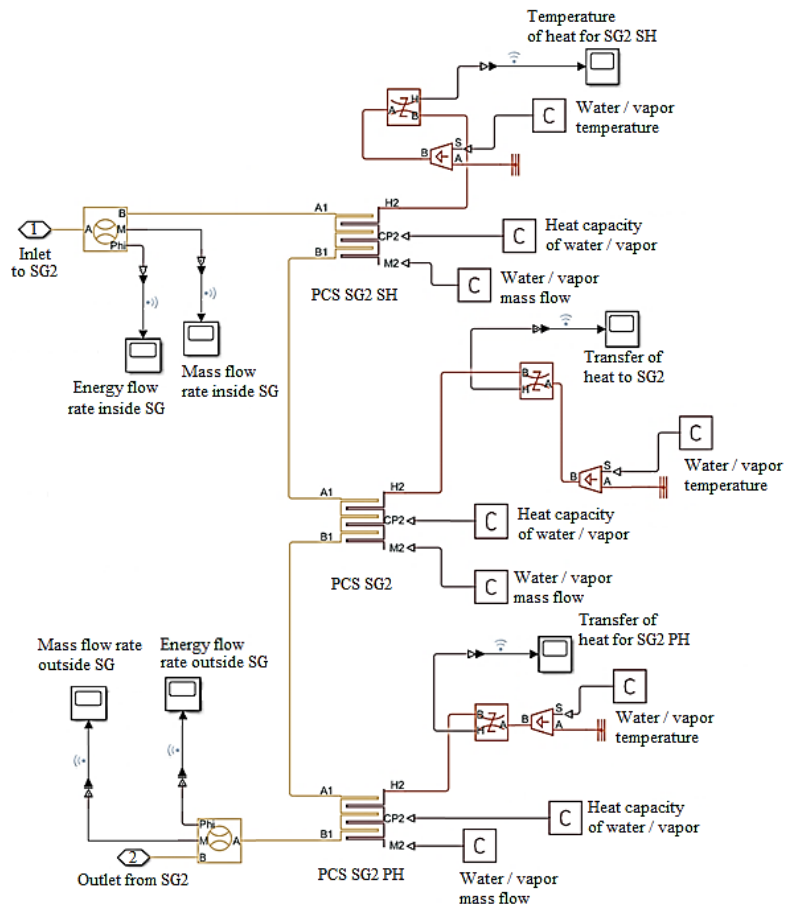


Fig. 5.7: PCS SG2 module with pre-heater, steam generator and super-heater [182], extended with control sensors for mass and energy flow rates.

### 5.3 Development of DEMO PCS simulation model

The scheme of DEMO PCS simulation model is presented in Fig. 5.8. It differs from the original MATLAB® Library Rankine Cycle model, see Appendix A.7, by replacement of steam boiler with coupling of PCS pre-heater, steam generator and super-heater to PH, SG and SH modules from the side of DEMO IHTS model. This presumes the support with initial data for convective heat transfer by coupling of DEMO PCS model with DEMO PHTS-IHTS model, where HITEC temperature at PCS SG stage inlet is given as heat input source. Besides SH, SG and PH modules, the model includes a high pressure (HP) and a low pressure (LP) steam turbine, two steam re-heaters SR1 and SR2, a steam condenser (SC), as well as one feedwater (FW) pump.

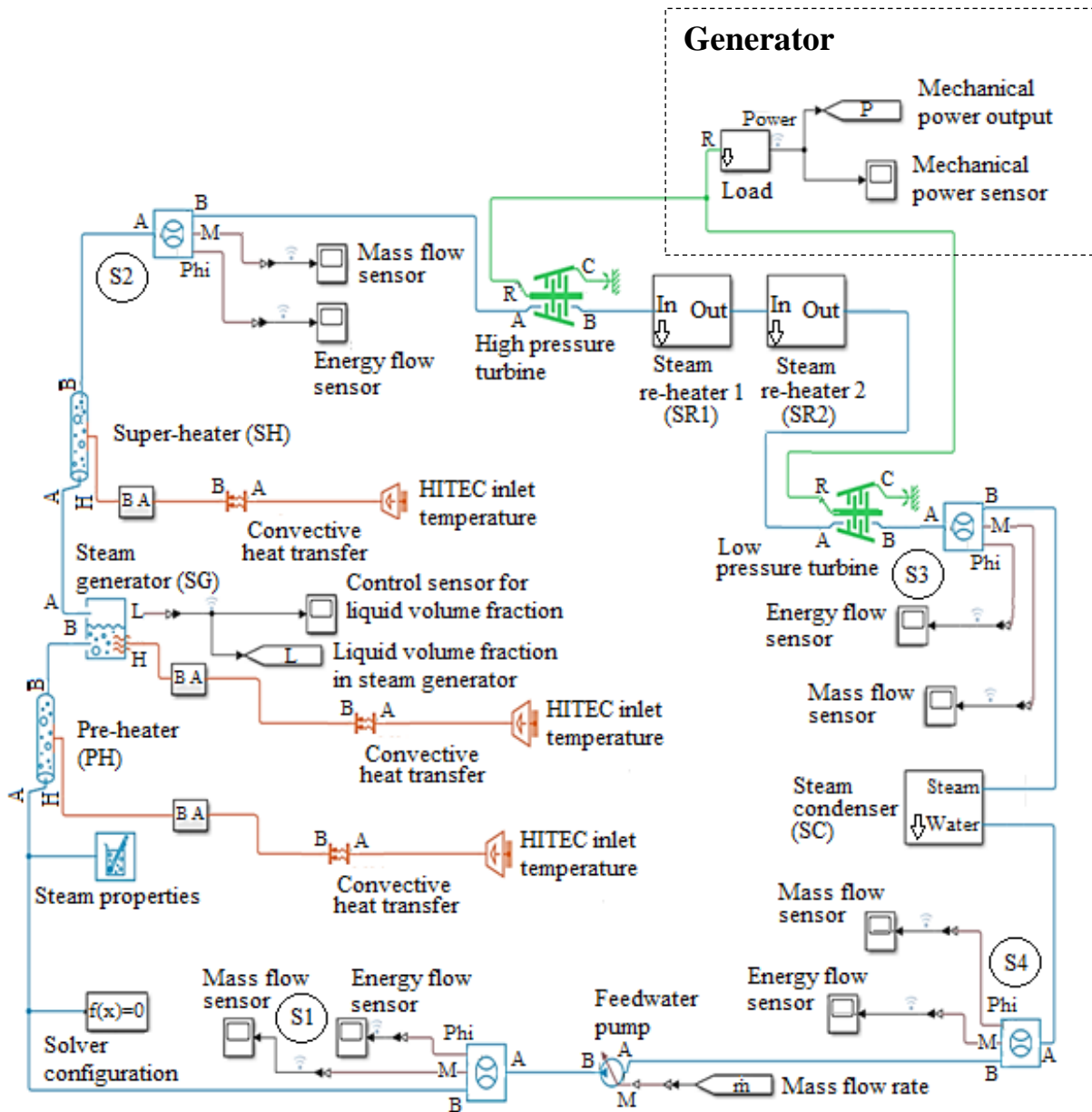


Fig. 5.8: Scheme of simulation model for DEMO PCS.

The components of DEMO PCS system are discussed in ref. [47, 53, 84, 98, 223]. The design and operational parameters of DEMO PCS, used for MATLAB®/Simulink numerical simulations, are presented in Appendix A.5, Table A5.4, and in Appendix A.6, Table A6.3 and Table A6.4.

To reduce the complexity, the proposed DEMO PCS simulation model contains only primary systems. The drain, supplemental FW heaters and PCS pumps, deaerator, as well as secondary heat sources, which are in this case the divertor and vacuum vessel pump with a supplemental heat exchanger, are excluded. Throttle, check and extraction valves for DEMO PCS are excluded too, as no offers for such specific regulation and process control are known to be yet available on the current industrial market. A two-phase fluid network is chosen with water and steam as two-phase heat transfer fluids. Regarding mass flow at inlet/outlet of the components, the customized module for water/steam properties is fitted to DEMO PCS operation conditions. Considering identical inlet/outlet medium, the re-heaters are modelled as thermal two-phase fluid pipes. The length of pipes in pre-heater and super-heater is equal to the length of a simple fluid pipe. Heat transfer is applied only through convection. For each PCS HX, a heat transfer module with corresponding temperature source is given. The volume of condensed water is calculated as the product of volumetric flow rate and corresponding time interval. This refers to time of 7200 sec for pulse operation during a single operation cycle. The initial liquid volume fraction of 0.7 in SG module is considered. The secondary inlet temperature of water is used as a coolant input source. The secondary inlet temperature of HITEC is assumed as initial heat input source.

## **5.4 Modules of DEMO PCS simulation model**

### **5.4.1 Steam generator module**

The coupling of PCS pre-heater, steam generator and super-heater modules is schematically presented in Fig. 5.9. Dash lines represent the fluid flow, solid lines represent convective heat flow between the components, and dash-point lines are used to connect the control sensor for maintaining liquid volume fraction in PCS SG. Referring to steam properties module, water and steam parameters for various temperature and pressure are used in form of vectors and matrices. The normalized and specific internal energy is given in vector form. Water and steam properties are listed in Appendix A.6, Table A6.3. The liquid level inside PCS SG module is specified as volume fraction inside the saturated chamber and is equal to the quotient of water amount and total fluid volume.

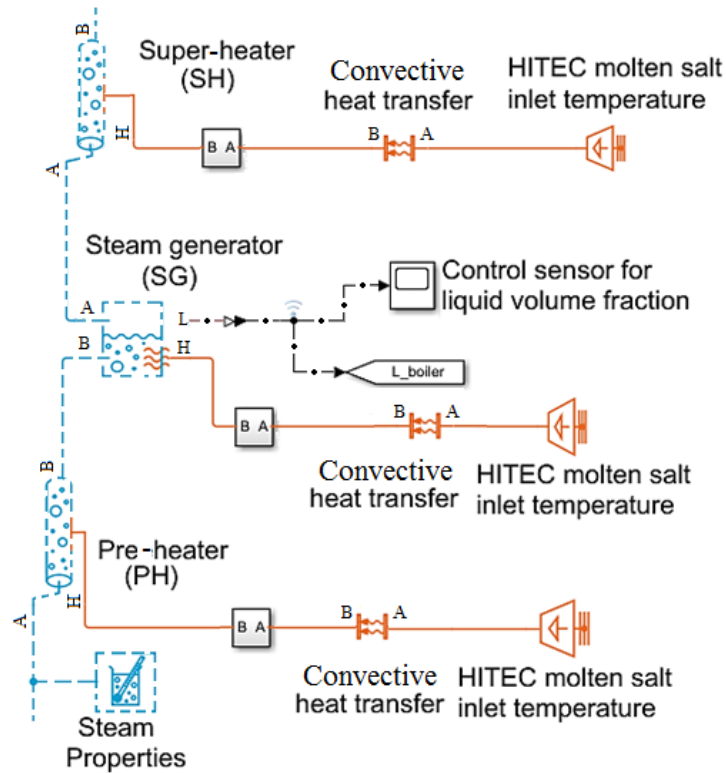


Fig. 5.9: Scheme of coupling of PCS pre-heater, steam generator and super-heater modules.

The mass of fluid in saturated fluid chamber varies with density, which comes with the property that in a two-phase fluid the form is generally considered as a function of pressure and temperature. The fluid enters, when pressure at inlet rises above that in the chamber, and exits, when pressure gradient is reversed. The volume of chamber is fixed in spite of fluid compressibility, when its mass changes with pressure and temperature.

Pre-heater is used to raise the temperature of feedwater to saturation level. Steam generator is used for generation of saturated steam. Super-heater is applied for steam generation with respect to mechanical power production [215, 218-220]. The inlet/outlet operating pressure in pre-heater is 126 bar uniformly. In steam generator and in super-heater, it is 125 bar uniformly.

HITEC inlet temperature in pre-heater is 609 K, in steam generator it is 699 K and in super-heater it is 738 K. The volumetric flow inside steam generator is 1.085 m<sup>3</sup>/s [98]. Total fluid volume is calculated by multiplying the volumetric flow with pulse time of 7200 sec. Heat transfer area and overall heat transfer coefficients are required for convective heat transfer modules, which are coupled to PCS PH-SG-SH modules. Heat transfer rate is proportional to the temperature difference, as well as heat transfer coefficient and surface area in contact with the fluid. The design and operational parameters of pre-heater, steam generator and super-heater are listed in Appendix A.6, Table A6.3 and Table A6.4.



Steam generator module is modelled as a chamber with fixed volume of two-phase fluid. Through inlet port B, as well as outlet port A, flows a constant volume of saturated fluid in a two-phase fluid network, whereas volume is divided into saturated vapor and saturated liquid. Here, an unidirectional flux exchange is considered. Operating pressure and temperature are based on liquid compressibility and thermal capacity. Port A of SH is connected to saturated vapor volume. Fluid leaving port A of SG is always in a saturated vapor state. Port B of SG is connected to saturated liquid volume. Fluid entering port B is always in a saturated liquid state. The fluid volume can exchange heat with thermal network through port H, which is a thermal conserving port associated with fluid temperature inside the chamber. Physical signal port L reports the control for liquid volume fraction. Regarding water and steam specific settings, MATLAB®/Simulink Library implemented data for liquid and vapour properties are used [215]. The inlet pressure and temperature are considered as initial conditions (see Appendix A.6, Table A6.3).

The modules' governing equations are presented in Table 5.6. The rate of mass accumulation in the chamber is equivalent to mass flow rate through ports A and B, which is calculated by eq. (5.39), where the left-hand side describes the rate of mass accumulation [215]. The smoothing introduces a small numerical error, where the module is adjusted by adding the correction term  $\epsilon_M$  to mass balance, being calculated according to eq. (5.40). The specific volume  $V/V$  is defined by water properties module [224]. The characteristic time to equilibrium of a phase-change event, that takes place in the chamber, is set to  $\tau = 0.1$  sec. The partial derivatives in mass balance equation are calculated using finite-difference method to tabulate the data in two-phase fluid properties module and to interpolate the results [215]. They are smoothed by means of cubic polynomial functions at phase-transition boundaries. These functions apply between two-phase mixture and super-heated vapor phase domains, when vapor quality is varied in a range of 0.3–0.9 [215, 225]. In our case, liquid volume fraction of 0.7 is applied.

Energy enters and exits the chamber in two ways, namely with fluid flow through ports A and B and with heat flow through port H. No work is carried out, neither on nor by fluid inside the chamber. The rate of energy accumulation in internal fluid volume is described by eq. (5.42), see Table 5.6. Neglecting kinetic energy of fluid, total energy in the chamber is described by eq. (5.43). As a boundary condition, fluid specific internal energy of 1500 kJ/kg is taken for the chamber. The temperature in interior is equal to that at thermal port. The momentum balance in the chamber is described by eq. (5.44), see Table 5.6 [215].


Title	Governing equation	Equation	Remark
Chamber			Module models accumulation of mass and energy in a chamber, containing a fixed volume of two-phase fluid.
Rate of mass accumulation	$\left[ \left( \frac{\partial \rho}{\partial p} \right)_u \cdot \frac{dp}{dt} + \left( \frac{\partial \rho}{\partial u} \right)_p \cdot \frac{du}{dt} \right] \cdot V = \dot{m}_A + \dot{m}_B + \epsilon_M$	(5.39)	
Correction term	$\epsilon_M = \frac{M - V/v}{\tau}$	(5.40)	
Fluid mass	$\frac{dM}{dt} = \dot{m}_A + \dot{m}_B$	(5.41)	
Energy balance	$\dot{E} = \dot{E}_A + \dot{E}_B + \dot{Q}_H$	(5.42)	
Total energy	$E = M \cdot u$	(5.43)	
Momentum balance	$p = p_A = p_B$	(5.44)	
Abbreviations:			
$\rho$ - density		$\dot{E}_A$ - energy flow rate at port A	
$p$ - pressure		$\dot{E}_B$ - energy flow rate at port B	
$u$ - specific internal energy		$\dot{E}$ - total energy flow	
$V$ - volume		$\dot{Q}_H$ - heat flow rate	
$\dot{m}$ - mass flow rate		$p$ - pressure in internal fluid volume	
$M$ - fluid mass in the chamber		$p_A$ - pressure at port A	
$v$ - specific volume		$p_B$ - pressure at port B	
$\tau$ - characteristic duration of a phase-change event			
Assumptions, conditions and simplifications:			
			<ul style="list-style-type: none"> <li>• Flow resistance between inlet and interior of chamber is assumed to be negligible.</li> <li>• Pressure in interior is equal to that at inlet of chamber.</li> <li>• Thermal resistance between thermal port and interior of chamber is neglected.</li> <li>• Temperature in interior is equal to temperature at thermal port.</li> <li>• Chamber has a fixed volume of fluid.</li> <li>• Kinetic energy of fluid in chamber is negligible.</li> </ul>

Table 5.6: Governing equations for PCS SG module as a chamber with fixed volume of two-phase fluid [215].

#### 5.4.2 Pre-heater and super-heater modules

The pre-heater and super-heater are designed as thermal liquid pipe modules, which model the flow dynamics of a two-phase fluid inside a rigid pipe. Pre-heater and super-heater parameters are specified in Appendix A.6, Table A6.3 and Table A6.4. The modules' governing equations, as well as the assumptions, are joined in Table 5.7 [215]. The module provides an option to model the fluid inertia and resistance to sudden changes in mass flow rate.


Title	Governing equation	Equation	Remark
Thermal liquid pipe			Module models the flow dynamics of a two-phase fluid inside a rigid pipe and provides an option to model fluid inertia with resistance to sudden changes in mass flow rate.
Energy balance	$M \cdot \dot{u}_I + (\dot{m}_A + \dot{m}_B) \cdot u_I = \dot{E}_A + \dot{E}_B + \dot{Q}_H$	(5.45)	Heat transfer between pipe wall and internal fluid volume is modelled as a convective process.
Heat flow rate	$\dot{Q}_H = h_{\text{coeff}} \cdot S_{\text{surf}} \cdot (T_H - T_I)$	(5.46)	
Heat transfer coefficient	$h_{\text{coeff}}^* = \frac{k_I^* \cdot \text{Nu}^*}{D_h}$	(5.47)	Coefficient for subcooled liquid and superheated vapor phases - asterisk denotes a value specific to phase considered (liquid or vapor).
	$h_{\text{coeff}}^M = \frac{k_{I,SL}^M \cdot \text{Nu}^M}{D_h}$	(5.48)	Coefficient for two-phase mixture: subscript M denotes the value specific to two-phase mixture and subscript SL indicates the value obtained for saturated liquid.
Nusselt number	$\text{Nu}^* = \frac{\frac{f}{8} \cdot (\text{Re}^* - 1000) \cdot \text{Pr}_I^*}{1 + 12.7 \cdot \sqrt{\frac{f}{8}} \cdot (\text{Pr}_I^{*2/3} - 1)}$	(5.49)	Liquid-vapor interface for turbulent flow according to Gnielinski correlation.
	$\text{Nu}^M = 0.05 \cdot \left[ \left( 1 - x_I + x_I \cdot \sqrt{\frac{v_{SV}}{v_{SL}}} \right)^{0.8} \right] \cdot \text{Pr}_{SL}^{0.33}$	(5.50)	Two-phase mixture inside turbulent flow: Cavallini and Zecchin correlation, where subscript SL denotes a value for saturated liquid and subscript SV denotes a value for saturated vapor.
Friction factor	$f = \left\{ -1.8 \cdot \log_{10} \left[ \frac{6.9}{\text{Re}^*} + \left( \frac{\epsilon_r}{3.7} \right)^{1.11} \right] \right\}^{-2}$	(5.51)	For turbulent flow.
Reynolds number	$\text{Re}^* = \frac{ \dot{m}_{\text{Avr}}  \cdot D_h \cdot v_I^*}{S \cdot \nu_I^*}$	(5.52)	Liquid-vapor interface, where subscript Avr denotes an average value between the ports.
	$\text{Re}^* = \frac{ \dot{m}_{\text{Avr}}  \cdot D_h \cdot v_{SL}}{S \cdot \nu_{SL}}$	(5.53)	For saturated liquid.

Table 5.7, Continued

Mass balance	$\left[ \left( \frac{\partial \rho}{\partial p} \right)_u \cdot \dot{p}_I + \left( \frac{\partial \rho}{\partial u} \right)_p \cdot \dot{u}_I \right] \cdot V = \dot{m}_A + \dot{m}_B + \epsilon_M$	(5.54)	$\epsilon_M$ accounts for smoothing of density partial derivatives across phase transition boundaries.
	$\epsilon_M = \frac{1}{\tau} \cdot \left( M - \frac{V}{v_I} \right)$	(5.55)	Constant $\tau$ ensures that phase changes do not occur instantaneously, introducing a time lag, whenever they occur.
Sum of mass flows	$\dot{M} = \dot{m}_A + \dot{m}_B$	(5.56)	Total mass flow.
Momentum balance	$p_A - p_I = \frac{\dot{m}_A}{S} \cdot \left  \frac{\dot{m}_A}{S} \cdot (v_I - v_A) \right  + F_{\text{visc},A} + I_A$	(5.57)	In half pipe adjacent to port A.
	$I_A = \dot{m}_A \cdot \frac{L}{2S}$	(5.58)	
	$p_B - p_I = \frac{\dot{m}_B}{S} \cdot \left  \frac{\dot{m}_B}{S} \cdot (v_I - v_B) \right  + F_{\text{visc},B} + I_B$	(5.59)	In half pipe adjacent to port B.
	$I_B = \dot{m}_B \cdot \frac{L}{2S}$	(5.60)	
Viscous friction forces	$F_{\text{visc},A}^{\text{turb}} = \frac{\dot{m}_A \cdot  \dot{m}_A  \cdot f_A \cdot L_{\text{wff}v_I}}{4 \cdot D_H \cdot S^2}$	(5.61)	Turbulent flow. Adjustment to port A.
	$F_{\text{visc},B}^{\text{turb}} = \frac{\dot{m}_B \cdot  \dot{m}_B  \cdot f_B \cdot L_{\text{wff}v_I}}{4 \cdot D_H \cdot S^2}$	(5.62)	Turbulent flow. Adjustment to port B.
Darcy friction factor adjusted to port A and port B	$f = \left\{ -1.8 \cdot \log_{10} \left[ \frac{6.9}{\text{Re}_A} + \left( \frac{\epsilon_r}{3.7} \right)^{1.11} \right] \right\}^{-2}$	(5.63)	Turbulent flow. Adjustment to port A.
	$\text{Re}_A = \frac{ \dot{m}_A  \cdot D_h \cdot v_I}{S v_I}$	(5.64)	
	$f = \left\{ -1.8 \cdot \log_{10} \left[ \frac{6.9}{\text{Re}_B} + \left( \frac{\epsilon_r}{3.7} \right)^{1.11} \right] \right\}^{-2}$	(5.65)	Turbulent flow. Adjustment to port B.
	$\text{Re}_B = \frac{ \dot{m}_B  \cdot D_h \cdot v_I}{S v_I}$	(5.66)	

Table 5.7, Continued

Abbreviations		
	M - fluid mass inside pipe	$v_I$ - specific volume
	$u_I$ - specific internal energy of fluid inside pipe	$\nu_I$ - kinematic viscosity
	$\dot{E}_A$ - energy flow rate into pipe through port A	$x_I$ - vapor quality
	$\dot{E}_B$ - energy flow rate into pipe through port B	$\rho$ - fluid density
	$\dot{Q}_H$ - heat flow rate into pipe through pipe wall, represented by port H	$p_I$ - pressure inside pipe
	$h_{\text{coeff}}$ - average heat transfer coefficient in pipe	V - fluid volume in pipe
	$S_{\text{Surf}}$ - pipe surface area	$\dot{m}_A$ - mass flow rate into pipe through port A
	$T_H$ - pipe wall temperature	$\dot{m}_B$ - mass flow rate into pipe through port B
	$T_I$ - temperature of fluid in pipe	$\epsilon_M$ - correction term
	Nu - Nusselt number in pipe	$\tau$ - phase-change time constant
	$k_I$ - average thermal conductivity in pipe	$p_A$ and $p_B$ - pressures at port A and port B
	$D_h$ - hydraulic diameter of pipe	$v_A$ and $v_B$ - fluid specific volumes at port A and port B
	f - friction factor of pipe	$F_{\text{visc},A}$ and $F_{\text{visc},B}$ - viscous friction forces in half pipe adjacent to port A and port B
	Re - Reynolds number	$I_A$ and $I_B$ - fluid inertia at port A and port B
	$Pr_I$ - Prandtl number	L - pipe length
	$\epsilon_r$ - roughness of pipe	$f_A$ - Darcy friction factor for turbulent flow in half pipe adjacent to port A
	S - cross-sectional area of pipe	$f_B$ - Darcy friction factor for turbulent flow in half pipe adjacent to port B

Assumptions and simplifications:

- Dynamic compressibility and thermal capacity of fluid are assumed as non-negligible.
- Pipe wall is rigid.
- Flow is fully developed.
- Effect of gravity is negligible.
- Heat transfer is calculated with respect to temperature of fluid volume in pipe.
- In transitional region between laminar and turbulent flow, a cubic polynomial function blends the Nusselt number, what ensures a smooth transition between different flow regimes.

Table 5.7: Governing equations for rigid conduit of fluid flow in two-phase fluid systems, representing the pre-heater and super-heater modules [215].

Two-phase fluid conserving ports A and B represent the pipe inlet and outlet. Thermal conserving port H represents the pipe wall, through which heat transfer with pipe surroundings takes place [215]. In the model, cylindrical pipes are applied and hydraulic diameter is the same as pipe’s actual diameter. Cross-section area is constant along the pipe length, which is defined as the distance between pipe inlet and outlet. With default of fluid inertia, the modelling is turned off. This setting is appropriate, when pressure forces, driving the flow, far exceed the inertial forces acting on the flow.

The internal surface roughness enables the calculation of friction factor, adjusted to port A and B, in the turbulent flow regime according to Darcy’s law, see eq. (5.51) and eqs. (5.63)-(5.65). Energy and mass conservation eqs. (5.45) and (5.54) are defined, respectively. Momentum conservation eqs. (5.57)-(5.60) are presented for every half of pipe adjacent to inlet and outlet, correspondingly. Heat transfer is calculated with respect to temperature of fluid volume in the pipe. Heat transfer between pipe wall and internal fluid volume is modelled as a convective process, see eqs. (5.46)-(5.48). In Table 5.7, eqs. (5.49) and (5.50) are defined predominantly for turbulent flow conditions.

**5.4.3 High-pressure and low-pressure steam turbines with re-heater modules**

The single steam turbine stage (see Fig. 5.10) includes high-pressure (HP) and low-pressure (LP) turbines with steam re-heaters SR1 and SR2 in-between [84]. The governing equations for steam turbine module are joined in Table 5.8. The steam turbine design and operational parameters as input data are listed in Appendix A.6, Table A6.3 and Table A6.4.

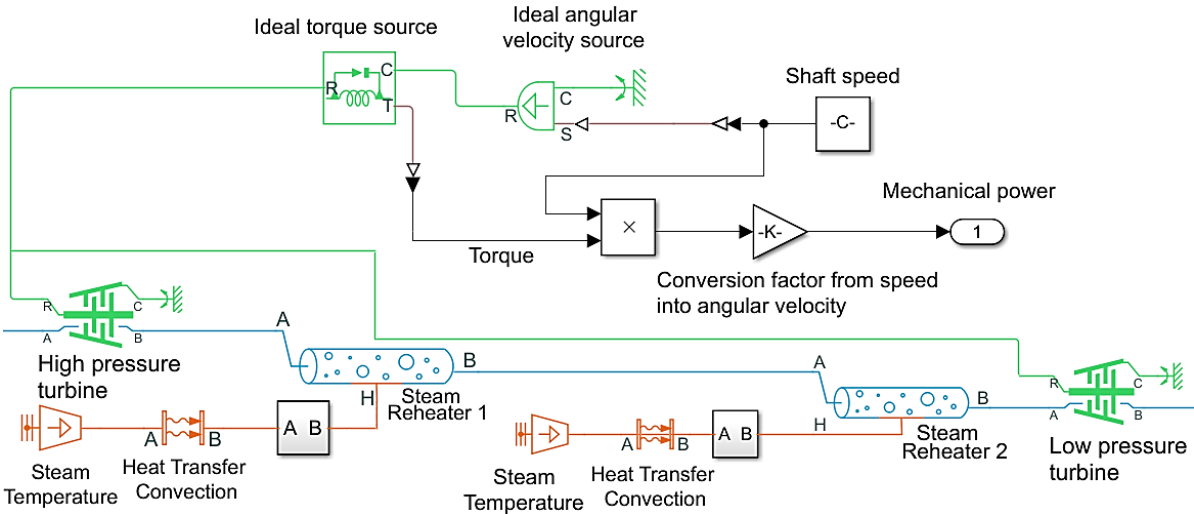


Fig. 5.10: Sketch of a single steam turbine stage.


Title	Governing equation	Equation	Remark
Module			Module models a turbine in a two-phase (2P) fluid network.
Mass balance	$\dot{m}_A + \dot{m}_B = 0$	(5.67)	Stationary condition.
Energy balance	$\dot{E}_A + \dot{E}_B - P_{\text{fluid}} = 0$	(5.68)	$P_{\text{fluid}}$ is determined from change in total fluid specific enthalpy.
Fluid work	$P_{\text{fluid}} = \dot{m}_A \cdot \Delta h_{\text{total}}$	(5.69)	
Corrected mass flow rate	$\dot{m}_A \cdot \sqrt{\frac{T_A}{T_{\text{corr}}}} = \dot{m}_{\text{corr}} \cdot \frac{p_A}{p_{\text{corr}}}$	(5.70)	
Corrected speed	$\omega_{\text{corr}} = \frac{\omega}{\sqrt{\frac{T_A}{T_{\text{corr}}}}}$	(5.71)	
Shaft torque	$\tau = \frac{\eta_{\text{mech}} \cdot \dot{m}_A \cdot \Delta h_{\text{total}}}{\omega}$	(5.72)	
Steam flow rate	$\dot{m}_{\text{steam}} = \chi \cdot \frac{p_{\text{in}}}{\sqrt{T_{\text{in}}}} \cdot \sqrt{1 - \left(\frac{p_{\text{out}}}{p_{\text{in}}}\right)^2}$	(5.73)	It is characterized by Stodola's cone law.
Turbine shaft power	$P_S = \dot{m}_{\text{steam}} \cdot c_p \cdot T_{\text{in}} \left[ \left(\frac{p_{\text{out}}}{p_{\text{in}}}\right)^{\frac{n-1}{n}} - 1 \right]$	(5.74)	See [249].
Abbreviations:			
$\dot{m}_A$ - mass flow rate at port A	$\Delta h_{\text{total}}$ - total change in fluid specific enthalpy		
$\dot{m}_B$ - mass flow rate at port B	$\eta_{\text{mech}}$ - mechanical efficiency		
$\dot{E}_A$ - energy flow rate at port A	$\omega$ - relative shaft angular velocity		
$\dot{E}_B$ - energy flow rate at port B	$p_{\text{in}}$ and $p_{\text{out}}$ - pressure at inlet and outlet		
$P_{\text{fluid}}$ - work done by fluid	$T_{\text{in}}$ - steam temperature at inlet of turbine		
$T_A$ - temperature at port A	$\chi$ - swallowing capacity of a turbine as coefficient of turbine that is determined during design calculation		
$T_{\text{corr}}$ - correct adjusted temperature	$P_S$ - steam turbine shaft power		
$\dot{m}_{\text{corr}}$ - correct adjusted mass flow rate	$n = 1.25$ - polytropic index for steam		
$p_A$ - pressure at port A	$c_p$ - specific heat capacity of steam		
$p_{\text{corr}}$ - corrected pressure			
Assumptions and simplifications:			
<ul style="list-style-type: none"> <li>• Module assumes that superheated fluid enters the inlet.</li> <li>• Shaft does not rotate under reversed flow conditions.</li> <li>• Reversed flow from port B to port A is outside of typical turbine operation mode and may not return accurate results.</li> </ul>			

Table 5.8: Governing equations for steam turbine module [215].

For running of simulations, the turbine rotation speed of 3000 rpm is chosen. The HP and LP steam turbines input temperatures are 719 K and 579 K, respectively. The inlet/outlet fluid flow area of turbines is calculated using industrial design data for inlet/outlet turbine diameters. The pressure and temperature data are based on compressibility and thermal capacity of vapor volume. The pressure ratio is defined as the ratio between turbine inlet and outlet pressure. The re-heaters are modelled as thermal liquid pipes.

Ports A and B are related to re-heater's inlet and outlet. Port H corresponds to thermal conserving port for its pipe wall. Other ports A and B are two-phase fluid conserving ports, associated with steam turbine inlet and outlet. Ports R and C are mechanical, rotational conserving ports. The fluid, which flows from port A to port B, generates the torque. Port R reports the shaft torque and angular velocity relative to port C, which represents the turbine casing. In our case, the fluid flow from port A to port B drives a positive rotation of port R relative to port C. Mechanical conserving port R of torque sensor is coupled to conserving terminal R of HP and LP steam turbines. The shaft speed output is connected to physical signal port S of an ideal angular velocity source. The torque, relative to shaft speed, is measured at sensor port T, whereas the measured torque and shaft speed are converted into mechanical power by the conversion factor, following the “gain” module.

#### 5.4.4 Steam condenser module

The scheme of steam condenser module is shown in Fig. 5.11. The governing equations are presented in Table 5.9. The required water and steam properties are listed in Appendix A.6, Table A6.3, and the modelling parameters of steam condenser are joined in Appendix A.6, Table A6.3 and Table A6.4.

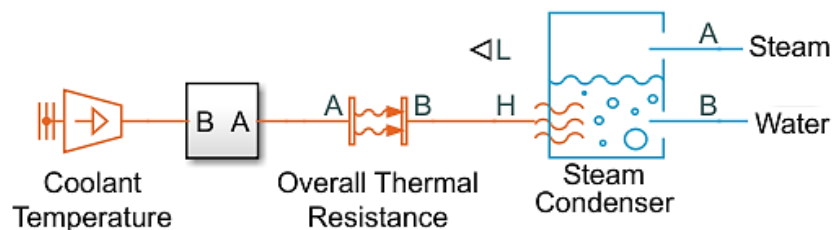


Fig. 5.11: Scheme of steam condenser module.

Ports A and B are two-phase fluid conserving ports, which are connected to saturated vapour volume. Port L controls the liquid volume fraction. Port H is thermal conserving port associated with fluid temperature inside the chamber. The steam in the condenser is condensed over the pipes, through which cold water flows. Steam is condensed and collected at the bottom in a hot well. The condenser pipes are split into three parts, namely at inlet of the condenser in touch with the steam, within the condensate, and then again in contact with steam at outlet of the condenser. The thermal energy of steam is exchanged with coolant temperature by means of convective heat transfer module. The coolant temperature of the condenser depends on ambient temperature level, what influences the heat losses [228].



Title	Governing equation	Equation	Remark
Energy balance	$q_{hd} = f_{cm} \cdot \gamma$	(5.75)	Heat of steam is equal to heat transferred to cooling water.
	$q_{hd} = H_{tc} \cdot \left[ \frac{T_{olt} - T_{cilt}}{\ln \frac{T_{CD} - T_{cilt}}{T_{CD} - T_{olt}}} \right]$	(5.76)	
	$\frac{dT_{olt}}{dt} = \frac{F_{cwm}}{M_{cwm}} \cdot (T_{cilt} - T_{olt}) + \frac{q_{hd}}{M_{cwm} \cdot C_h}$	(5.77)	
Mass balance	$\frac{dP_r}{dt} = \frac{S_r \cdot T_{CD}}{V_c} \cdot (F_{steam} - f_{cm})$	(5.78)	Based on constant volume assumption.

Abbreviations:

$q_{hd}$ - condenser heat duty	$F_{cwm}$ - cooling water flow rate
$f_{cm}$ - mass flow rate	$M_{cwm}$ - hold-up (cooling water mass)
$\gamma$ - steam latent heat	$C_h$ - cooling water heat capacity
$H_{tc}$ - heat transfer coefficient (overall)/heat transfer area	$P_r$ - condenser pressure
$T_{olt}$ - cooling water outlet temperature	$S_r$ - gas constant
$T_{CD}$ - condensation temperature	$V_c$ - volume of condenser
$T_{cilt}$ - inlet temperature of cooling water	$F_{steam}$ - flow rate of steam

Table 5.9: Governing equations for steam condenser module [215, 226, 227].

### 5.4.5 Feedwater pump module

The feedwater (FW) pump module is presented schematically in Fig. 5.12. The design and operational parameters are listed in Appendix A.6, Table A6.3 and Table A6.4. The FW pump is installed between steam condenser and pre-heater (see Fig. 5.8). For numerical simulations, the inlet/outlet cross-sectional area of 0.16 m<sup>2</sup> is taken, inlet/outlet volumetric flow rate is 0.712 m<sup>3</sup>/s and medium fluid velocity is 4.48 m/s.

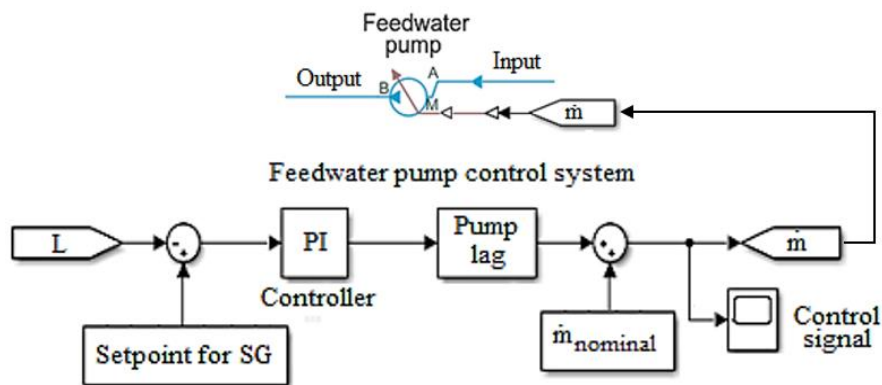


Fig. 5.12: Feedwater pump module with control function unit

The controlled mass flow rate source, representing the FW pump for DEMO PCS, defines an ideal mechanical energy source in a two-phase fluid network, in which no irreversible losses are assumed, and no heat exchange is considered with the environment [215]. Regulated water mass flow is determined by fluid density.

Positive mass flow rate in FW pump comes from port A to port B. Water mass flow rate is controlled at pump inlet through the signal, being applied at pump port M.

The difference between pump outlet and inlet pressure is given as

$$\rho_{Aver} = \frac{\rho_A + \rho_B}{2}, \quad (5.79)$$

where  $\rho_A$  and  $\rho_B$  is fluid mixture density at port A and B, respectively, and  $\rho_{Aver}$  is average density of the fluid mixture.

Mechanical work is calculated by

$$W_{mech} = \dot{m} \cdot \frac{p_B - p_A}{\rho_{Aver}}, \quad (5.80)$$

where  $p_A$  and  $p_B$  are given as pressures at ports A and B, as well as  $\dot{m}$  is defined as FW mass flow rate [215].

The FW pump control system contains a proportional integral (PI) controller with pump lag unit, whose technical data are listed in Appendix A.6, Table A6.4. Regarding the control circuit of FW pump, steam generator liquid level is applied as input data [225]. It is compared with the set value at 0.7 of liquid level in the steam generator, meanwhile the signal is sent to PI controller and pump lag of DEMO PCS feedwater pump, which generate a control signal for FW mass flow rate.

## 5.5 Conclusions

The simulation models of DEMO PHTS-IHTS and DEMO PCS systems are developed using MATLAB<sup>®</sup>/Simulink.

DEMO PHTS-IHTS model includes PHTS OB/IB HXs, cold and hot thermal storage tanks and pipelines with corresponding novel customized modules for simulation of heat losses to environment, two fixed-displacement pumps and a single PCS SG stage with PH-SG-SH heat exchanger modules. The simulation model excludes any kind of fittings like valves and auxiliary control equipment, due to lack of such data bank on current industrial market.

For DEMO PCS model, which is developed using MATLAB<sup>®</sup>/Simulink, the Rankine Cycle model is applied, though the steam generator is modelled as a two-phase fluid constant volume chamber. Pre-heater, super-heater, as well as the re-heaters between HP and LP steam turbines, are modelled as two-phase fluid pipes.

The MATLAB<sup>®</sup>/Simulink modules, which are used in DEMO PHTS-IHTS and DEMO PCS models, are described. The involved governing equations are tabulated, as well as the design and operational parameters, which are applied as input data for the simulations, are highlighted.



## **6 Simulation of temporal evolution of mass and heat flows in DEMO PHTS-IHTS and DEMO PCS systems**

### **6.1 Simulation of temporal evolution of molten salt filling level in DEMO IHTS thermal storage tanks**

Regarding the simulation of HITEC molten salt filling level in DEMO IHTS thermal storage tanks, it is assumed that pumps 1 and 2, which are sketched in Fig. 6.1, start their operation at simulation time of  $t_{sim} = 0$  sec. A single operation cycle lasts for 7800 sec. Pulse operation takes place for 7200 sec and dwell operation lasts for 600 sec.

The analysis is carried out for four time intervals: 1)  $t_1 = 0-160$  sec, 2)  $t_2 = 160-7040$  sec, 3)  $t_3 = 7040-7200$  sec, and 4)  $t_4 = 7200-7800$  sec (see Table 6.1 and Fig. 6.2-6.4). At the beginning of pulse operation, MS mass flow rates through the pumps grow until they reach stable operation state. During simulation time between 0-30 sec, the change of MS filling level in thermal storage tanks is small, see Fig. 6.2 and Fig. 6.3. Later, during time interval  $t_1$ , molten salt filling level in cold storage tank linearly decreases and in hot storage tank linearly increases.

During time interval  $t_2$ , which is characterized by stable operation modus of both pumps 1 and 2, MS filling level in cold storage tank continues to decrease, whereas MS filling level in hot storage tank further increases, what is displayed in Fig. 6.2.

The time interval  $t_3$  corresponds to the transition from pulse-to-dwell. During this time, MS mass flow rate through pump 1 decreases and through pump 2 it increases. According to simulation data, at time  $t_{sim} \approx 7080 \pm 20$  sec, a rather small change of MS filling level is observed in both thermal storage tanks. Further, with increase in molten salt mass flow rate through pump 2, MS filling level in cold storage tank (see Fig. 6.4) starts to grow according to eq. (6.3), see Table 6.1.

During time interval  $t_4$ , which corresponds to dwell operation period, a linear increase in MS filling level in cold storage tank (see Table 6.1, eq. (6.4)) and linear decrease in MS filling level in hot storage tank is observed. During dwell operation, MS mass flow rate through pump 2 is considerably higher than through pump 1. During time interval  $t_4$ , molten salt mass flow rate through pump 1 is strongly reduced, even though HITEC is pumped continuously into hot storage tank.

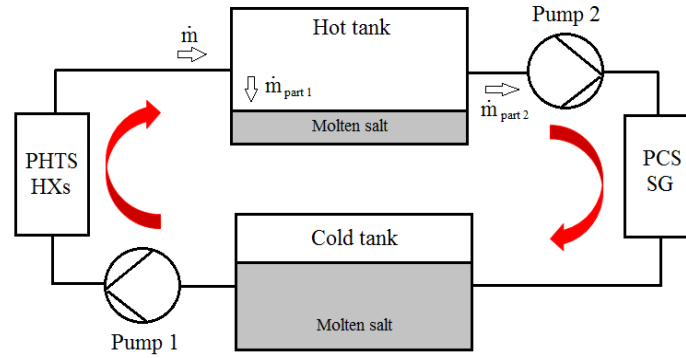


Fig. 6.1: Sketch of DEMO IHTS operation during pulse time.

Interval	Time interval	Cold tank filling level	Change of MS filling level in cold storage tank, temporal dependence	Equation	Operation conditions
1	$t_1$	$H_{\text{cold},1}$	$H_{\text{cold},1} = H_{\text{cold,max}} - v_{\text{cold},1} \cdot t_1 - \frac{1}{2} \cdot a_{\text{cold},1} \cdot t_1^2$	(6.1)	Increase in HITEC mass flow rate through pumps 1 and 2, when mass flow rate in pump 1 is higher than in pump 2.
2	$t_2$	$H_{\text{cold},2}$	$H_{\text{cold},2} = H_{\text{cold},1} - v_{\text{cold},2} \cdot t_2$	(6.2)	Rather constant MS mass flow rates for pumps 1 and 2.
3	$t_3$	$H_{\text{cold},3}$	$H_{\text{cold},3} = H_{\text{cold,min}} + v_{\text{cold},3} \cdot t_3 + \frac{1}{2} \cdot a_{\text{cold},3} \cdot t_3^2$	(6.3)	Increase in MS mass flow rate through pump 2 and decrease in MS mass flow rate in pump 1.
4	$t_4$	$H_{\text{cold},4}$	$H_{\text{cold},4} = H_{\text{cold},3} + v_{\text{cold},4} \cdot t_4$	(6.4)	Rather constant MS mass flow rates for pumps 1 and 2.

Abbreviations:  $v_{\text{cold},1}$  and  $a_{\text{cold},1}$  - velocity and acceleration of the change of MS filling level during 1<sup>st</sup> time interval  $t_1$   
 $v_{\text{cold},2}$  - velocity of the change of MS filling level in cold storage tank during 2<sup>nd</sup> time interval  $t_2$   
 $v_{\text{cold},3}$  and  $a_{\text{cold},3}$  - velocity and acceleration of the change of MS filling level during 3<sup>rd</sup> time interval  $t_3$   
 $v_{\text{cold},4}$  - velocity of the change of MS filling level in cold storage tank during 4<sup>th</sup> time interval  $t_4$

Assumptions:

- Total mass flow rate of molten salt is calculated as  $\dot{m} = \dot{m}_{\text{part 1}} + \dot{m}_{\text{part 2}}$
- Before beginning of the first operation cycle, both pumps 1 and 2 are switched off.
- During dwell operation, pump 1 works with reduced MS mass flow rate.
- During pulse operation, pump 2 is used for pumping of HITEC molten salt flowing to DEMO PCS SG HXs.

Table 6.1: Governing equations for temporal evolution of MS filling level in cold storage tank.

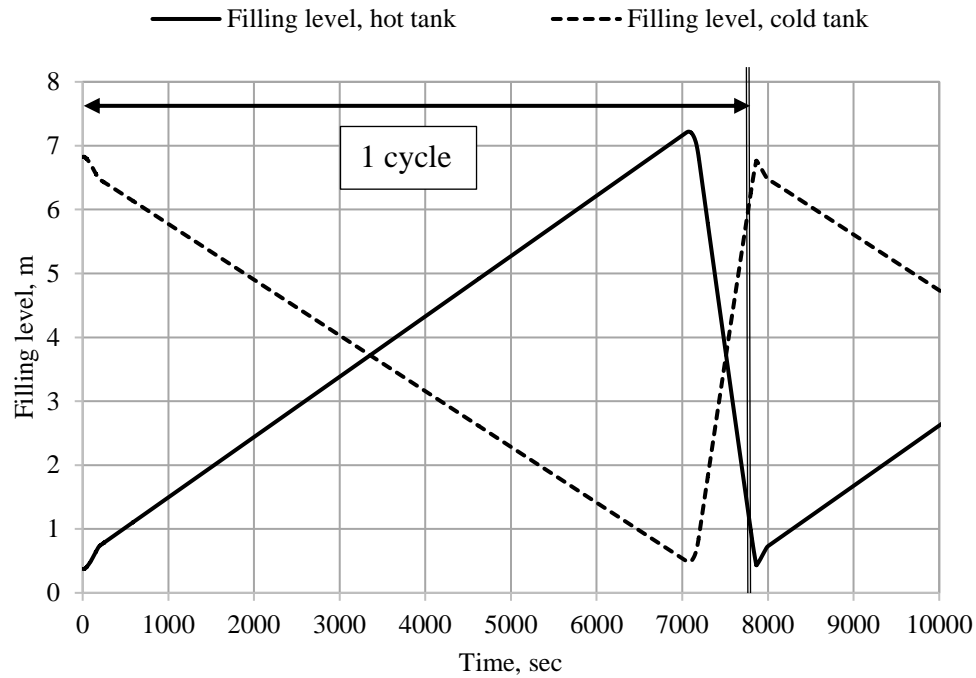


Fig. 6.2: Simulated temporal evolution of HITEC filling level in cold and hot storage tanks during single operation cycle.

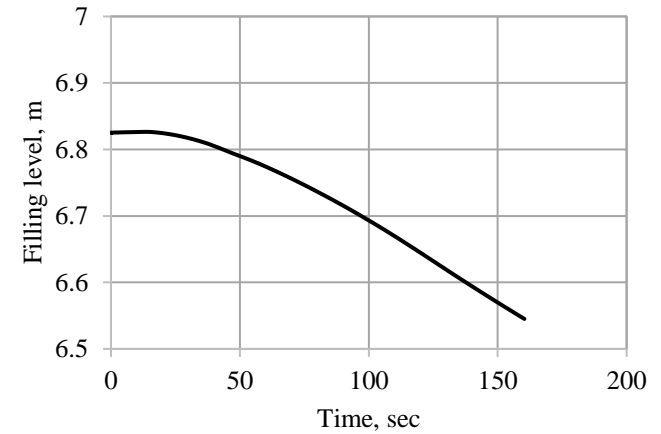


Fig. 6.3: Cold storage tank filling level for simulation time between 0-160 sec.

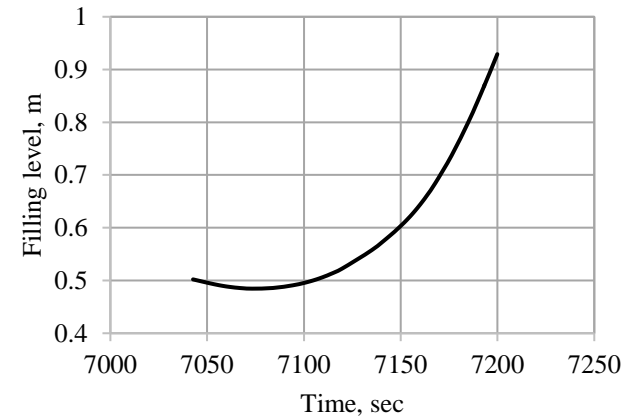


Fig. 6.4: Cold storage tank filling level for simulation time between 7040-7200 sec.

The temporal evolution of MS filling level in DEMO IHTS storage tanks' is simulated for 11 pulse/dwell operation cycles, what corresponds to 1 day of transient fusion reactor operation. The comparison between Fig. 6.5 and Fig. 6.2 shows a good cycle-to-cycle repeatability, adequate to single operation cycle.

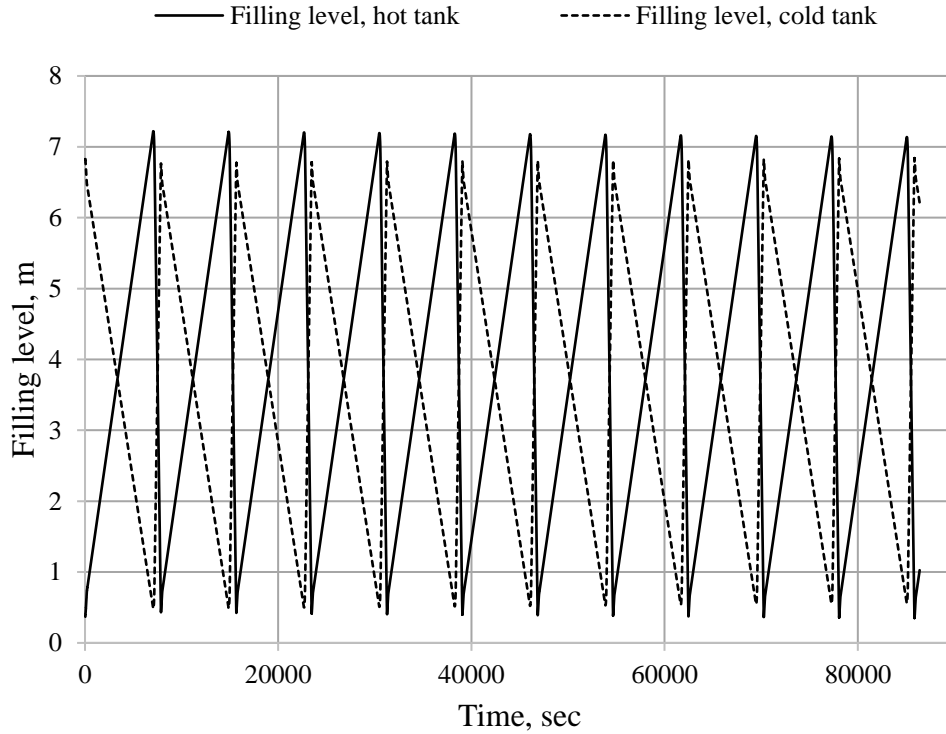


Fig. 6.5: Temporal evolution of HITEC filling level in storage tanks for 11 operation cycles.

During pulse operation, a part of molten salt mass flow  $\dot{m}_{\text{part1}}$  remains in hot storage tank. Simultaneously, another part of molten salt flow rate  $\dot{m}_{\text{part2}}$  is pumped via pump 2 back to cold storage tank through DEMO PCS SG HXs (see Fig. 6.1). The simulations for temporal evolution of MS filling level, see Fig. 6.2, allows the prediction of MS mass flow  $\dot{m}_{\text{part1}}$ . According to simulation data, the linear approximation of MS filling level curve for time interval  $t_2$  gives the value of  $\dot{m}_{\text{part1}} \approx 735$  kg/s. Analysing the results of simulations, it is possible to define the change of HITEC molten salt filling levels in both thermal storage tanks as  $\Delta H_{\text{cold}} = H_{\text{cold,max}} - H_{\text{cold,min}}$  and  $\Delta H_{\text{hot}} = H_{\text{hot,max}} - H_{\text{hot,min}}$ . Here, the parameters  $H_{\text{cold,min}}$ ,  $H_{\text{hot,min}}$  and  $H_{\text{cold,max}}$ ,  $H_{\text{hot,max}}$  are MS minimum and maximum filling levels in cold and hot storage tanks, respectively. Assuming constant HITEC molten salt mass, the results of simulation show that  $\Delta H_{\text{hot}} > \Delta H_{\text{cold}}$  and  $\frac{\Delta H_{\text{hot}}}{\Delta H_{\text{cold}}} = f\left(\frac{\rho_{\text{HITEC,cold}}}{\rho_{\text{HITEC,hot}}}\right)$ , what correlates well with the simulation data for temperature dependent MS density, see chapter 2, §2.3.



## 6.2 Simulation of temporal evolution of mass flow in DEMO PHTS-IHTS system

The results of simulation of temporal evolution of HITEC mass flow in DEMO IHTS cold storage tank, for a single operation cycle, are presented in Fig. 6.6. During pulse operation, the increase in MS mass flow rate takes place at outlet of cold storage tank, being stabilized after  $\sim 160$  sec, what correlates well with simulation data for MS filling level, see Fig. 6.2.

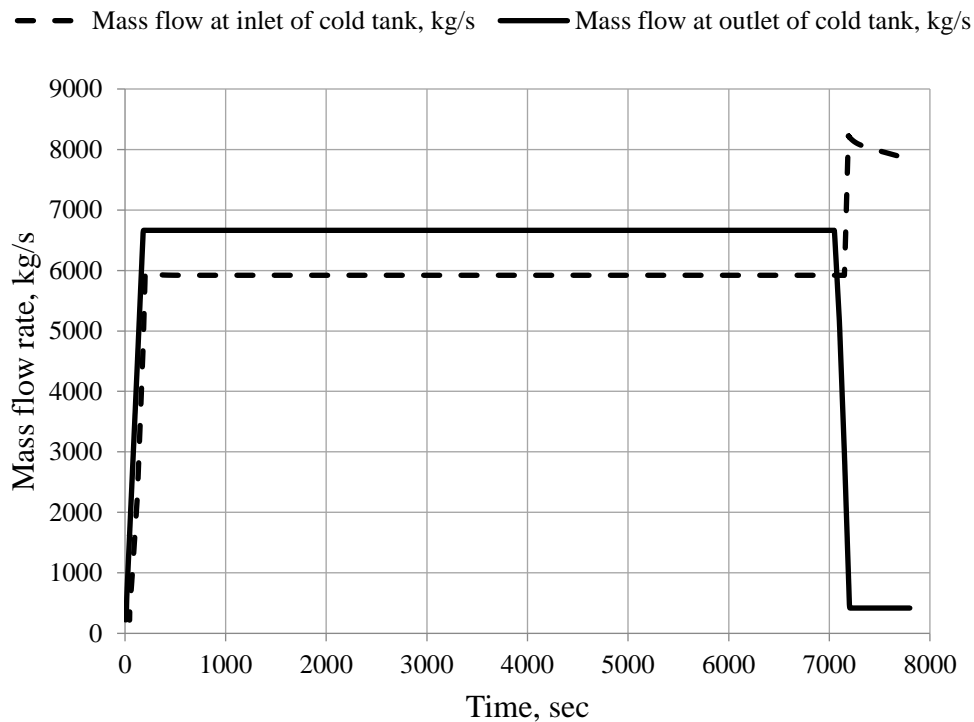


Fig. 6.6: Simulated HITEC mass flow at cold tank inlet and outlet for single operation cycle.

For time interval  $t_2$ , which lasts for 6880 sec, the MS mass flow rate of  $\dot{m}_{MS} = 6660$  kg/s is obtained at outlet of cold storage tank, as well as at inlet of hot storage tank. The simulated value of HITEC mass flow rate at outlet of hot storage tank, as well as at inlet of cold storage tank, is  $\dot{m}_{part\ 2} = 5920$  kg/s. The molten salt mass flow, which remains in hot storage tank, is calculated as  $\dot{m}_{part\ 1} = \dot{m} - \dot{m}_{part\ 2} = 740$  kg/s, what correlates well with  $\dot{m}_{part\ 1} = 735$  kg/s, which is defined by linear approximation of simulation curve for temporal evolution of MS filling level in hot storage tank for time interval  $t_2 = 160 - 7040$  sec, see Fig. 6.2.

The simulations indicate that during dwell operation the pump 1 continues to pump the molten salt into hot storage tank with a mass flow rate of  $\sim 418$  kg/s, what does not exceed the value of  $\sim 6.3\%$  from total MS mass flow rate in pump 1 during pulse operation. During time interval  $t_3$ ,

the MS mass flow rate through pump 2 quickly increases from mean value 5980 kg/s to 8120 kg/s, what takes place during time interval of 7155-7200 sec, see Fig. 6.6. For this time, the MS mean mass flow of ~7050 kg/s can be estimated. Furthermore, MS flow rate linearly decreases during dwell operation from 8120 kg/s at the beginning to 7840 kg/s at the end of dwell operation. Hence, for dwell operation the mean flow rate of ~7980 kg/s for HITEC molten salt is estimated, which is pumped with pump 2. The results of simulations of HITEC mass flow at inlet and outlet of cold storage tank for 11 operation cycles are presented in Fig. 6.7.

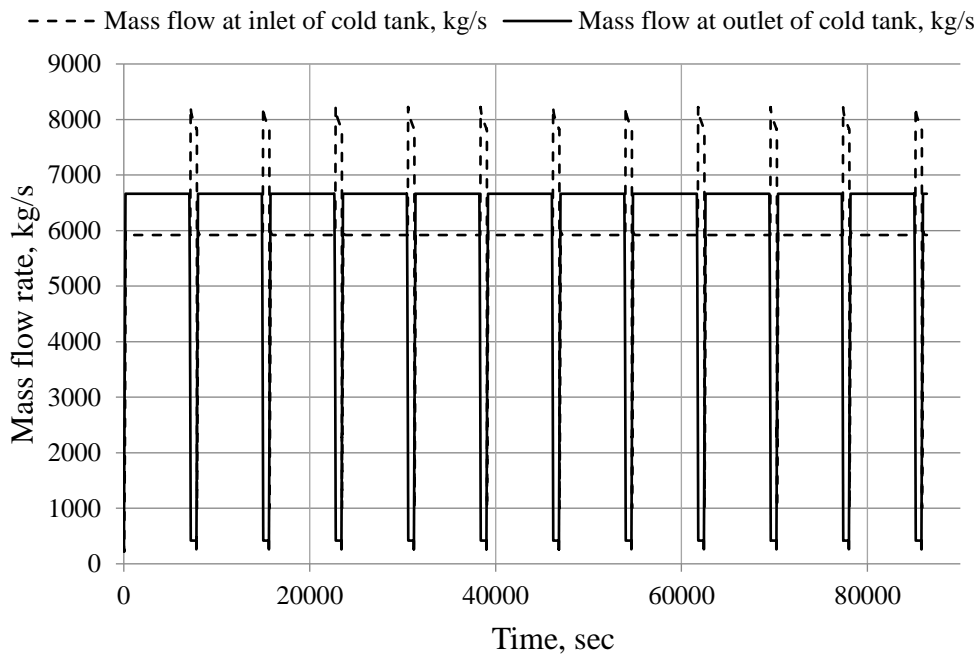


Fig. 6.7: Simulated HITEC mass flow at cold tank inlet and outlet for 11 operation cycles.

The simulated data show good temporal repeatability, confirming the ability of developed model to predict well the temporal evolution of MS mass flow in DEMO IHTS system for long-term operation conditions.

### 6.3 Simulation of temporal evolution of heat flow in DEMO PHTS-IHTS system

For simulations, constant helium mass flow rate of 1842 kg/s is taken in PHTS OB/IB HXs. Gas specific heat capacity is 5193 J/(kg·K). The difference between gas inlet and outlet temperatures is  $\Delta T_{\text{He}} = 220$  K. Taking into consideration for heat input the relation

$$\dot{Q}_{\text{He}} = \dot{m}_{\text{He}} \cdot c_{p,\text{He}} \cdot \Delta T_{\text{He}}, \quad (6.5)$$

the calculated heat flow rate from helium to HITEC during pulse operation is  $\sim 2.1$  GW.

The simulation of temporal evolution of heat flow at inlet and outlet of DEMO IHTS hot storage tank (see Fig. 6.8) shows that for pulse time during stable operation of pumps, the thermal energy flow into hot storage tank is  $\dot{E}_{\text{hot,in}} = 1.76$  GW. For corresponding conditions, the thermal energy flow rate at outlet of hot storage tank is  $\dot{E}_{\text{part 2}} = 1.58$  GW and the value  $\dot{E}_{\text{part 1}}$  is calculated as

$$\dot{E}_{\text{part 1}} = \dot{E}_{\text{hot,in}} - \dot{E}_{\text{part 2}} = 0.18 \text{ GW}. \quad (6.6)$$

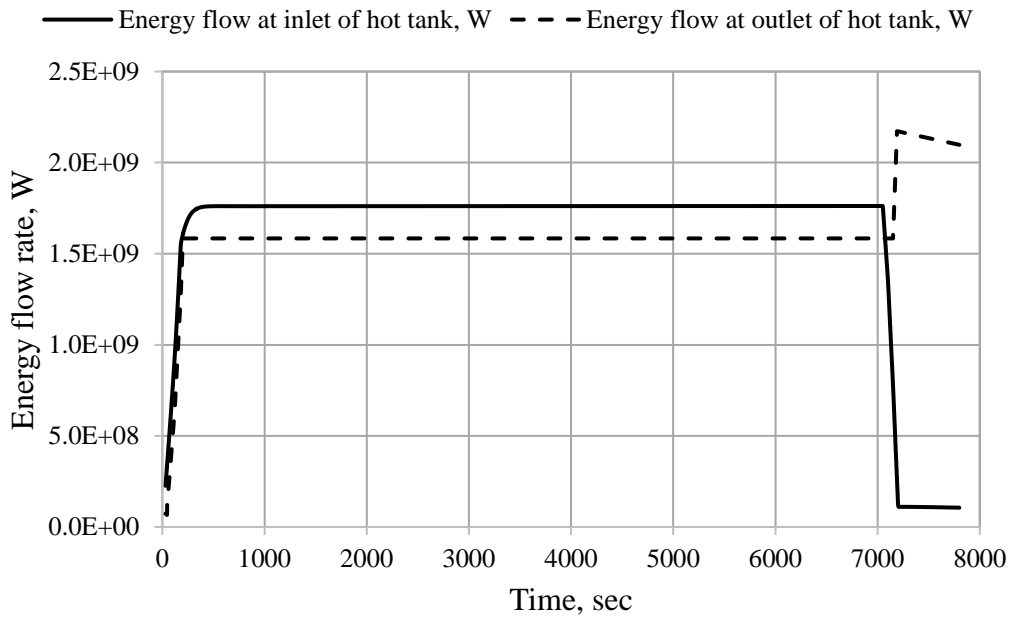


Fig. 6.8: Thermal energy flow at inlet and outlet of hot storage tank for single operation cycle.

The simulation graph shows, see Fig. 6.8, that at the beginning of dwell operation, the heat flow rate to PCS SG is  $\sim 2.16$  GW and after time interval of  $\sim 600$  sec it slightly decreases to  $\sim 2.1$  GW. These results correlate well with the data, which are calculated by eq. (6.5). During dwell operation, in PHTS HXs there is no heat transfer from helium to HITEC.

According to chapter 5, §5.2.1, the simulation model allows the control of heat losses from pipelines to environment. For example, the results of simulation of heat losses to environment from pipelines 1 and 2 are presented in Fig. 6.9. The simulations predict mainly heat losses of  $\sim 0.085$  MW from pipeline 1 with cold molten salt and heat losses of  $\sim 0.185$  MW from pipeline 2 with hot molten salt. The estimated total heat losses of  $\sim 0.33$  MW to environment from all pipelines 1-6 are calculated [33].

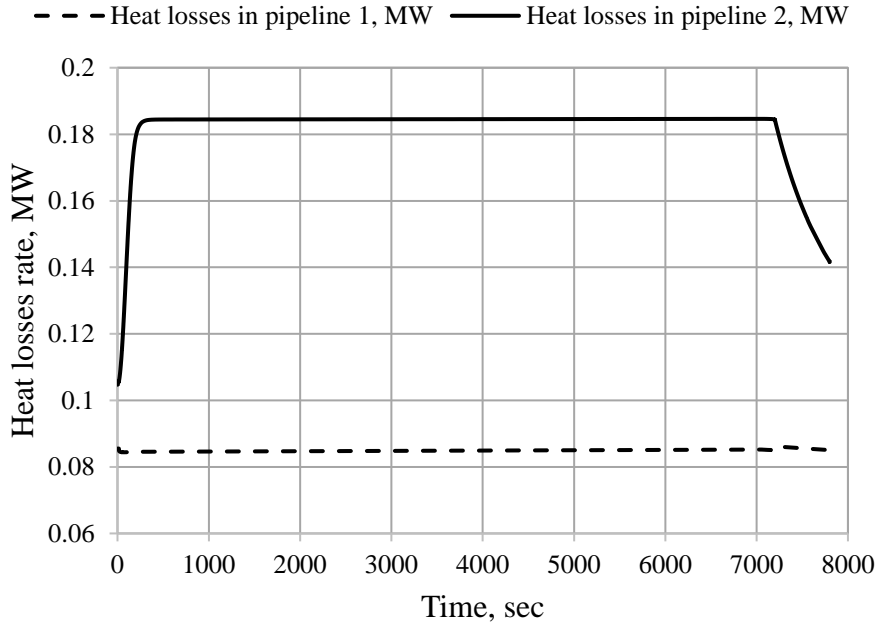


Fig. 6.9: Temporal evolution of heat losses from pipelines 1 and 2 for single operation cycle.

#### 6.4 Simulation of temporal evolution of liquid volume fraction in DEMO PCS steam generator

Referring to simulation of temporal evolution of liquid volume fraction, following steam generator parameters are used: heat transfer coefficient of  $1698 \text{ W}/(\text{m}^2\cdot\text{K})$ , heat transfer area of  $7723 \text{ m}^2$  and SG pipe length of  $10.71 \text{ m}$  [98]. The total fluid volume is calculated by multiplying volumetric flow of  $1.085 \text{ m}^3/\text{s}$  with pulse time of  $7200 \text{ s}$ , or with dwell time of  $600 \text{ s}$ , correspondingly. For pulse and dwell operation, SG fluid volume of  $7812 \text{ m}^3$  and  $651 \text{ m}^3$  each is selected. Temporal evolution of liquid volume fraction is simulated for SG inlet/outlet at variable pressure of  $p_{\text{min}/\text{max}} = 121/125 \text{ bar}$  for pulse operation and  $p_{\text{min}/\text{max}} = 134/138 \text{ bar}$  for dwell operation. The growing pressure supposes an increase in fluid volume, which is transformed into steam. During dwell operation, the surges in pressure are due to circulation of larger mass flow of hot molten salt.

The results of simulations of temporal evolution of SG liquid volume fraction for pulse and dwell operation are shown in Fig. 6.10 and Fig. 6.11, respectively. SG liquid volume fraction is simulated for pulse and dwell time separately. At the beginning of simulations, fluctuations of curves take place around SG liquid volume fraction value of  $0.7$ , especially in the first  $30 \text{ sec}$ . The simulations show that liquid volume fraction fluctuates regressively between minimum and maximum values, with a fluctuation difference of  $\text{max. } \pm 0.01$ .

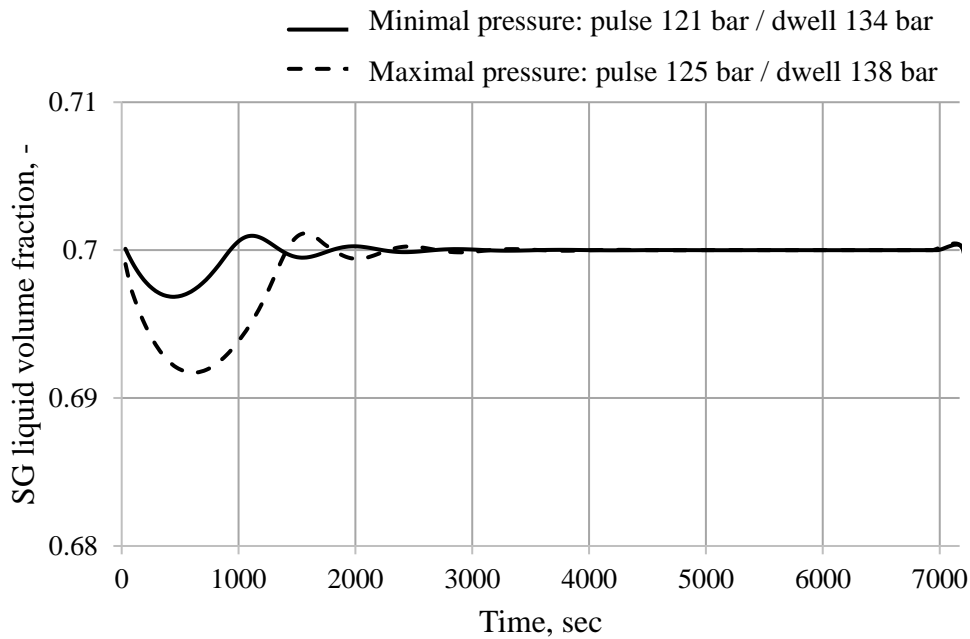


Fig. 6.10: Simulated temporal evolution of SG liquid level during pulse operation.

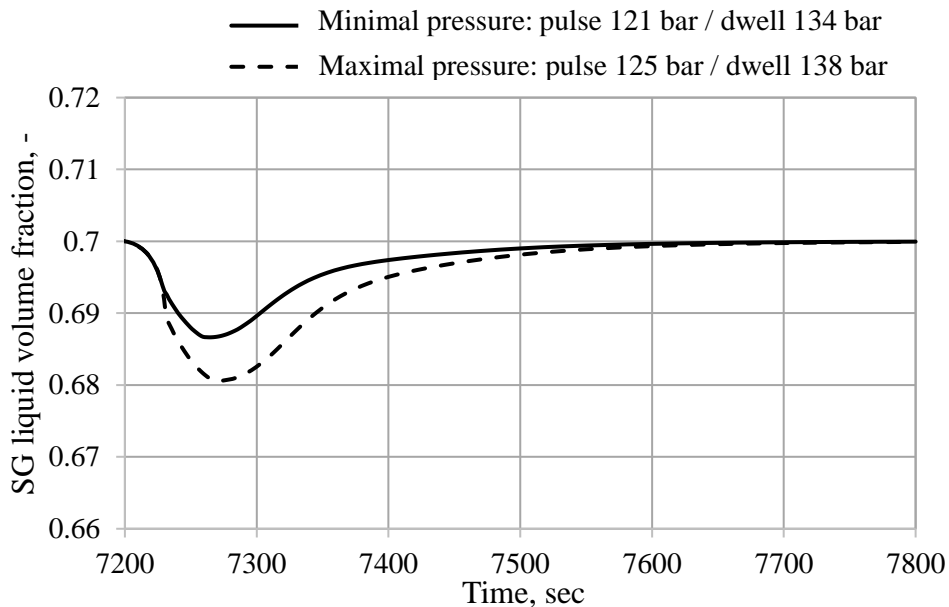


Fig. 6.11: Simulated temporal evolution of SG liquid level during dwell operation.

Focusing only on stable operation conditions, the behavior of simulated curves is analyzed for time interval between  $30 \leq t \leq 7200$  sec for pulse operation, see Fig. 6.10, and between  $7200 \leq t \leq 7800$  sec for dwell operation, see Fig. 6.11. For pulse operation, at the beginning of simulation, SG liquid volume fraction decreases with  $\sim 0.5\%$  at  $p_{\min} = 121$  bar and with  $\sim 1.2\%$  at  $p_{\max} = 125$  bar in comparison to initial value of 0.7. At  $p_{\min} = 121$  bar, SG liquid volume fraction reaches its constant value of 0.7 after  $\sim 3000$  sec. At  $p_{\max} = 125$  bar, the simulated curve appropriates its stability after  $\sim 3500$  sec. At  $p_{\min} = 134$  bar, the simulated value of SG liquid

volume fraction reaches its minimum of 0.686 after ~7264 sec and the curve reaches its stable value of 0.7 at ~7550 sec. At  $p_{\max} = 138$  bar, the data for SG liquid volume fraction are rather like the data at  $p_{\min} = 134$  bar, reaching minimal value of 0.681 after ~7272 sec. The curve reaches the value of 0.7 after ~7600 sec. The analysis shows, that in comparison with pulse time, during the start-up phase of dwell operation, the increase in pressure results in growing amplitude of fluctuations.

### 6.5 Simulation of temporal evolution of mass flow in DEMO PCS modules

Referring to simulations, in the steam condenser the volumetric fluid flow of  $2.46 \text{ m}^3/\text{s}$  is taken. The area of pre-heater is given as  $6074 \text{ m}^2$ , area of steam generator is  $7723 \text{ m}^2$ , area of super-heater is given as  $5040 \text{ m}^2$ , and area of steam condenser is stated as  $61648 \text{ m}^2$ . The inlet pressure in HP turbine is 121 bar for pulse operation and 134 bar for dwell operation. The inlet pressure in LP turbine is 11 bar both for pulse and dwell operation.

To control the mass flow rates, sensors S1-S4 are introduced into DEMO PCS model, see Fig. 5.8. The results of simulations of fluid mass flow downstream single PCS PH-SG-SH stage for pulse and dwell operation time are presented in Fig. 6.12 and Fig. 6.13, correspondingly.

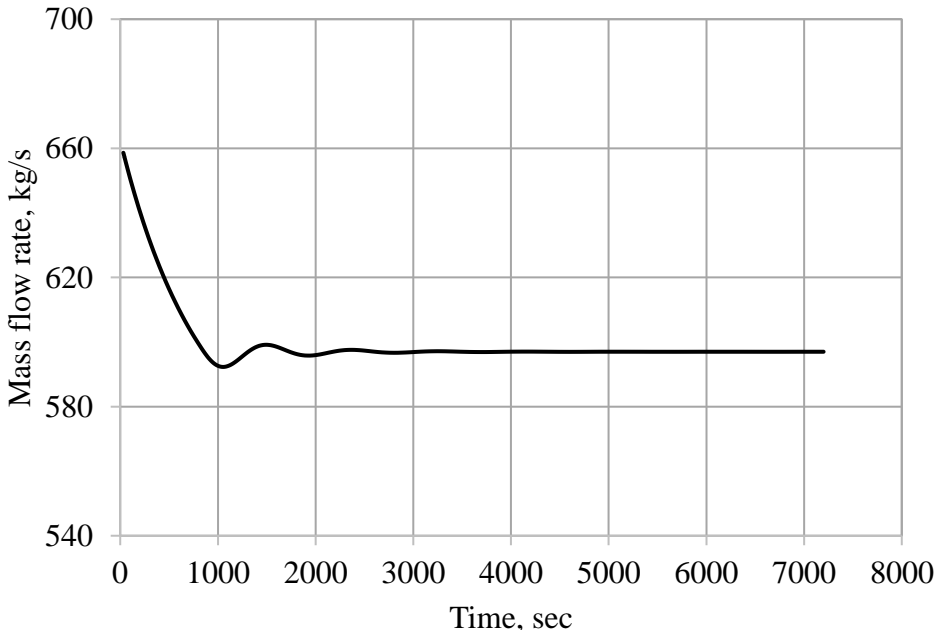


Fig. 6.12: Temporal evolution of mass flow during pulse operation at located sensor S2 downstream PCS PH-SG-SH module.

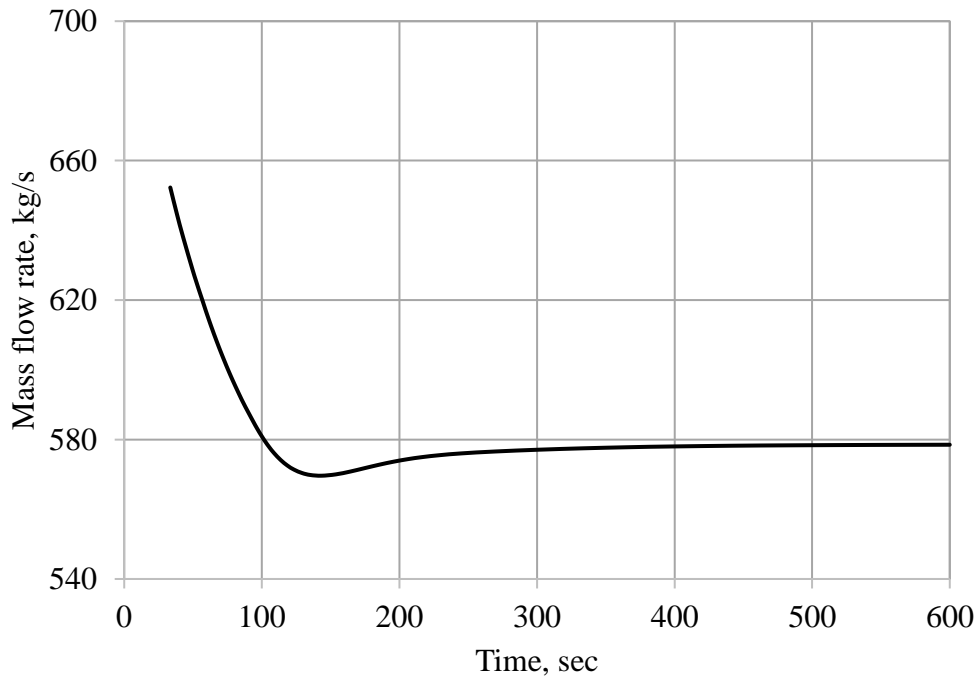


Fig. 6.13: Temporal evolution of mass flow during dwell operation at located sensor S2 downstream PCS PH-SG-SH module.

The simulations for pulse and dwell operation are carried out separately to distinguish and to analyze better the process flow in evolution of time. At the beginning of simulations, fluctuations of simulated curves occur both for pulse and dwell operation. The required time for curves' stabilization is equal compared to the time of stabilization of simulated curves for SG liquid level fraction, which are shown in Fig. 6.10 and Fig. 6.11.

The character of curves' fluctuations for SG liquid level fraction, as well as fluid mass flow rates, is similar. Considering operation stability, the fluid mass flow rate reaches its stable value of 597 kg/s for pulse operation and the value of 578 kg/s for dwell time, what shows a difference of ~2.5% between simulated data.

## 6.6 Simulation of temporal evolution of heat flow in PCS PH-SG-SH modules

The simulation of heat flow requires the knowledge of temperature distribution in pre-heater, steam generator and super-heater. For this purpose, temperature difference sensors are introduced into the model, shown in Fig. 6.14. Every sensor represents a device that determines the temperature difference, measured between two points without drawing any heat.

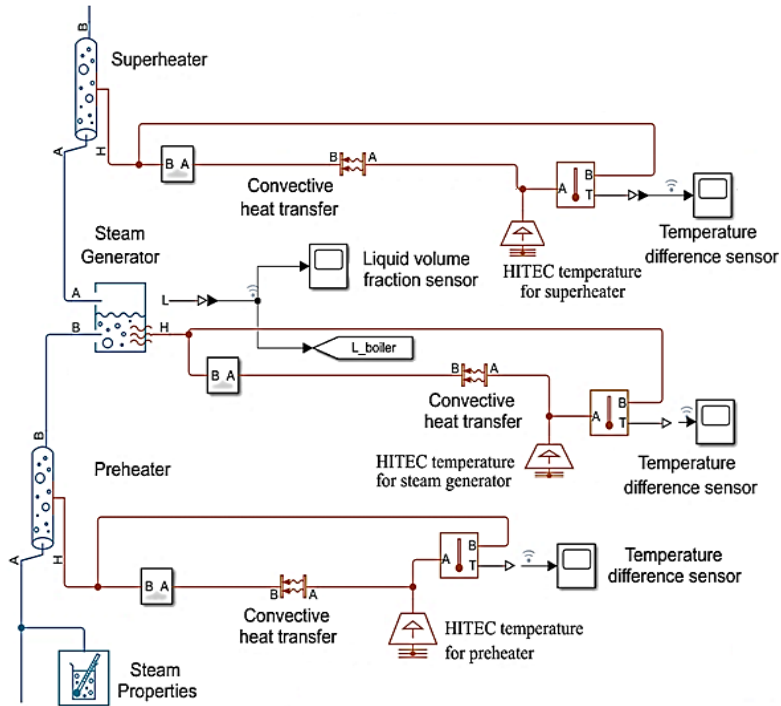


Fig. 6.14: Schema of DEMO PCS PH-SG-SH module with temperature difference sensors.

Thermal conserving port A is associated with sensor positive probe, while port B is associated with sensor negative probe. Ports A and B connect two points, where the allocated temperature is monitored. In our case, positive direction is determined from port A to port B. Port T is a signal port that outputs the temperature difference calculated as  $\Delta T = T_A - T_B$ .

For pulse operation, the results of simulation of temporal evolution of temperature difference in PCS PH-SG-SH module are presented in Fig. 6.15.

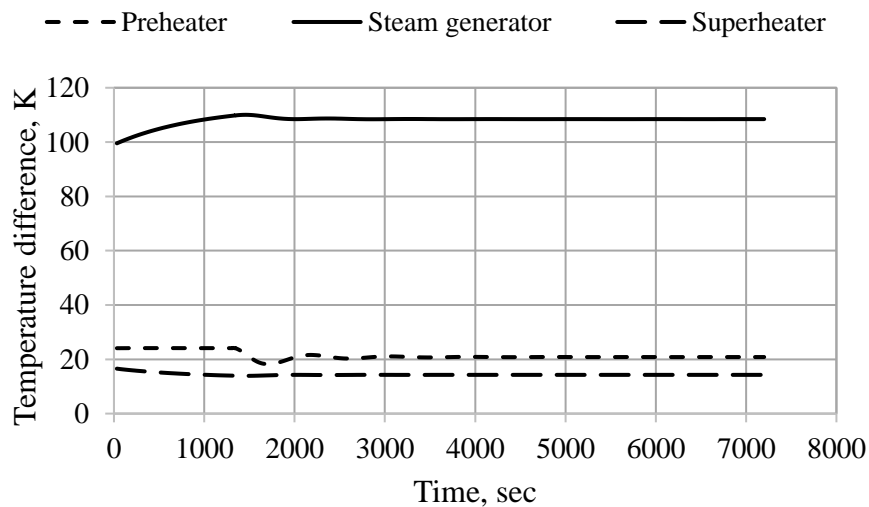


Fig 6.15: Temporal evolution of temperature difference in PCS PH-SG-SH module at pulse operation time interval of  $30 \leq t \leq 7200$  sec.



The corresponding simulation curves of temporal evolution of heat flow through pre-heater, steam generator and super-heater are shown in Fig. 6.16. During stable operation, the mean heat flow rates through pre-heater, steam generator and super-heater are 104 MW, 1424 MW and 66 MW, correspondingly. Taking the heat flow rate through SG as reference value, the calculated percentage ratios for heat flow through pre-heater and super-heater are  $\sim 7.3\%$  and  $\sim 4.6\%$ , respectively. During pulse operation, simulated total heat flow rate through PCS PH-SG-SH module is  $\sim 1594$  MW. These data correlate well with heat flow rate of  $\sim 1580$  MW, which is calculated at the outlet of IHTS hot storage tank during pulse operation, see Fig. 6.8.

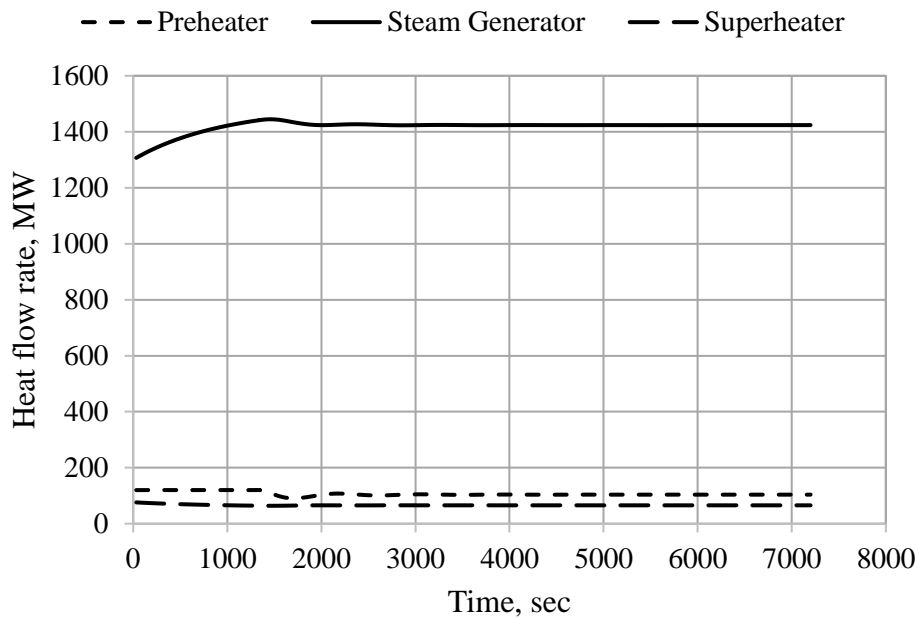


Fig. 6.16: Temporal evolution of heat flow in pre-heater, steam generator and super-heater at pulse operation time interval of  $30 \leq t \leq 7200$  sec.

The results of simulation of temporal evolution of heat flow in PCS SG for pulse and dwell operation are presented in Fig. 6.17. The diagram for pulse operation includes the data for time interval between  $30 < t \leq 7200$  sec. The diagram for dwell operation includes the data for time interval between  $7200 < t \leq 7800$  sec. For the first 30 sec, which assume the start of simulated dwell time for the first operation cycle, constant heat flow rate corresponds to the value simulated for pulse operation time at  $t_{sim} = 7200$  sec. During pulse operation, see Fig. 6.16, taking stable operation conditions, the heat flow rate is  $\sim 1424$  MW. During dwell operation, the curve tends to attain its stable heat flow rate with the value of  $\sim 1373$  MW, which differs with 3.6% from the value of heat flow rate at the end of pulse operation time.

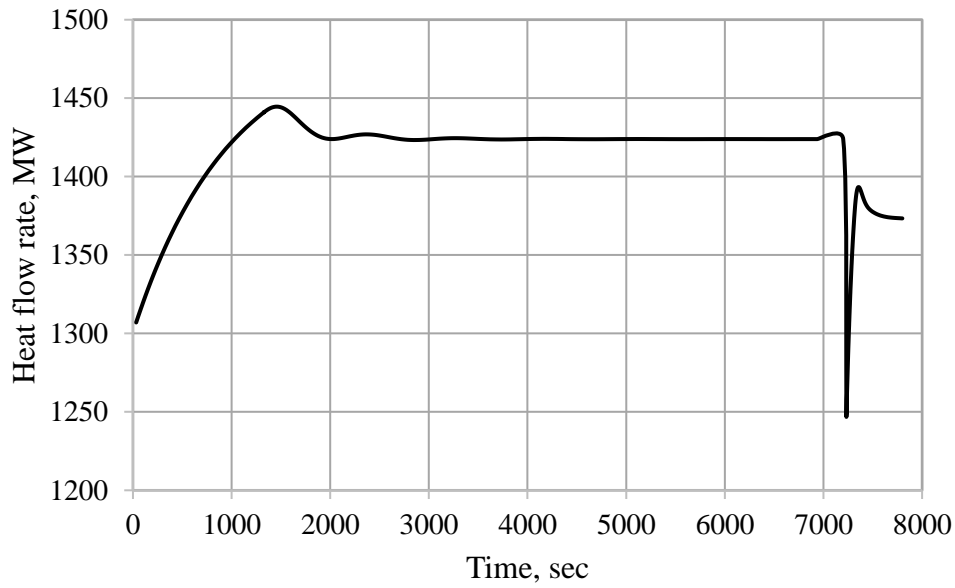


Fig. 6.17: Temporal evolution of heat flow in PCS SG.

### 6.7 Simulation of temporal evolution of DEMO PCS mechanical power

The simulations are carried out for mechanical power output downstream HP and LP steam turbines during pulse and dwell operation. The results are presented in Fig. 6.18 in form of a joint diagram.

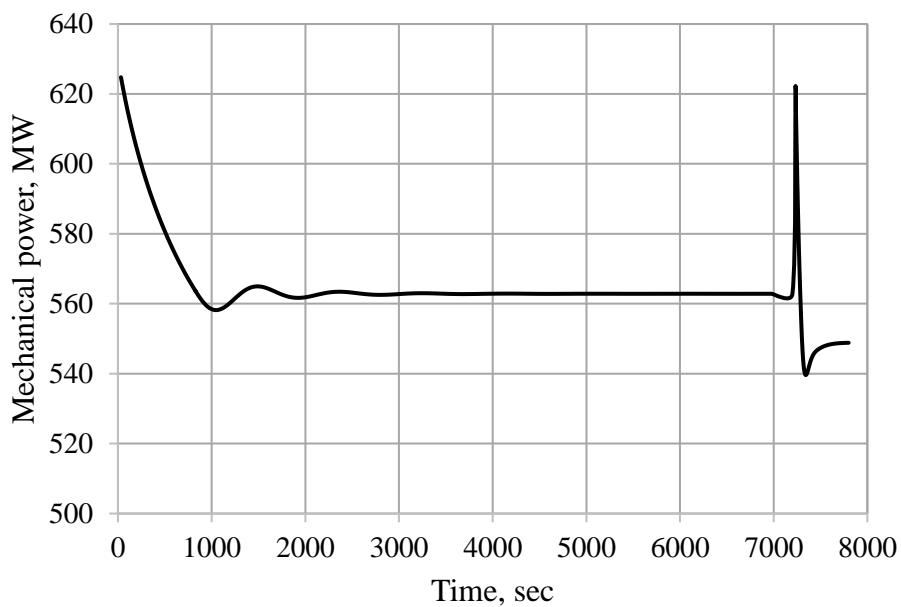


Fig. 6.18: Temporal evolution of mechanical power output downstream the HP and LP steam turbines.

The curves are joined, showing the results without start-up phase of first 30 sec. At the beginning of dwell operation, constant mechanical power output is equal to the value of simulated one for pulse operation at 7200 sec. The curves for pulse and dwell operation show similar dynamics in their temporal evolution like the curves for PCS SG liquid volume fraction (Fig. 6.10 and Fig. 6.11) and heat flow (Fig. 6.17). Mechanical power increases at the beginning of simulations. Afterwards follow the fluctuations and, at the end, the stabilization is reached. Regarding pulse operation, after regressive fluctuations, mechanical power is stabilized after ~2200 sec at value of ~563 MW. For dwell operation, it stabilizes after ~370 sec at the value of ~548 MW. The difference between the values for pulse and dwell operation lies around 2.7%.

The thermal efficiency can be defined by the equation

$$\eta_{\text{therm}} = \frac{\dot{W}_{\text{turb,mech}}}{\dot{Q}_{\text{in}}}. \quad (6.7)$$

In our case, having  $\dot{W}_{\text{turb,mech}} = 563$  MW (see Fig. 6.18) and  $\dot{Q}_{\text{in}} = 1594$  MW (see Fig. 6.16), the thermal efficiency of  $\eta_{\text{therm}} \approx 0.354$  is calculated, what corresponds well to thermal efficiency of ~0.35 for Rankine Cycle (see ref. [225]), taken as reference MATLAB<sup>®</sup> Library model, see Appendix A.7.

## 6.8 Evaluation of the results of numerical simulations

### 6.8.1 Verification of simulation data for DEMO PHTS-IHTS model

The results of simulations using MATLAB<sup>®</sup>/Simulink are evaluated and verified through comparison with data of quasi-stationary simulations, using EBSILON<sup>®</sup> [51, 98, 99, 101]. The comparative analysis is feasible due to application of similar DEMO BoP ICD concept, with the usage of two tank DEMO IHTS, as well as similarity of most DEMO BoP design and operational parameters, which are applied for simulation models as initial data.

In the simulation models, a single operation cycle for fusion reactor lasts for 7800 sec, e.g. 7200 sec for pulse operation and 600 sec for dwell operation. During pulse operation, molten salt is accumulated in hot storage tank. During dwell operation, MS is pumped through DEMO PCS HXs into cold storage tank, ensuring stable operation of DEMO BoP.

In simulations with EBSILON<sup>®</sup>, HITEC<sup>XL</sup> molten salt has been used [99], whereas in simulations using MATLAB<sup>®</sup>/Simulink, HITEC molten salt is applied. Even though HITEC<sup>XL</sup> and HITEC have rather similar properties, the chemical composition differs between the salts.

For running of simulations with EBSILON<sup>®</sup>, constant molten salt specific heat capacity of  $c_p = 1.56167 \text{ kJ}/(\text{kg}\cdot\text{K})$  is taken [98]. In simulations using MATLAB<sup>®</sup>/Simulink, HITEC specific heat capacity is a temperature dependent parameter. In simulations with EBSILON<sup>®</sup>, for DEMO IHTS pumps stable operation modus is assumed during pulse operation time of 7200 sec. In MATLAB<sup>®</sup>/Simulink model, for pulse operation, the time interval of 6880 sec is considered for stable operation of DEMO IHTS pumps, see Fig. 6.6.

The simulation with EBSILON<sup>®</sup> shows molten salt flow rate of  $\dot{m}_{\text{part } 1} = 708 \text{ kg/s}$ , which remains in hot storage tank during pulse operation. Hence, the total mass of molten salt, which is accumulated in hot storage tank during pulse operation, is  $m_E = 5097600 \text{ kg}$ . Using MATLAB<sup>®</sup>/Simulink, the mean MS mass flow rate, which remains in hot storage tank, is  $\dot{m}_{\text{part } 1} = 740 \text{ kg/s}$  and the total mass of HITEC, which is accumulated during time interval of 6680 sec, is  $m = 5091200 \text{ kg}$ . For MATLAB<sup>®</sup>/Simulink model, the analysis of the results of simulation (see Fig. 6.6) shows two time intervals, which are characterized by change of MS mass flow rates through DEMO IHTS pumps: 0-160 sec and 7040-7200 sec, respectively. In time interval of 0-160 sec, at the beginning of simulations, the stabilization of MS mass flow rate through the pumps takes place. The results of dynamic simulations indicate that only after  $\sim 145 \text{ sec}$  MS mass flow rate through the pump 1 overcomes the threshold of 5920 kg/s, what is equal to outlet mass flow rate from hot storage tank. In this case, the mass of molten salt, which is accumulated in hot storage tank during time interval of 145-160 sec, is amounted to  $\sim 5300 \text{ kg}$ . Hence, for time interval of 0-7040 sec, the accumulated mass of molten salt in hot storage tank is  $m_{\text{MS}} \approx 5096500 \text{ kg}$ . During simulated time interval of 7040-7200 sec, due to quick increase in MS mass flow through pump 2 and quick decrease in MS flow through pump 1, after 7040 sec the income of MS mass into hot storage tank is rather small. Thus, for accumulated MS mass, the comparison of the data, which are simulated using EBSILON<sup>®</sup> ( $m_E = 5097600 \text{ kg}$ ), as well as through MATLAB<sup>®</sup>/Simulink ( $m_{\text{MS}} \approx 5096500 \text{ kg}$ ), shows a difference of  $\sim 0.02\%$  between the values, without considering MS mass, which is accumulated in hot storage tank during operation time interval of 7040-7200 sec.

The simulations, using MATLAB<sup>®</sup>/Simulink, show the change of MS mass flow rates through the pumps during the transience from pulse to dwell operation. The mass flow rate in pump 1 decreases from 6660 kg/s to 418 kg/s, obtaining a reduction of  $\sim 93.7\%$ . The rising MS mass flow rate from 5920 kg/s to 8120 kg/s in pump 2 is not so pronounced, having a difference of  $\sim 37.2\%$ . In upcoming cycle, during pulse operation, the mass flow rate through pump 1 quickly increases from 418 kg/s to 6660 kg/s and in pump 2 it decreases from 7840 kg/s to 5920 kg/s.

The results of dynamic simulations using MATLAB<sup>®</sup>/Simulink indicate that from the point of view of control, as well as regulation of MS mass flow rates through the pumps during transient time intervals, pump 1 is operated at more detrimental conditions than pump 2. Hence, the big difference between minimum and maximum HITEC mass flow rates could be critical for pumps' long-term stable operation.

For time interval of 7201-7800 sec (see Fig. 6.2), the simulations display that at the beginning of dwell operation, HITEC mass flow rate at outlet of hot storage tank reaches the value of 8120 kg/s. Later, MS mass flow rate through the pump 2 continuously decreases, reaching the end value of 7840 kg/s at 7800 sec. Assuming, on the one hand, HITEC mean mass flow rate of 7980 kg/s during dwell operation, this value corresponds to pumped MS mass of  $m_1 = 4788000$  kg. On the other hand, the simulations (see Fig. 6.4) show that if a linearly increase of mass flow rate through pump 2 from 5980 kg/s to 8120 kg/s is supposed for time interval of 7155-7200 sec, the mean value of 7050 kg/s for MS mass flow rate could be estimated. Multiplying this value with time frame of ~45 sec, the value of pumped MS mass of  $m_2 = 317250$  kg is obtained. Adding  $m_1$  and  $m_2$ , the calculated molten salt total mass reaches the value of  $m_{total} = 5105250$  kg, which differs with ~0.17% from the simulated values of  $m_{MS}$  and  $m_E$ , respectively.

At the beginning, the volume of molten salt in hot storage tank has to ensure the stability of DEMO IHTS operation. The simulations show that for stable operation, even before start-up, molten salt needs to be redistributed between cold and hot storage tanks. This is important in order to ensure the pumping rate of 5920 kg/s through the pump 2 during pulse operation up to time of ~145 sec, when MS mass flow rate in pump 1 is lower than in pump 2.

The dynamic simulations of heat losses to environment, see chapter 4, §4.4, indicate that the time for molten salt cooling, until HITEC reaches its critical temperature, depends on storage tank geometry, thermal insulation properties, as well as operating temperature and mass of molten salt, which is stored in the tank. The redistribution of molten salt inside the storage tanks decreases the time of MS cooling, until HITEC reaches crystallization point. Therefore, the application of electrical heat tracing for DEMO IHTS thermal storage tanks, pipelines and auxiliary equipment is mandatory before and during the start-up time, during maintenance service of DEMO IHTS, as well as in any other case, when fusion reactor is out of operation.

Assuming molten salt mass flow rate of  $\dot{m} = 6660$  kg/s, MS temperature of  $T_1 = 543$  K and specific heat capacity of  $c_p = 1430$  J/(kg·K) at the inlet of PHTS-IHTS HXs, MS temperature of  $T_2 = 738$  K and specific heat capacity of  $c_p = 1225$  J/(kg·K) at the outlet of PHTS-IHTS HXs,

with a difference of  $\Delta T = T_2 - T_1 = 195$  K, the simulated energy flow rates reach the values of  $\dot{E}_{T_1} \approx 1.857$  GW and  $\dot{E}_{T_2} \approx 1.675$  GW, correspondingly. Taking into consideration the linear dependence of HITEC  $c_p(T)$  on MS temperature, the mean value of energy flow rate to hot storage tank can be calculated as  $\dot{E}_{\text{mean}} = \frac{\dot{E}_{T_1} + \dot{E}_{T_2}}{2} \approx 1.766$  GW, what corresponds well to the simulation data, presented in Fig. 6.8.

The numerical simulations show that, assuming a constant HITEC mass flow rate and specific heat capacity  $c_p$  as a temperature dependent parameter, the simulated heat flow rate decreases from inlet to outlet of DEMO IHTS HXs. This means that in future, if HITEC molten salt should be used in DEMO IHTS, an extended experimental study of molten salt properties has to be carried out before taking any final decisions. If other functional correlations have to be selected for numerical simulation of HITEC thermo-physical properties, this would change the simulated values of molten salt mass and heat flow rates, even though the simulation model of DEMO IHTS system would remain unchangeable.

If to assume, that MS specific heat capacity at inlet of DEMO IHTS HXs is  $c_p \approx 1560$  J/(kg·K) (see Table 2.3) and remains constant with increase in MS temperature, the energy flow rate of  $\dot{E} \approx 2.026$  GW to hot storage tank can be estimated. These data appropriate to the value of  $\dot{E} \approx 2.104$  GW, calculated through EBSILON® (see Appendix A.2).

Taking into consideration any kind of possible heat losses in SDHT modules and the change of energy transfer rate regarding temperature dependence of molten salt specific heat capacity, the efficiency of energy transfer between DEMO PHTS and DEMO IHTS can be calculated as

$$\eta_{\text{IHTS}} = \frac{\dot{E}_{\text{IHTS}}}{\dot{E}_{\text{PHTS}}} = \frac{1.76 \text{ GW}}{2.1 \text{ GW}} \approx 0.838. \quad (6.8)$$

During pulse operation, the accumulation of molten salt in hot storage tank (see Fig. 6.8) results in heat flow rate of  $\dot{E}_{\text{PCS}} \approx 1.58$  GW towards DEMO PCS. In this case, the efficiency of heat transfer is calculated as

$$\eta_{\text{PCS}} = \frac{\dot{E}_{\text{PCS}}}{\dot{E}_{\text{IHTS}}} \approx 0.9. \quad (6.9)$$

Coming to MATLAB®/Simulink simulation model, the energy flow rate to DEMO PCS can be specified as

$$\dot{E}_{\text{PCS}} = \eta_{\text{IHTS}} \cdot \eta_{\text{PCS}} \cdot \dot{Q}_{\text{PHTS}} \approx 0.75 \cdot \dot{Q}_{\text{PHTS}}. \quad (6.10)$$

According to eq. (6.10), it is possible to state that ~75% of heat flow is transferred from DEMO PHTS to DEMO PCS, considering the calculated thermal efficiency of DEMO IHTS and DEMO PCS systems, using equations (6.8) and (6.9).

### **6.8.2 Verification of simulation data for DEMO PCS model**

Regarding MATLAB®/Simulink model for DEMO PCS system, a single SG stage with one pre-heater and one super-heater is used. The EBSILON® model uses an additional SG stage with a supplemental pre-heater and super-heater, as well as secondary heat sources, such as deaerator and further PCS pumps.

In EBSILON® numerical code, the steam generator is modelled as a shell-and-tube heat exchanger. In MATLAB®/Simulink, the steam generator is modelled as a chamber with fixed volume of two-phase fluid.

According to simulation with EBSILON®, fixed data are given for stable operation period, which lasts for 7200 sec for pulse and 600 sec for dwell operation. For simulation using MATLAB®/Simulink, the following time intervals are taken into consideration: i)  $t_{sim} = 30$  sec since beginning of simulation, at the time where strong fluctuations of curves are finished, see Fig. 6.12 and Fig. 6.13, ii) time interval, when DEMO PCS system is in stable operation.

Referring to simulation data, the fluid mass flow rates during DEMO PCS stable operation are lower than the data for  $t_{sim} = 30$  sec, especially, at the beginning of simulations ( $t < 30$  sec), when strong fluctuations are observed.

For simulations using MATLAB®/Simulink, the data from process control sensors S1 and S3 (Fig. 5.8) are used. Sensor S1 is positioned upstream the pre-heater module and sensor S3 is installed at the outlet of LP steam turbine. According to the simulation using MATLAB®/Simulink for pulse operation at  $t_{sim} = 30$  sec, the value for fluid mass flow rate at located sensor S1 is 710 kg/s (see Fig. 5.8), whereas fluid mass flow rate, simulated with EBSILON®, is 719 kg/s [84]. The difference between these values lies within ~1.3%. MATLAB®/Simulink shows for located sensor S3 at  $t_{sim} = 30$  sec the steam mass flow rate of 660 kg/s. The fluid mass flow rate, simulated with EBSILON®, is 667 kg/s. The difference of about 1% is observed between these simulated data.

For DEMO PCS stable operation time (see Fig. 6.12), the simulations using MATLAB®/Simulink show the fluid mass flow rate of 597 kg/s, what is lower than the value of 719 kg/s, which is simulated with EBSILON®. Referring to control sensor S3, the steam mass flow rate is 597 kg/s for simulation using MATLAB®/Simulink. The value of 667 kg/s is obtained for mass flow rate downstream HP and LP steam turbine through simulation with EBSILON®. The reason for such difference between the results using MATLAB®/Simulink and EBSILON® can be the adjusting of the solver, as well as modelling boundary and running conditions, and the constellation of simulation models.

Regarding sensor S1 for dwell operation at  $t_{sim} = 30$  sec, the value of  $\sim 710$  kg/s using MATLAB®/Simulink, is lower in comparison to the value of  $\sim 821$  kg/s, attained with EBSILON®. However, for control sensor S1 the values above 800 kg/s are observed during time interval at  $t_{sim} < 30$  sec. As for control sensor S3 at  $t_{sim} = 30$  sec, the fluid mass flow rate of 655 kg/s for MATLAB®/Simulink correlates well with the value of 638 kg/s, obtained with EBSILON®. The value of 638 kg/s is attained (see Fig. 6.12) after  $t_{sim} = 30$  sec. For DEMO PCS stable operation, the value of fluid mass flow rate using MATLAB®/Simulink model remains at level of 578 kg/s with a difference of  $\sim 9.4\%$  in comparison with the value of 638 kg/s, which is calculated with EBSILON®.

The simulation data for “DEMO 1990, EBSILON® code” model, calculated for HP steam turbine pressure of 110 bar, show thermal efficiency of  $\eta_{therm} \approx 0.368$ . The data for “DEMO HCPB 2019, EBSILON® code” model, calculated for HP steam turbine pressure of 121 bar, give thermal efficiency of  $\eta_{therm} \approx 0.361$ . Using MATLAB®/Simulink (see Fig. 6.18), the calculation of thermal efficiency at HP steam turbine pressure of 121 bar provides the value of  $\eta_{therm} \approx 0.354$ , showing a good correlation between these results.

According to simulation data, see Fig. 6.16, the pre-heater and super-heater can ensure a supplementary heat transfer of 170 MW. Assuming DEMO PCS thermal efficiency of  $\eta_{therm} \approx 0.354$ , from heat input of 170 MW a mechanical power gain of  $\sim 60$  MW can be expected. If additional pre-heater and super-heater are applied, then this can increase the thermal power output during pulse operation from  $P_{mech,1} \approx 671$  MW up to  $P_{mech,2} \approx 731$  MW according to EBSILON® model [84]. Considering the generator coupling efficiency of 95%, according to ref. [59], the active power output of  $\sim 695$  MW can be achieved at electrical generator level. With a deviation of  $\sim 7.3\%$ , for pulse operation period these results correlate



well with the value of  $\sim 750$  MW, obtained through the quasi-stationary simulations with EBSILON<sup>®</sup>, see Appendix A.6, Table A6.

Using eq. (6.10), the subsequent equation follows

$$P_{\text{mech}} = \eta_{\text{therm}} \cdot \eta_{\text{IH\textsubscript{TS}}} \cdot \eta_{\text{PCS}} \cdot \dot{Q}_{\text{PHTS}}. \quad (6.11)$$

Hence, the mechanical power is  $P_{\text{mech}} \approx 0.266 \cdot \dot{Q}_{\text{PHTS}}$ , reaching the value of  $P_{\text{mech}} \approx 559$  MW, whereby MS thermo-physical parameters are temperature dependent functions. If HITEC specific heat capacity of  $c_p = 1560$  J/(kg·K) is constant, then the thermal efficiency  $\eta_{\text{IH\textsubscript{TS}}}$  can increase from  $\sim 0.838$  up to  $\sim 0.993$ . In this case, the mechanical power  $P_{\text{mech}}$  can rise from  $P_{\text{mech}} \approx 559$  MW to  $P_{\text{mech}} \approx 662$  MW. With a deviation of  $\sim 1.48\%$ , the last value correlates well with literature survey data, see ref. [40], where the nominal power of  $\sim 675$  MW downstream the steam turbines is estimated for DEMO FPP, see Appendix A.1.

## 6.9 Conclusions

The simulations of temporal evolution of HITEC filling level in DEMO IHTS thermal storage tanks are carried out for single and multi-cycling operation of fusion reactor. HITEC filling level in cold and hot storage tanks depends on temperature expansion of molten salt, those results of simulations correlating well with temperature evolution of molten salt density.

The simulations of heat flow show that at the beginning a corresponding time span is necessary for stabilization of pumps' operation. Afterwards, DEMO IHTS pumps operate stable, without any visible fluctuations. The transition from pulse to dwell and from dwell to pulse is characterized by obliged change of MS pumping rates.

The increase in HITEC mass flow rate during dwell operation through PCS SG stage results in increased heat flow rates through PCS PH-SG-SH modules. The transition from dwell to pulse is characterized by a short-term decrease in heat transfer due to change of MS mass flow rate in pump 1.

At the beginning of simulations, liquid volume fraction in DEMO PCS steam generator fluctuates regressively between minimum and maximum values. The stabilization of the curve for steam generator is observed for pulse operation after ~3000 sec. The fluctuation time increases with growing operation pressure, both for pulse and dwell operation. The analysis of the curves for temporal evolution of fluid mass flow confirms the curves' fluctuations at the beginning of simulations, both for pulse and dwell operation.

The results of simulations of temporal evolution of mechanical power output downstream HP and LP steam turbines indicate firstly the fluctuations at the beginning of simulations, followed by stabilization of simulated parameter.

The results of simulations using MATLAB®/Simulink are evaluated and verified through the comparison with the data, obtained through the quasi-stationary simulations using EBSILON®. The possibility for verification is based on the similarity of most design and operational parameters of DEMO PHTS, IHTS and PCS, used as initial data for simulation models. A good agreement between the data for simulations using MATLAB®/Simulink and EBSILON® is confirmed.

## 7 Simulation model of DEMO BoP energy transfer chain

### 7.1 Development of simulation model for DEMO BoP energy transfer chain

The content of forthcoming paragraph is dedicated to the solution of final task of the thesis, which is directed to the development of simulation model for the study of transient behaviour of DEMO BoP energy transfer chain. The objective sketch of the model is presented in Fig. 7.1.

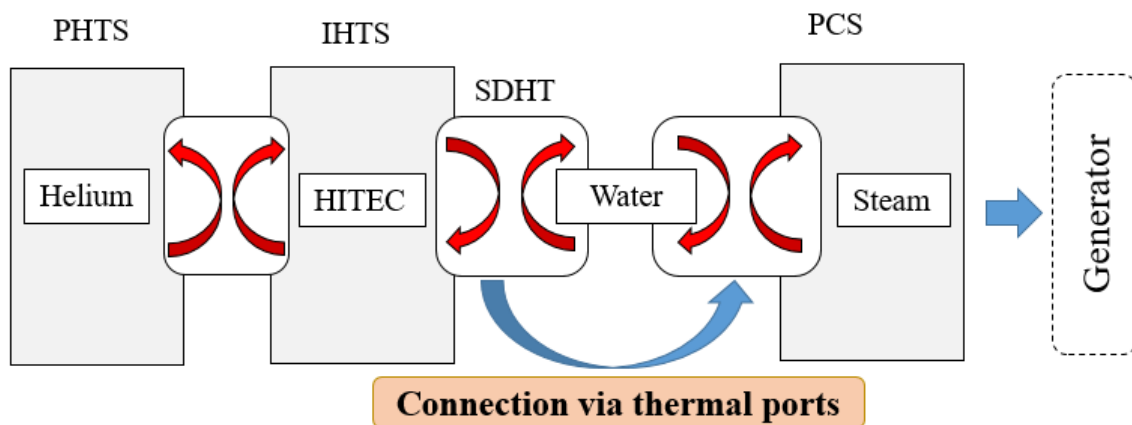


Fig. 7.1: Sketch of the model for DEMO BoP energy transfer chain.

In the DEMO PHTS HXs, the heat transfer takes place between hot helium and HITEC molten salt, which circulates through DEMO IHTS system. In DEMO PCS SG stage, the heat transfer occurs between hot molten salt and water. Vapour circulates through the steam turbines, which are connected to generators, being used for generation of electrical power.

Regarding MATLAB<sup>®</sup>/Simulink Library, there is no module, in which heat transfer is simulated between three phases simultaneously, especially between HITEC molten salt, water and steam. Hence, for modelling of DEMO BoP energy transfer chain, an approach is proposed, which assumes the coupling of DEMO IHTS and DEMO PCS models through corresponding thermal ports.

Schematically, the simulation model for the study of transient behaviour of DEMO BoP energy transfer chain is shown in Fig. 7.2. In the model, the 1<sup>st</sup> step of heat transfer takes place between hot helium and HITEC molten salt in PHTS-IHTS HXs. The 2<sup>nd</sup> step includes the heat transfer between hot molten salt and water in IHTS-PCS HXs. The 3<sup>rd</sup> step assumes the heat transfer in PCS PH-SG-SH modules between water and vapor.

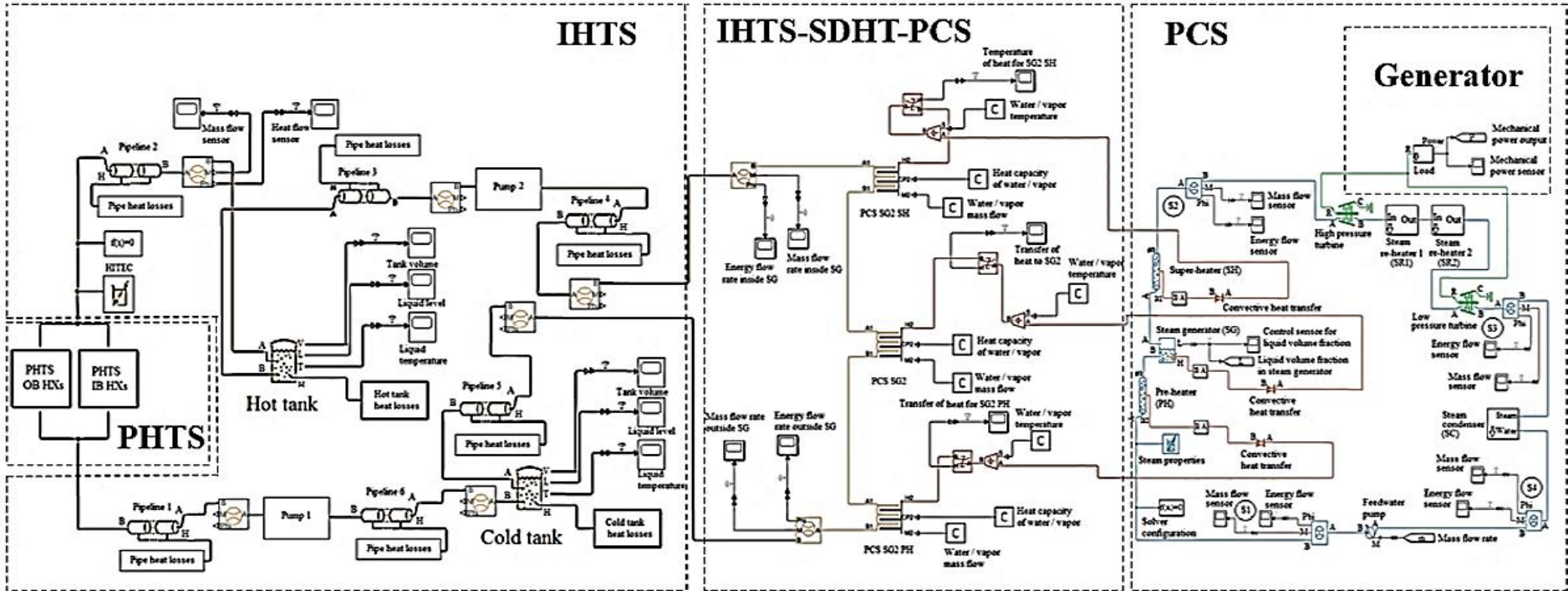


Fig. 7.2: Simulation model for DEMO BoP energy transfer chain.

Afterwards, the vapor flows into steam turbines, whereas the energy of vapor flow is transformed into mechanical energy. The developed model includes DEMO PHTS-IHTS model, an intermediate Specific Dissipation Heat Transfer (SDHT) module and DEMO PCS model. In DEMO PCS model, the previous temperature sources, as heat input to PCS PH-SG-SH, are eliminated. They are substituted with coupling through thermal ports. Only one solver block is used, namely the customized module for simulation of HITEC thermo-physical properties. The properties of water/steam are considered as constant values.

The temporal evolution of heat flow in PCS PH-SG-SH modules for time interval over two operation cycles is shown in Fig. 7.3. The Fig. 7.4 gives the detail view to the simulation curves for transient time interval between first and second operation cycles of fusion reactor. The decrease in heat flow rates during time interval of 5 sec, i.e. between 7865-7870 sec, occurs due to simulation algorithm, discussed in ref. [225], which assumes simultaneous quick increase in MS mass flow rate through pump 1 and quick decrease in MS mass flow rate through pump 2 at the beginning of each pulse operation cycle.

The results of previous simulations (see chapter 6) allow the calculation of thermal efficiency for DEMO PHTS-IHTS and DEMO PCS systems. However, the prediction of total thermal efficiency of DEMO BoP energy transfer chain (see Fig.7.2) demands the knowledge of heat efficiency  $\eta_{SDHT}$  for intermediate SDHT module, which is applied.

For stable operation conditions without PH and SH modules, the heat flow rate through PCS SG is ~660 MW (see Fig. 7.4). Considering DEMO PCS system itself, the heat flow rate through PCS SG without PH and SH modules (see Fig. 6.16) is 1424 MW. Hence, according to the results of simulations, the heat efficiency for SDHT module has to be  $\eta_{SDHT} \approx 0.463$ .

Taking into consideration the eq. (6.11) and Fig. 7.2, for the DEMO BoP energy transfer chain the mechanical power can be calculated as

$$P_{mech} = \eta_{therm} \cdot \eta_{IHTS} \cdot \eta_{SDHT} \cdot \eta_{PCS} \cdot \dot{Q}_{PHTS}. \quad (7.1)$$

According to eq. (7.1), the mechanical power output is  $P_{mech} \approx 0.123 \cdot \dot{Q}_{PHTS}$ .

Consequently, for  $\dot{Q}_{PHTS} \approx 2.1$  GW the value of mechanical power output is  $P_{mech} \approx 260$  MW. So, the usage of an intermediate SDHT module between DEMO IHTS and DEMO PCS models (see Fig. 7.2) results in decreasing simulated heat flow rates.

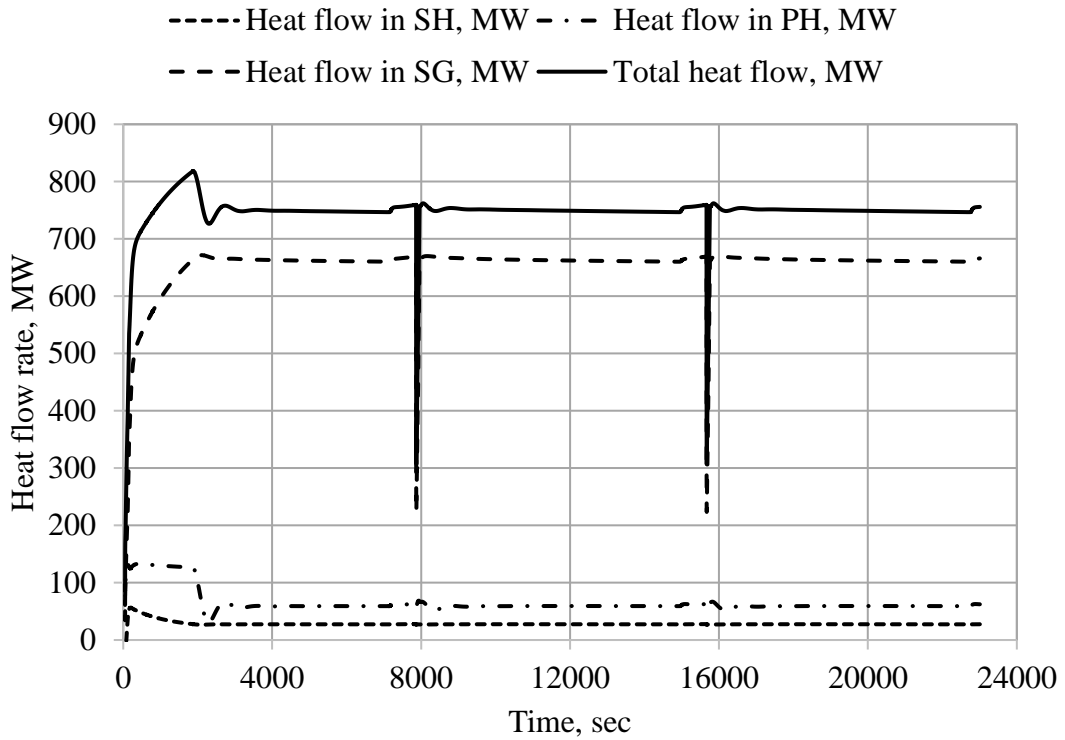


Fig. 7.3: Temporal evolution of heat flow in a single PCS steam generator stage with PH-SG-SH modules for two operation cycles of fusion reactor.

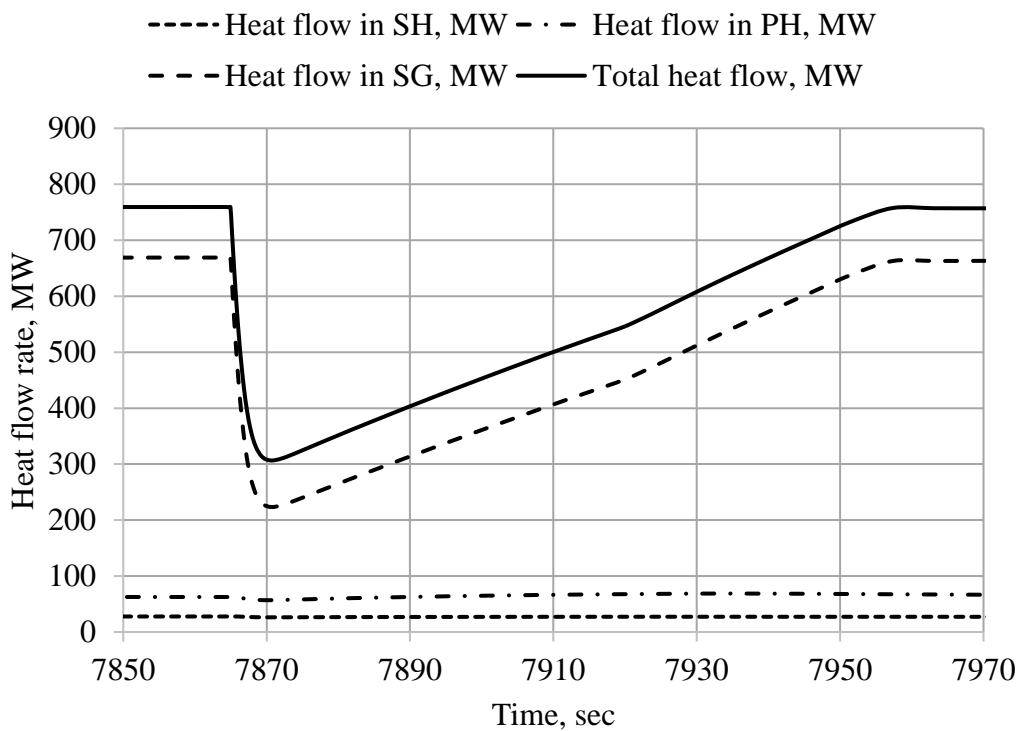


Fig. 7.4: Temporal evolution of heat flow in PCS PH-SG-SH stage for transition between the 1<sup>st</sup> and 2<sup>nd</sup> operation cycle of fusion reactor.

For DEMO BoP energy transfer chain, the results of simulation for temporal evolution of mechanical power output downstream DEMO PCS system are shown in Fig. 7.5. The obtained data demonstrate a small increase in simulated parameter during dwell operation, related with increase in heat transfer to DEMO PCS by rising mass flow rate of HITEC molten salt, which is pumped through pump 2 during time interval of 600 sec.

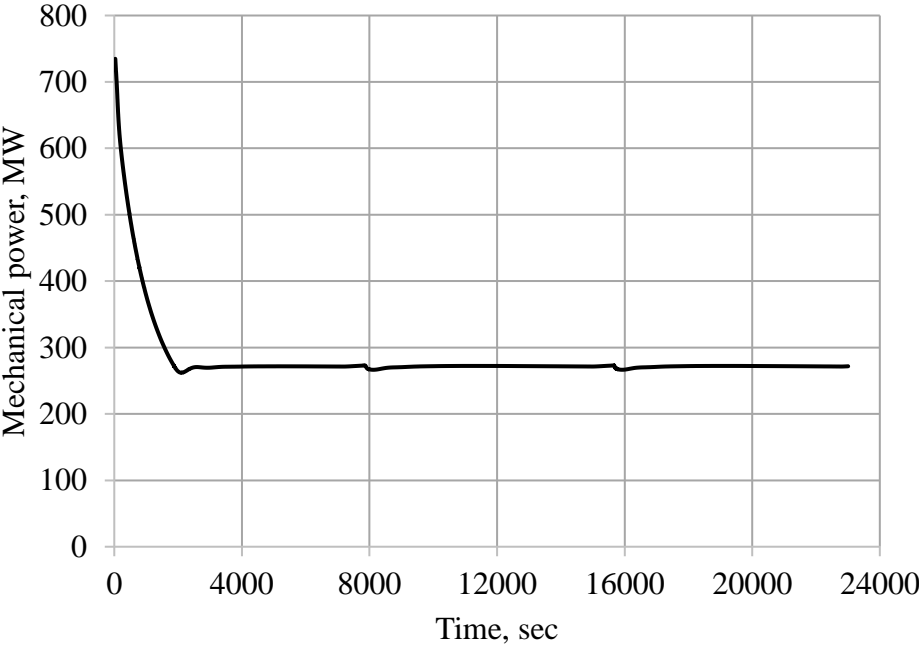


Fig. 7.5: Temporal evolution of mechanical power output.

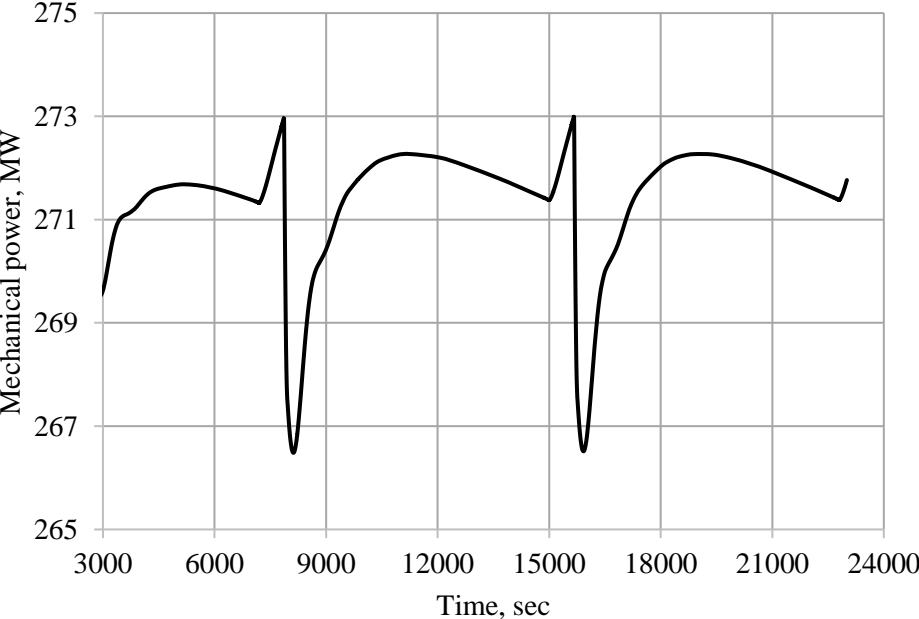


Fig. 7.6: Temporal evolution of mechanical power output, DEMO BoP stable operation.

According to Fig. 7.6, for stable operation conditions ( $t > 3000$  sec), the simulated mean value of mechanical power output is  $\sim 272$  MW. With deviation of  $\sim 4.4\%$ , this result correlates well with the data, which are calculated using eq. (7.1). The use of DEMO IHTS enhances the operation stability of DEMO BoP energy transfer chain, permitting the decrease in peak-to-peak difference for heat flow rates and mechanical power output during the transience between pulse-to dwell and dwell-to-pulse (see Fig. 7.6). The use of DEMO IHTS should ensure stable operation of steam turbines, which are connected to electrical generators. The achieved power deviations below 3% (see Fig. 7.6) are acceptable for steam turbine operation.

The time-dependent simulations give the opportunity for evaluation of DEMO BoP parameters, in order to process the optimization in terms of power change rates. That is necessary, for instance, to restart the power generation machines with a black start capacity from TOKAMAK shutdown, without the supply from external electrical grid.

## **7.2 Coupling of DEMOnstration Fusion Power Plant to external electrical grid**

Despite the fact, that the interface of Fusion Power Plant with external electrical grid is outside the frame of simulation study, it is essential to highlight here some prospective tasks.

By coupling to European high voltage electrical grid, DEMO FPP should be able to produce and distribute electrical power throughout Europe [38, 41, 60], expected in range around 700-800 MW [57, 59]. The internal power demand of the power plant is expected in the range around 300-500 MW. Hence, the power system needs to include an electrical switchyard (see Fig. 1.3), through which DEMO FPP will receive and deliver power to two 400 kV transmission lines.

According to total peak active pulsed power demand, DEMO FPP needs to be located in a very well interconnected node of EU electrical grid, characterized by a high short-circuit power system. An in-and-out connection needs to be performed with implementation of a new station on an existing transmission line.

The operation stability of DEMO FPP is essential for integration into the external electrical grid. The interface of DEMO FPP with the electrical grid requires the knowledge of technical, economic, and environmental performance data of DEMOnstration Fusion Power Plant, to ensure real-time energy supply and demand balance [60, 229, 230].



The sufficient data-base needs to be available for an entire continental European network, to investigate the dynamic behaviour and stability of transmission system and its interactions in the European interconnected system [11].

For coupling of DEMO FPP to electrical grid, the operation stability of power generators is a decisive point. Here, the steady-state stability relates to response of synchronous machine to a gradually increasing load [229, 231].

The plant control system needs to be operated in estimated regime and deviations need to be early detected with plant operation software [50]. A reactive power compensation system has to ensure the reactive power, which is absorbed from the grid and has not to exceed the level imposed by Electrical Transmission System Operator. Getting proper operation, DEMO FPP has to fulfil ENTSO-E requirements for grid connection of generators [57]. The most restrictive value here is the power control capability of 10%.

Ensuring stable operation of electrical grid, the maintenance of frequency stability is a key prerequisite [11, 57]. Here, an effective way is to use the operation of Frequency Sensitive Mode for Power Generating Module, in which the power output changes in response to a change in system frequency.

The system needs to react effectively to different kinds of faults, defined as any failures that interfere with normal current flow to the load [231-240]. The sudden output interruptions are limitation factors for the interface to the grid [72]. Hence, the more renewable and nuclear sources are linked to the electrical grid, the greater disturbance the grid might experience upon a sudden output interruption of DEMOnstration Fusion Power Plant.

### **7.3 Conclusions**

The statements, which are directed towards the dynamic simulations, are followed by the development of simulation model for the study of transient behaviour of DEMO BoP energy transfer chain.

The simulation model of DEMO BoP energy transfer chain is realized, using MATLAB<sup>®</sup>/Simulink, by means of coupling of DEMO PHTS-IHTS model with DEMO PCS model through thermal ports.

The results of simulations, which are focused on temporal evolution of mechanical power output downstream DEMO PCS steam turbines for pulse and dwell operation of fusion reactor, correlate well with the results of quasi-stationary simulations and with the data from literature survey.

The obtained results confirm the ability of MATLAB<sup>®</sup>/Simulink simulation model to predict the temporal evolution of mass and energy flows in DEMO BoP during the transient fusion reactor operation.

The results of dynamic simulations using MATLAB<sup>®</sup>/Simulink can be applied for prospective integration of DEMO FPP into the European electrical grid, being in line with purpose of whole EUROfusion roadmap, whereas EU-DEMO should be modelled as a real power plant prototype.

## 8 Summary and outlook

### 8.1 Summary

In the framework of formulated objectives and tasks, the scope of the thesis, which focuses on the simulation study of transient behaviour of DEMOnstration Balance of Plant energy transfer chain during pulse and dwell operation of fusion reactor, is entirely realized.

The novelty of study consists in dynamic simulation using MATLAB<sup>®</sup>/Simulink, which is applied for the first time for numerical study of temporal evolution of mass and heat flows in primary DEMO BoP systems. The simulation model of DEMO BoP energy transfer chain begins with DEMO PHTS heat exchangers and ends at the outlet of DEMO PCS steam turbines.

The MATLAB<sup>®</sup>/Simulink Library standard as well as novel customized modules are applied for model development, involving corresponding governing equations and assumptions.

For dynamic simulations, the design and operational parameters of DEMO Primary Heat Transfer System, Intermediate Heat Transfer and Storage System as well as Power Conversion System are analyzed and systematized.

The novelty is the use of HITEC molten salt in DEMO IHTS as both heat transfer fluid and sensible thermal energy storage medium. HITEC thermo-physical properties, as well as molten salt chemical and thermal stability and its compatibility with constructive materials, are reviewed through extended literature survey.

A set of analytical correlations is selected for numerical simulation of HITEC thermo-physical properties for defined DEMO IHTS operating temperatures. A novel customized MATLAB<sup>®</sup> module for simulation of HITEC thermo-physical parameters is developed and applied.

Further novelty positions include the development of simulation model for heat losses to environment from DEMO IHTS thermal storage tanks and pipelines. The thermal storage tank is described as a thermal liquid container with variable fluid volume.

Next novelty comprise the development of simulation models of heat and mass transfer in DEMO BoP systems, as well as of simulation model for DEMO BoP energy transfer chain, which implies the coupling of DEMO PHTS-IHTS and PCS models through thermal ports.

The simulation model of DEMO IHTS system includes PHTS-IHTS heat exchangers, thermal storage tanks with corresponding pipelines, two fixed-displacement pumps and PCS heat

exchangers. The simulation model of DEMO PCS system is based on MATLAB<sup>®</sup> Rankine Cycle model, though it differs by modelling of PCS steam generator as a two-phase fluid constant volume chamber and through modelling of PCS pre-heater, super-heater as well as re-heaters as two-phase fluid pipes.

In the thesis, following results of simulation study are discussed:

- Temperature dependency of HITEC molten salt thermo-physical parameters.
- Sensitivity of HITEC simulated parameters on operating temperature.
- Interplay between thermal storage tank geometry and HITEC filling level.
- Impact of tank height and thermal insulation thickness on heat losses to environment.

The simulated thermo-physical parameters of HITEC molten salt are decreasing functions with rising MS temperature. The increase in temperature results in thermal expansion of molten salt, what has to be considered for design and safe operation of DEMO IHTS thermal storage tanks.

The temporal evolution of following parameters is simulated:

- HITEC filling level in cold and hot storage tanks.
- Mass and heat flows in DEMO PHTS-IHTS system.
- Liquid volume fraction in DEMO PCS steam generator.
- Mass and heat flows in DEMO PCS during pulse/dwell operation of fusion reactor.
- Mechanical power output downstream HP and LP steam turbines.
- Heat flow and mechanical power output for DEMO BoP energy transfer chain.

The simulated MS filling level for cold and hot storage tanks correlates well with temperature evolution of HITEC density. The results of simulations of heat flow show that a corresponding time span is required for stabilization of pumps' operation. Afterwards, DEMO IHTS pumps operate stable without visible mass flow rate fluctuations. Increase in HITEC mass flow rate during dwell operation results in rising heat flow rate through PCS PH-SG-SH modules. At the beginning of simulations, the liquid volume fraction in PCS SG fluctuates regressively between minimum and maximum values. Both for pulse and dwell operation, the fluctuation time increases with growing operation pressure. The simulation of temporal evolution of fluid mass flows shows similar fluctuation characteristics of the curves at the beginning of simulations, both for pulse and dwell operation. Regarding mechanical power output, the results of simulations indicate regressing fluctuations, followed by the curve stabilization. The stabilization period for mechanical power during dwell operation is shorter in comparison to the pulse one.

The results of the study shows that, due to lack of data concerning experimental studies with DEMO IHTS storage tanks, the validation of developed MATLAB®/Simulink simulation model for heat losses to environment is not suitable.

In the thesis, the results of MATLAB®/Simulink simulation of heat losses to environment from DEMO IHTS cold and hot storage tanks are evaluated through comparison with known data from literature survey. The main argument for evaluation is the similarity of models' constellation, which is used for description of heat losses from thermal storage tanks to environment.

The results of simulations of mass and heat flows in DEMO PHTS-IHTS and DEMO PCS systems, using MATLAB®/Simulink, are verified by comparison with numerical data for quasi-stationary simulation of DEMO BoP via EBSILON® code. The opportunity for evaluation is based on the similarity of most design and operational parameters of DEMO PHTS-IHTS and DEMO PCS systems, which are used as initial data in the simulation models.

The evaluation of the results of simulations confirms the ability of MATLAB®/Simulink simulation model:

- To predict heat losses from DEMO IHTS thermal storage tanks to environment.
- To study temporal evolution of mass and heat flows in DEMO PHTS-IHTS and DEMO PCS systems.
- To study temporal evolution of mechanical power output downstream DEMO PCS steam turbines.
- To simulate transient behaviour of DEMOnstration Balance of Plant energy transfer chain during pulse and dwell operation of fusion reactor.

## 8.2 Outlook

In DEMO IHTS, the switch-on process of the pumps is characterized by steep temperature gradients, as well as by temporally reduction in thermal power. Thus, the modelling of thermal processes in the pumps and auxiliary units defines the next generation of tasks.

The simulation of MS heat tracing is out of frame of the study. However, the modelling of supplemental auxiliary systems is necessary for power plant safe operation and for holding HTF temperature above the freezing point inside the pipelines and thermal storage tanks.

The next task can include the management of energy supply for heating of HITEC molten salt, as well as water/steam to avoid pinch point problem for pre-heater and super-heater.

In the developed simulation model, constant environment conditions are considered. However, real weather changings, which differ from the simulated stationary ambient conditions, has to be in focus of forthcoming studies.

The subsequent task can involve the development of the regulation and process control procedures, paying attention to prospective modelling of smoothing start-up and shutdown processes.

Getting to forthcoming research issues, the simulation model can be extended with:

- Customized MATLAB<sup>®</sup> modules, which simulate the heat transfer between three phases, namely HITEC molten salt, water and steam.
- Customized MATLAB<sup>®</sup>/Simulink modules for simulation of supplemental DEMO BoP systems' auxiliary equipment.
- Simulation model for auxiliary electric power generation system, what is favourable for integration of the developed simulation model of DEMO BoP energy transfer chain into the prospective hybrid model of multi-modal energy system.

## References

- [1] World Energy Scenarios. 2016. World Energy Council. The Grand Transition Summary Report. ISBN 978-0-946121-57-1, 28 p. [https://www.worldenergy.org/assets/downloads/World-Energy-Scenarios-2016\\_Summary-Report.pdf](https://www.worldenergy.org/assets/downloads/World-Energy-Scenarios-2016_Summary-Report.pdf) (valid on 16.11.2023)
- [2] World Energy Scenarios. 2019. World Energy Council. The Future of Nuclear: Diverse Harmonies in the Energy Transition Report. Published by the World Energy Council, 66 p. [https://www.worldenergy.org/assets/downloads/Nuclear\\_Scenarios\\_Report\\_FINAL.pdf](https://www.worldenergy.org/assets/downloads/Nuclear_Scenarios_Report_FINAL.pdf) (valid on 16.11.2023)
- [3] Romanelli, F. et al. 2012. Fusion Electricity. A Roadmap to the Realisation of Fusion Energy, European Fusion Development Agreement. ISBN 978-3-00-040720-8, 75 p. [https://www.euro-fusion.org/fileadmin/user\\_upload/Archive/wp-content/uploads/2013/01/JG12.356-web.pdf](https://www.euro-fusion.org/fileadmin/user_upload/Archive/wp-content/uploads/2013/01/JG12.356-web.pdf) (valid on 16.11.2023)
- [4] Global Energy Transformation. A Roadmap to 2050. 2019. International Renewable Energy Agency. ISBN 978-92-9260-121-8, 52 p. [https://www.irena.org/-/media/Files/IRENA/Agency/Publication/2019/Apr/IRENA\\_Global\\_Energy\\_Transformation\\_2019.pdf?rev=6ea97044a1274c6c8ffe4a116ab17b8f](https://www.irena.org/-/media/Files/IRENA/Agency/Publication/2019/Apr/IRENA_Global_Energy_Transformation_2019.pdf?rev=6ea97044a1274c6c8ffe4a116ab17b8f) (valid on 16.11.2023)
- [5] World Energy Scenarios. 2019. World Energy Council. European Regional Perspectives. Published by the World Energy Council, 76 p. [https://www.worldenergy.org/assets/downloads/European\\_Scenarios\\_FINAL\\_for\\_website\\_v2.pdf](https://www.worldenergy.org/assets/downloads/European_Scenarios_FINAL_for_website_v2.pdf) (valid on 16.11.2023)
- [6] World Energy Issues Monitor. World Energy Council. Global and Regional Perspectives. 2019. Published by the World Energy Council, 44 p. <https://www.worldenergy.org/assets/downloads/3.-World-Energy-Issues-Monitor-2019-Interactive-Executive-Summary.pdf> (valid on 16.11.2023)
- [7] Gi, K., Sano, F., Akimoto, K., Hiwatari, R., Tobita, K. 2020. Potential Contribution of Fusion Power Generation to Low-Carbon Development under the Paris Agreement and Associated Uncertainties. *Energy Strategy Reviews*, Vol. 27, Article No.: 100432, 11 p. <https://doi.org/10.1016/j.esr.2019.100432>
- [8] Energie System 2050: Lösungen für die Energiewende. 2020. Presseinformation 084/2020. Karlsruher Institut für Technologie. [https://www.kit.edu/kit/pi\\_2020\\_084\\_energie-system-2050-losungen-fur-die-energiewende.php](https://www.kit.edu/kit/pi_2020_084_energie-system-2050-losungen-fur-die-energiewende.php) (valid on 16.11.2023)
- [9] Müller, C. et al. 2019. Integrated Planning and Evaluation of Multi-Modal Energy Systems for Decarbonization of Germany. *Energy Procedia*, Vol. 158, p. 3482-2487. <https://doi.org/10.1016/j.egypro.2019.01.923>
- [10] Energy for Germany - Facts. 2018. World Energy Council. Perspectives and Positions in a Global Context. Weltenergierat - Deutschland e.V., 54 p. [https://www.weltenergierat.de/wp-content/uploads/2018/07/83130\\_DNK\\_Energie2018\\_E.pdf](https://www.weltenergierat.de/wp-content/uploads/2018/07/83130_DNK_Energie2018_E.pdf) (valid on 16.11.2023)

- [11] Netzentwicklungsplan Strom 2030. 2019. 2. Entwurf, 238 p. [https://www.netzentwicklungsplan.de/sites/default/files/paragraphs-files/NEP\\_2030\\_V2019\\_2\\_Entwurf\\_Teil1.pdf](https://www.netzentwicklungsplan.de/sites/default/files/paragraphs-files/NEP_2030_V2019_2_Entwurf_Teil1.pdf) (valid on 16.11.2023)
- [12] Gawlick, J., Hamacher, T., Kuhn, P., Pittel, K., Wackerbauer, J. 2020. Szenarien für die bayerische Stromversorgung bis 2040 - Impulse für die Wirtschaftspolitik, ifo-Studie im Auftrag der IHK für München und Oberbayern, 68 p. <https://www.ifo.de/publikationen/2020/monographie-autorenschaft/szenarien-fuer-die-bayerische-stromversorgung-bis-2040> (valid on 16.11.2023)
- [13] Shahbakhsh, A., Nieße, A. 2019. Modeling Multimodal Energy Systems. *at-Automatisierungstechnik*, Vol. 67, Iss. 11, p. 893-903. <https://doi.org/10.1515/auto-2019-0063>
- [14] Jesse, B., Morgenthaler, S., Gilessen, B., Burges, S., Kuckshinrichs, W. 2020. Potential for Optimization in European Power Plant Fleet Operation. *Energies*, Vol. 13, Iss. 3, Article No.: 718, 22 p. <https://doi.org/10.3390/en13030718>
- [15] Sass, S., Faulwasser, T., Hollermann, D. E., Hagenmeyer, V. et al. 2020. Model Compendium, Data and Optimization Benchmarks for Sector-Coupled Energy Systems. *Computers and Chemical Engineering*, Vol. 135, Article No.: 106760, 19 p. <https://doi.org/10.1016/j.compchemeng.2020.106760>
- [16] Wolter, M., Hagenmeyer, V. 2019. Modeling and Control of Multimodal and Hybrid Energy Systems. *at-Automatisierungstechnik*, Vol. 67, Iss. 11, p. 891-892. <https://doi.org/10.1515/auto-2019-0112>
- [17] Jakob, W., González Ordiano, J. Á., Ludwig, N., Mikut, R., Hagenmeyer, V. 2017. Towards Coding Strategies for Forecasting-Based Scheduling in Smart Grids and the Energy Lab 2.0. GECCO '17: Proceedings of the Genetic and Evolutionary Computation Conference Companion, 15-19 July 2017, Berlin, Germany, ISBN 978-1-4503-4939-0, p. 1271-1278. <https://doi.org/10.1145/3067695.3082481>
- [18] Renewable Capacity Statistics. 2019. International Renewable Energy Agency (IRENA). ISBN 978-92-9260-123-2, 60 p. [https://www.irena.org/-/media/Files/IRENA/Agency/Publication/2019/Mar/IRENA\\_RE\\_Capacity\\_Statistics\\_2019.pdf?rev=02227cbaf26144a28138dc87376ec2ba](https://www.irena.org/-/media/Files/IRENA/Agency/Publication/2019/Mar/IRENA_RE_Capacity_Statistics_2019.pdf?rev=02227cbaf26144a28138dc87376ec2ba) (valid on 16.11.2023)
- [19] Helmholtz. Energy System 2050. <https://www.helmholtz.de/en/research/energy/energy-system-2050/> (valid on 16.01.2023)
- [20] Erdmann, A., Çakmak, H. K., Kühnapfel, U., Hagenmeyer, V. 2019. A New Communication Concept for Efficient Configuration of Energy Systems Integration Co-Simulation. Proceedings of 23<sup>rd</sup> Intern. Symp. on Distributed Simulation and Real Time Applications (DS-RT), 7-9 October 2019, Cosenza, Italy, ISBN 978-1-7281-2923-5, 8 p. <https://doi.org/10.1109/DS-RT47707.2019.8958665>



- [21] Çakmak, H. K., Anselm, E., Kyesswa, M., Kühnapfel, U., Hagenmeyer, V. 2019. A New Distributed Co-Simulation Architecture for Multi-Physics Based Energy Systems Integration. *at - Automatisierungstechnik*, Vol. 67, Iss. 11, p. 972-983. <https://doi.org/10.1515/auto-2019-0081>
- [22] Kyesswa, M., Çakmak, H. K., Groll, L., Kühnapfel, U., Hagenmeyer, V. 2019. A Hybrid Analysis Approach for Transient Stability Assessment in Power Systems. Proceedings of IEEE Milan PowerTech, 23-27 June 2019, Milan, Italy, ISBN 978-1-5386-4722-6, 6 p. <https://ieeexplore.ieee.org/stamp/stamp.jsp?tp=&arnumber=8810745>
- [23] Kyesswa, M., Çakmak, H. K., Kühnapfel, U., Hagenmeyer, V. 2017. Generator Model Extension for Higher Accuracy Simulation of Power System Transients in OpenModelica. Proceedings of the 4<sup>th</sup> International Conference on Mathematics and Computers in Sciences and in Industry (MCSI), 24-27 August 2017, Corfu, Greece, ISBN 978-1-5386-2820-1 <https://ieeexplore.ieee.org/stamp/stamp.jsp?tp=&arnumber=8326813>
- [24] Kyesswa, M., Çakmak, H. K., Kühnapfel, U., Hagenmeyer, V. 2018. A Matlab-Based Simulation Tool for the Analysis of Unsymmetrical Power System Transients in Large Networks. Proceedings of the 32<sup>nd</sup> European Conference on Modelling and Simulation, 22-26 May 2018, Wilhelmshaven, Germany, ISSN 2522-2422, 8 p. <https://doi.org/10.7148/2018-0246>
- [25] Kyesswa, M., Çakmak, H. K., Kühnapfel, U., Hagenmeyer, V. 2017. A Matlab-Based Dynamic Simulation Module for Power System Transients Analysis in the eASiMOV Framework. Published in 2017 European Modelling Symposium (EMS), 20-21 November 2017, Manchester, UK, ISSN 2473-3539, 6 p. <https://ieeexplore.ieee.org/stamp/stamp.jsp?tp=&arnumber=8356806>
- [26] Holbein, B., Isele, J., Spatafora, L., Wiegeler, F., Hagenmeyer, V. 2018. Multivalent Neighbourhood Heat Grid Including Power-to-Heat & Shared Storage Concept. Grand Renewable Energy Proceedings 2018, 17-22 June 2018, Yokohama, Japan, Article No.: O-He-1-3, 4 p. [https://www.jstage.jst.go.jp/article/gre/1/0/1\\_311/\\_article](https://www.jstage.jst.go.jp/article/gre/1/0/1_311/_article)
- [27] Erdmann, A., Hagenmeyer, V. 2020. On Verification of Designed Energy Systems Using Distributed Co-simulations. Proceedings of the IEEE/ACM 24<sup>th</sup> International Symposium on Distributed Simulation and Real Time Applications (DS-RT), 14-16 September 2020, Prague, Czech Republic, ISSN 1550-6525, 8 p. <https://doi.org/10.1109/DS-RT50469.2020.9213689>
- [28] ENERGY ATLAS. 2018. Facts and Figures about Renewables in Europe, 56 p. [https://www.boell.de/sites/default/files/energyatlas2018\\_facts-and-figures-renewables-europe.pdf.pdf](https://www.boell.de/sites/default/files/energyatlas2018_facts-and-figures-renewables-europe.pdf.pdf) (valid on 16.11.2023)
- [29] Sheffield, J., Brown, W., Garrett, G., Hilley, J. 2001. A Study of Options for the Deployment of Large Fusion Power Plants. *Fusion Science and Technology*, Vol. 40, Iss. 1, p.1-36. <https://doi.org/10.13182/FST40-1-1>
- [30] Meier, W., Najmabadi, F., Schmidt, J., Sheffield, J. 2002. Role of Fusion Energy in a Sustainable Global Energy Strategy. *Energy & Environment*, Vol. 13, Iss. 4-5, p. 647-665. <https://doi.org/10.1260/095830502320939606>

- [31] Tokimatsu, K., Hondo, H., Ogawa, Y., Okano, K., Yamaji, K., Katsurai, M. 2000. Energy Analysis and Carbon Dioxide Emission of Tokamak Fusion Power Reactors. *Fusions Engineering and Design*, Vol. 48, Iss. 3-4, p. 483-498. [https://doi.org/10.1016/S0920-3796\(00\)00157-5](https://doi.org/10.1016/S0920-3796(00)00157-5)
- [32] Cabal, H., Lechón, Y., Bustreo, C., Graceva, F., Biberacher, M., Ward, D., Dongiovanni, D., Grohnheit, P. E. 2017. Fusion Power in a Future Low Carbon Global Electricity System. *Energy Strategy Reviews*, Vol. 15, p. 1-8. <https://doi.org/10.1016/j.esr.2016.11.002>
- [33] Bologna, M.-V., Bubelis, E., Hering, W. 2021. Parameter Study and Dynamic Simulation of the DEMO Intermediate Heat Transfer and Storage System Design Using MATLAB®/Simulink. *Fusion Engineering and Design*, Vol. 166, Article No.: 112291, 8 p. <https://doi.org/10.1016/j.fusengdes.2021.112291>
- [34] Maisonnier, D., Cook, I., Sardain, P., Andreani, R., Di Pace, L., Forrest, R., Giancarli, L., Hermsmeyer, S., Norajitra, P., Taylor, N., Ward, D. 2005. A Conceptual Study of Commercial Fusion Power Plants. Final Report of the European Fusion Power Conceptual Study, Report No.: EFDA-RP-RE-5.0, Chapter 5, p. 13-15. [https://fire.pppl.gov/eu\\_ppcs\\_full\\_2005.pdf](https://fire.pppl.gov/eu_ppcs_full_2005.pdf)
- [35] Ward, D. J., Cook, I., Lechon, Y., Saez, R. 2005. The Economic Viability of Fusion Power. *Fusion Engineering and Design*, Vol. 75-79, p. 1221-1227. <https://doi.org/10.1016/j.fusengdes.2005.06.160>
- [37] EUROfusion. 2018. European Research Roadmap to the Realization of Fusion Energy. ISBN 978-3-00-061152-0, 76 p. [https://www.eurofusion.org/fileadmin/user\\_upload/EUROfusion/Documents/2018\\_Research\\_roadmap\\_long\\_version\\_01.pdf](https://www.eurofusion.org/fileadmin/user_upload/EUROfusion/Documents/2018_Research_roadmap_long_version_01.pdf) (valid on 16.11.2023)
- [37] Nuclear Fusion Reactors. 2017. Safety and Radiation Protection Considerations for Demonstration Reactors that Follow the ITER Facility. IRSN Report 2017/199, ISSN 2117-7791, 88 p. [https://www.irsn.fr/FR/Larecherche/publications-documentation/collection-ouvrages-IRSN/Documents/ITER-VA\\_web\\_non\\_imprimable.pdf](https://www.irsn.fr/FR/Larecherche/publications-documentation/collection-ouvrages-IRSN/Documents/ITER-VA_web_non_imprimable.pdf)
- [38] Federici, G. et al. 2018. DEMO Design Activity in Europe: Progress and Updates. *Fusion Engineering and Design*, Vol. 136, Part A, p. 729-741. <https://doi.org/10.1016/j.fusengdes.2018.04.001>
- [39] Federici, G. et al. 2016. Overview of the Design Approach and Prioritization of R&D Activities Towards an EU DEMO. *Fusion Engineering and Design*, Vol. 109-111, Part B, p. 1464-1474. <https://doi.org/10.1016/j.fusengdes.2015.11.050>
- [40] Minucci, S., Panella, S., Ciattaglia, S., Falvo, M.C., Lampasi, A. 2020. Electrical Loads and Power Systems for the DEMO Nuclear Fusion Project. *Energies*, Vol. 13, Iss. 9, Article No.: 2269, 21 p. <https://doi.org/10.3390/en13092269>
- [41] Federici, G. et al. 2019. Overview of the DEMO Staged Design Approach in Europe. *Nuclear Fusion*, Vol. 59, No. 6, Article No.: 066013, 25 p. <https://iopscience.iop.org/article/10.1088/1741-4326/ab1178>

- [42] Gliss, C., Ciattaglia, S., Korn, W., Moscato, I. 2018. Initial Layout of DEMO Buildings and Configuration of the Main Plant Systems. *Fusion Engineering and Design*, Vol. 136, Part A, p. 534-539. <https://doi.org/10.1016/j.fusengdes.2018.02.101>
- [43] Jin, X. Z., Carloni, D., Boccaccini, L. V., Stieglitz, R., Pinna, T., Dongiovanni, D. 2015. Preliminary Safety Studies for the DEMO HCPB Blanket Concept. *Fusion Engineering and Design*, Vol. 98-99, p. 2157-2161. <https://doi.org/10.1016/j.fusengdes.2015.01.029>
- [44] Nunnenmann, E., Fischer, U., Stieglitz, R. 2017. Sensitivity and Uncertainty Analysis for the Tritium Breeding Ratio of a DEMO Fusion Reactor with a Helium Cooled Pebble Bed Blanket. *EPJ Web of Conferences*, Vol. 146, Article No.: 09025, 4 p. <https://doi.org/10.1051/epjconf/201714609025>
- [45] Gliss, G., Bachmann, C., Ciattaglia, S., Drumm, B., Gracia Camacho, M., Moscato, I., Mull, T., Palermo, I. 2022. Integrated Design of Tokamak Building Concepts Including Ex-Vessel Maintenance. *Fusion Engineering and Design*, Vol. 177, Article No.: 113068, 10 p. <https://doi.org/10.1016/j.fusengdes.2022.113068>
- [46] Hering, W., Jin, X.Z., Bubelis, E., Perez-Martin, S., Ghidersa, E. B. 2017. Operation of the Helium Cooled DEMO Fusion Power Plant and Related Safety Aspects. Published in *Challengers for Coolants in Fast Neutron Spectrum Systems, IAEA TECDOC Series No. 1912*, ISBN 978-92-0-107820-6, p. 223-229. [https://www-pub.iaea.org/MTCD/Publications/PDF/TE-1912\\_web.pdf](https://www-pub.iaea.org/MTCD/Publications/PDF/TE-1912_web.pdf)
- [47] Barucca, L., Ciattaglia, S., Chantant, M., Del Nevo, A., Hering, W., Martelli, E., Moscato, I. 2018. Status of EU DEMO Heat Transport and Power Conversion Systems. *Fusion Engineering and Design*, Vol. 136, Part B, p. 1557-1566. <https://doi.org/10.1016/j.fusengdes.2018.05.057>
- [48] Ciattaglia, S., Federici, G., Barucca, L., Stieglitz, R., Taylor, N. 2019. EU DEMO Safety and Balance of Plant Design and Operating Requirements. Issues and Possible Solutions. *Fusion Engineering and Design*, Vol. 146, Part B, p. 2184-2188. <https://doi.org/10.1016/j.fusengdes.2019.03.149>
- [49] Bubelis, E., Hering, W., Perez-Martin, S. 2018. Industry Supported Improved Design of DEMO BoP for HCPB BB Concept with Energy Storage System. 30<sup>th</sup> International Symposium on Fusion Technology (SOFT 2018), 16-21 September 2018, Giardini Naxos, Italy, Book of Abstracts, Contribution ID.: 48, 1 p. <https://publikationen.bibliothek.kit.edu/1000085673>
- [50] Barucca, L. et al. 2021. Pre-Conceptual Design of EU DEMO Balance of Plant Systems: Objectives and Challenges. *Fusion Engineering and Design*, Vol. 169, Article No.: 112504. <https://doi.org/10.1016/j.fusengdes.2021.112504>
- [51] Hering, W., Bubelis, E., Perez-Martin, S. 2020. HCPB PHTS & BOP Indirect Coupling Option - Design Description Documents. Final Report on Deliverable HCPB PHTS & BOP Overview ICD (Indirect Coupling Option), Ref. No.: BOP-2.1-T034, IDM-Link: EFDA\_D\_2MSD7D.

- [52] Bubelis, E., Hering, W., Perez-Martin, S. 2018. Conceptual Designs of PHTS, ESS and PCS for DEMO BoP with Helium Cooled BB Concept. *Fusion Engineering and Design*, Vol. 136, Part A, p. 367-371, <https://doi.org/10.1016/j.fusengdes.2018.02.040>
- [53] Bubelis, E., Hering, W., Perez-Martin, S. 2019. Industry Supported Improved Design of DEMO BoP for HCPB BB Concept with Energy Storage System. *Fusion Engineering and Design*, Vol. 146, Part B, p. 2334-2337. <https://doi.org/10.1016/j.fusengdes.2019.03.183>
- [54] Hesch, K., Boccaccini, L.V., Stieglitz, R. 2018. Blankets - Key Element of a Fusion Reactor - Functions, Design and Present State of Development. *Kerntechnik*, Vol. 83, No. 3, p. 241-250. <https://doi.org/10.3139/124.110923>
- [55] Hering, W., Bubelis, E., Perez-Martin, S., Bologna, M.-V. 2021. Overview of Thermal Hydraulic Optimization and Verification for the EU-DEMO HCPB BOP ICD Variant. *Energies*, Vol. 14, Article No.: 7894, 13 p. <https://doi.org/10.3390/en14237894>
- [56] Hering, W., Perez-Martin, S., Bubelis, E. 2020. HCPB PHTS & PCS Rationale for the Selection of the Variant. Final Report, Report No.: BOP-2.1-T060-D001, IDM-Link: EFDA\_D\_2NMYYY.
- [57] Ciattaglia, S., Falvo, M. C., Lampasi, A., Proietti Cosimi, M. 2020. Energy Analysis for the Connection of the Nuclear Reactor DEMO to the European Electrical Grid. *Energies*, Vol.13, Iss. 9, Article No.: 2157, 19 p. <https://doi.org/10.3390/en13092157>
- [58] Malinowski, L., Lewandowska, M., Bubelis, E., Hering, W. 2020. Design and Analysis of the Secondary Circuit of the DEMO Fusion Power Plant for the HCPB BB Option without the Energy Storage System and with the Auxiliary Boiler. *Fusion Engineering and Design*, Vol. 160, Article No.: 112003. <https://doi.org/10.1016/j.fusengdes.2020.112003>
- [59] Minucci, S., Panella, S., Ciattaglia, S., Falvo, M. C., Lampasi, A. 2020. Electrical Loads and Power Systems for the DEMO Nuclear Fusion Project. *Energies*, Vol. 13, Iss. 9, Article No.: 2269, 23 p. <https://doi.org/10.3390/en13092269>
- [60] Ciattaglia, S., Federici, G., Lampasi, A., Minucci, S., Barucca, L., Moscato, I. 2017. The European DEMO Fusion Reactor: Design Status and Challenges from Balance of Plant Point of View. Proceedings of the 2017 IEEE International Conference on Environment and Electrical Engineering and 2017 IEEE Industrial and Commercial Power Systems Europe (EEEIC/I&CPS Europe), 06-09 June 2017, Milan, Italy, ISBN 978-1-5386-3917-7, 6 p. <https://doi.org/10.1109/EEEIC.2017.7977853>
- [61] Barucca, L. et al. 2022. Maturation of Critical Technologies for the DEMO Balance of Plant Systems. *Fusion Engineering and Design*, Vol. 179, Article No.: 113096, 16 p. <https://doi.org/10.1016/j.fusengdes.2022.113096>
- [62] Federici, G., Biel, W., Gilbert, M. R., Kemp, R., Taylor, N., Wenninger, R. 2017. European DEMO Design Strategy and Consequences for Materials. *Nuclear Fusion*, Vol. 57, No. 9, Article No.: 092002, 26 p. <https://doi.org/10.1088/1741-4326/57/9/092002>

- [63] Moscato, I., Barucca, L., Ciattaglia, S., Di Maio, P. A. 2019. On the Thermal Dynamic Behaviour of the Helium-Cooled DEMO Fusion Reactor. *Journal of Physics: Conf. Series*, Vol. 1224, Article No.: 012033, 13 p. <https://iopscience.iop.org/article/10.1088/1742-6596/1224/1/012033>
- [64] Hernandez, F. A. et al. 2017. Overview of the HCPB Research Activities in EUROfusion. *IEEE Transactions on Plasma Science*, Vol. 46, No. 6, p. 2247-2261. <https://doi.org/10.5445/IR/1000076732>
- [65] Hernandez, F. A., Pereslavtsev, P., Kang, Q., Norajitra, P., Kiss B., Nádas, G., Bitz, O. 2017. A New HCPB Breeding Blanket for the EU DEMO: Evolution, Rationale and Preliminary Performances. *Fusion Engineering and Design*, Vol. 124, p. 882-886. <https://www.sciencedirect.com/science/article/pii/S0920379617300911>
- [66] Bereruelo, I. F. 2016. Analysis of Availability, Functional Integration and Remote Maintenance for the Design of Critical Components and Systems in Nuclear Fusion Technology. Doctoral Thesis, Departamento de Energia, Universidad de Oviedo, 470 p. [http://www-fusion.ciemat.es/PhDThesis/Fernandez\\_Berceruelo.pdf](http://www-fusion.ciemat.es/PhDThesis/Fernandez_Berceruelo.pdf)
- [67] Spagnuolo, G. A. 2020. Integrated Multi-Physics Design Tool for Fusion Breeding Blanket Systems - Development and Validation. Doctoral Thesis, Department of Mechanical Engineering, Karlsruhe Institute of Technology, 183 p. <https://publikationen.bibliothek.kit.edu/1000123701>
- [68] Arp, V. D., McCarty, R. D., Friend, D. G. 1998. Thermalphysical Properties of Helium-4 from 0.8 to 1500 K with Pressures to 2000 MPa. NIST Technical Note 1334 (Revised), National Institute of Standards and Technology, U.S. Government Printing Office, Washington, DC 20402-9325, 158 p. <https://archive.org/details/thermalphysicalpr1334arpv/page/n3/mode/2up>
- [69] Tarallo, A. 2020. Model Description (Indirect Coupling Option). EUROfusion Report No.: BOP-2.1-T037-D007: HCPB PCS CAD, EFDA\_D\_2P7ASJ.
- [70] Bender, A., Gil Pascual, S., Sommer, H. 2018. DEMO Balance of Plant - Conceptual Design of a Molten Salt Steam Generator. Kraftanlagen Heidelberg GmbH, Technical Notes Doc. No.: BoP-0010\_DN.
- [71] Reddy, R.G. et al. 2013. Novel Molten Salts Thermal Energy Storage for Concentrating Solar Power Generation. US Department of Energy, Final Scientific/Technical Report, Contract No.: DE-FG36-08GO18153, 57 p. <https://www.osti.gov/servlets/purl/1111584/>
- [72] Herrmann, U., Kearney, D. W. 2002. Survey of Thermal Energy Storage for Parabolic Trough Power Plants. *Journal of Solar Energy Engineering*, Vol. 124, Iss. 2, p. 145-152. <https://doi.org/10.1115/1.1467601>
- [73] Flueckiger, S.M., Yang, Z., Garimella, S.V. 2013. Design of Molten-Salt Thermocline Tanks for Solar Thermal Energy Storage. *Heat Transfer Engineering*, Vol. 34, Iss. 10, p. 787-800. <https://core.ac.uk/download/pdf/10241087.pdf>

- [74] Fernandes, D., Pitie, F., Careres, G., Baeyens, J. 2012. Thermal Energy Storage: How Previous Findings Determine Current Research Priorities. *Energy*, Vol. 39, Iss. 1, p. 246-257. <https://doi.org/10.1016/j.energy.2012.01.024>
- [75] Dinçer, I., Rosen, M.A. 2010. Thermal Energy Storage, Systems and Applications. John Wiley&Sons, ISBN 978-0-470-74706-3, New York, 620 p. <https://www.researchgate.net/file.PostFileLoader.html?id=574d5d57f7b67eba9d4c929f&assetKey=AS:367742109667328@1464687959319>
- [76] Gil, A., Medrano, M., Martorell, I., Lozano, A., Dolado, P., Zalba, B., Cabeza, L.F. 2010. State of the Art on High Temperature Thermal Energy Storage for Power Generation. Part 1. Concepts, Materials and Modellization. *Renewable and Sustainable Energy Reviews*, Vol. 14, Iss. 1, p. 31-55. <https://doi.org/10.1016/j.rser.2009.07.035>
- [77] Kuravi, S., Trahan, J., Goswami, D.Y., Rahman, M. M., Stefanokos, E. K. 2013. Thermal Energy Storage Technologies and Systems for Concentrating Solar Power Plants. *Progress in Energy and Combustion Science*, Vol. 39, Iss. 4, p. 285-319. <https://doi.org/10.1016/j.pecs.2013.02.001>
- [78] Nithyanandam, K., Pitchumani, R. 2014. Cost and Performance Analysis of Concentrating Solar Power Systems with Integrated Latent Thermal Energy Storage. *Energy*, Vol. 64, p. 793-810. <https://doi.org/10.1016/j.energy.2013.10.095>
- [79] Manenti, F., Ravaghi-Ardebili, Z. 2013. Dynamic Simulation of Concentrating Solar Power Plant and Two-Tanks Direct Thermal Energy Storage. *Energy*, Vol. 55, p. 89-97. <https://doi.org/10.1016/j.energy.2013.02.001>
- [80] Stieglitz, R., Heinzl, V. 2012. Thermische Solarenergie, Kapitel 1: Energiebedarf (p. 1-21) / Kapitel 8: Energiespeicher (p. 595-635), Springer Verlag, Berlin, ISBN 9783642294754. <https://www.springer.com/gp/book/9783642294747>
- [81] Valmiki, M.M., Karaki, W., Li, P., Lew, J. T. V., Chan, C. L., Stephens, J. 2012. Experimental Investigation of Thermal Storage Processes in a Thermocline Tank. *Journal of Solar Energy Engineering*, Vol. 134, Iss. 4, Article No.: 041003, 9 p. <https://doi.org/10.1115/1.4006962>
- [82] Ravaghi-Ardebili, Z., Manenti, F., Corbetta, M., Lima, N. M. N., Lilan, L. Z., Papisidero, D. 2013. Assessment of Direct Thermal Energy Storage Technologies for Concentrating Solar Power Plant. *Chemical Engineering Transactions*, Vol. 35, p. 547-552. <https://doi.org/10.3303/CET1335091>
- [83] Flueckiger, S., Yang, Z., Garimella, S. V. 2011. An Integrated Thermal and Mechanical Investigation of Molten-Salt Thermocline Energy Storage. *Applied Energy*, Vol. 88, Iss. 6, p. 2098-2105. <https://doi.org/10.1016/j.apenergy.2010.12.031>
- [84] Bubelis, E., Hering, W. 2019. DEMO 16 Sectors: HCPB BB FW Cooled in Series with BZ & Plant Configuration with IHTS+ESS - Conceptual Designs and Sizing of PHTS, IHTS, ESS and PCS Components. Report No.: BOP-2.1-T022.

- [85] Herrmann, U., Kelly, B., Price, H. 2004. Two-Tank Molten Salt Storage for Parabolic Trough Solar Power Plants. *Energy*, Vol. 29, Iss. 5-6, p. 883-893. [https://doi.org/10.1016/S0360-5442\(03\)00193-2](https://doi.org/10.1016/S0360-5442(03)00193-2)
- [86] Zavoico, A. B. 2001. Solar Power Tower: Design Basis Document, San Francisco, California, Report No.: SAND2001-2100, 148 p. <https://www.osti.gov/biblio/786629-solar-power-tower-design-basis-document-revision>
- [87] Flesch, J., Niedermeier, K., Fritsch, A., Musaeva, D., Marocco, L., Uhlig, R., Baake, E., Buck, R., Wetzell, T. 2017. Liquid Metals for Solar Power Systems. *IOP Conference Series / Materials Science and Engineering*, Vol. 228, Article No.: 012012, 15 p. <https://doi.org/10.1088/1757-899X/228/1/012012>
- [88] Libby, C. 2010. Solar Thermal Storage Systems: Preliminary Design Study. Electric Power Research Institute, Palo-Alto, California, USA, Report No.: 1019581, 188 p. <https://www.epri.com/research/products/1019581>
- [89] McMahan, A. C. 2006. Design and Optimization of Organic Rankine Cycle Solar-Thermal Power Plants. Master Thesis, University of Wisconsin-Madison, USA, 216 p. <https://minds.wisconsin.edu/handle/1793/7889>
- [90] Mawire, A., McPherson, M. 2008. Experimental and Simulated Temperature Distribution of an Oil-Pebble Bed Thermal Energy Storage System with a Variable Heat Source. *Applied Thermal Engineering*, Vol. 29, Iss. 5-6, p. 1086-1095. <https://doi.org/10.1016/j.applthermaleng.2008.05.028>
- [91] Bousselamti, L., Cherkaoui, M. 2019. Modelling and Assessing the Performance of Hybrid PV-CSP Plants in Morocco: A Parametric Study. *International Journal of Photoenergy*, Vol. 2019, Article ID.: 5783927, p. 1-15. <https://doi.org/10.1155/2019/5783927>
- [92] Ruegamer, T., Kamp, H., Kuckelkorn, T., Schiel, W., Weinrebe, G., Nava, P., Riffelmann, K., Richert, T. 2014. Molten Salt for Parabolic Trough Applications: System Simulation and Scale Effects. *Energy Procedia*, Vol. 49, p. 1523-1532. <https://doi.org/10.1016/j.egypro.2014.03.161>
- [93] Riffelmann, K., Richert, T., Nava, P., Schweitzer, A. 2014. Ultimate Trough - A Significant Step towards Cost Competitive CSP. *Energy Procedia*, Vol. 49, p. 1831-1839. <https://doi.org/10.1016/j.egypro.2014.03.194>
- [94] Reilly, H. R., Kolb, G. 2001. An Evaluation of Molten-Salt Power Towers Including Results of the Solar Two Project. Solar Thermal Technology Department, Sandia National Laboratories, Report No.: SAND2001-3674, 99 p. <https://www.osti.gov/servlets/purl/791898>
- [95] Roman, C., Fireteanu, V., Etay, J., Fautrelle, Y. 2011. An Overview on Solar Energy, Molten Salts and Electromagnetic Pumping Technologies. Proceedings of the 10<sup>th</sup> International Conference on Environment and Electrical Engineering, 08-11 May 2011, Rome, Italy, ISBN 978-1-4244-8782-0, 4 p. <https://ieeexplore.ieee.org/stamp/stamp.jsp?tp=&arnumber=5874692>

- [96] Cavallaro, F. 2010. Fuzzy TOPSIS Approach for Assessing Thermal-Energy Storage in Concentrated Solar Power (CSP) Systems. *Applied Energy*, Vol. 87, Iss. 2, p. 496-503. <https://doi.org/10.1016/j.apenergy.2009.07.009>
- [97] Roviro, A., Sanchez, C., Montes, M.J., Munoz, M. 2019. DEMO 16 Sectors, HCPB BB FW Cooled in Series with BZ and Plant Configuration with IHTS+ESS: BOP Preliminary Evaluation of Cost. WPBOP Deliverable Report No.: BOP-3.1-T011-D001.
- [98] Roviro, A., Bubelis E., Hering, W. 2019. DEMO 16 sectors - HCPB BB PHTS Preliminary Design in the Plant Configuration with IHTS+ESS - FW Cooled in Series with BZ. WPBOP Deliverable Report No.: BOP-2.1-T023-D001
- [99] Bubelis, E., Hering, W. 2017. Conceptual Designs of PHTS, ESS and PCS Components for DEMO BoP with Helium Cooled BB Concept. Deliverable INR Report No.: 01/17-FUSION 491.
- [100] Bubelis, E., Hering, W. 2018. Deliverable DEMO HCPB BB with FW Cooled in Series with BZ & Plant Configuration with IHTS+ESS - Conceptual Designs and Sizing of PHTS, IHTS, ESS and PCS Components. Internal INR Report No.: 02/18 - FUSION 493.
- [101] Bubelis, E., Hering, W. 2018. DEMO Configuration with IHTS + ESS - HCPB BB FW Cooled in Series with BZ Option. DIV PHTS Preliminary Design. Deliverable Report No.: BOP-2.1-T011-D001.
- [102] Klee, H., Allen, R. 2017. Simulation of Dynamic Systems with MATLAB and Simulink. 3<sup>rd</sup> Ed., CRC Press, ISBN 978-1498787772, 821 p. <https://de.mathworks.com/academia/books/simulation-of-dynamic-systems-with-matlab-and-simulink-klee.html>
- [103] Heilmann, P. 2012. Evaluation, Neuentwicklung und Optimierung des Eigenschaftsprofils von Salzschnmelzen für die Verwendung als Wärmeträgerfluide. Dissertation, eingereicht im Fachbereich C - Mathematik und Naturwissenschaften der Bergischen Universität Wuppertal, 157 p. <https://d-nb.info/1046902768/34>
- [104] Picard, G., Flament, T., Tremillon, B., Saint-Paul, P., Spiteri, P. 1985. Process for Stabilizing a Mixture of Molten Alkali Metal Nitrates and Alkali Metal Nitrites Usable Particularly as a Heat Transfer Fluid Stabilized Mixture Thus Obtained, US Patent No.: 4559993, Data: 24.12.1985. <https://depatisnet.dpma.de/DepatisNet/depatisnet?action=pdf&docid=US000004559993A&xxfull=1>
- [105] Flamant, G., Gauthier, D., Benoit, H., Sans, J.-L., Boissière, B., Ansart, R., Hemati, M. 2014. A New Heat Transfer Fluid for Concentrating Solar Systems: Particle Flow in Tubes. *Energy Procedia*, Vol. 49, p. 617-626. <https://doi.org/10.1016/j.egypro.2014.03.067>
- [106] Fritsch, A. 2018. Potenzialanalyse von Solarturmkraftwerken mit Flüssigmetallen als Wärmeträgermedium. Dissertation, Fakultät für Maschinenwesen, Rheinisch-Westfälischen Technischen Hochschule Aachen, ISBN 978-3-8325-4724-0, 268 p. <https://doi.org/10.18154/RWTH-2018-226448>



- [107] Li, C.-J., Li, P., Wang, K., Molina, E.E. 2014. Survey of Properties of Key Single and Mixture Halide Salts for Potential Application as High Temperature Heat Transfer Fluids for Concentrated Solar Thermal Power Systems. *AIMS Energy*, Vol. 2, Iss. 2, p 133-157. doi: [10.3934/energy.2014.2.133](https://doi.org/10.3934/energy.2014.2.133)
- [108] Zhai, W., Liu, G., Yu, F., Wang, Y. 2014. Study of Modification of Hitec Molten Salt and its Properties Tests. *Advanced Materials Research*, ISSN 1662-8985, Vols. 1073-1076, p. 66-72. <https://www.scientific.net/AMR.1073-1076.66.pdf>
- [109] Santini, R., Tadriss, T., Pantaloni, J., Cerisier, P. 1984 Measurement of Thermal Conductivity of Molten Salts in the Range 100-500°C. *Int. J. Heat Mass Transfer*, Vol. 27, Iss. 4, p. 623-626. [https://doi.org/10.1016/0017-9310\(84\)90034-6](https://doi.org/10.1016/0017-9310(84)90034-6)
- [110] Kearney, D., Herrmann, U., Nava, P., Kelly, B., Mahoney, R., Pacheco, J., Cable, R., Potrovitza, N., Blake, D., Price, H. 2003. Assessment of a Molten Salt Heat Transfer Fluid in a Parabolic Trough Solar Field. *Journal of Solar Energy Engineering*, Vol. 125, Iss. 2, p. 170-176. <https://doi.org/10.1115/1.1565087>
- [111] Bauer, T., Pflieger, N., Laing, D., Steinmann, W.-D., Eck, M., Kaesche, S. 2013. High Temperature Molten Salts for Solar Power Application. *Molten Salts Chemistry. From Lab to Applications*, Elsevier, ISBN 978-0-12-398538-5, Chapter 20, p. 415-438. <https://doi.org/10.1016/B978-0-12-398538-5.00020-2>
- [112] Daubner, M., Fellmoser, F., Stoppel, S. 2011. Technische Beschreibung der Versuchsanlage ALINA zur Untersuchung eines Natrium-Freistrahls. Forschungsbericht 7570. Karlsruher Institute für Technologie, Institut für Kern- und Energietechnik, ISBN 978-3-86644-620-5, 60 p. <https://publikationen.bibliothek.kit.edu/1000021682>
- [113] Pacio, J., Daubner, M., Fellmoser, F., Hering, W., Jäger, W., Stieglitz, R., Wetzel, T. 2019. Construction of Experimental Liquid-Metal Facilities. *Thermal Hydraulics Aspects of Liquid Metal Cooled Nuclear Reactors*. Ed.: F. Roelofs, Woodhead Publishing, ISBN 978-0-08-101980-1, Chapter 3, p. 107-125. <https://doi.org/10.1016/B978-0-08-101980-1.00013-2>
- [114] Siegel, N. P. 2012. Thermal Energy Storage for Solar Power Production. *WIREs Energy Environ* 2012, Vol. 1, p. 119-131. <https://onlinelibrary.wiley.com/doi/pdf/10.1002/wene.10>
- [115] Heinzl, A., Hering, W., Stieglitz, R. et al. 2017. Liquid Metals as Efficient High Temperature Heat Transport Fluids. *Energy Technology*, Vol. 5, Iss. 7, p. 1026-1036. <https://doi.org/10.1002/ente.201600721>
- [116] Hering, W., Onea, A., Jianu, A., Reiser, J., Ulrich, S., Stieglitz, R. 2019. Liquid Metals, Materials and Safety Measures to Progress to CSP 2.0. *AIP Conference Proceedings* 2126, Article No.: 080002, 8 p. <https://doi.org/10.1063/1.5117597>
- [117] Hering, W., Onea, A., Diez de los Rios Ramos, N., Stieglitz, R. 2013. Direct Energy Conversion Using Liquid Metals. E2C 2013 - 3<sup>rd</sup> European Energy Conference, 27-30 October 2013, Budapest, Hungary, *EPJ Web of Conferences*, Vol. 79, Article No.: 03010, 9 p. <https://doi.org/10.1051/epjconf/20137903010>

- [118] Benages-Vilau, R., Calvet, T., Cuevas-Diarte, M. A., Oonk, H. A. J. 2016. The NaNO<sub>3</sub>-KNO<sub>3</sub> Phase Diagram. *Phase Transitions*, Vol. 89, Iss. 1, 20 p. <https://doi.org/10.1080/01411594.2015.1083567>
- [119] Sohal, M. S., Ebner, M. A., Sabharwall, P., Sharpe, P. 2010. Engineering Database of Liquid Salt Thermophysical and Thermochemical Properties. Idaho National Laboratory, U.S. Department of Energy, INL/EXT-10-18297, Contract No.: DE-AC07-05ID14517, 70 p. <https://inldigitallibrary.inl.gov/sites/sti/sti/4502650.pdf>
- [120] Rodriguez-Garcia, M. M., Bravo, E.R. 2016. Testing a New Design of Latent Storage, Proceedings of the 11<sup>th</sup> ISES EuroSun Conference, 11-14 October 2016, Palma De Mallorca, Spain, ISBN 978-3-9814659-6-9, p. 587-592. <https://proceedings.ises.org/eurosun2016/EuroSun2016-Proceedings.pdf>
- [121] Grogan, D. 2013. Development of Molten-Salt Heat Transfer Fluid Technology for Parabolic Trough Solar Power Plants. Final Technical Report, Award No.: DE-FC36-08GO18038, 35 p. [https://digital.library.unt.edu/ark:/67531/metadc842212/m2/1/high\\_res\\_d/1090096.pdf](https://digital.library.unt.edu/ark:/67531/metadc842212/m2/1/high_res_d/1090096.pdf)
- [122] Bradschaw, R., Siegel, N. 2008. Molten Nitrate Salt Development for Thermal Energy Storage in Parabolic Trough Solar Power System, Proc. Energy Sustainability 2008 (ES2008), 10-14 August 2008, Jacksonville, Florida USA, Report No.: SAND2008-4727C, 7 p. <https://www.osti.gov/servlets/purl/1142924>
- [123] Baudis, U., Kreuz, M. 2001. Technologie der Salzschnmelzen: Wärmebehandlung, Härtetechnik, Wärmeübertragung, Reinigung. Die Bibliothek der Technik Band 224, Verlag Moderne Industrie, ISBN 3-478-93260-2, p. 54-62. <https://www.nitriersalze.com/pdfs/leseprobe.pdf>
- [124] Kearney, D., Kelly, B., Herrmann, U., Cable, R., Pacheco, J., Mahoney, R., Price, H., Blake, D., Nava, P., Potrovitza, N. 2004. Engineering Aspects of a Molten Salt Heat Transfer Fluid in a Trough Solar Field. *Energy*, Vol. 29, Iss. 5-6, p. 861-870. [https://doi.org/10.1016/S0360-5442\(03\)00191-9](https://doi.org/10.1016/S0360-5442(03)00191-9)
- [125] Carling, R. W., Mar, R.W. 1981. Industrial Use of a Molten Nitrate/Nitrite Salts. Sandia National Laboratories, Report No.: SAND81-8020 DE82 010032, 34 p. <https://www.osti.gov/servlets/purl/5257229>
- [126] Wortmann, J., Lutz, M., Ter Maat, J., Schierle-Arndt, K., Maurer, S., Ladenberger, M., Geyer, K., Garlichs, F. 2013. Nitrate Salt Compositions Comprising Alkali Metal Carbonate and Their Use as Heat Transfer Medium or Heat Storage Medium, US Patent No.: 2013/0264514, Date: 10.10.2013. <https://depatisnet.dpma.de/DepatisNet/depatisnet?action=pdf&docid=US020130264514A1&xxfull=1>
- [127] Ozeryanaya, I. N. 1985. Corrosion of Metals by Molten Salts in Heat-Treatment Processes. *Metal Science and Heat Treatment*, Vol. 27, Iss. 3, p. 184-188. <https://doi.org/10.1007/BF00699649>

- [128] Onea, A., Perez-Martin, S., Jäger, W., Hering, W., Stieglitz, R. 2017. Liquid Metals as Heat Transfer Fluids for Science and Technology. *Advances in New Heat Transfer Fluids: From Numerical to Experimental Techniques*, Taylor & Francis Group, CRC Press, ISBN 9781315368184, Chapter 12, p. 305-376. <https://doi.org/10.1201/9781315368184>
- [129] Wetzel, T., Stieglitz, R., Hering, W. et al. 2014. Liquid Metal Technology for Concentrated Solar Power Systems: Contribution by the German Research Program. *AIMS Energy*, Vol. 2, Iss. 1, p. 89-98. <https://doi.org/10.3934/energy.2014.1.89>
- [130] Anderson, F. A. 1967. A Primer for the Safe Use of Liquid Alkali Metals. Technical Report No.: ORNLTM-1740, Contract No.: W-7605-eng-26, Oak Ridge National Laboratory, U.S. Atomic Energy Commission, 31 p. <https://www.osti.gov/servlets/purl/4453499>
- [131] Mohammad, M. B. 2016. High Temperature Properties of Molten Nitrate Salt for Solar Thermal Energy Storage Application. Doctoral Thesis, Mechanical Engineering Department, Swinburne University of Technology, 388 p. <https://researchbank.swinburne.edu.au/file/31d0fc65-38b3-4e15-b7c3-ae8432361f05/1/Mehedi%20Bin%20Mohammad%20Thesis.pdf>
- [132] Stieglitz, R., Möslang, A., Gonzalez de Vicente, S.M. 2017. Overview on Impact of Coolant Choice on Design and Performance of Fast Neutron Systems. Challenges for Coolants in Fast Neutron Spectrum Systems, IAEA-TECDOC-1912, International Atomic Energy Agency, Vienna, Austria, ISBN 978-92-0-107920-6, p. 5-23. <https://inis.iaea.org/collection/NCLCollectionStore/Public/51/079/51079091.pdf?r=1>
- [133] Bologa, M.-V. 2017. Analyse des mit TiC beschichteten Feststoffelektrolyten einer AMTEC-Zelle, Abschlussarbeit – Master, Fakultät für Maschinenbau, Karlsruher Institut für Technologie, HGF Programm 35.12.01 (POF III, LK 01) Flüssigmetall-Technologie, Juli 2017, KITopen-ID: 1000079757, 127 p. <https://publikationen.bibliothek.kit.edu/1000079757>
- [134] Federsel, K., Wortmann, J., Ladenberger, M. 2015. High-Temperature and Corrosion Behaviour of Nitrate Nitrite Molten Salt Mixtures Regarding Their Applications in Concentrating Solar Power Plants. *Energy Procedia*, Vol. 69, p. 618-625. <https://doi.org/10.1016/j.egypro.2015.03.071>
- [135] Wetzel, T., Stieglitz, R., Marocco, L., Pacio, J., Hering, W., Dietrich, B. 2013. Flüssigmetalle als Wärmeträgerfluide für Hochtemperaturprozesse. *Chemie Ingenieur Technik*, Vol. 85, No. 9, p. 1373-1374. <https://doi.org/10.1002/cite.201250703>
- [136] Hering, W., Wetzel, T., Stieglitz, R. 2012. Application of Liquid Metals for Solar Energy Systems. *The European Physical Journal Conferences*, Vol. 33, Article No.: 03003, 7 p. <https://doi.org/10.1051/epjconf/20123303003>
- [137] Onea, A., Diez de los Rios Ramos, N., Bologa, M.-V., Hering, W., Stieglitz, R., Stüber, M., Sven, U. 2017. Considerations on Thermal Radiation of Direct Solar Thermal Power Generation Systems for Space Propulsion. 6<sup>th</sup> CEAS Air & Space Conference, Aerospace Europe 2017, 2-6 October, 2017, Bucharest, Romania, Paper No. 194, 10 p. [https://www.researchgate.net/publication/321937904\\_Considerations\\_on\\_thermal\\_radiation\\_of\\_direct\\_solar\\_thermal\\_power\\_generation\\_systems\\_for\\_space\\_propulsion](https://www.researchgate.net/publication/321937904_Considerations_on_thermal_radiation_of_direct_solar_thermal_power_generation_systems_for_space_propulsion)

- [138] Foust, O. J. 1972. Sodium-NaK Engineering Handbook. Volume: I. Sodium Chemistry and Physical Properties. Science Publishers Inc., New York, ISBN 0-677-03020-4, 339 p. <https://www.osti.gov/servlets/purl/4631555>
- [139] Knebel, J. U., Fazio, C., Konys, J., Müller G., Stieglitz, R. 2007. Overview on Corrosion and Thermal-Hydraulic Issues of Liquid Metal Coolants, Proceedings AccApp'07, 29 July - 02 August 2007, Pocatello, Idaho, p. 18-28. <https://www.researchgate.net/publication/267566631>
- [140] Liu, C., Cheng, M. S., Zhao, B. C., Dai, Z. M. 2017. Thermal Performance Analysis of a Thermocline Thermal Energy Storage System with FLiNaK Molten Salt. *IOP Conf. Series: Earth and Environmental Science*, Vol. 52, Article No.: 012029, 9 p. <https://iopscience.iop.org/article/10.1088/1742-6596/52/1/012039/pdf>
- [141] Zhai, W., Yang, B., Li, M., Li, S., Xin, M., Lin, J. 2015. Modify Hitec Molten Salt and its Properties Tests by Orthogonal Experiment. Proceedings of 2<sup>nd</sup> International Workshop on Materials Engineering and Computer Sciences, 10-11 October 2015, Jinan, Shandong, China, ISBN 10.2991/iwmecs-15.2015.52, p. 271-276. <http://doi.org/10.2991/iwmecs-15.2015.52>
- [142] Peng, Q., Ding, J., Wei, X., Yang, J., Yang, X. 2010. The Preparation and Properties of Multi-Component Molten Salts. *Applied Energy*, Vol. 87, Iss. 9, p. 2812-2817. <https://doi.org/10.1016/j.apenergy.2009.06.022>
- [143] Green, M., Sabharwall, P., Mckellar, M. G., Yoon, S.-J., Abel, C., Petrovic, B., Curtis, D. 2013. Nuclear Hybrid Energy System: Molten Salt Energy Storage. Idaho National Laboratory, IN/EXT-13-31768, Contract No.: DE-AC07-05ID14517, 51 p. <http://large.stanford.edu/courses/2015/ph240/dodaro2/docs/6339782.pdf>
- [144] Boerema, N., Morrison, G., Taylor, R., Rosengarten, G. 2012. Liquid Sodium Versus Hitec as a Heat Transfer Fluid in Solar Thermal Central Receiver Systems. *Solar Energy*, Vol. 86, Iss. 9, p. 2293-2305. <https://doi.org/10.1016/j.solener.2012.05.001>
- [145] Wu, Y.-T., Chen, C., Liu, B., Ma, C.-F. 2012. Investigation of Forced Convective Heat Transfer of Molten Salts in Circular Tubes. *International Communications in Heat and Mass Transfer*, Vol. 39, Iss. 10, p. 1550-1555. <https://doi.org/10.1016/j.icheatmasstransfer.2012.09.002>
- [146] Chen, Y. C., Wu, Y. T., Ren, N., Ma, C. F. 2011. Experimental Study of Viscosity Characteristics of High-Temperature Heat Transfer Molten Salt. *Science China Technological Sciences*, Vol. 54, No. 11, p. 3022-3026. <https://doi.org/10.1007/s11431-011-4530-x>
- [147] Villada, C., Bolivar, F., Jaramillo, F., Castano, J.G., Echeverria, F. 2014. Thermal Evaluation of Molten Salts for Solar Thermal Energy Storage. *Renewable Energy and Power Quality Journal*, ISSN 2172-038 X, Vol. 1, No. 12, p. 622-625. <http://doi.org/10.24084/repqj12.431>
- [148] Bovesecchi, G., Coppa, P., Pistacchio, S. 2018. A New Thermal Conductivity Probe for High Temperature Tests for the Characterization of Molten Salts. *Review of Scientific Instruments*, Vol. 89, Article No.: 055107, p. 1-7. <https://aip.scitation.org/doi/abs/10.1063/1.5019776>

- [149] Janz, G. J., Tomkins, R. P. T. 1981. Physical Properties Data Compilations Relevant to Energy Storage - IV Molten Salts: Data on Additional Single and Multi-Component Salt Systems. National Standard Reference Data System, National Bureau of Standards Rep., Accession No.: ADD095219, NSRDS-NBS 61, Part IV, 873 p. <https://apps.dtic.mil/sti/citations/ADD095219>
- [150] Xiao, X., Zhang, G., Ding, Y., Wen, D. 2019. Rheological Characteristics of Molten Salt Seeded with Al<sub>2</sub>O<sub>3</sub> Nanopowder and Graphene for Concentrated Solar Power. *Energies*, Vol. 12, No. 3, Article No.: 467, 16 p. <https://doi.org/10.3390/en12030467>
- [151] Iverson, B. D., Broome, S. T., Kruijenga, A. M., Cordaro, J. G. 2012. Thermal and Mechanical Properties of Nitrate Thermal Storage Salts in the Solid-Phase. *Solar Energy*, Vol. 86, Iss. 10, p. 2897-2911. <https://doi.org/10.1016/j.solener.2012.03.011>
- [152] Singer, C., Buck, R., Pitz-Paal, R. Müller-Steinhagen, H. 2009. Assessment of Solar Power Tower Driven Ultra Supercritical Steam Cycles Applying Tubular Central Receivers with Varied Heat Transfer Media. Proceeding of the Energy Sustainability 2009, 19-23 July 2009, San Francisco. ISBN 978-0-7918-4890-6, Paper No.: ES2009-90476, p. 707-716. <https://doi.org/10.1115/ES2009-90476>
- [153] Pacio, J., Fritsch, A., Singer, C., Uhlig, R. 2014. Liquid Metals as Efficient Coolants for High-Intensity Point-Focus Receivers: Implications to the Design and Performance of Next-Generation CSP Systems. *Energy Procedia*, Vol. 49, p. 647-655. <https://doi.org/10.1016/j.egypro.2014.03.070>
- [154] Flesch, J., Marocco, L., Fritsch, A., Niedermeier, K., Wetzel, T. 2020. Entropy Generation Minimization Analysis of Solar Salt, Sodium, and Lead-Bismuth Eutectic as High Temperature Heat Transfer Fluids. *Journal of Heat Transfer*, Vol. 142, Iss. 4, Article No.: 042103, 10 p. <https://doi.org/10.1115/1.4046302>
- [155] Delise, T., Tizzoni, A. C., Votyakov, E. V., Turchetti, L., Corsaro, N., Sau, S., Licoccia, S. 2020. Modeling the Total Ternary Phase Diagram of NaNO<sub>3</sub>-KNO<sub>3</sub>-NaNO<sub>2</sub> Using the Binary Subsystems Data. *International Journal of Thermophysics*, Vol. 41, Article No.: 1, 20 p. <https://doi.org/10.1007/s10765-019-2577-2>
- [156] Jin, Y., Cheng, J., An, X., Su, T., Zhang, P., Li, Z. 2016. Accurate Viscosity Measurement of Nitrates/Nitrites Salts for Concentrated Solar Power. *Solar Energy*, Vol. 137, p. 385-392. <https://doi.org/10.1016/j.solener.2016.08.037>
- [157] Kearney, D., Kelly, B., Cable, R., Potrovitza, N., Herrmann, U, Nava, P., Mahoney, R., Pacheco, J., Blake, D., Price, H. 2003. Overview on Use of a Molten Salt HTF in a Trough Solar Plant. NREL Parabolic Trough Thermal Energy Storage Workshop, Golden, CO, 20-21 February 2003, Presentation, NREL/PR-550-40028, 27 p. <https://www.nrel.gov/docs/fy03osti/40028.pdf>
- [158] HITEC Heat Transfer Salt. 2009. Coastal Chemical Co., 10 p. <http://stoppingclimatechange.com/MSR%20-%20HITEC%20Heat%20Transfer%20Salt.pdf> (valid on 16.11.2023)

- [159] Lai, C. C., Chang, W.-C., Hu, W.-L., Wang, Z. M., Lu, M.-C., Chuen, Y.-L. 2014. A Solar-Thermal Energy Haversting Scheme: Enhanced Heat Capacity of Molten HITEC Salt Mixed with Sn/SiO<sub>x</sub> Core-Shell Nanoparticles. *Nanoscale*, Vol. 6, Iss. 9, p. 4555-4559. <https://doi.org/10.1039/C3NR06810B>
- [160] Pan, C. A., Ferruzza, D., Guédez, R., Dinter, F., Laumert, B., Haglind, F. 2018. Identification of Optimum Molten Salts for Use as Heat Transfer in Parabolic Trough CSP Plants. A Techno-Economic Comparative Optimization. *AIP Conference Proceedings*, Vol. 2033, Article No.: 030012, 8 p. <https://doi.org/10.1063/1.5067028>
- [161] Silverman, M. D., Engel, J. R. 1977. Survey of Technology for Storage of Thermal Energy in Heat Transfer Salt. OAK Ridge National Laboratory, Technical Report No.: ORNL/TM-5682, Contract No.: W-7405-eng-26, 32 p. <http://moltensalt.org/references/static/downloads/pdf/ORNL-TM-5682.pdf>
- [162] Janz, G. J., Truong, G. N. 1983. Melting and Premelting Properties of the KNO<sub>3</sub>-NaNO<sub>2</sub>-NaNO<sub>3</sub> Eutectic System. *J. Chem. Eng. Data*, Vol. 28, Iss. 2, p. 201-202. <https://doi.org/10.1021/jc00032a022>
- [163] Molten Salt Safety Study. 1980. Martin Marietta Aerospace. Denver, Colorado, Technical Report, SAND 808179, Report No.: MCR-80-1305, Contract No.: 83-3638, 26 p. <https://ntrl.ntis.gov/NTRL/dashboard/searchResults/titleDetail/SAND808179.xhtml>
- [164] Subari, F., Maksom, H. F., Zawawi, A. 2015. Corrosion Behavior of Eutectic Molten Salt Solution on Stanless Steel 316L. *Prodecia-Social and Behavioral Sciences*, Vol. 195, p. 2699-2708. <http://doi.org/10.1016/j.sbspro.2015.06.465>
- [165] Zou, L.-L., Chen, X., Wu, Y.-T., Wang, X., Ma, C.-F. 2019. Experimental Study of Thermophysical Properties and Thermal Stability of Quaternary Nitrate Molten Salt for Thermal Energy Storage. *Solar Energy Materials and Solar Cells*, Vol. 190, p. 12-19. <https://doi.org/10.1016/j.solmat.2018.10.013>
- [166] Kotyla, J. 2017. Molten Salt Composition and Composites for Improved Latent Heat Thermal Energy Storage. *PAM Review Energy Science & Technology*, Vol. 4, Subject 68412, p. 46-58. <http://doi.org/10.5130/pamr.v4i0.1445>
- [167] Bernagozzi, M., Panesar, A., Morgan, R. 2019. Low Temperature Molten Salts in Sustainable Energy Production. Proceedings of 7<sup>th</sup> European Conference on Renewable Energy Systems (ECRES 2019), 10-12 June 2019, Madrid, Spain, ISBN 786058691179, p. 260-265. [https://cris.brighton.ac.uk/ws/portalfiles/portal/6353965/Low\\_Temperature\\_Molten\\_Salts\\_in\\_Sustainable\\_Energy\\_Production\\_Eur\\_Conf\\_Ren\\_Energy\\_Sys.pdf](https://cris.brighton.ac.uk/ws/portalfiles/portal/6353965/Low_Temperature_Molten_Salts_in_Sustainable_Energy_Production_Eur_Conf_Ren_Energy_Sys.pdf)
- [168] Xiao, X., Jia, H., Pervaiz, S., Wen, D. 2020. Molten Salt/Metal Foam/Graphene Nanoparticle Phase Change Composites for Thermal Energy Storage. *ACS Appl. Nano Mater.* Vol. 3, No. 6, p. 5240–5251. <https://doi.org/10.1021/acsanm.0c00648>
- [169] Du Pont Company, 1976. HITEC<sup>®</sup> Heat Transfer Salt: Properties, Uses, Storage and Handling. Industrial Chemicals Department, E. I. Du Pont de Nemours & Co., Wilmington, Delaware, Technical Brochure E-08161, 9 p.

- [170] Ene Hts-2 Molten Salt / Hitec Salt. Shenzhen Enesoon Science & Technology Co. Ltd. Product Description. <http://www.tcntcn.com/product/702857.html> (valid on 16.11.2023)
- [171] Dunlop, T. O., Jarvis, D. J., Voice, W. E., Sullivan, J. H. 2018. Stabilization of Molten Salt Materials Using Metal Chlorides for Solar Thermal Storage. *Scientific Reports*, Vol. 8, Article No.: 8190, 7 p. <https://doi.org/10.1038/s41598-018-26537-8>
- [172] D'Aguanno, B., Karthik, M., Grace, A. N., Floris, A. 2018. Thermostatic Properties of Nitrate Molten Salts and Their Solar and Eutectic Mixtures. *Scientific Reports*, Vol. 8, Article No.: 10485, 15 p. <https://doi.org/10.1038/s41598-018-28641-1>
- [173] Fernandez, A. G., Galleguillos, H., Fuentealba, E., Perez, F. J. 2015. Thermal Characterization of HITEC Molten Salt for Energy Storage in Solar Linear Concentrated Technology. *Journal of Thermal Analysis and Calorimetry*, Vol. 122, p. 3-9. <https://doi.org/10.1007/s10973-015-4715-9>
- [174] Morin, G., Karl, M., Mertins, M., Selig, M. 2015. Molten Salt as a Heat Transfer Fluid in a Linear Fresnel Collector - Commercial Application Backed by Demonstration. *Energy Procedia*, Vol. 69, p. 689-698. <https://doi.org/10.1016/j.egypro.2015.03.079>
- [175] Bohlmann, E. G. 1972. Heat Transfer Salt for High Temperature Steam Generation. Oak Ridge National Laboratory, Technical Report No.: ORNL-TM-3777, Contract No.: W-7405-eng-26, 48 p. <https://www.osti.gov/servlets/purl/4595737>
- [176] Moore, R. C., Siegel, N. P., Kolb, G. J., Vernon, M. E., Ho, C. K. 2010. Design Considerations for Concentrating Solar Power Tower Systems Employing Molten Salt. Sandia National Laboratories, Report No.: SAND2010-6978, 51 p. <https://doi.org/10.2172/1008140>
- [177] Goods, S. H., Bradshaw, R. W. 2004. Corrosion of Stainless Steels and Carbon Steel by Molten Mixtures of Commercial Nitrate Salts. *Journal of Materials Engineering and Performance*, Vol. 13, p. 78-87. <https://doi.org/10.1361/10599490417542>
- [178] Xiao, X., Wen, D. 2018. Investigation of Thermo-Physical Properties of Molten Salt Enhanced with Nanoparticle and Copper Foam. Proceedings of the 7<sup>th</sup> International Conference on Renewable Energy Research and Applications (ICRERA), 14-17 October 2018, Paris, France. ISBN 978-1-5386-5982-3, p. 1445-1449. <http://doi.org/10.1109/ICRERA.2018.8566907>
- [179] Zhu, C., Tie, S., Han, H. 2019. Factors Affecting the Stability of Nitrate Molten Salts at a High Temperature. *Energy Storage Science and Technology*, Vol. 8, Iss. 1, p. 173-179. <http://www.energystorage-journal.com/EN/10.12028/j.issn.2095-4239.2018.0184>
- [180] Serrano-López, R., Fradera, J., Cuesta-López, S. 2013. Molten Salts Database for Energy Applications. *Chemical Engineering & Processing: Process Intensification*, Vol. 73, p. 87-102. <https://doi.org/10.1016/j.cep.2013.07.008>
- [181] Qiu, Y., He, Y. L., Wang, W. Q., Du, B. C., Wang, K. 2018. An Experimental Study on the Heat Transfer Performance of a Prototype Molten-Salt Rod Baffle Heat Exchanger for Concentrated Solar Power. *Energy*, Vol. 156, p. 63-72. <https://doi.org/10.1016/j.energy.2018.05.040>

- [182] Oliveira, J. 2018. Dynamic Simulation Using MATLAB®/Simulink to Improve the Current DEMO-IHTS Design, Master Thesis, Department of Mechanical Engineering, Karlsruhe Institute of Technology / HECTOR School of Engineering and Management, 110 p.
- [183] Qiu, Y., Li, Mi.-J., Li, Me.-J., Zhang, H.-H., Ning, B. 2019. Numerical and Experimental Study on Heat Transfer and Flow Features of Representative Molten Salts for Energy Applications in Turbulent Tube Flow. *International Journal of Heat and Mass Transfer*, Vol. 135, p. 732-745. <https://doi.org/10.1016/j.ijheatmasstransfer.2019.02.004>
- [184] Sharma, G., Goindi, G. S. 2018. Experimental Analysis of Binary Salt Mixture of NaNO<sub>3</sub>:KNO<sub>3</sub> for Low-Grade Waste Heat Recovery System. *Indian Journal of Science and Technology*, Vol. 11, Iss. 28, p.1-4. <https://indjst.org/articles/experimental-analysis-of-binary-salt-mixture-of-nano3-kno3-for-low-grade-waste-heat-recovery-system>
- [185] Ho, M. X., Pan, C. 2014. Optimal Concentration of Alumina Nanoparticles in Molten Hitec Salt to Maximize its Specific Heat Capacity. *International Journal of heat and Mass Transfer*, Vol. 70, p. 174-184. <https://doi.org/10.1016/j.ijheatmasstransfer.2013.10.078>
- [186] Pandey, J. P., Chaturvedi, B. R., Pandey, R. P. 1981. Surface Tension of Molten Salts. *J. Phys. Chem.*, Vol. 85, Iss. 12, p. 1750-1752. <https://doi.org/10.1021/j150612a031>
- [187] Ayyad, A. H. 2017. On the Surface Tension of Molten Salts and its Temperature Dependence. *Physics and Chemistry of Liquids*, Vol. 55, No. 1, p. 120-130. <https://doi.org/10.1080/00319104.2016.1183007>
- [188] Cantor, S., Grimes W. R. 1974. Fused-Salt Corrosion and its Control in Fusion Reactors. *Nuclear Technology*, Vol. 22, Iss. 1, p. 120-126. <https://doi.org/10.13182/NT74-A16281>
- [189] Breon, S. R., Chellew, N. R., Clemmer, R. G., Hoh, J. C. 1980. Gamma Irradiation of Nitrate-Based Salts, Fusion Power Program, Argonne National Laboratory, Illinois, Report No.: ANL/FPP/TM-129, 31 p. <https://inis.iaea.org/collection/NCLCollectionStore/Public/11/551/11551829.pdf?r=1>
- [190] Zaversky, F., Garcia-Barberena, J., Sanchez, M., Astrain, D. 2013. Transient Molten Salt Two-Tank Thermal Storage Modeling for CSP Performance Simulations. *Solar Energy*, Vol. 93, p. 294-311. <https://doi.org/10.1016/j.solener.2013.02.034>
- [191] Stern, H. K. 2001. High Temperature Properties and Thermal Decomposition of Inorganic Salts with Oxyanions. CRC Press, ISBN 9780849302565, 288 p. <https://www.routledge.com/High-Temperature-Properties-and-Thermal-Decomposition-of-Inorganic-Salts/Stern/p/book/9780849302565>
- [192] Pacheco, J., Showalter, S., Kolb, W. 2002. Development of a Molten-Salt Thermocline Thermal Storage System for Parabolic Trough Plants. *Journal of Solar Energy Eng.*, Vol. 124, p. 153-159. <https://doi.org/10.1115/1.1464123>
- [193] Bradshaw, R. W., Goods, S. H. 2001. Corrosion of Alloys and Metals by Molten Nitrates. Sandia National Laboratories, Report No.: SAND2000-8727, 34 p. <https://www.osti.gov/servlets/purl/1545803>



- [194] Tufeu, B., Petitet, J. P., Denielou, L., Neindre, B. L. 1985. Experimental Determination of the Thermal Conductivity of Molten Pure Salts and Salt Mixtures. *International Journal of Thermalphysics*, Vol. 6, No. 4, p. 315-330. <https://doi.org/10.1007/BF00500266>
- [195] Tian, H., Du, L., Huang, C., Wie, X., Wang, W., Ding, J. 2017. Enhanced Specific Heat of Chloride Salt with Mg Particles for High-Temperature Thermal Energy Storage. *Energy Procedia*, Vol. 105, p. 4402-4407. <https://doi.org/10.1016/j.egypro.2017.03.934>
- [196] Isaza-Ruiz, M. Osorio, F.B. 2021. Thermal Properties of HITEC Salt-Based Nanofluids Synthesized by New Two-Step Method. *Procedia Environmental Science, Engineering and Management*, Vol. 8, Iss. 1, p. 147-155. [http://procedia-esem.eu/pdf/issues/2021/no1/17\\_02.17.Ruiz\\_21.pdf](http://procedia-esem.eu/pdf/issues/2021/no1/17_02.17.Ruiz_21.pdf)
- [197] Alexander Jr., J., Hindin, S. G. 1947. Phase Relations in Heat Transfer Salt Systems. *Industrial and Engineering Chemistry*, Vol. 39, Iss. 8, p. 1044-1049. <https://doi.org/10.1021/ie50452a026>
- [198] Lovering, D. G. 1982. Molten Salt Technology. 1<sup>st</sup> Ed., Springer US, Plenum Press, ISBN 978-1-4757-1724-2, New York. <https://www.springer.com/gp/book/9781475717266>
- [199] Carling, R. W. et al. 1981. Molten Nitrate Salt Technology - Development Status Report. Sandia National Labs. Energy Report No.: SAND80-8052, 112 p. [https://digital.library.unt.edu/ark:/67531/metadc1192408/m2/1/high\\_res\\_d/6853207.pdf](https://digital.library.unt.edu/ark:/67531/metadc1192408/m2/1/high_res_d/6853207.pdf)
- [200] Nissen, D. A., Meeker, D. E. 1983. Nitrate/Nitrite Chemistry in Sodium Nitrate-Potassium Nitrate Melts. *Inorganic Chemistry*, Vol. 22, No. 5, p. 716-721. <https://doi.org/10.1021/ic00147a004>
- [201] Blander, M. 1962. Thermodynamic Properties of Molten Salt Solutions. Selected Topics in Molten-Salt Chemistry, Reactor Chemistry Division, Report No.: ORNL-3293, Contract No.: W-7405-eng-26, 103 p. <http://www.thmfgcs.com/ORNL-3293.pdf>
- [202] Bradshaw, R. W., Meeker, D. E. 1990. High-Temperature Stability of Ternary Nitrate Molten Salts for Solar Thermal Energy Systems. *Solar Energy Materials*, Vol. 21, Iss. 1, p. 51-60. [https://doi.org/10.1016/0165-1633\(90\)90042-Y](https://doi.org/10.1016/0165-1633(90)90042-Y)
- [203] Gimenez, P., Fereres, S. 2015. Effect of Heating Rates and Composition on the Thermal Decomposition of Nitrate Based Molten Salts. *Energy Procedia*, Vol. 69, p. 654-662. <https://doi.org/10.1016/j.egypro.2015.03.075>
- [204] Passerini, S. 2010. Optical and Chemical Properties of Molten Salt Mixtures for Use in High Temperature Power Systems. Thesis for the Degree of Master of Science, Department of Nuclear Science and Engineering, Massachusetts Institute of Technology, 107 p. <https://core.ac.uk/download/pdf/4427296.pdf>
- [205] Cramer, S. D., Covino Jr., B. S. 2003. ASM Handbook Volume 13A: Corrosion - Fundamentals, Testing and Protection. 10<sup>th</sup> Ed., ASM International, ISBN 978-0-87170-705-5, Ohio, 1135 p. [https://www.asminternational.org/search/-/journal\\_content/56/10192/06494G/PUBLICATION](https://www.asminternational.org/search/-/journal_content/56/10192/06494G/PUBLICATION)

- [206] Zamboni, L. 2013. Getting Started with Simulink. Published by Packt Publishing Ltd., Birmingham, UK, ISBN 9781461949220, 120 p. <https://searchworks.stanford.edu/view/12965090>
- [207] Perelmuter, V. 2016. Renewable Energy Systems - Simulation with Simulink® and SimPowerSystems™. CRC Press, ISBN 978-1-3153-1624-6. <https://www.taylorfrancis.com/books/mono/10.1201/9781315316246/renewable-energy-systems-viktor-perelmuter>
- [208] Flueckiger, S., Garimella, S. V. 2012. Second-Law Analysis of Molten-Salt Thermal Energy Storage in Thermoclines. *Solar Energy*, Vol. 86, Iss. 5, p. 1621-1631. <https://doi.org/10.1016/j.solener.2012.02.028>
- [209] Yang, X., Qin, F. G. F., Jiang, R. 2016. Experimental Investigation of a Molten Salt Thermocline Storage Tank. *International Journal of Sustainable Energy*, Vol. 35, No. 6, p. 606-614. <https://doi.org/10.1080/14786451.2014.930465>
- [210] Heller, L. 2013. Literature Review on Heat Transfer Fluids and Thermal Energy Storage Systems in CSP Plants. STERG Report, 83 p. [http://sterg.sun.ac.za/wp-content/uploads/2011/08/HTF\\_TESmed\\_Review\\_2013\\_05\\_311.pdf](http://sterg.sun.ac.za/wp-content/uploads/2011/08/HTF_TESmed_Review_2013_05_311.pdf)
- [211] Gibbs, A., Robinson, B.W., Rougé, S., Jouhara, H., Asaduzzaman, A. K. M., Chowdhury, M., Kjellgren, P., Martí, A. M., Pardelli, P. T., Ciuffi, N. 2019. Heat Recovery at High Temperature by Molten Salts for High Temperature Processing Industries. *AIP Conference Proceedings*, Vol. 2191, Article No.: 020088, 10 p. <https://doi.org/10.1063/1.5138821>
- [212] Chang, Z. S., Li, X., Xu, C., Chang, C., Wang, Z. F. 2015. The Design and Numerical Study of a 2 MWh Molten Salt Thermocline Tank. *Energy Procedia*, Vol. 69, p. 779-789. <https://doi.org/10.1016/j.egypro.2015.03.094>
- [213] Yang, X., Yang, X., Ding, J., Shao, Y., Qin, F., Jiang, R. 2012. Criteria for Performance Improvement of a Molten Salt Thermocline Storage System. *Applied Thermal Engineering*, Vol. 48, p. 24-31. <https://doi.org/10.1016/j.applthermaleng.2012.04.046>
- [214] Iverson, B. D., Cordaro, J. G., Kruiuzenga, A. M. 2011. Thermal Property Testing of Nitrate Thermal Storage Salts in Solid-Phase. Proceedings of the ASME 2011 5<sup>th</sup> Intern. Conf. Energy Sustainability, 7-10 August 2011, Washington, DC. USA, ISBN 978-0-7918-5468-6, Paper No.: ES2011-54159, p. 495-502. <https://doi.org/10.1115/ES2011-54159>
- [215] MathWorks. 2019. SimScape. [https://de.mathworks.com/products/simscape.html?s\\_tid=srchtitle](https://de.mathworks.com/products/simscape.html?s_tid=srchtitle) (valid on 16.11.2023)
- [216] Peet, M. J., Hasan, H. S., Bhadeshia, H. K. D. H. 2011. Prediction of Thermal Conductivity of Steel. *Internat. Journal of Heat and Mass Transfer*, Vol. 54, Iss. 11-12, p. 2602-2608. <https://doi.org/10.1016/j.ijheatmasstransfer.2011.01.025>
- [217] Xu, C., Wang, Z., He, Y., Li, X., Bai, F. 2012. Sensitivity Analysis of the Numerical Study on the Thermal Performance of a Packed-Bed Molten Salt Thermocline Thermal Storage System. *Applied Energy*, Vol. 92, p. 65-75. <https://doi.org/10.1016/j.apenergy.2011.11.002>

- [218] Bachelier, C., Stieglitz, R. 2017. Design and Optimization of Linear Frensel Power Plants Based on the Direct Molten salt Concept, *Solar Energy*, Vol. 152, p. 171-192, <http://dx.doi.org/10.1016/j.solener.2017.01.060>
- [219] Zhang, X., Wu, Y., Ma, C., Meng, Q., Hu, X., Yang, C. 2019. Experimental Study on Temperature Distribution and Heat Losses of a Molten Salt Heat Storage Tank. *Energies*, Vol. 12, No. 10, Article No.: 1943, 14 p. <https://doi.org/10.3390/en12101943>
- [220] Suárez, C., Iranzo, A., Pino, F. J., Guerra, J. 2015. Transient Analysis of the Cooling Process of Molten Salt Thermal Storage Tanks due to Standby Heat Loss. *Applied Energy*, Vol. 142, p. 56-65. <https://doi.org/10.1016/j.apenergy.2014.12.082>
- [221] Bologna, M.-V., Stieglitz, R., Hering, W., Bubelis, E., Oliveira J. 2019. Parameter Study and Dynamic Simulation of Current DEMO Intermediate Heat Transfer and Storage System Design via MATLAB®/Simulink. Proceedings of the 14<sup>th</sup> Internat. Symp. on Fusion Nuclear Technology, 22-27 September 2019, Budapest, Hungary, ISBN 978-615-5270-58-1, Book of Abstracts, Abstract No: P2-030, p. 131. [http://isfnt-14.org/wp-content/uploads/ISFNT-14\\_Book\\_of\\_Abstracts.pdf](http://isfnt-14.org/wp-content/uploads/ISFNT-14_Book_of_Abstracts.pdf)
- [222] Tutorials Point. MATLAB® Tutorial: MATLAB® - Simulink. [https://www.tutorialspoint.com/matlab/matlab\\_simulink.htm](https://www.tutorialspoint.com/matlab/matlab_simulink.htm) (valid on 16.11.2023)
- [223] Szogradi, M., Norrman, S., Bubelis, E. 2020. Dynamic Modelling of the Helium-Cooled DEMO Fusion Power Plant with an Auxiliary Boiler in Apros. *Fusion Engineering and Design*, Vol. 160, Article No.: 111970. <https://doi.org/10.1016/j.fusengdes.2020.111970>
- [224] Zohuri, B. 2017. Heat Exchanger Types and Classifications. In Retracted Book: Compact Heat Exchangers, Springer, Cham., ISBN 978-3-319-29835-1, Retracted Chapter, p. 19-56. [https://doi.org/10.1007/978-23-319-29835-1\\_2](https://doi.org/10.1007/978-23-319-29835-1_2)
- [225] Nawaz, H. 2020. Dynamic Modelling of Power Conversion System for a Fusion Power Plant. Master Thesis, Department of Mechanical Engineering, Karlsruhe Institute of Technology (Cooperation between KIT and University of Applied Science in Karlsruhe), 94 p.
- [226] Shaukut, N., Khan, B., Ali, S.M., Munawar, U., Ullah, Z. 2017. Comparative Study of Control Methods for Steam Condenser, International Conference on Energy Conservation and Efficiency (ICECE), 22-23 November, 2017, Lahore, Pakistan, ISBN 978-1-5386-3606-0, p. 32-37. <https://ieeexplore.ieee.org/document/8248825>
- [227] Jibril, M., Tadese, E.A., Tadese, M. 2020. Comparison of Mixed  $H_2/H_\infty$  with Regional Pole Placement Control and  $H_2$  Optimal Control for the Design of Steam Condenser. International Journal of Advanced Research and Innovative Ideas in Education, ISSN No. (online): 2395-4396, Vol. 6, Iss. 2, Paper ID 11630, p. 773-780. DOI: 16.0415/IJARIIE-11630. [http://ijariie.com/AdminUploadPdf/Comparison\\_of\\_Mixed\\_H\\_2\\_H%E2%88%9E\\_with\\_Regional\\_Pole\\_Placement\\_Control\\_and\\_H\\_2\\_Optimal\\_Control\\_for\\_the\\_Design\\_of\\_Steam\\_Condenser\\_ijariie11630.pdf](http://ijariie.com/AdminUploadPdf/Comparison_of_Mixed_H_2_H%E2%88%9E_with_Regional_Pole_Placement_Control_and_H_2_Optimal_Control_for_the_Design_of_Steam_Condenser_ijariie11630.pdf)

- [228] Samantaray, A. K., Bouamama, B. O. 2008. Model-Based Process Supervision - A Bond Graph Approach. *Advances in Industrial Control*. Springer, London, ISBN 978-1-84800-159-6. 483 p. [https://www.researchgate.net/publication/257073596\\_Model-Based\\_Process\\_Supervision\\_A\\_Bond\\_Graph\\_Approach](https://www.researchgate.net/publication/257073596_Model-Based_Process_Supervision_A_Bond_Graph_Approach)
- [229] Norrman, S. 2019. DEMO 16 sectors, HCPB BB FW Cooled in Series with BZ - Extended Thermodynamic Activities with Apros for Simulating DEMO Configuration with IHTS+ESS. IDM-link: EFDA\_D\_2MHGKJ.
- [230] Bachmann, C., Ciattaglia, S., Cismondi, F., Federici, G., Keech, G., Maviglia, F., Siccino, M. 2019. Critical Design Issues in DEMO and Solution Strategies. *Fusion Engineering and Design*, Vol. 146, Part A, p. 178-181. <https://doi.org/10.1016/j.fusengdes.2018.12.013>
- [231] Morris, J., Kovari, M. 2017. Time-Dependent Power Requirements for Pulsed Fusion Reactors in Systems Codes. *Fusion Engineering and Design*, Vol. 124, p. 1203-1206. <https://doi.org/10.1016/j.fusengdes.2017.04.033>
- [232] Deshpande, M. V. 2009. Elements of Electrical Power Station Design. PHI Learning Private Limited, New Delhi, ISBN 978-8120336476, 468 p.
- [233] Takeda, S., Konishi, S., Yamamoto, Y., Kasada, R., Sakurai, S. 2015. Dynamic Simulation-Based Case Study of Fusion on Small-Scale Electrical Grids. *Fusion Science and Technology*, Vol. 68. Iss. 2, p. 341-345. <https://doi.org/10.13182/FST15-106>
- [234] Kakilli, A. 2013. System Analysis with the MVA Method for Symmetrical Three-Phase Faults. *TEM Journal*, Vol. 2, No. 1, p. 51-56. <https://www.temjournal.com/documents/vol2no1/pdf/System%20Analysis%20with%20the%20MVA%20Method%20for%20Symmetrical%20Three-Phase%20Faults.pdf>
- [235] McDonald, M. et al. 2005. Power Swing and Out-of-Step Considerations on Transmission Line. Power System Relaying Comm., IEEE Power Eng. Society. IEEE Report No.: PSRC WG D6, 59 p. [www.ewh.ieee.org/r6/san\\_francisco/pes/pes\\_pdf/OutOfStep/PowerSwingOOS.pdf](http://www.ewh.ieee.org/r6/san_francisco/pes/pes_pdf/OutOfStep/PowerSwingOOS.pdf) (valid on 16.11.2023)
- [236] Novosel, D., Bartok, G., Henneberg, G., Mysore, P., Tziouvaras, D., Ward, S. 2010. IEEE PRSC Report on Performance of Relaying During Wide-Area Stressed Conditions. *IEEE Transactions on Power Delivery*, Vol. 25, No. 1, p. 3-16. <https://doi.org/10.1109/TPWRD.2009.2035202>
- [237] Jeong, Y.-S., Sul, S.-K., Schulz, S., Patel, N. 2003. Fault Detection and Fault Tolerant Control of Interior Permanent Magnet Motor Drive System for Electric Vehicle. Proceedings of the 38<sup>th</sup> IAS Annual Meeting on Conference Record of the Industry Applications Conference, 12-16 October 2003, Salt Lake City, UT, USA, INSPEC Accession No.: 7792930, 6 p. <https://doi.org/10.1109/IAS.2003.1257749>

- [238] Yamayee, Z., A., Bala, J. L. Jr. 1993. Electromechanical Energy Devices and Power Systems. 1<sup>st</sup> Ed., John Wiley & Sons, ISBN 978-0471572176, New York, 528 p. <https://www.wiley.com/en-us/Electromechanical+Energy+Devices+and+Power+Systems+-p-9780471572176>
- [239] Kastha, D., Bose, B. K. 1994. Investigation of Fault Modes of Voltage-Fed Inverter System for Induction Motor Drive. *IEEE Transactions on Industry Applications*, Vol. 30, No. 4, p. 1028-1038. <https://ieeexplore.ieee.org/document/297920>
- [240] Sun, T., Lee, S., Hong, J. 2007. Faults Analysis and Simulation for Interior Permanent Magnet Synchronous Motor Using Simulink@Matlab. Proceedings of the International Conference on Electrical Machines and Systems, 8-11 October 2007, Seoul, Korea, ISBN 978-89-86510-07-2, p. 900-905. [https://www.researchgate.net/publication/224298795\\_Faults\\_analysis\\_and\\_simulation\\_for\\_interior\\_permanent\\_magnet\\_synchronous\\_motor\\_using\\_SimulinkMATLAB](https://www.researchgate.net/publication/224298795_Faults_analysis_and_simulation_for_interior_permanent_magnet_synchronous_motor_using_SimulinkMATLAB)
- [241] Raeder, J. 1995. Report on the European Safety and Environmental Assessment of Fusion Power (SEAFP). *Fusion Engineering and Design*, Vol. 29, p. 121-140. [https://doi.org/10.1016/0920-3796\(95\)80014-O](https://doi.org/10.1016/0920-3796(95)80014-O)
- [242] Van Lew, J. T., Li, P., Chan, C. L., Karaki, W., Stephens J. 2011. Analysis of Heat Storage and Delivery of a Thermocline Tank Having Solid Filler Material. *Journal of Solar Energy Engineering*, Vol. 133, No. 2, Article No.: 021003, 10 p. <https://doi.org/10.1115/1.4003685>
- [243] Brosseau, D., Hlava, P. F., Kelly, M. J. 2004. Testing Thermocline Filler Materials and Molten Salt Heat Transfer Fluids for Thermal Energy Storage Systems Used in Parabolic Trough Solar Power Plants. Sandia National Laboratories, Report No.: SAND2004-3207, 95 p. <https://www.osti.gov/servlets/purl/919178>
- [244] Meier, A., Winkler, C., Wuillemin, D. 1991. Experiment for Modeling High Temperature Rock Bed Storage. *Solar Energy Materials*, Vol. 24, Iss. 1-4, p. 255-264. [https://doi.org/10.1016/0165-1633\(91\)90066-T](https://doi.org/10.1016/0165-1633(91)90066-T)
- [245] Beasley, D. E., Clark, C. J. 1984. Transient Response of a Packed Bed for Thermal Energy Storage. *International Journal of Heat and Mass Transfer*, Vol. 27, Iss. 9, p. 1659-1669. [https://doi.org/10.1016/0017-9310\(84\)90278-3](https://doi.org/10.1016/0017-9310(84)90278-3)
- [246] Brosseau, D., Kelton, J. W., Ray, D., Edgar, M., Chisman, K., Emms, B. 2005. Testing of Thermocline Filler Materials and Molten-Salt Heat Transfer Fluids for Thermal Energy Storage Systems in Parabolic Trough Power Plants. *Journal of Solar Energy Engineering*, Vol. 127, Iss. 1, p. 109-116. <https://doi.org/10.1115/1.1824107>
- [247] Cocco, D., Serra, F. 2015. Performance Comparison of Two-Tank Direct and Thermocline Thermal Energy Storage Systems for 1 MW<sub>e</sub> Class Concentrating Solar Power Plants. *Energy*, Vol. 81, p. 526-536. <https://doi.org/10.1016/j.energy.2014.12.067>

- [248] Hänchen, M., Brückner, S., Steinfeld, A. 2011. High-Temperature Thermal Storage Using a Packed Bed of Rocks - Heat Transfer Analysis and Experimental Validation. *Applied Thermal Eng.*, Vol. 31, Iss. 10, p. 1798-1806. <https://doi.org/10.1016/j.applthermaleng.2010.10.034>
- [249] Kolb, G. J. 2011. Evaluation of Annual Performance of 2-tank and Thermocline Thermal Storage Systems for Trough Plants. *Journal of Solar Energy Engineering*, Vol. 133, No. 3, Article No.: 031023. <https://doi.org/10.1115/1.4004239>
- [250] Singh, H., Saini, R. P., Saini, J. S. 2010. A Review on Packed Bed Solar Energy Storage Systems. *Renewable and Sustainable Energy Reviews*, Vol. 14, Iss. 10, p. 1059-1069. <https://doi.org/10.1016/j.rser.2009.10.022>
- [251] Pacheco, J. E., Showalter, S. K., Kolb, W. J. 2002. Thermocline Thermal Storage System for Parabolic Trough Plants. *Journal of Solar Energy Engineering*, Vol. 124, No. 2, p. 153-159. <https://doi.org/10.1115/1.1464123>
- [252] Angelini, G., Lucchini, A., Manzolini, G. 2014. Comparison of Thermocline Molten Salt Storage Performances to Commercial Two-Tank Configuration. *Energy Procedia*, Vol. 49, p. 694-704. <https://doi.org/10.1016/j.egypro.2014.03.075>
- [253] Cascetta, M., Cau, G., Puddu, P., Serra F. 2014. Numerical Investigation of a Packed Bed Thermal Energy Storage System with Different Heat Transfer Fluids. *Energy Procedia*, Vol. 45, p. 598-607. <https://doi.org/10.1016/j.egypro.2014.01.064>
- [254] Niedermeier, K. 2019. Numerical Investigation of a Thermal Storage System Using Sodium as Heat Transfer Fluid. KIT Scientific Report No.: KIT-SR 7755, ISBN 978-3-7315-0930-1, 208 p. <https://doi.org/10.5445/KSP/1000093902>
- [255] Niedermeier, K., Marocco, L., Flesch, J., Mohan, G., Coventry, J., Wetzel, T. 2018. Performance of Molten Sodium vs. Molten Salts in a Packed Bed Thermal Energy Storage. *Applied Thermal Engineering*, Vol. 141, p. 368-377. <https://doi.org/10.1016/j.applthermaleng.2018.05.080>

## **Publications, conferences, seminars and supervision contribution**

### **Publications**

Hering, W., Bubelis, E., Perez-Martin, S., Bologna, M.-V. 2021. Overview of Thermal Hydraulic Optimization and Verification for the EU-DEMO HCPB BOP ICD Variant. *Energies*, 14(23), Article No.: 7894. <https://doi.org/10.3390/en14237894>

Bologna M.-V., Bubelis, E., Hering, W. 2021. Parameter Study and Dynamic Simulation of the DEMO Intermediate Heat Transfer and Storage System Design Using MATLAB®/Simulink. *Journal Fusion Engineering and Design*, Vol. 166, Article No.: 112291. <https://doi.org/10.1016/j.fusengdes.2021.112291>

Bologna M.-V., Stieglitz, R., Hering W., Bubelis E. 2019. Parameter Study and Dynamic Simulation of Current DEMO Intermediate Heat Transfer and Storage System Design via MATLAB®/Simulink. 14<sup>th</sup> International Symposium on Fusion Nuclear Technology (ISFNT-14), Budapest, Hungary, September 22-27, 2019. <https://publikationen.bibliothek.kit.edu/1000099197/45106288>

Onea A., Diez de los Rios Ramos, N., Bologna, M.-V., Hering W., Stieglitz, R., Stüber, M., Sven, U. 2017. Considerations on Thermal Radiation of Direct Solar Thermal Power Generation Systems for Space Propulsion. Aerospace Europe 6<sup>th</sup> Council of European Aerospace Societies (CEAS) Conference, 2017, Paper No. 194. <https://www.fzt.haw-hamburg.de/pers/Scholz/ewade/2017/CEAS2017/194-final.pdf>

### **Conferences and seminars**

Bologna, M.-V. 2021. Dynamic Simulation of Energy Transfer Chain for DEMONstration Balance of Plant. Presentation at the Seminar of the Institute for Neutron Physics and Reactor Technology, April 26<sup>th</sup>, 2021.

Bologna M.-V. 2020. Dynamic Simulation of Power Conversion System for DEMONstration Balance of Plant via MATLAB®/Simulink. Abstract and Presentation at 6<sup>th</sup> INR Ph.D. Students Seminar, Haus der Kirche, Bad Herrenalb, October 14<sup>th</sup> - 15<sup>th</sup>, 2020.

Bologna M.-V. 2020. Dynamic Model of Energy Transfer Chain for DEMONstration Fusion Power Plant. Presentation at Workshop for Energy System Integration at Research Centre, Jülich, Germany, January 28<sup>th</sup>, 2020.

Bologna M.-V. 2019. Dynamic Modelling of Energy Transfer Chain for DEMONstration Fusion Power Plant. Presentation at 6<sup>th</sup> Energy System Integration Coordination Meeting, Fraport Conference Center, Frankfurt am Main, November 12<sup>th</sup>, 2019.

Bologna M.-V. 2019. Dynamic Simulation of Single-Tank Thermocline Storage System for DEMO Fusion Power Plant. Abstract and Presentation at 5<sup>th</sup> INR Ph.D. Students Seminar, Haus der Kirche, Bad Herrenalb, October 8<sup>th</sup>, 2019.

Bologa M.-V. 2019. Dynamic Simulation of IHTS, PCS & Synchronous Generator Model for DEMONstration Fusion Power Plant. Presentation at ES2050 Doctoral Seminar, Parkhotel am Taunus, Oberursel, September 4<sup>th</sup> - 5<sup>th</sup>, 2019.

Bologa M.-V. 2019. Dynamic Simulation of IHTS, PCS & Synchronous Generator Model for DEMONstration Fusion Power Plant. Seminar Presentation at Institute for Neutron Physics and Reactor Technology, KITopen-ID: 1000098242, HGF Programme 31.03.05 (POF III, LK 01) - Plant Engineering, July 8<sup>th</sup>, 2019.

Bologa M.-V. 2019. Dynamic Simulation of Current Generator Design for DEMONstration Fusion Power Plant via MATLAB®/Simulink, 9<sup>th</sup> KIT Fusion Ph.D. Students Seminar, Kurhaus Trifels, Annweiler, Germany, May 23<sup>rd</sup> - 24<sup>th</sup>, 2019.

Bologa M.-V. 2019. Dynamic Modelling and Optimization of Intermediate Heat Transfer and Storage System of DEMO Fusion Power Plant. Presentation at Energy System Integration 2050+WP1 Meeting, Frankfurt am Main, May 9<sup>th</sup>, 2019.

Bologa M.-V. 2018. Dynamic Modeling and Optimization of Intermediate Heat Transfer and Storage System of DEMO Fusion Power Plant. 4<sup>th</sup> INR Ph.D. Students Seminar, Haus der Kirche, Bad Herrenalb, Germany, October 10<sup>th</sup> – 11<sup>th</sup>, 2018.

Bologa M.-V. 2018. Modeling of Intermediate Heat Transfer and Storage System of DEMO Fusion Power Plant. 8<sup>th</sup> KIT Fusion Ph.D. Students Seminar, Haus am Weinberg, St. Martin, Germany, June 6<sup>th</sup> - 7<sup>th</sup>, 2018.

## **Supervision of Master Thesis and International Internship**

Oliveira, J. 2018. Dynamic Simulation Using MATLAB®/Simulink to Improve the Current DEMO-IHTS Design. Master Thesis, Department of Mechanical Engineering, Karlsruhe Institute of Technology / HECTOR School of Engineering and Management (Cooperation with Kraftanlagen Heidelberg GmbH), 110 p.

Pasquet, C. 2019. Dynamic Simulation of a Single-Tank Thermocline Storage System for DEMO-IHTS using MATLAB®/Simulink. International Internship of a Master Student (Cooperation between KIT and École Polytechnique, Paris-Sud, France), Presentation at INR, September 3<sup>rd</sup>, 2019, 28 p.

Nawaz, H. 2020. Dynamic Modelling of Power Conversion System for a Fusion Power Plant. Master Thesis, Department of Mechanical Engineering, Karlsruhe Institute of Technology (Cooperation between KIT and University of Applied Science in Karlsruhe), 94 p.



# A Appendix

## A.1 DEMONstration Balance of Plant coupling design concepts

Direct Coupling Design (DCD) concept, which is discussed in ref. [55], involves Direct-AUXB (DCD-1), as well as Direct-Small ESS (DCD-s1 and DCD-s2) design approaches. For DCD-1 design (see Table A1.1), the avoidance of generator synchronization loss in dwell period is accomplished by using a boiler, that provides steam flow to turbine and maintains power train in operation. The disadvantage is that the auxiliary boiler power has to reach the level of several hundred MWs during dwell time, what implies additional infrastructure. Another drawback is temperature and pressure transients, which are achieved in pulse operation. In DCD-s1 concept (see Table A1.2), a part of thermal energy is collected in ESS during pulse operation. The main challenge is that ESS has difficulties in providing thermal energy, which has to be stored in relatively short time as required for dwell time. The DCD-s2 concept (see Table A1.2) is based on application of molten salt and an electrical heater upstream hot storage tank. This approach allows maximizing electrical power production in pulse operation, while maintaining the electrical generator synchronized to grid in dwell phase, whereby steam turbine is designed to operate at minimum required load of 10% [63].

The scheme of DEMO DCD concept is shown in Fig. A1.1 [40, 47, 55-58, 241]. For DEMO DCD concept, the nominal power of  $\sim 790$  MW is evaluated for steam turbines [57]. Considering 5% losses due to coupling between turbine and synchronous generator, nominal electrical power output of  $\sim 750$  MW is estimated (see Fig. A1.2). However, for DCD concept, pulse operation of fusion reactor and abrupt changes in steam mass flow are detrimental to turbines, as thermo-mechanical stresses can lead to premature failures of turbines.

The idea of Indirect Coupling Design (ICD) concept (see Table A1.1) is to reduce the stress of steam turbines and to ensure a constant electrical power output at generator's level [40, 41, 47, 52, 53, 55, 69]. The DEMO ICD provides the decoupling using a HTF storage loop, which accumulates thermal power in pulse operation that is released to DEMO PCS in dwell operation.

The DEMO ICD concept, in which DEMO IHTS provides Thermal Energy Storage between DEMO PHTS and DEMO PCS systems, is schematically presented in Fig. A1.3 [47, 59, 70, 97, 98]. Here, the nominal power of  $\sim 675$  MW for turbines is estimated [40]. With generators' coupling efficiency of 95%, the resulting active power output of  $\sim 640$  MW is assumed at electrical generator level (see Fig. A1.4) [57].

<b>System</b>		<b>Direct Coupling Design DCD-1 (DIRECT-AUXB)</b>	<b>Indirect Coupling Design (ICD)</b>
<b>PHTS</b>	Interface PHTS and IHTS/PCS	Helium-water steam generator	Helium-molten salt heat exchangers
	PHTS HX/SG pressure	High	Low
<b>IHTS</b>	Fluid	-	Molten salt
	Storage capacity	-	2·3000 m <sup>3</sup>
	Additional thermal storage	-	-
	Auxiliary heating system	Gas (220 MW <sub>th</sub> )	-
	Gas-fired boiler supply	Large	-
	Space	Large (auxiliary system)	Large (IHTS/ESS)
<b>PCS</b>	Turbine loads	Frequent ramps	Steady
	System feasibility	Under investigation	Yes
	Tolerant to frequent transients	Under investigation	Under investigation
<b>Total</b>	Critical components	Helium-water heat exchangers, external gas boiler, steam turbine	Helium-molten salt heat exchangers, steam generator, PCS heat exchangers
	Required supplemental power	Gas	-

Table A1.1: Direct Coupling Design (DCD-1) with Auxiliary Boiler (DIRECT-AUXB) and Indirect Coupling Design (ICD) concepts.

System	DIRECT-Small Energy Storage System		
		DCD-s1	DCD-s2
<b>PHTS</b>	Interface PHTS and IHTS/PCS	Helium-water steam generator	Helium-water steam generator
	PHTS HX/SG pressure	High	High
<b>IHTS</b>	Fluid	-	Molten salt
	Storage capacity	-	2-400 m <sup>3</sup>
	Additional thermal storage	Concrete	-
	Auxiliary heating system	Gas (93 MW <sub>th</sub> )	Electric (41.2 MW <sub>el</sub> )
	Gas-fired boiler supply	Medium	-
	Space	Large (auxiliary system/concrete)	Medium (electric/ESS)
	<b>PCS</b>	Turbine loads	Frequent ramps
	System feasibility	-	Under investigation
	Tolerant to frequent transients	-	Under investigation
<b>Total</b>	Critical components	ESS, helium-water heat exchangers	Helium-molten salt heat exchangers, helium-water heat exchangers, steam turbine
	Required supplemental power	Gas	Electrical power

Table A1.2: Direct-Small Energy Storage System (DIRECT-Small ESS) coupling design concepts DCD-s1 and DCD-s2.

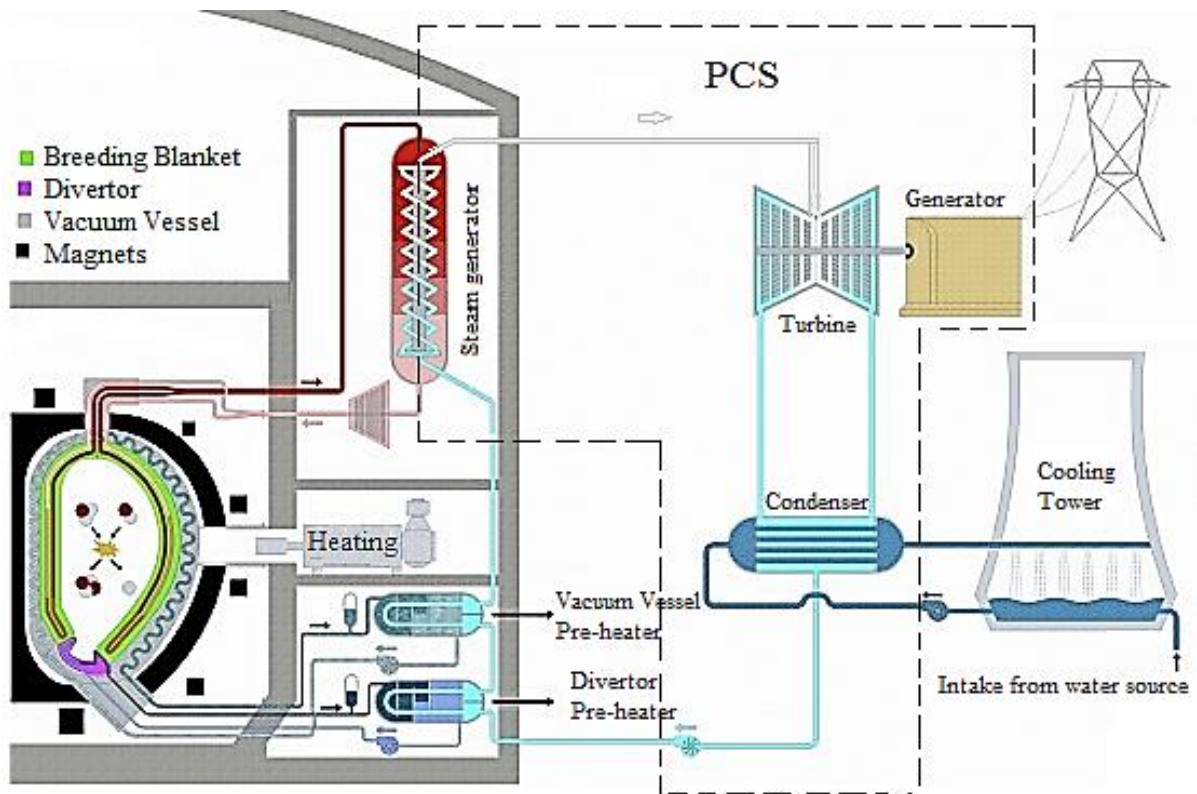


Fig. A1.1: DEMO BoP Direct Coupling Design concept [47].

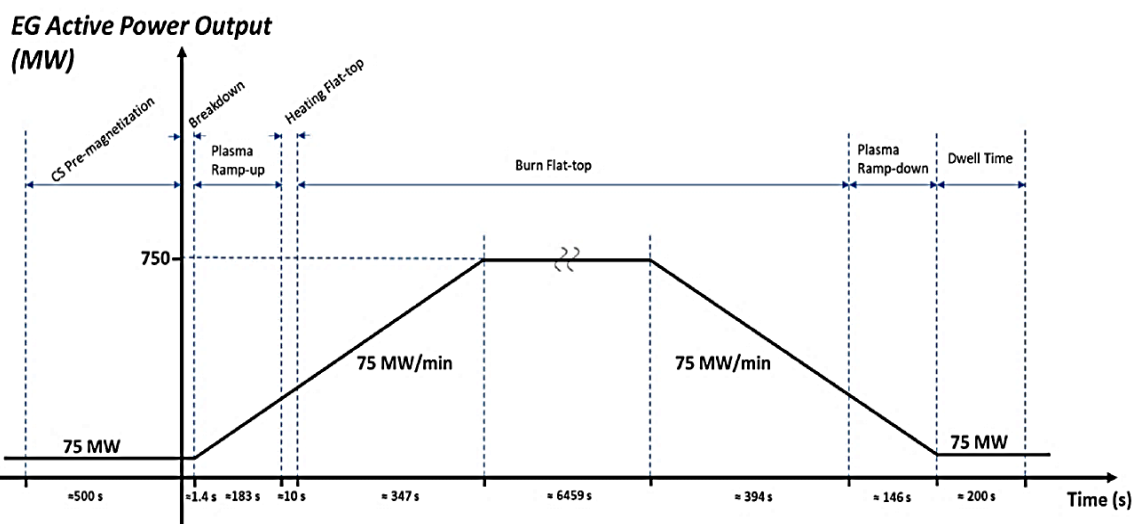


Fig. A1.2: Electrical power output profile for DEMO DCD concept [57].

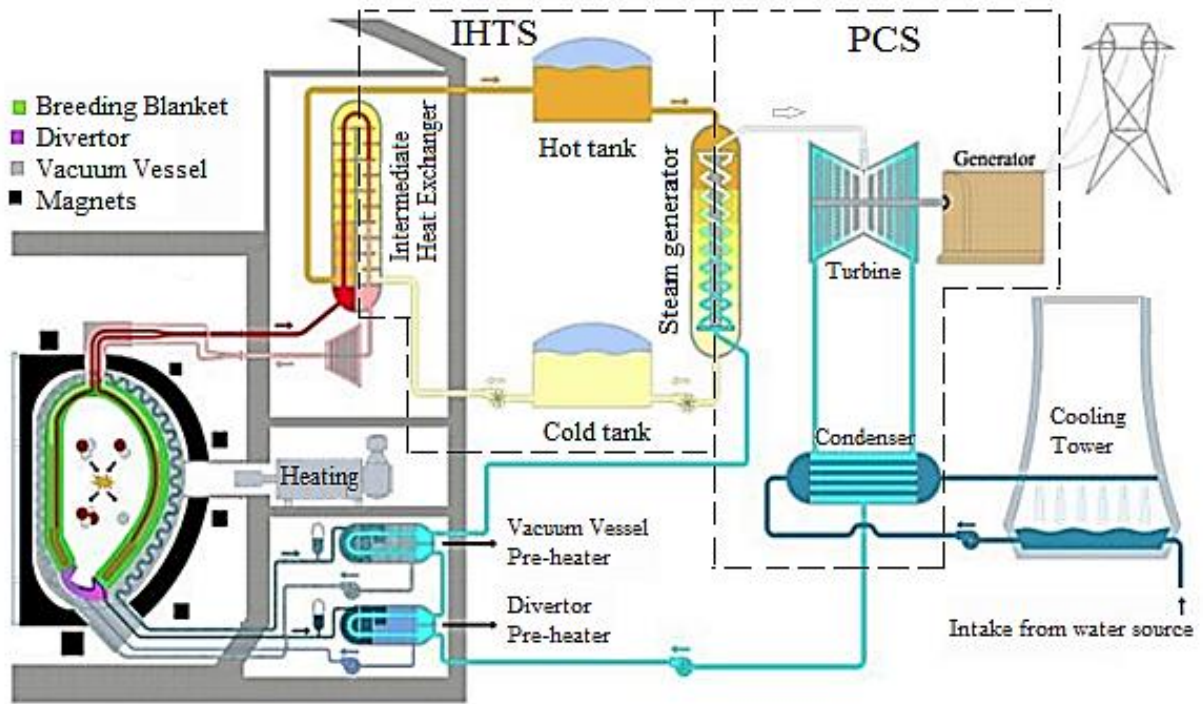


Fig. A1.3: DEMO BoP Indirect Coupling Design concept [47].

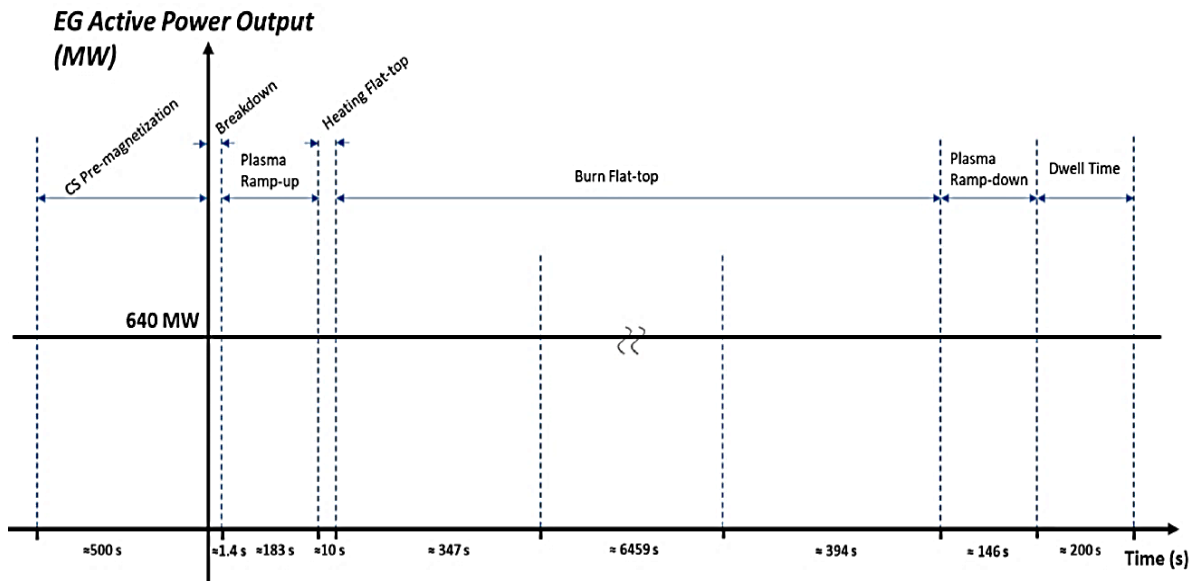


Fig. A1.4: Electrical power output profile for DEMO ICD concept [57].

## A.2 DEMO BoP quasi-stationary simulation model

The schemes of DEMO BoP quasi-stationary model for fusion reactor pulse and dwell operation, simulated using EBSILON<sup>®</sup>, are presented in Fig. A2.1 and Fig. A2.2, respectively [84, 97-102]. The main operational parameters of DEMO BoP are listed in Table A2.1.

Referring to simulation model, DEMO PHTS architecture relies on the adoption of eight cooling loops. The IB is cooled by means of four loops, whereas the remaining four circuits are used to remove thermal power from OB portion. DEMO IHTS model includes two thermal storage tanks, pumps with air-cooled equipment, pipelines, auxiliary systems, ventilation equipment, as well as control sensors and diagnostics [98]. Thermal storage tanks have identical geometry. The regulator of hot HTF flow is responsible to keep operating temperature continuously. DEMO PCS model includes a steam generator with two stages, each out of eight units for High Pressure (HP) and Low Pressure (LP) System [84]. The model includes several HP and LP steam turbines with two steam re-heaters and drain in between, a condenser, feedwater heat exchangers, a vacuum vessel pump and a turbo-generator. Additionally, there are two more each LP and HP feedwater pre-heaters. Steam generator stages include a pre-heater, a heat exchanger and a super-heater. Each feedwater aggregate consists of a booster pump, gearbox, electrical motor and main pump, being connected in series. The deaerator has an operation regime, which is acceptable because of a controlled condensate by-pass system.

<b>Parameter</b>	<b>Ref. [99]</b>	<b>Ref. [100]</b>	<b>Ref. [84]</b>
Fusion power, MW		2037	
Thermal energy demand (pulse), MW	2389		2102
Thermal energy demand (dwell), MW	17		21
<b>Steady-state conditions</b>			
Gross electrical power, MW	1005	1009	987
Net electrical power, MW	854	841	839
<b>Fusion reactor pulse operation</b>			
Gross electrical power, MW	818	916	893
Net electrical power, MW	667	750	758
<b>Fusion reactor dwell operation</b>			
Dwell time, min	30	15	10
Gross electrical power, MW	706	803	930
Net electrical power, MW	686	783	892

Table A2.1: Main operational parameters of DEMO BoP calculated using EBSILON<sup>®</sup> code.

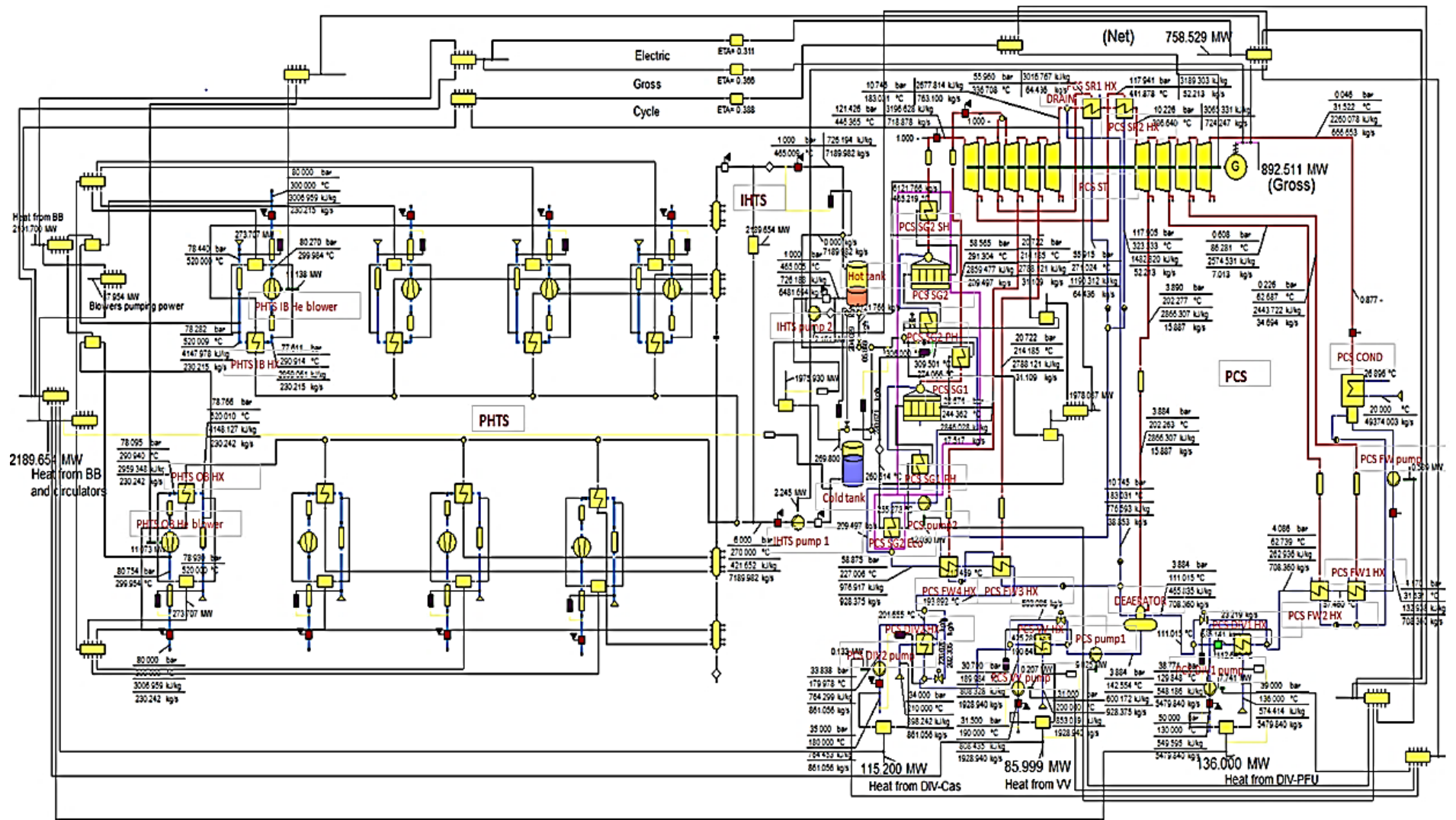


Fig. A2.1: DEMO BoP simulation model using EBSILON® code, pulse operation time [84].

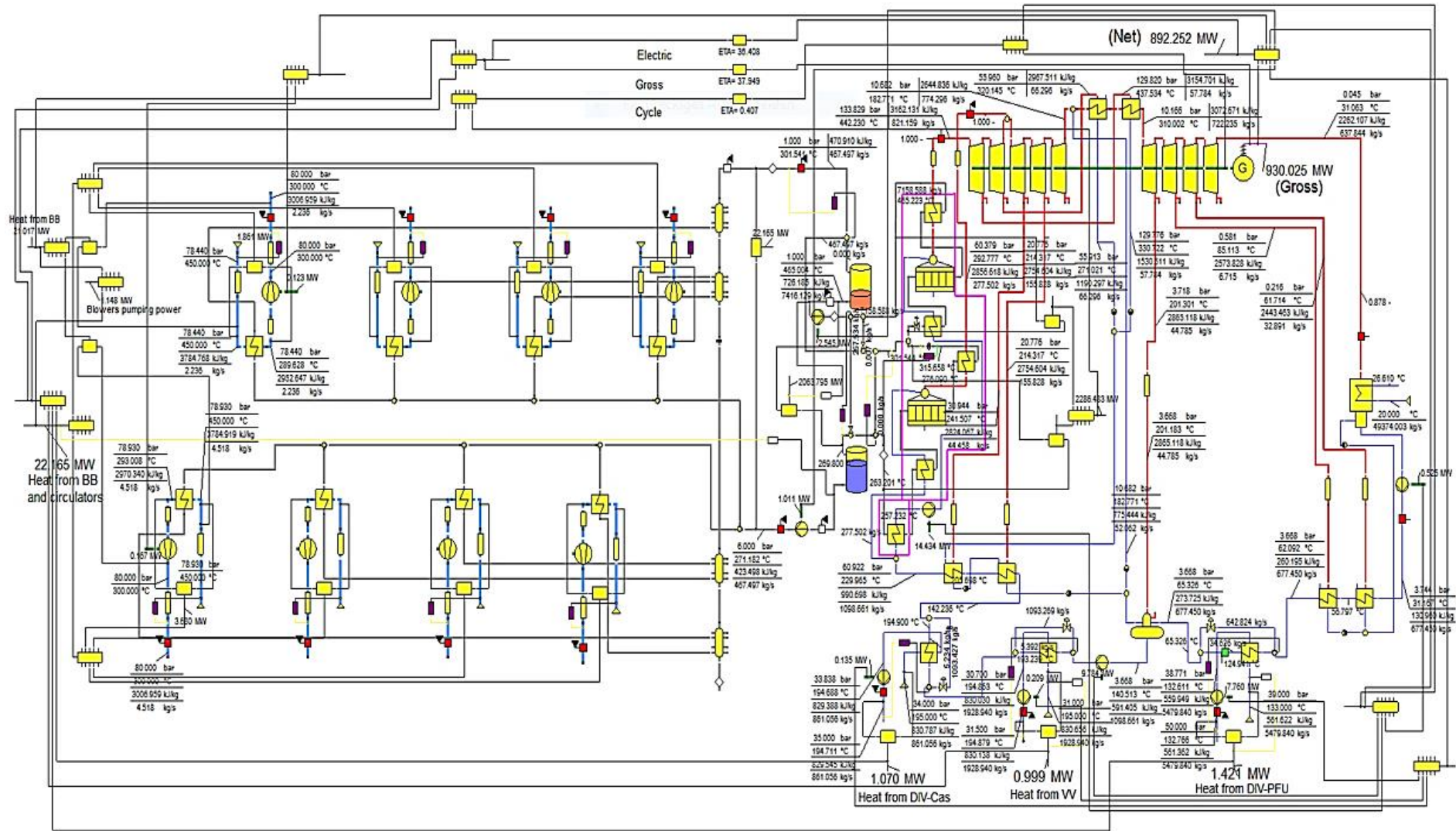


Fig. A2.2: DEMO BoP simulation model using EBSILON® code, dwell operation time [84].



### **A.3 TES single tank design concept**

The design concept of a single tank, which includes hot and cold sections, separated by a temperature gradient inside the tank, is discussed in ref. [94, 95, 111, 124, 125]. Due to large buoyancy forces, relative to mixing forces, a cold HTF lies in lower portion of the storage tank, meanwhile hot HTF lies in upper one. Transitional temperatures between hot and cold levels are observed within a heat exchange region. During heat charging, hot HTF flows down the storage tank, transferring thermal energy to solid material. During heat discharging, cold HTF flows up the storage tank, extracts thermal energy from solid material and flows out at high temperature.

The energy storage depends on tank's dimensions, properties of HTF and filler material, fluid velocity and charging/discharging time [95, 129, 242-253]. The storage efficiency depends on energy value, recovered after every charging/discharging cycle, as well as on maximum storable thermal energy. The discharge efficiency grows with increase in stored thermal energy and decreases with augment in discharge power [94, 95, 107, 115, 131-134]. However, repeated cycles result in progressive reduction of energy, being stored in solid material. An increase in temperature threshold tolerance improves energy storage capacity.

For thermocline design concept, taller thermal storage tanks with smaller diameters are preferable [124]. Tall and thin storage tanks show better thermal stratification and higher discharge efficiency. Thermocline tanks with larger height effectively extend the discharge state, wherein HTF temperature is maintained at a high level [95].

High volumetric heat capacity of filler material increases total thermal energy, being stored in the tank. The stratification within the filler material reduces mixing within storage tank. The decrease in filler material diameter improves thermal stratification and sustained outflow of HTF with a higher thermal quality. In ref. [129] is shown that at particle size of 1.9 cm, heat transfer rates within the particles, among them and HTF, are large. If particle diameter is over 10 cm, HTF outlet temperature decreases faster, what reduces discharging time and operation efficiency. Usually, filler material is non-hazardous and cost-effective [124, 126, 128, 131, 135, 136, 141-143].

The simulations of thermocline tank are highlighted in ref. [82, 107, 108, 112, 132, 134-138]. In ref. [132], CFD modelling is used to study the influence of Reynolds number on storage process characteristics. In ref. [135], MATLAB® tool is used for process simulations. In ref. [137, 138], a set-up with a heated packed pebble bed, using hot air flow, is modelled. The influence of HTF and solid material properties, tank's dimensions and packing schemes of solid filler, as well as duration of charging/discharging time, on the energy storage effectiveness is discussed. In ref. [254, 255],

a 2-phase 2D-model, using MATLAB<sup>®</sup>, is applied for simulation of fluid dynamic processes inside a thermocline tank of a Concentrated Solar Power Plant. Simulations are carried out for a single packed-bed storage tank with a height of 9.9 m, diameter-to-height ratio of 0.5 and capacity of 40 MWh<sub>th</sub>.

The reduction of costs is the main reason for application of a single thermocline tank [246-253]. In comparison to a two tank system, the usage of thermocline system allows reduction of energy production cost [96, 192, 247, 249]. The single tank design needs less stainless steel and thermal insulation material, smaller volume of HTF and less expansive pumping system. A thermocline tank requires  $\sim 2/3$  of cost associated with an equivalent two tank TES [73, 94, 141, 249]. Nevertheless, for an overall cost estimation, the costs of tank material, instrumentation, piping, as well as total storage capacity are required [88, 115, 134, 192].

In comparison to two tank system, a thermocline tank is not able to fully exploit its energy storage volume [247-252]. The thermocline TES uses only a portion of its energy storage volume. A part of HTF, being stored in thermocline tank, is at an average temperature between maximum and minimum values, what differs from two tank systems, where HTF is steadily withdrawn at nominal temperature. Owing to presence of temperature gradient inside the storage tank, thermocline systems are less efficient than two tank systems. The reason therefore is that the useful thermal energy recovered during discharging phase is lower than that supplied during charging phase [247, 253]. For a two tank system, the discharge efficiency can reach the value of 100%, while the thermocline storage manages to supply only 64% of stored heat [247-252].

#### A.4 TES operational parameters for DEMO BoP and CSP plants

<b>Parameter</b>	<b>Demonstration Solar Tower Plant Project “Solar Two” [95, 106, 110, 123]</b>	<b>Solar Energy Generating Systems [92]</b>	<b>DEMO BoP [84]</b>
Place	Daggett, Mojave Desert, CA, USA	Daggett, Mojave Desert, CA, USA	Under investigation
Type	Solar Power Tower	Ultimate Parabolic Trough Power Plant	DEMO BoP with IHTS
Case	Closed case	Operational	Under investigation
Commission date	1995-1999	2013	Under investigation
HTF	Molten salt 60% NaNO <sub>3</sub> 40% KNO <sub>3</sub>	Molten salt 60% NaNO <sub>3</sub> 40% KNO <sub>3</sub>	Molten salt 7% NaNO <sub>3</sub> 53% KNO <sub>3</sub> 40% NaNO <sub>2</sub>
Number of parallel tank pair (cold & hot tank)	1	1	1
Active salt inventory, tons	4778	-	5040
Thermal storage capacity, MWh <sub>th</sub>	105	3233	426
Cold tank dimensions, H [m] and D [m]	12 and 16.6	-	7.8 and 23.8
Hot tank dimensions, H [m] and D [m]	12 and 16.8	-	7.8 and 23.8
Operating temperature in cold tank, K	-	573	543
Operating temperature in hot tank, K	-	823	738
Operating temperature difference, K	-	250	195
Equivalent full load hours for thermal storage capacity, h	1	3	2

Table A4.1: Thermal Energy Storage operational parameters.

## A.5 DEMONstration Balance of Plant parameters

Parameter	PHTS Heat Exchanger (HX)	
	Inner Blanket HX	Outer Blanket HX
Units	4	4
Prim. Medium / Sec. Medium	Helium (gas) / HITEC (liq.)	
$\Delta P_{\text{tubes}}$ , bar	0.67	
$\Delta P_{\text{shell}}$ , bar	1.05	1.03
Specific dissipation, kW/K	1095.50	1095.48
Prim. inlet/outlet diameter, m	1.2/1.0	
Sec. inlet/outlet diameter, m	0.5	
Prim. work pressure (inlet/outlet), bar	78.3/77.6	78.8/78.1
Sec. work pressure (inlet/outlet), bar	6/5	
Prim. work temperature (inlet/outlet), K	793/563	
Sec. work temperature (inlet/outlet), K	543/738	
Prim. medium vol. flow (inlet/outlet), m <sup>3</sup> /s	49/35.4	48.7/35.2
Sec. medium vol. flow (inlet/outlet), m <sup>3</sup> /s	0.48/0.52	
Prim./Sec. medium mass flow, kg/s	230/899	
Prim. medium density (inlet/outlet), kg/m <sup>3</sup>	4.7/6.5	4.7/6.6
Sec. medium density (inlet/outlet), kg/m <sup>3</sup>	1888/1741	
Prim. medium velocity (inlet/outlet), m/s	43.4/45	43.1/44.8
Sec. medium velocity (inlet/outlet), m/s	2.4/2.6	

Table A5.1: DEMO PHTS heat exchangers' parameters [84].

<b>Parameter</b>	<b>Value</b>
Coolant	Helium
Inlet/outlet temperature, K	793/573
Coolant inlet pressure, MPa	8
Coolant outlet pressure in IB/OB, MPa	7.79/7.83
Segment pressure drop in IB/OB, MPa	0.214/0.174
Coolant mass flow rate, kg/s	204
Coolant enthalpy at inlet/outlet, kJ/kg	3007/4148

Table A5.2: DEMO PHTS parameters [84, 100].

<b>Parameter</b>	<b>Cold tank</b>		<b>Hot tank</b>	
	<b>Ref. [100]</b>	<b>Ref. [84]</b>	<b>Ref. [100]</b>	<b>Ref. [84]</b>
Required storage tank volume, m <sup>3</sup>		2669	2895	2897
HTF vol. flow (inlet), m <sup>3</sup> /s		3.88	4.22	4.13
HTF mass flow (inlet), kg/s	7322	6481	7338	7189
HTF mass flow (outlet), kg/s	7338	7189	7322	6481
HTF density (inlet/outlet), kg/m <sup>3</sup>		1888		1741
HTF velocity (inlet/outlet), m/s		2.53	2.74	2.68
Amount of MS for dwell time, kg			5040000	
Temperature of molten salt, K		543		738

Table A5.3: DEMO IHTS parameters.

<b>Parameter</b>	<b>Ref. [100]</b>	<b>Ref. [84]</b>
<b>1<sup>st</sup> stage steam generator / 2<sup>nd</sup> stage steam generator</b>		
<b>Fusion reactor pulse operation time</b>		
Steam temperature (inlet/outlet), K	555/721	564/719
Steam pressure (inlet/outlet), bar	57.11/22.54	58.56/121.43
<b>Fusion reactor dwell operation time</b>		
Steam temperature (inlet/outlet), K	555/718	566/715
Steam pressure (inlet/outlet), bar	57.11/133.86	60.38/133.83

Table A5.4: DEMO PCS parameters.

## A.6 DEMONstration Balance of Plant systems' design and operational parameters

Table A6.1 Beginning

Parameter	Quasi-stationary simulation		Dynamic simulation	Comment
	Ref. [100]	Ref. [84]	Value	
<b>PHTS IB/OB HXs</b>				
Each IB heat transfer loop				
Helium flow rate, kg/s	195.2	230.2	920	Helium mass flow is divided uniformly between 4 HXs: ~230·4
Each OB heat transfer loop				
Helium flow rate, kg/s	240.1	230.2	920	Helium mass flow is divided uniformly between 4 HXs: ~230·4
Helium temperature, PHTS inlet, °C	-	520	520	
Helium heat capacity, J/(kg·K)	-	-	5193	Initial data
<b>HCPB BB PHTS IB/OB HXs</b>				
Total generation of power, MW	2101.7	2101.7	2100	Theoretically calculated
<b>HCPB BB PHTS IB/OB HXs (tube &amp; shell HX)</b>				
Configuration	tube & shell		tube & shell	
Cross-section area at HX inlet/outlet, m <sup>2</sup>	-	-	0.196/0.196	Required parameter for HX module
Specific dissipation OB/IB HX, kW/K	-	-	1095.50/ 1095.48	Required parameter for HX module
Helium volume, m <sup>3</sup>	53.2	-	229	Volume of 4 units, increase with ~8%
Pressure drop OB/IB HX, kPa	264.6	-	103/105	Required parameter for HX module
<b>PHTS IB HX</b>				
Total units	3	4	4 HX blocks	Modules are installed in parallel
Prim. Medium	Helium (gas)	Helium (gas)	Helium (gas)	

Table A6.1 Continuation

Sec. Medium	HITEC (liq.)	HITEC (liq.)	HITEC (liq.)	
Reference inflow pressure, MPa	-	-	0.01	Required parameter inside HX module
Prim. Work temperature (inlet/outlet), °C	500/287	520/290.9	520	
Sec. Work temperature (inlet/outlet), °C	270.2/465	270/465	270	Required parameter inside HX module
Reference inflow temperature, °C	-	-	200	Required parameter inside HX module
Prim. Medium mass flow, kg/s	195.22	230.22	230	Inlet helium mass flow for HX module
Sec. Medium mass flow, kg/s	709.37	898.75	899	Required parameter inside HX module
Mass flow threshold for flow reversal, -	-	-	10 <sup>-3</sup>	Fixed parameter inside HX module
<b>PHTS OB HX</b>				
Total units	6	4	4	Modules are installed in parallel
Prim. Medium	Helium (gas)	Helium (gas)	Helium (gas)	
Sec. Medium	HITEC (liq.)	HITEC (liq.)	HITEC (liq.)	
Reference inflow pressure, MPa	-	-	0.01	Required parameter inside HX module
Prim. Work temperature (inlet/outlet), °C	500/288	520/290.9	520	
Sec. Work temperature (inlet/outlet), °C	270.2/465	270/465	270	Required parameter inside HX module
Reference inflow temperature, °C	-	-	200	Required parameter inside HX module
Prim. Medium mass flow, kg/s	240.13	230.24	230	Inlet helium mass flow for HX module
Sec. Medium mass flow, kg/s	868.37	898.75	899	Required parameter inside HX module
Mass flow threshold for flow reversal, -	-	-	10 <sup>-3</sup>	Fixed parameter inside HX module

**Abbreviations:**

BB - Breeding Blanket

IB - Inner Blanket

HCPB - Helium Cooled Pebble Bed

HX - Heat Exchanger

OB - Outer Blanket

PHTS - Primary Heat Transfer System

Table A6.1: DEMO Primary Heat Transfer System parameters.

Table A6.2 Beginning

Parameter	Quasi-stationary simulation		Dynamic simulation	Comment
	Ref. [100]	Ref.[84]	Value	
<b>DEMO IHTS tanks design parameters</b>				
Tank diameter (D), m	23.8	23.8	24	
Tank height (H), m	6.8	7.8	7.5 – 10	Variable in simulations
Required volume of tank (hot/cold), m <sup>3</sup>	2895.2/2669.7	2896.9/2671.3	3391	
Footprint of TES, m <sup>2</sup>	2550	2550	2550	Required parameter
Height for tank inlet/outlet diameter, m	-	-	0.4-0.7	Variable in simulations
Inlet/outlet pipeline diameter, m	1.40	1.40	1.40	
Inlet/outlet tank diameter, m	1.40	1.40	1.40	
Inlet/outlet pump diameter, m	1.40	1.40	1.40	Required parameter
Cross-section area (inlet/outlet), m <sup>2</sup>	-	-	1.5386	Customized module: properties f(T)
Heat transfer fluid	HITEC	HITEC	HITEC	
Required mass of MS per tank, t	5040	5043	5083	Pulse operation: stable operation of pump 1 for 180-7050 sec
Tank nominal volume (per tank), m <sup>3</sup>	3000	3000	Variable	Volume: f(D), f(H)
Tank heat storage capacity, MWh <sub>t</sub>	426	426	f(T)	Variable: cold/hot tank
HITEC mass flow difference, kg/s	-	-	740	Difference between mass flow at inlet and outlet of hot tank
HTF specific heat capacity, J/(kg·K)	-	-	f(T)	Variable: customized programme module
HTF critical temperature of HTF, °C	-	-	200	Required parameter: to avoid HITEC crystallization
Cover gas	Argon	Argon	Argon	
Argon thermal conductivity, W/(m·K)	0.0354	0.0354	0.0354	Hot tank (465 °C)
	0.0296	0.0296	0.0296	Cold tank (270 °C)
Model	Quasi-stationary		Dynamic	Variable solver
Modeling operation time intervals, sec			7200/600	Pulse/dwell
Default error of model, -	-	-	0.001	Required parameter
Computed state accuracy, %	-	-	0.1	Required parameter



Table A6.2 Continuation

Continued operation conditions	- No chemical reactions of HITEC with environment - No leaks in system - No contamination of HITEC			
Average wind velocity, m/s	-	-	5	
Air temperature at tank wall surface, °C	-	-	65	Boundary conditions [182]
Ambient temperature, °C	-	-	25	
Ambient pressure, Pa	-	-	101235	
Life time of TES system, years	-	-	50	
<b>IHTS hot tank operational parameters</b>				
Prim. Medium (liq.)	HITEC	HITEC	HITEC	MS properties are f(T)
Filling level of HTF in the tank, %	-	-	5/95	Min/Max, variable: f(H)
Work pressure (inlet/outlet), bar	1-2	1-2	1-2	Uniform throughout tank volume
Temperature of HTF at surface/bulk, °C	-	-	460/465	Put into code for storage tank
Work temperature (inlet/outlet), °C	465	465	465	Homogenous inside tank
Medium vol. flow (inlet/outlet) m <sup>3</sup> /s	4.22	4.13/3.72	f(T)	Variable
Medium mass flow (inlet), pulse, kg/s	7338.34	7189.98	6660	Calculated (sensor data), average value
Medium mass flow (outlet), pulse, kg/s	7322.38	6481.69	5920	
Medium mass flow (inlet), dwell, kg/s	-	-	418	
Medium mass flow (outlet), dwell, kg/s	-	-	7980	
Energy flow (inlet), pulse, GW	-	-	1.76	
Energy flow (outlet), pulse, GW	-	-	1.58	Calculated (sensor data), average value
Energy flow (inlet), dwell, GW	-	-	0.11	
Energy flow (outlet), dwell, GW	-	-	2.13	
Theoretical heat flow (inlet), pulse, GW	-	-	1.67	Theoretically calculated using operation data for HTF
Theoretical heat flow (outlet), pulse, GW	-	-	1.49	
Theoretical heat flow (outlet), dwell, GW	-	-	2	
Medium density (inlet/outlet), kg/m <sup>3</sup>	1740.81	1740.81	f(T)	Customized module
Medium velocity (inlet/outlet), m/s	2.74	2.68/2.42	f(T)	Variable

Table A6.2 Continuation

<b>IHTS cold tank operational parameters</b>				
Prim. Medium (liq.)	HITEC	HITEC	HITEC	MS properties are f(T)
Filling level of HTF in the tank, %	-	-	5/95	Min/Max, variable f(H)
Temperature of HTF at surface/bulk, °C	-	-	297/302	Put into code for storage tank
Work pressure (inlet/outlet), bar	1-2	1-2	1-2	Uniform throughout tank volume
Work temperature (inlet/outlet), °C	270	269.8	270	Homogenous inside tank
Medium vol. flow (inlet), m <sup>3</sup> /s	3.88	3.43/3.81	f(T)	Variable
Medium mass flow (inlet), pulse, kg/s	7322.38	6481.69	5920	
Medium mass flow (outlet), pulse, kg/s	7338.34	7189.98	6660	
Medium mass flow (inlet), dwell, kg/s	-	-	7980	Calculated (sensor data), average value
Medium mass flow (outlet), dwell, kg/s	-	-	418	
Medium density (inlet/outlet), kg/m <sup>3</sup>	1887.74	1887.81	f(T)	Customized module
Medium velocity (inlet/outlet), m/s	2.53	2.23/2.47	f(T)	Variable
<b>DEMO IHTS pipelines and pumps parameters</b>				
Segmented length, m	-		1/10/20/150/200	MATLAB <sup>®</sup> code: thermal fluid pipe is segmented and viewed as assembly of smaller pipes.
Length of pipelines 1 & 2, m	-		200	
Length of pipelines 3 & 6, m	-		10	
Length of pipelines 4 & 5, m	-		40	
Pipeline diameter, m	1.4		1.4	
Pipelines 1 and 2: Elevation gain, m	-		50	
Pipelines 4 and 5: Elevation gain, m	-		10	
Pipelines 3 and 6: Elevation gain, m	-		0	Required parameter inside pipe module
Aggregate equivalent length of local resistances, m	-		0.3	
Pipeline wall thickness, m	0.025		0.025	Stainless steel 1.4301 [182]
Internal surface absolute roughness, m	-		2·10 <sup>-6</sup>	Required parameters for thermal fluid pipe

Table A6.2 Continuation

Heat transfer fluid	HITEC		HITEC	Customized module
Pipe heat losses, MW	-		variable	Simulation in due course
Max. working temperature, °C	500		500	
Shape factor for laminar flow viscous friction, -	-		64	
Laminar flow upper Re number limit, -	-		2000	Required parameters for thermal fluid pipe module
Turbulent flow lower Re number limit, -	-		4000	
Nusselt number for laminar flow heat transfer, -	-		3.66	
Model, cold side pump	36ENL-3 CS		Fixed-displacement pump with controller	Simscape module
Model, hot side pump	36ENL-1 SS		Fixed-displacement pump with controller	Simscape module
<b>IHTS pump-1 operational parameters</b>				
Prim. Medium (liq.)	HITEC XL	HITEC	HITEC	MS properties are f(T)
Work pressure (inlet/outlet), bar	1/6	1/6	15	Max. value [182]
Friction torque vs. max. pressure gain coefficient, Nm/Pa	-	-	0.6	Boundary conditions for fixed-displacement pump module [182]
Nominal pressure gain, MPa	-	-	1.7	
No-load torque, N·m	-	-	0.05	Boundary condition for fixed-displacement pump module [182]
Work temperature (inlet/outlet), °C	270.1	270	270	f(T), mechanical module
Medium vol. flow (inlet), m <sup>3</sup> /s	3.89	3.81	3.89	
Medium mass flow, kg/s	7338.34	7189.98	7190	MATLAB <sup>®</sup> code: ideal value
Medium mass flow, pulse, kg/s	-	-	6660	Calculated, sensor data, average value
Medium mass flow, dwell, kg/s	-	-	418	
Medium density (inlet/outlet), kg/m <sup>3</sup>	1887.74	1887.81/ 1887.66	f(T)	Customized module
Medium velocity (inlet/outlet), m/s	2.53	2.47	2.50	

Table A6.2 Continuation

Nominal dynamic viscosity, Pa·s	-	-	0.00321	Boundary condition for fixed-displacement pump module [182]	
Pump angular velocity, rpm	-	-	1500		
Volumetric efficiency at nominal conditions,-	-	-	0.94		
Pump isentropic efficiency, -	-	0.85	0.85		MATLAB® code
Pump mechanical efficiency, -	-	0.998	0.998		MATLAB® code
Power consumption, MW	-	-	2.6		Calculated, sensor data
<b>IHTS pump-2 operational parameters</b>					
Prim. Medium (liq.)	HITEC XL	HITEC	HITEC	MS properties are f(T)	
Work pressure (inlet/outlet), bar	(1-2)/6	(1-2)/6	15	Maximum value	
Friction torque vs. max. pressure gain coefficient, N·m/Pa	-	-	0.6	Boundary condition for fixed-displacement pump module [182]	
Nominal pressure gain, MPa	-	-	1.7		
No-load torque, N·m	-	-	0.05	Boundary condition for fixed-displacement pump module [182]	
Work temperature (inlet/outlet), °C	465.1	465.01/ 465.22	465	f(T), mechanical module	
Medium vol. flow (inlet/outlet), m³/s	4.21	3.72	4.21		
Medium mass flow, kg/s	7322.38	6481.69	6481	MATLAB® code: ideal value	
Medium mass flow, pulse, kg/s	-	-	5920	Calculated, sensor data, average value	
Medium mass flow, dwell, kg/s	-	-	7980		
Medium density (inlet/outlet), kg/m³	1740.74	1740.82/ 1740.66	f(T)	Customized module	
Medium velocity (inlet/outlet), m/s	2.73	2.42	2.70		
Nominal dynamic viscosity, Pa·s	-	-	0.00321	Boundary condition for fixed-displacement pump module [182]	
Pump angular velocity, rpm	-	-	1500		
Volumetric efficiency at nominal conditions,-	-	-	0.94		
Pump isentropic efficiency, -	-	0.85	0.85		MATLAB® code
Pump mechanical efficiency, -	-	0.998	0.998		MATLAB® code
Power consumption, MW	-	-	3.0		Calculated, sensor data

Table A6.2: DEMO Intermediate Heat Transfer and Storage system parameters.

Table A6.3 Beginning

Parameter	Quasi-stationary simulation		Dynamic simulation	Comment
	Ref. [100]	Ref. [84]	Value	
<b>PCS-SG2-PH</b>				
Prim. Medium	Water (liq.)	Water (liq.)	Water (liq.)	
Sec. Medium	HITEC (liq.)	HITEC (liq.)	MS heat flow	Input only as temperature source, no input as fluid
Prim. inlet/outlet diameter, m	0.5	0.5	0.5	
Heat transfer area, m <sup>2</sup>	-	6074.1	6074	
Length, m	-	22.55	22.55	Tubes length in PH is equal to length of one simple fluid pipe.
Cross-sectional area, m <sup>2</sup>	-	-	0.2	Required parameter inside module
Aggregate equal length of local resistances, m	-	-	2.2	0.1 · total pipe length
Internal surface absolute roughness, m	-	-	15 · 10 <sup>-6</sup>	Required parameter inside module
Laminar flow upper Reynolds number limit, -	-	-	2000	Required parameter inside module
Turbulent flow lower Reynolds number limit, -	-	-	4000	Required parameter inside module
Laminar friction constant for Darcy friction factor, -	-	-	64	Required parameter inside module
Nusselt number for laminar flow heat transfer, -	-	-	3.66	Required parameter inside module
Global heat transfer coefficient, W/(m <sup>2</sup> ·°C)	-	819.63	820	Rounded value
Convection heat transfer coefficient of water (tube side), W/(m <sup>2</sup> ·°C)	-	21943.8	21943	Heat transfer area and overall heat transfer coefficient are required for convective heat transfer module coupled to PH.
<b>PCS-SG2</b>				
Prim. Medium	Water /steam	Water/steam	Water/steam	
Sec. Medium	HITEC	HITEC	MS heat flow	Input only as temperature source, no input as fluid
Prim. inlet/outlet diameter, m	0.5/0.6	0.5/0.6	0.5/0.6	
Heat transfer area, m <sup>2</sup>	-	7722.9	7723	
Global heat transfer coefficient, W/(m <sup>2</sup> ·°C)	-	1697.74	1700	
Total fluid volume, m <sup>3</sup>	-	-	7812	Multiplying vol. flow of 1.085 m <sup>3</sup> /s with time of 7200 s

Table A6.3 Continuation

Convection heat transfer coefficient of water (tube side), W/(m <sup>2</sup> ·°C)	-	195004.3	195004	Heat transfer area and overall heat transfer coefficient are required for convective heat transfer module coupled to SG.
Convection heat transfer coefficient of HITEC (shell side), W/(m <sup>2</sup> ·°C)	-	8728.6	8729	Shell-side convective heat transfer over tube bundle is considered.
<b>PCS-SG2-SH</b>				
Prim. Medium	Steam	Steam	Steam	
Sec. Medium	HITEC	HITEC	MS heat flow	Input only as temperature source, no input as fluid
Prim. inlet/outlet diameter, m	0.6/0.7	0.6/0.7	0.6/0.7	
Heat transfer area, m <sup>2</sup>	-	5039.2	5040	Rounded value
Length, m	-	24.98	25	Tubes length in SH is equal to length of one simple fluid pipe
Cross-sectional area, m <sup>2</sup>	-	-	0.28	Required parameter inside module
Global heat transfer coefficient, W/(m <sup>2</sup> ·°C)	-	912.77	913	Rounded value
Convection heat transfer coefficient of steam (tube side), W/(m <sup>2</sup> ·°C)	-	17764.3	17764	Heat transfer area and overall heat transfer coefficient are required for convective heat transfer module coupled to SH.
<b>Steam-steam-SR1-HX</b>				
Model	Heat exchanger	Heat exchanger	Customized, thermal two-phase fluid pipe module	Module design is simplified: heat transfer only through convection. Module models a super-heater that increases temperature of steam beyond saturation.
Prim. Medium	Steam	Steam	Steam	
Sec. Medium	Steam/water	Steam/water	-	
Prim. inlet/outlet diameter, m	2.2	2.2	2.2	Hydraulic diameter
Total pipe length, m	-	-	25	Required parameter inside module
Pipe area, m <sup>2</sup>	-	-	3.8	Required parameter inside module
Aggregate equal length of local resistances, m	-	-	2.5	0.1 · total pipe length
Internal surface absolute roughness, m	-	-	15·10 <sup>-6</sup>	Required parameter inside module
Laminar flow upper Reynolds number limit,-	-	-	2000	Required parameter inside module
Turbulent flow lower Reynolds number limit, -	-	-	4000	Required parameter inside module

Table A6.3 Continuation

Laminar friction constant for Darcy friction factor, -	-	-	64	Required parameter inside module
Nusselt number for laminar flow heat transfer, -	-	-	3.66	Required parameter inside module
Convective heat transfer area, m <sup>2</sup>	-	-	2520	Required parameter inside module
Heat transfer coefficient, W/(m·°C)	-	-	913	Required parameter inside module
<b>Steam-steam-SR2-HX</b>				
Model	Heat exchanger	Heat exchanger	Customized, thermal two-phase fluid pipe module	Module design is simplified where heat transfer is applied only through the convection. Module models a super-heater that increases temperature of steam beyond saturation.
Prim. Medium	Steam	Steam	Steam	
Prim. inlet/outlet diameter, m	2.2	2.2	2.2	Hydraulic diameter
Total pipe length, m	-	-	25	Required parameter inside module
Pipe area, m <sup>2</sup>	-	-	3.8	Required parameter inside module
Aggregate equal length of local resistances, m	-	-	2.5	0.1 · total pipe length
Internal surface absolute roughness, m	-	-	15·10 <sup>-6</sup>	Required parameter inside module
Laminar flow upper Reynolds number limit, -	-	-	2000	Required parameter inside module
Turbulent flow lower Reynolds number limit, -	-	-	4000	Required parameter inside module
Laminar friction constant for Darcy friction factor, -	-	-	64	Required parameter inside module
Nusselt number for laminar flow heat transfer	-	-	3.66	Required parameter inside module
Convective heat transfer area, m <sup>2</sup>	-	-	2520	Required parameter inside module
Heat transfer coefficient, W/(m·°C)	-	-	913	Required parameter inside module

Table A6.3 Continuation

<b>PCS Turbine</b>				
Prim. Medium	Steam	Steam	Steam	
High pressure fluid flow area (inlet/outlet), m <sup>2</sup>	-	-	0.38/3.8	
Low pressure fluid flow area (inlet/outlet), m <sup>2</sup>	-	-	3.8/380	Inlet/outlet fluid flow area for turbines is calculated using inlet/outlet diameter.
<b>PCS Condenser</b>				
Prim. Medium	Cooled water	Cooled water	Steam/ cooled water	
Pipe area, m <sup>2</sup>	-	-	0.16	Required parameter inside module
Pipe cross-section area, m <sup>2</sup>	-	-	380/3.8	Terminal A/B
Heat transfer area, m <sup>2</sup>	-	61648.3	61648	
Global heat transfer coefficient, W/(m·°C)	-	1537.90	1540	Rounded value
Volume of condensed water, m <sup>3</sup>	-	-	17713	Required parameter inside module. Condenser volume is reduced to a min. value by reducing volume of condensed water, being calculated.
<b>PCS feedwater pump</b>				
Prim. Medium	Water	Water	Water	
Cross section area, m <sup>2</sup>	-	-	0.16	Inlet A / Outlet B terminal
<b>Abbreviations</b>				
PCS - Power Conversion System				
PH - Pre-heater				
SG - Steam generator				
SH - Super-heater				
SR - Steam Re-heater				

Table A6.3: DEMO Power Conversion System design parameters.



Table A6.4 Beginning

Parameter	Quasi-stationary simulation		Dynamic simulation	Comment
	Ref. [100]	Ref. [84]	Value	
Gross power (pulse/dwell), MW	-	808/730 (downstream 5 HP/4 LP steam turb.)	Start phase: 651/560 Stable operation: 563/548	Defined using power sensor after load coupled to HP and LP steam turbines. One HP and LP steam turbine is considered.
Net power (pulse/dwell), MW	-	659/713	-	-
Gross/Net efficiency,%	-	36.5/30.7	30-35	Rankine Cycle efficiency
Model	-	-	-	Module provides fluid properties to attached two-phase fluid network. Fluid property tables are two-dimensional arrays in which the rows correspond to normalized liquid internal energy vector or normalized vapor internal energy vector, and the columns correspond to pressure vector. Saturated liquid specific internal energy vector and saturated vapor specific internal energy vector are one-dimensional arrays with same length as pressure vector.
<b>Water/steam properties</b>				
Minimum valid specific internal energy, kJ/kg	-	-	25	
Maximum valid specific internal energy, kJ/kg	-	-	4000	
Pressure vector, bar	-	-	0.01-1000	
Critical pressure, bar	-	-	220.64	
Thermal transport properties near critical point, -	-	-		Peak values are clipped
Fraction above and below critical pressure for clipping, -	-	-	0.12	
Atmospheric pressure, bar	-	-	1.013	
Dynamic pressure threshold for flow reversal, Pa	-	-	0.01	

Table A6.4 Continuation

<b>Liquid properties</b>				
Model	-	-	Source code	
Normalized liquid internal energy, -	-	-	- 1 up to 0	Vector
Liquid specific volume, m <sup>3</sup> /kg	-	-	0.001 - 0.00102	Table
Liquid specific entropy, kJ/(kg·K)	-	-	0.091 - 0.544	Table
Liquid temperature, K	-	-	279.097-796.167	Table
Liquid kinematic viscosity, mm <sup>2</sup> /s	-	-	1.474 - 0.127	Table
Liquid thermal conductivity, W/(m·K)	-	-	0.569 - 0.376	Table
Liquid Prandtl number, -	-	-	10.871 - 0.930	Table
Saturated liquid specific internal energy, kJ/kg	-	-	29.297-2240.407	Vector
<b>Steam properties</b>				
Model	-	-	Source code	
Normalized vapor internal energy, -	-	-	1-2	
Vapor specific volume, m <sup>3</sup> /kg	-	-	129.178 - 0.006	Table
Vapor specific entropy, kJ/(kg·K)	-	-	8.974- 6.790	Table
Vapor temperature, K	-	-	280.119-1353.073	Table
Vapor kinematic viscosity, mm <sup>2</sup> /s	-	-	1181.750 - 0.347	Table
Vapor thermal conductivity, W/(m·K)	-	-	0.017 - 0.257	Table
Vapor Prandtl number, -	-	-	1.005 - 0.663	Table
Saturated vapor specific internal energy, kJ/kg	-	-	2384.488 - 2240.407	Table
<b>H<sub>2</sub>O-MS-SG2-PH</b>				
Model	Heat exchanger	Heat exchanger		Customized thermal liquid pipe module. Module design is simplified where heat transfer is applied only through convection. Pipes contain a constant fluid volume and operating temperature/pressure are based on liquid compressibility and thermal capacity.
Prim. Medium	water (liq.)	water (liq.)	water (liq.)	

Table A6.4 Continuation

Sec. Medium	HITEC (liq.)	HITEC (liq.)		No circulation of HITEC
Prim. Work pressure (inlet/outlet), pulse operation, bar	130.5 (130.7/129.71)	125.697/125.37	126	Prim. Work pressure is 121 bar/126 bar
Prim. Work pressure (inlet/outlet), dwell operation, bar	-	-	139	Prim. Work pressure is 134 bar/139 bar
Prim. Work temperature (inlet/outlet), °C	235.47/325.04	258.78/322.95	259/323	Rounded values
Sec. Work temperature (inlet/outlet), °C	339.48/304.2 (-/304.21)	336.0/309.67	336	Secondary inlet temperature of HITEC is assumed as heat input source for SG 2 PH.
Sec. Work temperature difference, °C	35.21	26.33	20	Temperature difference is calculated using sensor data.
Prim. Medium mass flow (pulse/dwell), kg/s	842.06/421.03	718.88/821	710/710 597/578	After 30 s At 3500 s (stable)
Prim. Medium density (inlet/outlet), kg/m <sup>3</sup>	829.36/657.88	795.26/662.54	f(T,p)	Calculated at inlet of PH using mass flow rate sensor. Dependent on water/steam properties module.
Heat flow, MW	-	-	104	At 3500 s Calculated using heat flow sensor. Heat losses through convection are considered. During dwell time heat flow in PH is not considered.
<b>H<sub>2</sub>O-MS-SG2</b>				
Model block	Heat exchanger with Prim./Sec. fluids	Heat exchanger with Prim./Sec. fluids		Customized steam boiler type with one fluid in two phases (water and steam) that are not mixed together Simscape module includes a heat transfer sensor and a temperature input source. Fluid in SG exists as a saturated, homogenous mixture of steam and water at uniform pressure. SG module has a constant volume of saturated fluid in a two-phase fluid network, whereas volume is divided into saturated vapour and saturated liquid.
Liquid volume fraction, -	-	-	0.7	Liquid level inside SG2 is given as volume fraction inside saturated chamber. It is equal to quotient between water amount and total fluid volume. Liquid volume fraction levels between 0.4-0.9 are studied.
Prim. Medium	Water/steam	Water/steam		No circulation of HITEC

Table A6.4 Continuation

Sec. Medium	HITEC (liq.)	HITEC (liq.)		
Prim. Work pressure, pulse (inlet/outlet),bar	130.3 (131.71 /129.68)	125.37	125	Prim. Work pressure is 121 bar/125 bar
Prim. Work pressure, dwell (inlet/outlet),bar	-	-	138	Prim. Work pressure is 134 bar/138 bar
Prim. Work temperature (inlet/outlet), °C	325.04/331.04 330.68/330.66	322.95/328.04	323/328	
Sec. Work temperature (inlet/outlet), °C	426.67/339.48 (-/342.18)	425.89/336	426	Secondary inlet temperature of HITEC is assumed as heat input source for SG 2. No outlet temperature is required explicitly.
Sec. Work temperature difference, °C	87.19	89.59	114	Temperature difference is calculated using measuring sensor.
Prim. Medium vol. flow (inlet/outlet), m <sup>3</sup> /s	1.28/10.73	1.085/9.67	1.085	
Heat flow, pulse/dwell, MW	-	-	1424/1395	3500 s/7300 s : Calculated using data from heat flow sensor
<b>H<sub>2</sub>O-MS-SG2-SH</b>				
Model	Heat exchanger	Heat exchanger		Customized thermal liquid pipe module. Module design is simplified where heat transfer is applied only through convection. SH is used for generation of steam with respect to power production. Unidirectional flux exchange is considered. Pipe contains a constant fluid volume and operating temperature/pressure are based on liquid compressibility and thermal capacity.
Prim. Medium	Steam	Steam	Steam	
Sec. Medium	HITEC (liq.)	HITEC (liq.)		No circulation of HITEC
Prim. Work pressure (inlet/outlet), bar	130.3 129.68/124.69	125.37/125.12	125	Prim. Work pressure is 121 bar/125 bar
Prim. Work pressure, dwell (inlet/outlet),bar	-	-	138	Prim. Work pressure is 134 bar/138 bar
Prim. Work temperature (inlet/outlet), °C	331.04/445.82 (330.66/-)	328.04/448.48	328/448	
Sec. Work temperature (inlet/outlet), °C	465.22/426.67 (-/426.02)	465.22/425.89	465	Secondary inlet temperature of HITEC is assumed as heat input source for SG2 SH. No outlet temperature is required explicitly
Sec. Work temperature difference, °C	38.55	39.33	17	Temperature difference is calculated using measuring sensor.
Heat flow, pulse, MW	-	-	66	At 3500 s Calculated using heat flow sensor. Heat losses through convection are considered. During dwell time, heat flow into SH is not considered.

Table A6.4 Continuation

<b>Steam-steam-SR1-HX</b>				
Model	Heat exchanger	Heat exchanger	Customized, thermal two-phase fluid pipe module	Module design is simplified where heat transfer is applied only through the convection. Module models a super-heater that increases temperature of steam beyond saturation. Fluid inertia is not considered.
Prim. Medium	Steam	Steam	Steam	
Prim. Work pressure (inlet/outlet), bar	11.88/11.57	10.75	10.7/10.5	Initial steam pressure
Prim. Work temperature (inlet/outlet), °C	187.51/251.04	183.031/250.40	185	Initial steam temperature
Sec. Work temperature (inlet/outlet), °C	329.68/272.33	336.71/271.02	336.71/271	Furnace temperature
Phase change time constant, s	-	-	0.1	Required parameter inside module
<b>Steam-steam-SR2-HX</b>				
Model	Heat exchanger	Heat exchanger	Customized, thermal two-phase fluid pipe module	Module design is simplified where heat transfer is applied only through the convection. Module models a super-heater that increases temperature of steam beyond saturation. Fluid inertia is not considered.
Prim. Medium	Steam	Steam	Steam	
Prim. Work pressure (inlet/outlet), bar	11.57/11.25	10.49	10.4/10.2	Initial steam pressure
Prim. Work temperature (inlet/outlet), °C	251.04/307.15	250.40/306.64	250	Initial steam temperature
Sec. Work temperature (inlet/outlet), °C	441.11/328.46	441.87/323.33	441.87/323	Furnace temperature
Phase change time constant, s	-	-	0.1	Required parameter inside module
<b>Steam turbines</b>				
Model	Steam turbines	Steam turbines	Turbine module in a two-phase fluid network	Pressure drop and flow rate are scaled from specified nominal operation condition. Pressure and temperature data are based on compressibility and thermal capacity of vapour pressure.
Load	-	-	Calculation of mechanical power down-stream HP and LP steam turbine	Mechanical conserving port of torque sensor is coupled to conserving port of HP and LP steam turbines. Shaft speed is applied to physical signal port of an ideal angular velocity source. Torque relative to shaft speed is measured at sensor port, whereas the measured torque and shaft speed are converted into mechanical power via conversion factor in gain block.
Prim. Medium	Steam	Steam	Steam	

Table A6.4 Continuation

Number of HP/LP turbine stages	5/4	5/4	1/1	Single stage of HP/LP steam turbine is considered. Feedwater heaters for partly extraction of steam are not considered
Work pressure, pulse (HP inlet/outlet), bar	130/11.88	121.43/10.75	121/11	Pressure is rounded to a whole number
Work pressure, dwell (HP inlet/outlet), bar	-	-	134	Required parameter inside module
Work pressure, pulse/dwell (LP inlet/outlet), bar	11.25/0.049	10.75/0.046	11/0.046	Pressure is rounded to a whole number
Inlet nominal volume, HP turbine, m <sup>3</sup> /kg	-	-	0.014	Required parameter inside turbine module
Inlet nominal volume, LP turbine, m <sup>3</sup> /kg	-	-	0.19	Required parameter inside turbine module
Medium mass flow, HP inlet/outlet, pulse, kg/s	842.06/ 856.36	718.88/763.1	660/597	Only at inlet of HPT: After 30 s/At 3500 s (stable). Inlet mass flow of 719 kg/s is inserted inside the module as boundary condition. Calculated via mass flow rate sensor.
Medium mass flow, HP inlet, dwell, kg/s	-	821	655/578	Only at inlet of HPT: After 30 s/At 3500 s (stable). Inlet mass flow of 719 kg/s is inserted inside the module as boundary condition. Calculated via mass flow rate sensor.
Medium mass flow, LP inlet/outlet, pulse, kg/s	808.69/739.39	724.25/666.65	660/597	Only at outlet of LPT: After 30 s/At 3500 s (stable). Inlet mass flow of 724 kg/s is inserted inside the module as boundary condition. Calculated via mass flow rate sensor.
Medium mass flow, LP outlet, dwell, kg/s	-	638		
Max. PCS output, MW <sub>mech</sub>	1009	-	200	Theoretical output for each turbine
ST isentropic efficiency, -	0.88	0.88	0.88	
ST mechanical efficiency, -	0.998	0.998	0.998	
<b>Feedwater pump</b>				
Manufacturer	KSB	KSB	-	Feedwater pump is replaced and simplified. Control mass flow rate source with a PI controller. Module represents an ideal mechanical energy source in a two-phase fluid network that can maintain a controlled mass flow rate regardless of pressure differential. No flow resistance and no heat exchange with environment is supposed. When liquid level of SG achieves set-point, controller forms the nominal mass flow rate signal, which maintains liquid level through mass flow rate.
PI Controller	-	-	K <sub>p</sub> = 50000 K <sub>I</sub> = 0.01	Pump controller: Module implements continuous-time PI control algorithm, includes advanced feature “anti-windup”. Varied K <sub>p</sub> = 0.01,100, 50000 and K <sub>I</sub> = 0.01–50000 [225].

Table A6.4 Continuation

Back-calculation coefficient $K_b$ , -	-	-	1	Required parameter inside module
Prim. Medium	Water (liq.)	Water (liq.)	Water (liq.)	
Pump isentropic efficiency, -	0.85	0.85	-	Isentropic, no value is required
<b>Condenser</b>				
Model	Not same design as SG	Not same design as SG	Heat exchanger with same module design as steam generator	Module models a condenser that rejects heat from saturated steam and collects condensate. Condenser transforms dry steam coming from LP steam turbine to liquid in form of condensate. Steam is condensed over the tubes through which cold water flows. Water is pumped through tubes with steam, which condenses and is collected at bottom in a hot well. Water in tubes flows back to cooling tower.
Prim. Medium	Steam/water	Steam/water	Steam/water	
Liquid volume fraction, -	-	-	0.2/0.01/0.99	Initial/Min/Max
Prim. Work pressure (inlet/outlet), bar	0.049 (0.05/0.04)	0.046	0.046	Considered as initial inlet, saturation pressure
Sec. Work temperature (inlet/outlet), °C	20 (32.52)/ 27.52 (30.61)	20 (26.90)	20	Secondary initial inlet temperature of water is used as coolant input source.
Total fluid volume, m <sup>3</sup>	-	-	17713	Per second, taken from vol. flow
Prim. Medium mass flow (pulse/dwell), kg/s	739.39/ 369.70	667/677	710/710 597/578	After 30 s/At 3500 s (stable). Calculated at outlet of steam condenser using sensor data.
Abbreviations:				
HX – Heat Exchanger				
MS – Molten Salt				
PH – Pre-heater				
SG – Steam Generator				
SR – Steam Re-heater				

Table A6.4: DEMO Power Conversion System operational parameters.

## A.7 MATLAB®/Simulink Custom Library: Rankine Cycle model

The sketch of the model of a steam turbine system, which is based on the Rankine Cycle, is presented in Fig. A7.1. It includes super-heating and re-heating, which are used to prevent condensation at high-pressure and low-pressure turbines, respectively. The schemes of feedwater pre-heater, steam boiler, condenser and re-heater modules from MATLAB®/Simulink Custom Library are presented in Fig. A7.2-A7.5, correspondingly [215].

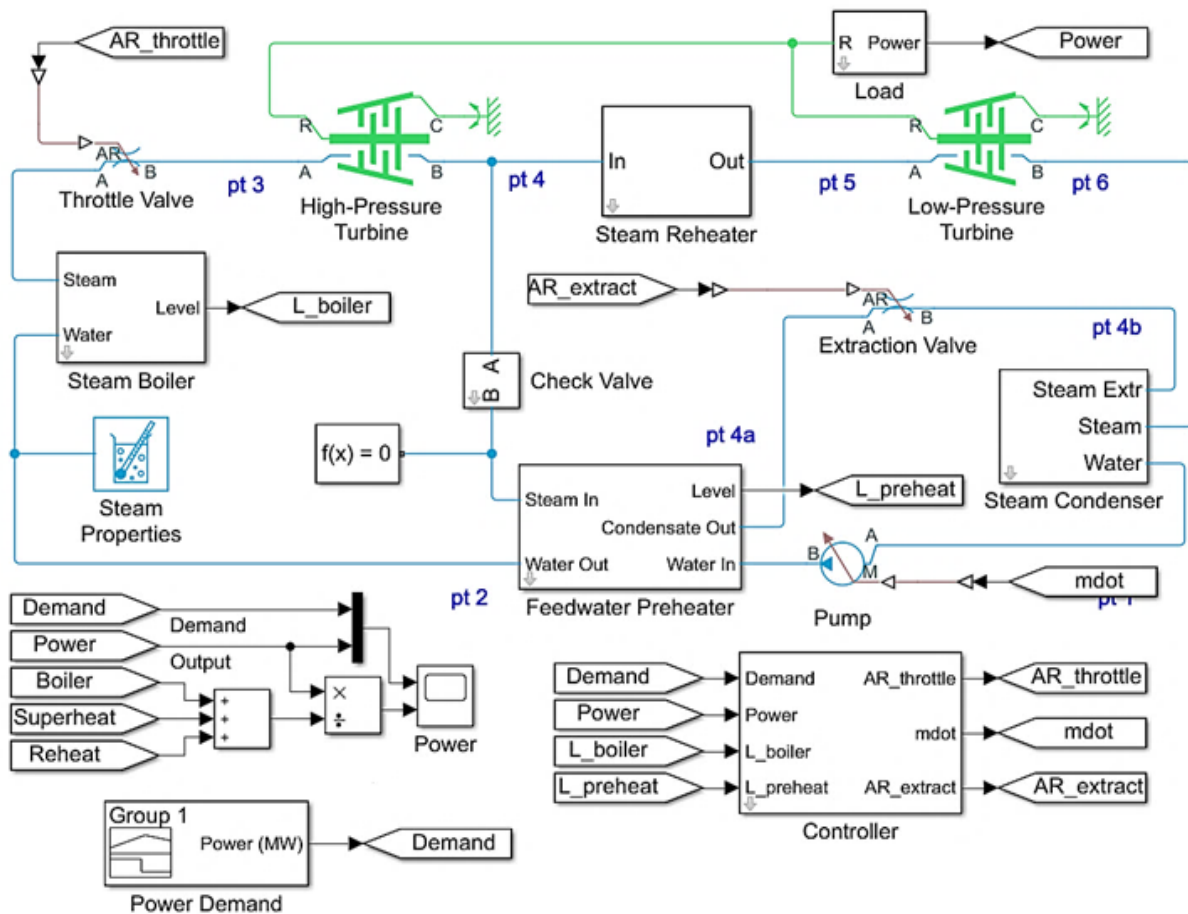


Fig. A7.1: Sketch of MATLAB®/Simulink Rankine Cycle model [215].



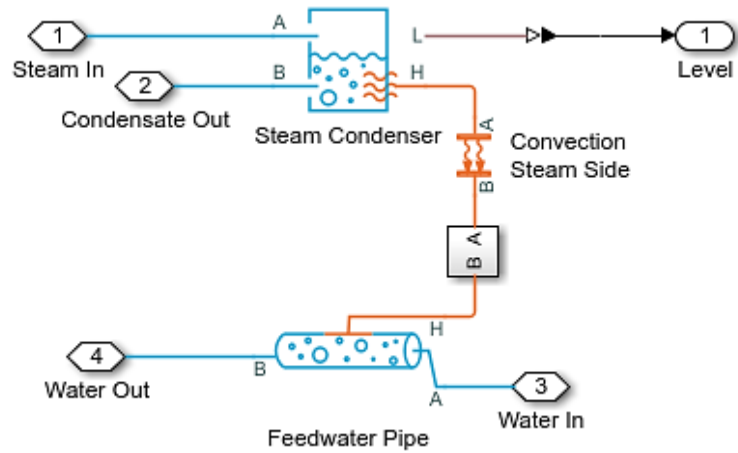


Fig. A7.2: Scheme of feedwater pre-heater module [215].

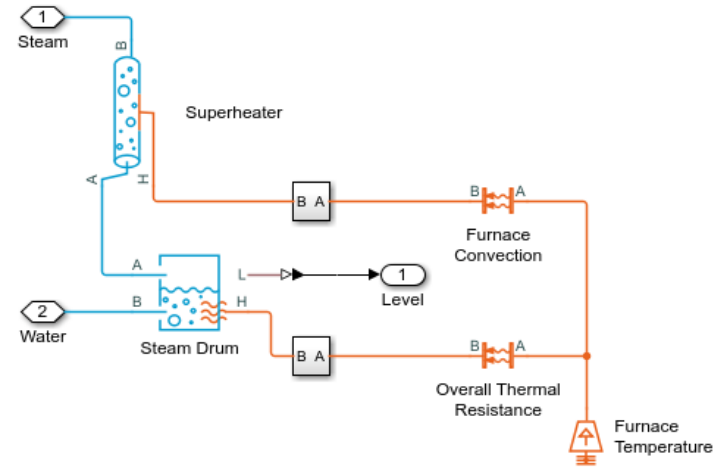


Fig. A7.3: Scheme of steam boiler module [215].

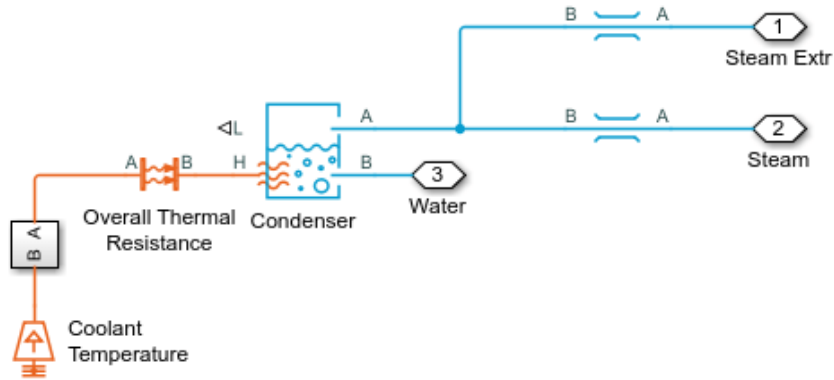


Fig. A7.4: Scheme of steam condenser module [215].

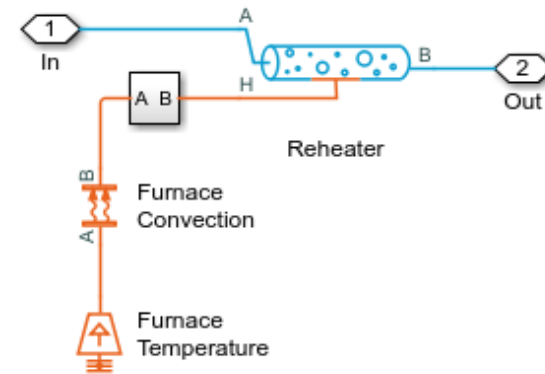


Fig. A7.5: Scheme of steam re-heater module [215].



## List of Figures

1.1 The European Fusion Roadmap [36] .....	2
1.2 Interface of the systems of DEMONstration Balance of Plant with Helium Cooled Pebble Bed Indirect Coupling Design (ICD) concept: BB – Breeding Blanket, ESS – Energy Storage System, VV – Vacuum Vessel, VVPSS – Vacuum Vessel Pressure Suppression System [51,55].....	3
1.3 DEMO BoP electrical distribution system [56] .....	4
1.4 Scheme of DEMO BoP design concept [33].....	5
1.5 Gravimetric storage density as function of maximum storage temperature [71].....	7
2.1 Calculated temperature dependence of HITEC density .....	21
2.2 Comparative diagrams for density difference according to eqs. (2.2) and (2.4)-(2.6).....	22
2.3 Comparison between simulated and experimental data for HITEC density, dashed line – calculated values according to eq. (2.5), black dots – experimental data from Table 2.3 .....	23
2.4 HITEC dynamic viscosity as function of MS temperature .....	24
2.5 HITEC specific heat capacity as function of MS temperature .....	25
2.6 HITEC thermal conductivity as function of MS temperature .....	26
2.7 Dependence of HITEC relative density and volume with increasing MS temperature .....	27
3.1 Model scheme of thermal storage tank with molten salt and cover gas.....	31
3.2 Scheme of simulation model of DEMO IHTS thermal storage tank [33].....	35
3.3 Customized module for heat losses to environment from a thermal storage tank .....	37
4.1 Storage tank volume for variable diameter and height .....	44
4.2 Storage tank lateral wall area for variable diameter and height .....	45
4.3 Storage tank total area for variable diameter and height.....	45
4.4 Temperature drop inside cold storage tank for various thermal insulation thickness .....	49
4.5 Temperature drop inside hot storage tank for various thermal insulation thickness.....	50
4.6 Temperature drop inside cold storage tank with various tank height .....	50

4.7 Temperature drop inside hot storage tank with various tank height .....	51
4.8 Change of molten salt temperature in storage tanks due to cooling phenomena .....	53
4.9 Temperature drop of molten salt in dependence of simulated time interval .....	53
4.10 Simulated transient heat loss per day for cold and hot storage tanks.....	54
4.11 Simulated transient heat loss per area from cold and hot storage tanks per day .....	55
5.1 Schematic view of DEMO BoP energy transfer chain [55] .....	57
5.2 Simulation model of DEMO PHTS-IHTS system [33, 221] .....	58
5.3 Pipeline module for heat losses to environment.....	62
5.4 Fixed-displacement pump module with working mode diagram.....	62
5.5 Scheme of PHTS Outer Blanket/Inner Blanket Loops module with heat exchangers.....	65
5.6 Module for control of heat transfer between different thermal liquid networks [215] .....	66
5.7 PCS SG2 module with pre-heater, steam generator and super-heater [182], extended with control sensors for mass and energy flow rates.....	69
5.8 Scheme of simulation model for DEMO PCS .....	70
5.9 Scheme of coupling of PCS pre-heater, steam generator and super-heater modules.....	72
5.10 Sketch of a single steam turbine stage .....	78
5.11 Scheme of steam condenser module .....	80
5.12 Feedwater pump module with control function unit .....	81
6.1 Sketch of DEMO IHTS operation during pulse time .....	86
6.2 Simulated temporal evolution of HITEC filling level in cold and hot storage tanks during single operation cycle.....	87
6.3 Cold storage tank filling level for simulation time between 0-160 sec.....	87
6.4 Cold storage tank filling level for simulation time between 7040-7200 sec.....	87
6.5 Temporal evolution of HITEC filling level in storage tanks for 11 operation cycles.....	88

6.6 Simulated HITEC mass flow at cold tank inlet and outlet for single operation cycle .....	89
6.7 Simulated HITEC mass flow at cold tank inlet and outlet for 11 operation cycles .....	90
6.8 Thermal energy flow at inlet and outlet of hot storage tank for single operation cycle.....	91
6.9 Temporal evolution of heat losses from pipelines 1 and 2 for single operation cycle.....	92
6.10 Simulated temporal evolution of SG liquid level during pulse operation.....	93
6.11 Simulated temporal evolution of SG liquid level during dwell operation .....	93
6.12 Temporal evolution of mass flow during pulse operation at located sensor S2 downstream PCS PH-SG-SH module. ....	94
6.13 Temporal evolution of mass flow during dwell operation at located sensor S2 downstream PCS PH-SG-SH module .....	95
6.14 Schema of DEMO PCS PH-SG-SH module with temperature difference sensors.....	96
6.15 Temporal evolution of temperature difference in PCS PH-SG-SH module at pulse operation time interval of $30 \leq t \leq 7200$ sec .....	96
6.16 Temporal evolution of heat flow in pre-heater, steam generator and super-heater at pulse operation time interval of $30 \leq t \leq 7200$ sec .....	97
6.17 Temporal evolution of heat flow in PCS SG.....	98
6.18 Temporal evolution of mechanical power output downstream the HP and LP steam turbines .....	98
7.1 Sketch of the model for DEMO BoP energy transfer chain.....	107
7.2 Simulation model for DEMO BoP energy transfer chain .....	108
7.3 Temporal evolution of heat flow in a single PCS steam generator stage with PH-SG-SH modules for two operation cycles of fusion reactor .....	110
7.4 Temporal evolution of heat flow in PCS PH-SG-SH stage for transition between the 1 <sup>st</sup> and 2 <sup>nd</sup> operation cycle of fusion reactor .....	110
7.5 Temporal evolution of mechanical power output .....	111
7.6 Temporal evolution of mechanical power output, DEMO BoP stable operation .....	111

A1.1 DEMO BoP Direct Coupling Design concept [47].....	148
A1.2 Electrical power output profile for DEMO DCD concept [57].....	148
A1.3 DEMO BoP Indirect Coupling Design concept [47].....	149
A1.4 Electrical power output profile for DEMO ICD concept [57] .....	149
A2.1 DEMO BoP simulation model using EBSILON <sup>®</sup> code, pulse operation time [84].....	151
A2.2 DEMO BoP simulation model using EBSILON <sup>®</sup> code, dwell operation time [84].....	152
A7.1 Sketch of MATLAB <sup>®</sup> /Simulink Rankine Cycle model [215].....	176
A7.2 Scheme of feedwater pre-heater module [215] .....	177
A7.3 Scheme of steam boiler module [215].....	177
A7.4 Scheme of steam condenser module [215].....	177
A7.5 Scheme of steam boiler module [215].....	177

## List of Tables

2.1 Characteristics of heat transfer fluids [106-119].....	14
2.2 Thermo-physical parameters of heat transfer fluids [80, 106-119].....	15
2.3 HITEC molten salt thermo-physical parameters .....	18
2.4 Functional relations for temperature dependence of HITEC density.....	21
2.5 Functional relations for temperature dependence of HITEC dynamic viscosity .....	23
2.6 Functional relations for temperature dependence of HITEC specific heat capacity .....	25
2.7 Functional relations for temperature dependence of HITEC thermal conductivity .....	25
2.8 Sensitivity of HITEC molten salt parameters with the change of MS temperature.....	27
2.9 Sensitivity of mass and heat transfer parameters with the change of MS temperature.....	28
3.1 Governing equations for model of thermal storage tank, simulated as a thermal liquid container with variable fluid volume [215].....	36
3.2 Simulation modules for conductive, convective and radiative heat transfer [215].....	38
4.1 Technical parameters of DEMO IHTS thermal storage tanks [33, 84, 99, 182].....	41
4.2 Volume of HITEC molten salt for variable operating temperature .....	46
4.3 Ratio between the volume of HITEC molten salt and storage tank volume .....	47
4.4 Comparative data for DEMO IHTS thermal storage tanks .....	47
5.1 Governing equations for thermal liquid pipeline module [215].....	60
5.2 Governing equations of pipeline module for heat losses to environment [215] .....	61
5.3 Governing equations for fix-displacement pump module [215] .....	63
5.4 Governing equations for Simple Heat Exchanger Interface module [215].....	67
5.5 Governing equations for Specific Dissipation Heat Transfer module [215].....	68
5.6 Governing equations for PCS SG module as a chamber with fixed volume of two-phase fluid [215].....	74

5.7 Governing equations for rigid conduit of fluid flow in two-phase fluid systems, representing the pre-heater and super-heater modules [215] .....	75
5.8 Governing equations for steam turbine module [215] .....	79
5.9 Governing equations for steam condenser module [215, 226, 227].....	81
6.1 Governing equations for temporal evolution of MS filling level in cold storage tank .....	86
A1.1 Direct Coupling Design (DCD-1) with Auxiliary Boiler (DIRECT-AUXB) and Indirect Coupling Design (ICD) concepts .....	146
A1.2 Direct-Small Energy Storage System (DIRECT-Small ESS) coupling design concepts DCD-s1 and DCD-s2 .....	147
A2.1 Main operational parameters of DEMO BoP calculated using EBSILON <sup>®</sup> code .....	150
A4.1 Thermal Energy Storage operational parameters .....	155
A5.1 DEMO PHTS heat exchangers' parameters [84].....	156
A5.2 DEMO PHTS parameters [84, 100] .....	157
A5.3 DEMO IHTS parameters.....	157
A5.4 DEMO PCS parameters.....	157
A6.1 DEMO Primary Heat Transfer System parameters .....	158
A6.2 DEMO Intermediate Heat Transfer and Storage System parameters.....	160
A6.3 DEMO Power Conversion System design parameters.....	165
A6.4 DEMO Power Conversion System operational parameters .....	169